



UNIVERSITY
OF ABERDEEN



Curtin University

THERMAL TRANSPORT IN MIXTURES

CRAIG MOIR
2020

THIS THESIS WAS SUBMITTED AS PART OF THE REQUIREMENT FOR
THE PHD IN ENGINEERING.

ABSTRACT

Classical continuum models have been used to predict the thermal conductivity of fluid mixtures for over a century; however, it is reported that real mixtures, including gases mixtures and nanofluids, exhibit thermal conductivities outside these bounds. While effects such as particle geometry and structural arrangement are well investigated, simultaneous diffusion and thermal diffusion effects, as well as their resulting time dependence, remain relatively unexplored. This thesis analyses these phenomena and explores the link between *microscopic* and *macroscopic* definitions of heat transfer. It also attempts to better define what is an anomalous thermal conductivity, and what are the limits of performance with nanotechnology/nanofluids.

The hard-sphere model is used throughout the thesis in order to simulate fluid mixtures. This is the simplest molecular model which includes the effects of molecular size, thus its results are fundamental and have wide application. The model has an accurate micro-to-macroscale description available via kinetic theory and exact results for the model can also be obtained efficiently using equilibrium and non-equilibrium event-driven molecular dynamics. These methods are applied here to determine the most useful microscopic definition of the thermal conductivity and to compare binary hard-sphere thermal conductivity values against the classical continuum bounds. It is conclusively shown that even this simple system can greatly exceed classical predictions.

Real gas mixtures which display this “anomalous” behaviour are predicted using dimensional analysis and this behaviour is confirmed in helium-hydrogen systems using data from the literature. Further comparison with experimental data shows that the hard-sphere model is strongly predictive for gas mixtures.

The hard-sphere model also predicts a dramatic transient thermal conductivity increase which has not yet been captured by experiment or previously reported. In order to investigate the magnitude and timescale of potential transient effects, a fully-coupled kinetic theory and hydrodynamic model is created which is able to solve for the time-evolution of hard-sphere systems in an efficient manner. This simulation method is found to agree strongly with exact molecular dynamics simulation in the case of mono-component hard-sphere systems, even under extreme flows such as thermally induced shock-waves. Finally, this thesis presents a novel algorithm for calculating the free energy of molecular systems.

CONTENTS

Abstract	3
Nomenclature	15
1 Introduction	19
2 Continuum models of mixture thermal conductivity	25
2.1 Series-parallel limits	25
2.2 Maxwell theory	27
2.2.1 Temperature profile around a single sphere	27
2.2.2 System of spheres	30
3 Experimental evidence for unusual thermal conductivity	35
3.1 Experimental thermal conductivity measurement techniques	35
3.1.1 Transient heated wire	36
3.1.2 Heated/guarded plates	39
3.2 Experimental studies	40
3.2.1 The helium-hydrogen gas mixture	40
3.2.2 Solid-liquid mixtures / nanofluids	41
3.3 Proposed nanofluid enhancement mechanisms / explanations	45
3.3.1 Interparticle layering	45
3.3.2 Nanoparticle clustering	46
3.3.3 Brownian motion / thermal diffusion	48
4 The hard-sphere model	51
4.1 Event-driven molecular dynamics	53
4.2 Equilibrium measurements	58
4.3 Non-equilibrium techniques	60
4.3.1 Heated walls	60
4.3.2 Energy exchange	61

5	Kinetic theory and full multi-component hydrodynamics	65
5.1	Reynolds transport theorem	65
5.2	Phase space and the Liouville equation	68
5.2.1	BBGKY Heirarchy	71
5.2.2	Collision integral	72
5.2.3	Multi-component systems	74
5.3	Hydrodynamic equations	75
5.3.1	Continuity equation	75
5.3.2	Momentum equation	77
5.3.3	Energy equation	79
5.4	Closing the hydrodynamic equations	80
5.4.1	Defining the heat flux	82
5.4.2	Phenomenological equations	83
6	Micro to macroscopic thermal conductivity	87
6.1	Phenomenological thermal conductivity L_{uu}	87
6.2	Steady-state thermal conductivity λ	90
6.2.1	Binary derivation	91
6.3	Initial thermal conductivity λ_I	95
7	Investigating anomalous thermal conductivity dehancement	99
7.1	Simulation method	101
7.2	Enskog theory comparison with MD	102
7.3	Mapping the dehancement	104
7.4	Conclusions and future work	106
8	Investigating anomalous thermal conductivity enhancement	109
8.1	Initial thermal conductivity enhancement	110
8.2	Enhancement relative to the steady-state value	113
8.3	Conclusions and future work	116
9	Fitting Enskog theory to real systems	119
9.1	Predicting the kinetic diameter	120
9.2	Enskog comparison	122
9.2.1	Mixture 1: Helium-Hydrogen	122
9.2.2	Mixture 2: Argon-Krypton	124
9.2.3	Mixture 3: Krypton-Nitrogen	125
9.3	Dehancement in ternary mixtures	126
9.4	Conclusions and future work	128

10 Hydrodynamic simulations of transient effects	131
10.1 Finite Volume Method	132
10.2 Hydrodynamic model implementation	134
10.3 Boundary conditions	136
10.4 Model validation	139
10.4.1 Steady-state regime	140
10.4.2 Transient regime	142
10.5 Conclusions and future Work	146
10.5.1 Frequency-dependent thermal conductivity	147
11 Novel method for hard-sphere free energy determination	149
11.1 Tethered systems	151
11.1.1 Fluid-solid transition in the tethered particle model	152
11.1.2 Thermodynamic integration	155
11.2 Phase space geometry	155
11.2.1 Collision rates and hypersurface areas in phase space	156
11.3 Calculation of the entropy	160
11.3.1 Method 1	160
11.3.2 Method 2	162
11.4 Fluid-solid coexistence	166
11.5 Conclusions and future work	168
12 Conclusions	173
A Oscillating wall temperature analytical solution	177
B Alternative λ derivation for binary mixtures	183
C Reprint: Anomalous heat transport in binary hard sphere gases	185

LIST OF FIGURES

1.1	Thermal conductivity of various materials	20
1.2	Measured thermal conductivity enhancement in a copper-ethylene glycol nanofluid and a transmission electron micrograph image of a copper-ethylene glycol nanofluid	21
1.3	Thermal conductivity of the hydrogen-helium gas mixture	22
2.1	Material configurations corresponding to the series and parallel thermal conductivity limits as well as the upper and lower Maxwell bounds	26
2.2	Coordinate system for a single sphere embedded in an infinite medium under the influence of a linear temperature gradient (Maxwell theory) . .	28
2.3	Final temperature distribution for a sphere in an infinite medium under constant heat flux	31
3.1	Diagram of the transient heated wire experimental technique	36
3.2	Example transient heated wire temperature profile over time	38
3.3	Diagram of a steady-state thermal conductivity experimental technique . .	39
3.4	Comparison of the series-parallel thermal conductivity limits with experimental measurements for the binary helium-hydrogen gas mixture	41
3.5	Experimental thermal conductivity measurements of a Copper-ethylene glycol nanofluid in relation to the series-parallel limit and the Maxwell bounds	42
3.6	Experimental thermal conductivity measurements of a water-iron oxide nanofluid and a water-fullerene nanofluid in relation to the series-parallel limit and the Maxwell bounds	43
3.7	Experimental thermal conductivity measurements of nanofluids using different techniques	44
3.8	Ordered layering of base fluid particles around solid nanoparticles in nanofluids	46
3.9	Nanoparticle clustering in nanofluids	47
4.1	Hard-sphere diagram and a graph of the hard-sphere potential	52
4.2	Hard-sphere phase diagram	52

4.3	Event-driven molecular dynamics collision detection and restituted velocity calculation	56
4.4	Event-driven molecular dynamics algorithm flowchart	57
4.5	Decay of microscopic fluctuations in a molecular dynamics simulation . .	58
4.6	NEMD parallel heated walls thermal conductivity measurement technique	60
4.7	NEMD energy exchange thermal conductivity measurement technique . .	62
5.1	Trajectories of an ensemble of molecular systems through phase space . .	69
5.2	Diagram of the hard-sphere collision integral	73
6.1	Heat transfer through a multicomponent hard-sphere fluid (a) at the onset of heat transfer and (b) at steady-state conditions illustrating the effects of thermal diffusion	88
6.2	Enskog prediction of the phenomenological thermal conductivity for a binary hard-sphere mixture showcasing potential thermal conductivity enhancement above the parallel limit	89
6.3	Comparison between Enskog predictions of the steady-state thermal conductivity for the helium-hydrogen binary gas mixture with experimental data.	94
7.1	Diagram of the binary hard-sphere model	101
7.2	Temperature and density profiles in a NEMD parallel heated walls simulation	102
7.3	NEMD measured thermal conductivity as a function of simulation length	103
7.4	Comparison between equilibrium and non-equilibrium MD thermal conductivity measurements and kinetic theory predictions for a binary hard-sphere gas	104
7.5	Deviation of steady-state thermal conductivity from the series-parallel limits mapped over binary hard-sphere parameter space	105
7.6	Deviation of steady-state thermal conductivity from the series-parallel limits predicted for binary mixtures of the noble gases, nitrogen, and hydrogen	106
8.1	Phenomenological, initial, and steady-state thermal conductivity as a function of mixture concentration for a binary hard-sphere gas	110
8.2	Maximum initial thermal conductivity enhancement above the parallel limit mapped over binary hard-sphere parameter space	111
8.3	Mixture concentration corresponding to the maximum initial thermal conductivity enhancement mapped over binary hard-sphere parameter space .	112
8.4	Maximum initial thermal conductivity enhancement relative to the steady-state value mapped over binary hard-sphere parameter space	114

8.5	Mixture concentration corresponding to the maximum initial thermal conductivity enhancement relative to the steady-state value mapped over binary hard-sphere parameter space	115
8.6	Maximum initial thermal conductivity enhancement relative to the steady-state value predicted for binary mixtures of the noble gases, nitrogen, and hydrogen	116
9.1	Thermal conductivity of the helium-hydrogen gas mixture: comparison of experimental results with Enskog theory predictions	123
9.2	Thermal conductivity of the argon-krypton gas mixture: comparison of experimental results with Enskog theory predictions	124
9.3	Thermal conductivity of the krypton-nitrogen gas mixture: comparison of experimental results with Enskog theory predictions	126
9.4	Steady-state thermal conductivity dehancement below the series limit and absolute steady-state thermal conductivity for a ternary hydrogen-helium-neon gas mixture	127
10.1	Diagram of an individual finite volume cell	133
10.2	Uniform rectangular finite volume grid	135
10.3	Boundary implementation for a 1-dimensional finite volume simulation .	136
10.4	Steady-state hard-sphere temperature and density profiles: comparison between NEMD simulation and a hydrodynamic-kinetic theory model for a monocomponent system	141
10.5	Steady-state hard-sphere temperature and density profiles: comparison between NEMD simulation and a hydrodynamic-kinetic theory model for a multicomponent system	142
10.6	Hard-sphere temperature and density profiles in the transient regime: comparison between NEMD simulation and a hydrodynamic-kinetic theory model for a monocomponent system	144
11.1	Schematic diagram of the tethered particle model (TPM) in three states: ideal TMP, TMP fluid, and conventional hard-sphere equivalent	151
11.2	Compressibility as a function of density for the hard-sphere TPM system showing the fluid-solid transition	153
11.3	Hard-sphere TPM phase diagram	154
11.4	Configurational phase space diagram for the TPM showing 3 states: a conventional hard-sphere system, a tightly tethered system, and a loosely tethered system	156
11.5	Tether potential event rate as a function of tether length	159
11.6	Entropy as a function of particle number showing the linear scaling to infinite system size	161

11.7 Deviation of the tether potential event rate from the ideal event rate as a function of the tether cell radius	163
11.8 Tether potential event rate as a function of the tether cell radius	163
11.9 Entropy as a function of particle number showing the linear scaling to infinite system size	164
11.10 Deviation of calculated entropy values, as well as literature values, from the extrapolated average value	167
11.11 Chemical potential as a function of pressure showing the predicted hard-sphere fluid-solid coexistence point	168

LIST OF TABLES

9.1	Equivalent hard-sphere diameters of the noble gases, hydrogen, and nitrogen calculated using measured thermal conductivity values	121
11.1	Calculated entropy for different particle numbers using constant tether cell volume fraction integration	161
11.2	Calculated entropy for different particle numbers using constant density, varying tether cell radius integration	164
11.3	Calculated entropy for constant density, varying tether length integration showing the infinite tether length entropy corrections	165
11.4	Extrapolated hard-sphere entropy at various number densities	166

NOMENCLATURE

Acronyms/Terminology

AMD	Advanced Micro Devices, 19
BMCSL	Boublik - Mansoori - Carnahan - Starling EOS, 59
CPU	Central processing unit, 19
DSMC	Direct simulation Monte Carlo, 147
EOS	Equation of state, 59
FCC	Face-centered cubic, 151
MC	Monte Carlo, 149
MD	Molecular dynamics, 23
NEMD	Non-equilibrium molecular dynamics, 60
SO	Single occupancy, 149
SVD	Singular value decomposition, 91
TPM	Tether particle model, 149

Operators

:	Double dot product, 81
+	Generalised inverse, 91
∇	Del operator, 27
T	Matrix transpose, 135

Notation

B	Boundary value, 137
*	Reduced quantity, 120
$-$	Volume average, 133

Variables/Constants

$\mathbf{1}$	Identity matrix, 83
A	Area, 40
A_C	Avagadro's constant, 120
α	Thermal diffusivity, 37

β	$\beta = 1/(k_B T)$, 59
c	Speed of sound, 59
χ	Two particle distribution function, 73
χ_{ab}	Two particle distribution function for species a and b , 75
$\dot{\mathcal{N}}$	Collision rate, 156
c_p	Specific heat capacity, 37
\mathbf{D}	Diffusion matrix, 90
d	Dimensionality, 72
δ	k_{in}/k_{out} (Maxwell derivation), 29
δV	Volume surface, 66
E	Total energy, 61
e	Specific energy, 80
Ω	Entropy production, 81
η	Shear viscosity, 83
η_B	Bulk viscosity, 83
F	Force, 69
f	Phase space distribution function, 68
$f^{(1)}$	single-particle distribution function, 70
$f_a^{(1)}$	Single particle distribution function for species a , 74
$f^{(n)}$	n -particle distribution function, 70
ω	Frequency, 148
γ	Euler's constant, 38
$\mathbf{\Gamma}$	Phase space position vector, 68
ΔH	Height difference, 40
h	Specific enthalpy, 82

λ_I	Initial thermal conductivity, 96		152
Ψ	Specific internal energy, 81	φ	Azimuthal angle, 27
\mathbf{J}	Diffusion flux vector, 90	π	Pi, 31
\mathbf{J}_a	Diffusive flux of species a , 76	\mathbf{P}^k	Pressure tensor kinetic component, 78
\mathbf{J}_q	Diffusive heat flux, 80	\mathbf{P}^Ψ	Pressure tensor collisional component, 78
\mathbf{J}_q^k	Diffusive heat flux kinetic component, 80	Q	Heat flux, 28
\mathbf{J}_q^Ψ	Diffusive heat flux collisional component, 80	\mathbf{r}	Position vector, 30
\mathbf{J}_s	Diffusive entropy flux, 81	R	Radius, 29
k	Thermal conductivity, 21	ρ	Mass density, 37
k_B	Boltzmann constant, 53	\mathbf{r}_{ij}	Relative position of particles i and j , 55
k^\parallel	Parallel thermal conductivity, 21	$\hat{\mathbf{r}}_{ij}$	Unit vector along the direction of \mathbf{r}_{ij} , 55
k^\perp	Series thermal conductivity, 21	r_T	Tether length (TPM), 151
l	Simulation length, 61	S	Entropy, 152
L_{ab}	Mutual diffusion coefficient of species a through species b , 59	s	Specific entropy, 81
L	Unit length scale, 53	σ	Diameter, 51
l^\parallel	Simulation length parallel to heat transfer, 101	σ_{ij}	Collision diameter between particles i and j , 51
l^\perp	Simulation length perpendicular to heat transfer, 101	λ	Steady-state thermal conductivity, 90
L_{ua}	Thermal diffusion coefficient of species a , 59	T	Temperature, 27
L_{uu}	Phenomenological thermal conductivity, 59	t	Time, 37
m	Mass, 51	\mathcal{T}_{ab}	Hard-sphere collision integral between species a and b , 74
M	Unit mass scale, 53	$\boldsymbol{\tau}$	Stress tensor, 81
μ_{ij}	Relative mass of particles i and j , 54	Δt_c	Collision time, 55
μ_a	Chemical potential of species a , 83	Θ	Heaviside step function, 66
$\hat{\mathbf{n}}$	Normal vector, 67	θ	Polar angle, 27
N	Total number of spheres, 30	τ	Unit time scale, 53
n	Number density, 80	\mathbf{U}	Thermal diffusion vector, 90
N_a	Number of spheres of species a , 59	\mathbf{u}	ensemble average velocity, 70
λ_N	Effective non-equilibrium thermal conductivity, 99	U_{ij}	Interparticle potential between particles i and j , 51
\mathbf{P}	Pressure tensor, 78	\mathbf{v}	Velocity vector, 54
p	Isotropic pressure, 83	V	Volume, 31
Ω	Configurational partition function, 152	\mathbf{V}_a	Peculiar velocity of species a , 76
		δ_V	Delta function which selects for the surface of volume V , 67

\mathbf{v}_{ij}	Relative velocity of particles i and j , 54
ϕ	Volume fraction, 21
\mathbf{V}_i	Peculiar velocity of particle i , 59
\mathbf{v}'_i	Restituted velocity of particle i , 54
v_a	Specific volume of species a , 96
W_a	Time integral of the microscopic mass flux of species a , 59
w_a	Mass fraction of species a , 59
W_u	Time integral of the microscopic kinetic energy flux, 59
\mathbf{X}	Concentration driving force vector, 90
x_a	Mol fraction of species a , 59
\mathbf{X}_u	Temperature driving force, 91
Z	Compressibility, 59
$\mathbf{0}$	Zero vector $\{0, 0, \dots, 0\}$, 137

INTRODUCTION

Heat management is becoming ever more critical as technology continues to advance and nowhere is this more important than in microelectronics where high power densities (W m^{-3}) place limits on new designs. For example, AMD's recently released Epyc CPUs have a peak output of 180 W of heat over 756 mm^2 of die (238 kW m^{-2}). In comparison, industrial fired heaters have a design flux of $\lesssim 40 \text{ kW m}^{-2}$, thus managing and transporting the heat produced by modern CPUs requires improved heat management systems which could benefit from novel heat transfer materials. Water and air are the most common heat transfer fluids in use presently as they are cheap to obtain and safe to use. Water also has a high heat capacity for its molecular weight as well as a useful low viscosity and favourable melting/boiling points which make it suitable for most general heat transfer applications; however, like most fluids, water has a relatively low thermal conductivity when compared with other materials. For example, as shown in Fig. 1.1, copper has a thermal conductivity which is approximately 650 times greater than water. There are many ways of potentially increasing the heat transfer capabilities of a heat management system, such as modifying the flow geometry to increase heat transfer area or adjusting the flow regime to promote convective transport; however, if the thermal conductivity of the heat transfer fluid itself can be increased, then heat transfer improves universally for all geometries and flow regimes.

The field of nanofluids seeks to enhance the thermal conductivity of conventional heat transfer fluids through the colloidal suspension of high-conductivity solid nanoparticles which have diameters $\lesssim 100 \text{ nm}$. There has been a great deal of interest in these nanoparticle suspensions since it was reported that there is a large "anomalous" enhancement of the thermal conductivity for low nanoparticle loadings. One of the first studies which reported these enhancements was performed by Eastman et al [5] using copper nanoparticles suspended in a base fluid of ethylene glycol. A thermal conductivity enhancement of 40% was reported for a nanoparticle volume fraction of just 0.3 vol% as shown in Fig. 1.2.

Since this study, a wide variety of nanoparticle and base fluid combinations have been investigated [6] and many have shown large thermal conductivity enhancements. Exper-

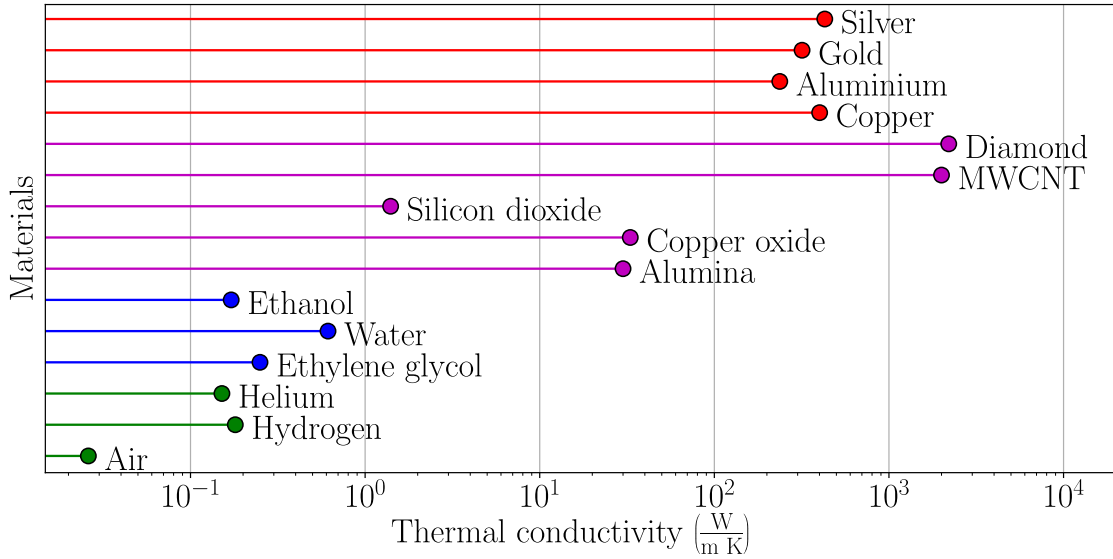


Figure 1.1: Chart showing the thermal conductivities of various materials near standard conditions. Metallic materials are shown in red, non-metallic solids are shown in purple, liquids are shown in blue, and gases are shown in green. The thermal conductivity of helium and hydrogen as well as the liquid materials are approximately one order of magnitude larger than air. In general the thermal conductivity of solid materials is 2-3 orders of magnitude larger than gaseous and liquid materials. Diamond and carbon nanotubes display the largest thermal conductivity of any quoted material and is several times larger than the highest conductivity metallic materials. Thermal conductivity data is taken from Refs. [1–4].

imental measurements have also generated substantial controversy [7], with confusion over what results might be unsurprising and what might be deemed “anomalous”. Even the seminal results of Eastmann et al in Fig. 1.2 have ill-defined aspects as detailed in the figure caption. Disagreements between different groups on the measured thermal conductivity of particular nanofluids as well as some surprising results ultimately led to a comprehensive study with double blind tests conducted as a collaboration between 71 authors across 34 institutions [8]. The primary conclusion of this benchmark study is that no anomalous behaviour was observed and the thermal conductivity is predicted by effective medium theory [9].

The nanofluids controversy is reminiscent of thermal conductivity measurements in the helium-hydrogen gas mixture. Early results in the 1960s [10, 11] showed a surprising minimum in the measured thermal conductivity as a function of mixture composition as shown in Fig 1.3. Such behaviour would be considered extremely anomalous in the nanofluid community as it implies that the addition of a more thermally-conductive component can actually make the resulting mixture more thermally insulating. Experiments on this gas mixture were carried out with very different techniques (e.g. hot wire, katharometer) and some studies displayed an additional controversial sharp dip at the location of the minimum. This was later dismissed as two experimental errors by other authors who could not reproduce the result [12, 13]; however, the minimum was repro-

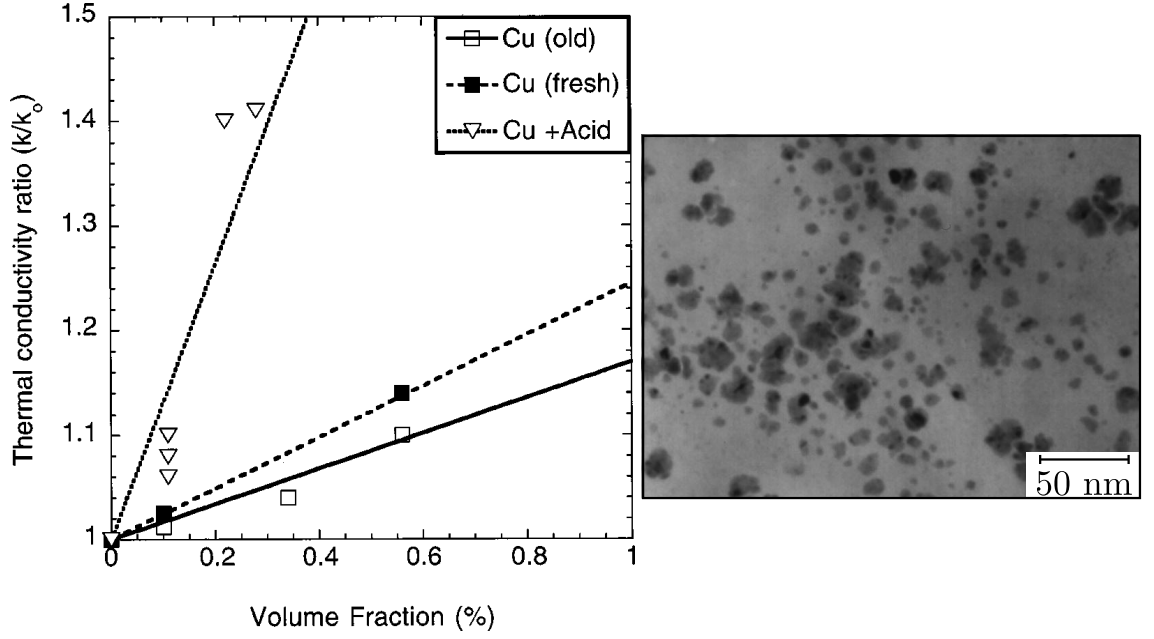


Figure 1.2: Thermal conductivity as a function of volume fraction of Cu nanoparticles dispersed in ethylene glycol (left) and a transmission electron micrograph of copper nanoparticles dispersed in ethylene glycol (right). Both figures are adapted from Ref. [5]. There is a remarkable 40 % thermal conductivity enhancement with the addition of just 0.3 vol% copper nanoparticles; however, this is also in the presence of <1% v/v thioglycolic acid which is used as a stabilising agent. Although the author described this as a small addition, it is highly significant compared to the nanofluid volume fraction. Other troubling aspects include a lack of repetition/error analysis and the effect of ageing of the sample (“fresh” here is defined as < 2 days from formulation and “old” is defined as up to two months from preparation). These uncertainties are characteristic of many published experimental nanofluid results.

duced.

Both of these experimental examples highlight our lack of understanding as well as the challenges in repeating measurements of thermal conductivity. Several questions remain:

1. What is a useful definition of an “anomalous” thermal conductivity?
2. Is “anomalous” thermal conductivity possible in general (and thus in nanofluids)?
and
3. Can we understand and/or predict “anomalous” thermal conductivity effects?

In searching for a useful definition of “anomalous” thermal conductivity, consensus in the literature has focused on results outside the bounds given by the series k^\perp and parallel k^\parallel limits of the thermal conductivity [9], which for a binary mixture are as follows,

$$\frac{1}{k^\perp} = \frac{(1 - \phi_2)}{k_1} + \frac{\phi_2}{k_2}, \quad k^\parallel = (1 - \phi_2)k_1 + \phi_2 k_2, \quad (1.0.1)$$

where ϕ_2 is the volume fraction of component 2 in the mixture, and k_1 and k_2 are the pure component thermal conductivities of component 1 and component 2 respectively.

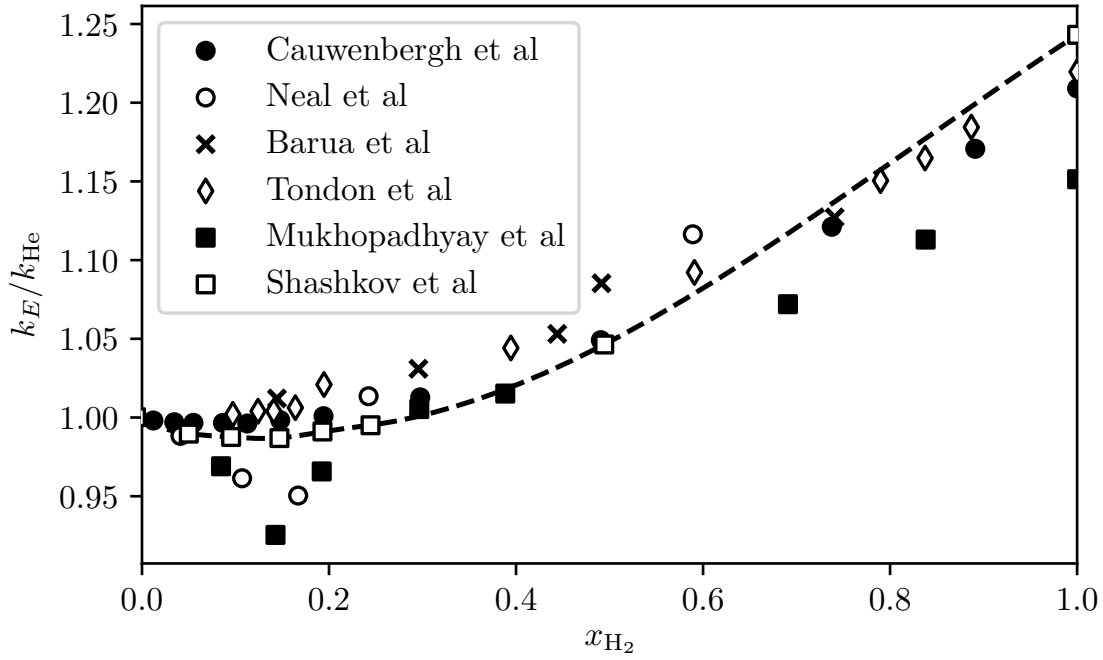


Figure 1.3: Reduced thermal conductivity of hydrogen-helium gas mixtures as a function of hydrogen mol fraction over 23.8–50 °C. The consensus is that a minimum is present, although a sharp minimum around $x_{H_2} \approx 0.15$ which is reported by two references has been dismissed as experimental error in later work [12]. The figure is adapted from Ref. [13] where further details on the references are given.

These limits represent the extremes of a continuum description, i.e., two continuum materials of constant thermal conductivity with no interfacial effects cannot be arranged in any way such that the combined thermal conductivity lies outside these bounds¹. The term “anomalous” is also commonly applied to thermal conductivities outside the bounds given by effective medium theory for well-dispersed particles. These so-called Maxwell bounds [14] are discussed in Chapter 2 and are narrower than the series/parallel limits. Results outside the Maxwell bounds, and even the series-parallel bounds, have been reported in the nanofluid literature and in an attempt to explain these measurements, several additional mechanisms beyond pure conduction have been proposed; such as interfacial particle layering, nanoparticle clustering, and Brownian motion. These are discussed in detail in Chapter 3; however, the general consensus is that these mechanisms alone cannot explain the observed trends and no predictive model for nanofluid thermal conductivity is yet available. Indeed, these models all fail to explain the behaviour of the helium-hydrogen gas mixture, thus some fundamental understanding is still missing.

The fact that the series-parallel model is unable to bound experimental results suggests that molecular (non-continuum) effects are important. A molecular model is therefore most appropriate when attempting to simulate the behaviour of nanofluids to gain

¹The parallel case does assume an insulating barrier between the two phases; however, this only serves to slightly widen the bounds and thus does not invalidate this statement.

further insight. Molecular Dynamics (MD) simulation involves directly simulating the motion of every molecule in a system and can be used to directly observe heat transfer in model molecular systems; however, it is computationally expensive and it is therefore difficult to simulate anything other than small systems over short times, e.g., a computationally large simulation of 10^6 molecules of air corresponds to a simulation box of only $300 \times 300 \times 300$ nm, while computationally-accessible simulation times are on the order of $\lesssim 1$ ns. Heat conduction in mixtures such as nanofluids involves coupled diffusion and heat conduction effects which might take seconds to come to steady state and depend strongly on the geometry of the heat transfer device, thus MD is only used here to explore fundamental properties of fluid mixtures but not their direct heat-transfer performance. In order to simulate realistic heat-transfer devices, a multi-scale model is developed which includes interactions at the molecular scale without incurring the cost of a direct MD simulation. One successful theory for molecular transport is Enskog-Chapman kinetic theory [15] (henceforth referred to as Enskog theory) which is a relatively computationally-inexpensive approximation for calculating the transport properties of single or multi-component hard-sphere fluids at equilibrium. In this thesis, this molecular model is integrated into a hydrodynamic model in order to connect the molecular and macroscopic scales and determine if truly “anomalous” thermal conductivity is possible, and if it can be exploited in real applications.

The structure of the thesis is as follows. This thesis examines classical continuum bounds of mixture thermal conductivity in Ch. 2 before reviewing experimental studies which report thermal conductivity values, for fluid/fluid-solid mixtures, which lie outwith these bounds in Ch. 3. In order to move beyond continuum theories, a molecular description is required. The hard-sphere model is used in order to model thermal conductivity in mixtures in this thesis, thus an overview of this model is given in Ch. 4 along with a outline of MD simulation. Ch. 5 gives a derivation of Enskog-kinetic theory which is used in order to derive full multicomponent hydrodynamics for hard-sphere mixtures. This complete hydrodynamic description is built upon in Ch. 6 which defines thermal conductivity in fluid mixtures, taking into account molecular effects. In Chs. 7 and 8, MD simulation and Enskog theory are used in order to investigate “anomalous” thermal conductivity values for binary hard-sphere fluids where it is shown that it is possible for hard-sphere mixtures to exhibit “anomalous” thermal conductivities. Ch. 9 then proceeds to investigate whether or not these findings are reflected in real mixtures. A coupled hydrodynamic - kinetic theory model is presented in Ch. 10 which is designed to model the detailed time-evolution of hard-sphere fluid systems with a view to modelling molecular heat transfer in macroscopic devices.

Finally, Ch. 11 presents two novel methods for computing the free energy of hard-sphere systems. High-precision estimates for both the solid and liquid free energies are determined which are then used in order to accurately determine the hard-sphere fluid-solid transition point.

References

- [1] M. Liu, C. Lin, and C. Wang. “Enhancement of thermal conductivities with Cu, CuO, and carbon nanotube nanofluids and application of MWNT/water nanofluid on a water chiller system”. In: *Nanoscale Res. Lett.* 6.297 (2011).
- [2] D. R. Lide, ed. *CRC handbook of chemistry and physics*. 84th ed. CRC Press, 2003.
- [3] K. Kadoya, N. Matsunaga, and A. Nagashima. “Viscosity and thermal Conductivity of dry air in the gaseous phase”. In: *J. Phys. Chem. Ref. Data* 14.947 (1985).
- [4] Y. Touloukian, P. Liley, and S. C. Saxena. *Thermal Conductivity - Nonmetallic Liquids and Gases*. Vol. 3. Thermophysical properties of matter - the TPRC data series. Thermophysical and electronic properties information analysis center, 1970.
- [5] J. A. Eastman et al. “Anomalously increased effective thermal conductivities of ethylene glycol-based nanofluids containing copper nanoparticles”. In: *Appl. Phys. Lett.* 78 (2001), pp. 718–720.
- [6] A. Sergis and Y. Hardalupas. “Anomalous heat transfer modes of nanofluids: a review based on statistical analysis”. In: *Nanoscale Res. Lett.* 6.1 (2011), p. 391.
- [7] P. Keblinski, R. Prasher, and J. Eapen. “Thermal conductance of nanofluids: is the controversy over?” In: *J. Nanopart. Res.* 10 (2008), pp. 1089–1097.
- [8] J. Buongiorno et al. “A benchmark study on the thermal conductivity of nanofluids”. English. In: *J. Appl. Phys.* 106 (2009), p. 094312.
- [9] J. Eapen et al. “The Classical Nature of Thermal Conduction in Nanofluids”. In: *J. Heat Transfer* 132 (2010), p. 102402.
- [10] W. Neal, J. Greenway, and P. Coutts. “Thermal conduction in helium-hydrogen gas mixtures”. In: *Proceedings of the physical society of London* 87 (1966), pp. 556–577.
- [11] P. Mukhopadhyay and A. K. Barua. “Thermal conductivity of hydrogen-helium gas mixtures”. In: *J. Appl. Phys.* 18.5 (1967), p. 635.
- [12] P. K. Tondon, J. M. Gandhi, and S. C. Saxena. “Thermal conductivity of H₂-He and D₂-He systems”. In: *Proc. Phys. Soc.* 92 (1967), pp. 253–255.
- [13] A. G. Shashkov, F. P. Kamchatov, and T. N. Abramenko. “Thermal conductivity of the hydrogen-helium mixture”. In: *J. Eng. Phys.* 24.4 (1973), pp. 461–464.
- [14] J. Maxwell. *Treatise on Electricity and Magnetism*. Vol. 1. Oxford at the Clarendon Press, 1873.
- [15] M. López de Haro, E. G. D. Cohen, and J. M. Kincaid. “The Enskog Theory for Multicomponent Mixtures. 1. Linear Transport-Theory”. In: *J. Chem. Phys.* 78.5 (1983), pp. 2746–2759.

CONTINUUM MODELS OF MIXTURE THERMAL CONDUCTIVITY

Several continuum models have been used in the past in attempts to predict thermal conductivity in fluid/fluid-solid mixtures, as well as to deem what is, or is not, “anomalous” thermal conductivity behaviour regarding measurements which deviate from these continuum predictions. These models have the advantage of relative simplicity and intuitiveness when compared to complete hydrodynamic descriptions of fluid mixtures; however, a common drawback of the models presented here is that they assume that a fluid is completely stationary. This implicitly assumes that diffusion plays no part in the transfer of energy and, therefore, that the only mechanism of heat transport is conduction. This is demonstrably false for fluid mixtures and is discussed in much more detail in Ch. 6.

2.1 Series-parallel limits

This chapter begins by presenting an overview of the most basic and intuitive model of thermal conductivity in mixtures: the series-parallel limits. Instead of predicting an exact value for the thermal conductivity, the series-parallel model gives upper and lower bounds for a given mixture based on two ideal material configurations. The configurations which correspond to the series and parallel thermal conductivity limits are shown in Fig. 2.1 where the direction of heat conduction through the system is labelled. Fig. 2.1(a) shows two continuous mediums, with thermal conductivities k_1 and k_2 , arranged in series relative to the direction of heat flow. This arrangement corresponds to the series limit and represents the minimum possible thermal conductivity for a given continuum mixture due to the fact that all heat is forced to travel through the lower thermal conductivity medium. Fig. 2.1(b) shows the same two mediums arranged in parallel which represents the maximum possible thermal conductivity. In this case there exists a “shortcut” for heat conduction, unlike in the series arrangement, where heat can completely bypass the lower thermal conductivity medium. The thermal conductivities in the series and parallel limits

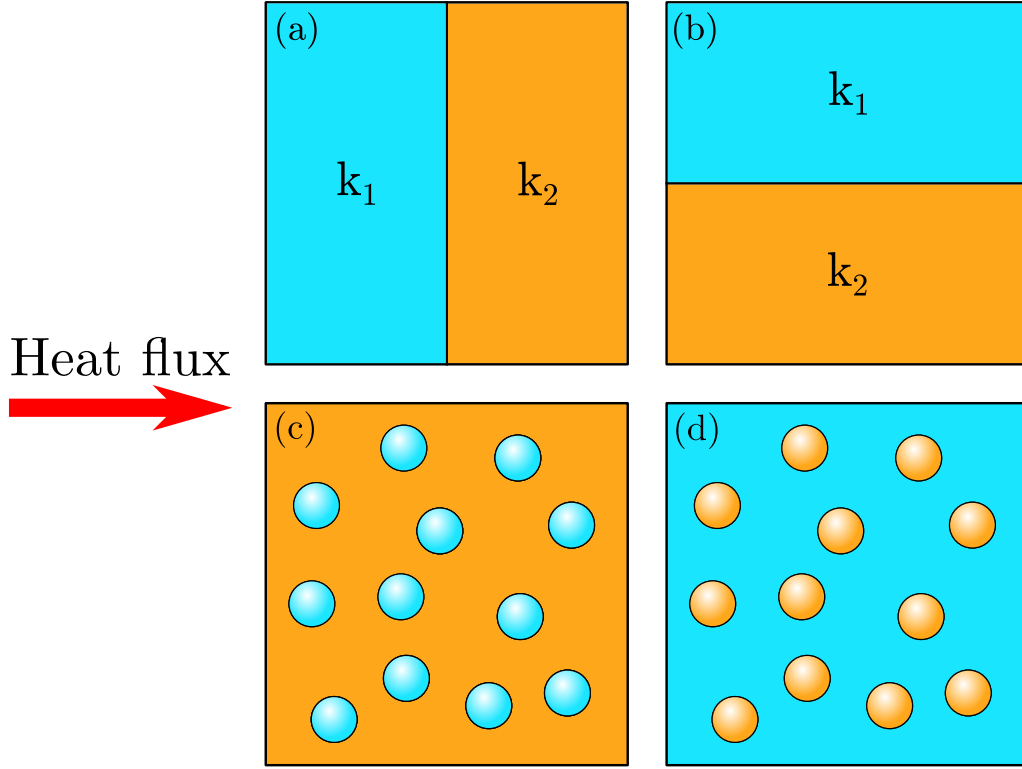


Figure 2.1: Four different configurations of two continuum materials with thermal conductivities k_1 and k_2 . (a) and (b) correspond to the series and parallel thermal conductivity limits respectively. (c) and (d) correspond to the Maxwell thermal conductivity bounds. If $k_1 > k_2$ then (c) corresponds to the lower Maxwell bound and (d) corresponds to the upper bound. The red arrow represents the direction of heat flow through the systems.

[1] are given in Ch. 1 and are restated here as follows,

$$\frac{1}{k^\perp} = \frac{(1 - \phi_2)}{k_1} + \frac{\phi_2}{k_2}, \quad k^\parallel = (1 - \phi_2)k_1 + \phi_2k_2, \quad (2.1.1)$$

where k^\perp and k^\parallel are the series and parallel thermal conductivities respectively, k_i is the thermal conductivity of component i , and ϕ_i is the volume fraction of component i .

One of the reasons that the series-parallel limits are so useful is that they give a clear indicator of whether or not a continuum description is appropriate for a given mixture. If any experimental measurements show a mixture with thermal conductivity outwith these upper and lower bounds (assuming that all other properties are known accurately, i.e. individual thermal conductivity values, volume fraction), it proves that this mixture is not behaving as a stationary continuum. In this case another mechanism is contributing to the mixture thermal conductivity other than pure conduction such as convection, thermal diffusion, etc.

2.2 Maxwell theory

Maxwell studied the thermal conductivity of solid-liquid mixtures in the 19th century [2], performing early experiments on sub-millimetre sized solid particles evenly dispersed in a liquid. At the time, Maxwell created a theory in order to predict the thermal conductivity of binary mixtures which performed well, producing bounds on the thermal conductivity which are narrower than the series-parallel limits. Fig. 2.1(c) and Fig. 2.1(d) show the material configurations which correspond to the Maxwell thermal conductivity bounds which assume, in the first case, that one material is present purely in the form of perfectly spherical particles which are dispersed in an infinite medium of the other material and vice versa for the second bound. Like in the series-parallel limits, it is assumed that all materials are stationary. A derivation of Maxwell theory is given here clearly laying out the assumptions of the method.

2.2.1 Temperature profile around a single sphere

Consider a single sphere with thermal conductivity k_{in} located at the origin and suspended in an infinite medium with thermal conductivity k_{out} where conduction is the only available method of heat transport. A uniform heat flux is imposed upon the system along the z -direction. The equation for the temperature distribution in this system at steady-state and with no generation or consumption of heat is given by the Laplace equation,

$$\nabla^2 T = 0, \quad (2.2.1)$$

where T is the temperature. The Laplace equation can be written in spherical coordinates as follows,

$$\frac{1}{r^2} \frac{\partial}{\partial r} \left(r^2 \frac{\partial T}{\partial r} \right) + \frac{1}{r^2 \sin \theta} \frac{\partial}{\partial \theta} \left(\sin \theta \frac{\partial T}{\partial \theta} \right) + \frac{1}{r^2 \sin^2 \theta} \frac{\partial^2 T}{\partial \varphi^2} = 0, \quad (2.2.2)$$

where r is the distance from the point of origin, θ is the polar angle measured from the positive z -axis in the y - z plane, and φ is the azimuthal angle measured from the positive x -axis in the x - y plane. This coordinate system is illustrated in Fig. 2.2. The system is symmetric in the azimuthal direction, i.e. $\partial T / \partial \varphi = 0$. Therefore, Eq. (2.2.2) can be simplified to

$$\frac{1}{r^2} \frac{\partial}{\partial r} \left(r^2 \frac{\partial T}{\partial r} \right) + \frac{1}{r^2 \sin \theta} \frac{\partial}{\partial \theta} \left(\sin \theta \frac{\partial T}{\partial \theta} \right) = 0. \quad (2.2.3)$$

Eq. (2.2.3) has multiple solutions including $T = 1$, $T = r \cos \theta$, and $T = \cos \theta / r^2$. Assuming that these are the only relevant solutions, a general solution can be made up of

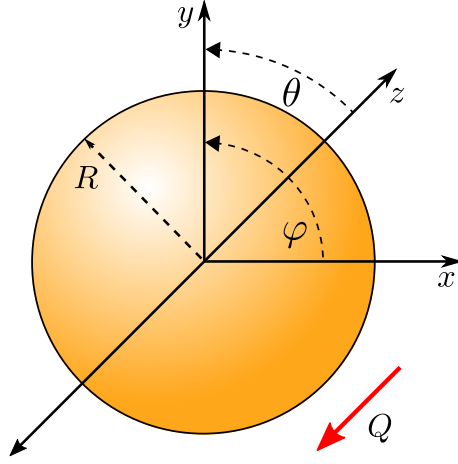


Figure 2.2: Schematic diagram of a single sphere embedded in an infinite medium under a temperature gradient. The red arrow labelled Q represents the direction of heat flux through the system which is parallel to the z axis, R represents the radius of the sphere, θ is the polar angle measured from the positive z -axis in the y - z plane, and φ is the azimuthal angle measured from the positive x -axis in the x - y plane.

a sum of these three terms, each with unknown constants,

$$T_\alpha = A_\alpha + B_\alpha r \cos \theta + C_\alpha \frac{\cos \theta}{r^2}, \quad (2.2.4)$$

where $\alpha \in [\text{in}, \text{out}]$ denotes the solution both inside and outside of the sphere. As the distance from the sphere increases, the effect of the sphere on the temperature distribution will decrease. Therefore, the temperature far away from the sphere, as $r \rightarrow \infty$, will approach the temperature of the infinite medium under the imposed uniform heat flux, $T_{\text{out}} \rightarrow T_0 + \left(\frac{dT}{dz}\right)_\infty z$, where T_0 is the temperature at $z = -\infty$ and $\left(\frac{dT}{dz}\right)_\infty$ is the linear temperature gradient which arises within the infinite medium as a result of the heat flux imposed on the system. Taking the limit $r \rightarrow \infty$ of the general solution outside of the sphere, the same functional form arises,

$$\lim_{r \rightarrow \infty} T_{\text{out}} = A_{\text{out}} + B_{\text{out}} r \cos \theta + \cancel{C_{\text{out}} \frac{\cos \theta}{r^2}}^0 \quad (2.2.5)$$

$$= A_{\text{out}} + B_{\text{out}} z, \quad (2.2.6)$$

where $z = r \cos \theta$ from trigonometry. Therefore $A_{\text{out}} = T_0$ and $B_{\text{out}} = \left(\frac{dT}{dz}\right)_\infty$, giving

$$T_{\text{out}} = T_0 + \left(\frac{dT}{dz}\right)_\infty r \cos \theta + C_{\text{out}} \frac{\cos \theta}{r^2}, \quad (2.2.7)$$

where the third constant C_{out} remains undetermined. Considering now the solution inside the sphere,

$$T_{\text{in}} = A_{\text{in}} + B_{\text{in}} r \cos \theta + C_{\text{in}} \frac{\cos \theta}{r^2}, \quad (2.2.8)$$

as we approach the centre of the sphere, $r \rightarrow 0$, the temperature T must remain finite. This therefore means that $C_{\text{in}} = 0$ as the third term is divided by r which leaves

$$T_{\text{in}} = A_{\text{in}} + B_{\text{in}}r \cos \theta. \quad (2.2.9)$$

The boundary conditions in this system are as follows,

$$T_{\text{in}} = T_{\text{out}} \quad \text{for } r = R \quad (2.2.10)$$

$$-k_{\text{in}} \frac{\partial T_{\text{in}}}{\partial r} = -k_{\text{out}} \frac{\partial T_{\text{out}}}{\partial r} \quad \text{for } r = R, \quad (2.2.11)$$

where R is the radius of the sphere. Eq. (2.2.10) states that there is no interfacial resistance between the sphere and the surrounding medium and Eq. (2.2.11) states that the heat flux out of the infinite medium is equal to the heat flux into the sphere. Inserting the expressions for T_{in} and T_{out} into Eq. (2.2.10) gives

$$A_{\text{in}} + B_{\text{in}}R \cos \theta = T_0 + \left(\frac{dT}{dz} \right)_{\infty} R \cos \theta + C_{\text{out}} \frac{\cos \theta}{R^2}. \quad (2.2.12)$$

As θ can vary independently, this equality is only satisfied if the corresponding terms containing $\cos \theta$, and not containing $\cos \theta$, are equal to each other, i.e.

$$A_{\text{in}} = T_0 \quad (2.2.13)$$

$$B_{\text{in}} = \left(\frac{dT}{dz} \right)_{\infty} + \frac{C_{\text{out}}}{R^3}. \quad (2.2.14)$$

The constant A_{in} is determined and we have an expression for B_{in} in terms of C_{out} . The expressions for T_{in} and T_{out} are now substituted into the second boundary condition, Eq. (2.2.11), giving

$$-k_{\text{in}}B_{\text{in}} \cos \theta = -k_{\text{out}} \left(\left(\frac{dT}{dz} \right)_{\infty} \cos \theta - 2 \frac{C_{\text{out}}}{R^3} \cos \theta \right), \quad (2.2.15)$$

which can be simplified to

$$\delta B_{\text{in}} = \left(\frac{dT}{dz} \right)_{\infty} - 2 \frac{C_{\text{out}}}{R^3}, \quad (2.2.16)$$

where a new term $\delta = k_{\text{in}}/k_{\text{out}}$ has been introduced. Again, an expression for B_{in} in terms of C_{out} is produced. Combining Eq. (2.2.16) with Eq. (2.2.13) allows the determination of the remaining unknown constants B_{in} and C_{out} as follows,

$$\delta \left(\left(\frac{dT}{dz} \right)_{\infty} + \frac{C_{\text{out}}}{R^3} \right) = \left(\frac{dT}{dz} \right)_{\infty} - 2 \frac{C_{\text{out}}}{R^3} \quad (2.2.17)$$

$$C_{\text{out}} = \frac{R^3 (1 - \delta)}{(2 + \delta)} \left(\frac{dT}{dz} \right)_{\infty}, \quad (2.2.18)$$

which means, therefore, that

$$B_{\text{in}} = \left(\frac{dT}{dz} \right)_{\infty} + \frac{(1-\delta)}{(2+\delta)} \left(\frac{dT}{dz} \right)_{\infty} \quad (2.2.19)$$

$$= \frac{3}{2+\delta} \left(\frac{dT}{dz} \right)_{\infty}. \quad (2.2.20)$$

Substituting the expressions for the constant terms, A_{in} , B_{in} , A_{out} , B_{out} , and C_{out} into Eq. (2.2.9) and Eq. (2.2.7) gives the complete temperature distribution for a sphere embedded in an infinite medium under the influence of a linear temperature gradient,

$$T_{\text{out}} = T_0 + z \left(\frac{dT}{dz} \right)_{\infty} + z \frac{R^3}{r^3} \frac{(1-\delta)}{(2+\delta)} \left(\frac{dT}{dz} \right)_{\infty}, \quad (2.2.21)$$

$$T_{\text{in}} = T_0 + z \frac{3}{2+\delta} \left(\frac{dT}{dz} \right)_{\infty}, \quad (2.2.22)$$

where we have made use of the fact that $\cos \theta = z/r$. This temperature distribution is visualised in Fig. 2.3 for both high and low thermal conductivity spheres.

2.2.2 System of spheres

Instead of a sphere located at the origin, we now generalise Eq. (2.2.21) to a sphere i located at position \mathbf{r}_i in the system,

$$T_{\text{out}} = T_0 + z \left(\frac{dT}{dz} \right)_{\infty} + z \frac{R^3}{|\mathbf{r} - \mathbf{r}_i|^3} \frac{(1-\delta)}{(2+\delta)} \left(\frac{dT}{dz} \right)_{\infty}, \quad (2.2.23)$$

where $\mathbf{r} = [x, y, z]$ is the position vector that the temperature is measured at. We note here that the temperature change caused by a single sphere i over the background linear temperature profile is

$$\Delta T_{\text{out},i} = z \left(\frac{dT}{dz} \right)_{\infty} \frac{R^3}{|\mathbf{r} - \mathbf{r}_i|^3} \frac{(1-\delta)}{(2+\delta)}. \quad (2.2.24)$$

Consider now an infinite medium that, instead of containing a single sphere, contains N spheres. It is assumed that individual spheres do not interact with one another which implies that the effect of the spheres on the outer temperature is purely the sum of their individual changes from the underlying linear temperature profile $\left(\frac{dT}{dz} \right)_{\infty}$,

$$T_{\text{out}} = T_0 + z \left(\frac{dT}{dz} \right)_{\infty} + \sum_i^N \Delta T_{\text{out},i} \quad (2.2.25)$$

$$= T_0 + z \left(1 + \sum_i^N \frac{R^3}{|\mathbf{r} - \mathbf{r}_i|^3} \frac{(1-\delta)}{(2+\delta)} \right) \left(\frac{dT}{dz} \right)_{\infty}. \quad (2.2.26)$$

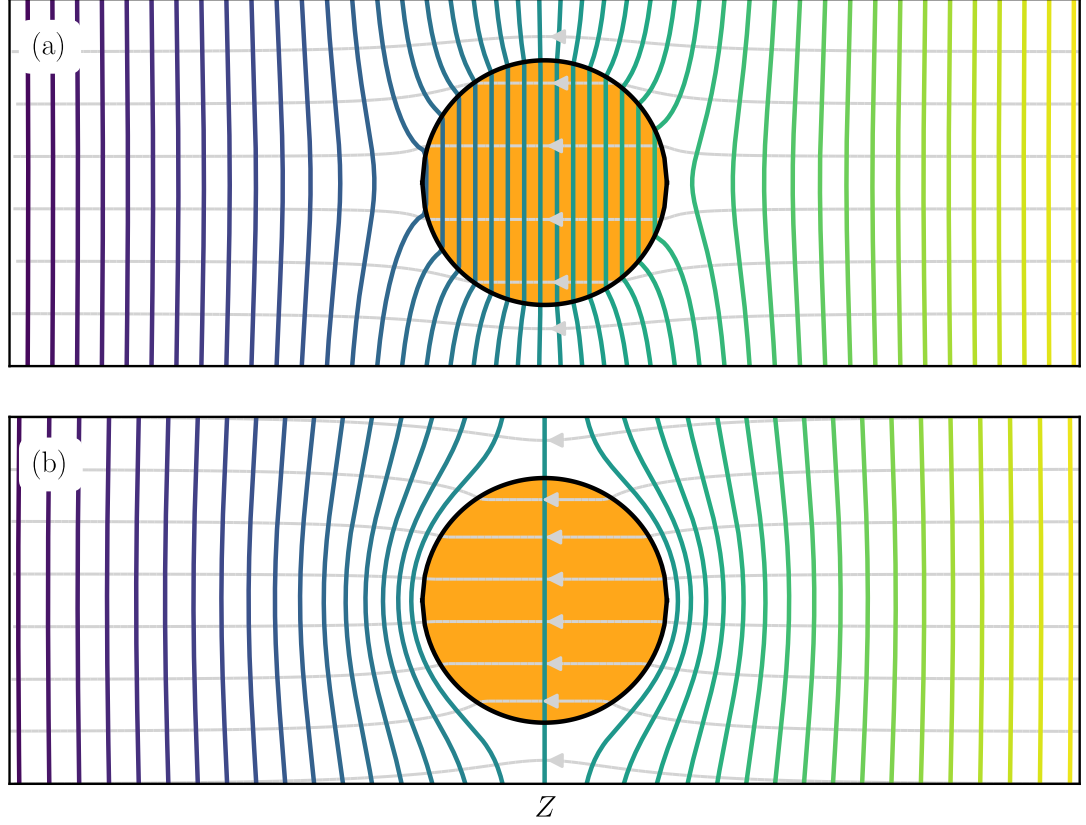


Figure 2.3: Contour plot showing the Maxwell temperature profile around a single sphere within an infinite medium under the influence of a linear temperature gradient (Eqs. (2.2.21) and (2.2.22)). The lines of contour represent the temperature going from low (black) to high (light yellow). Light grey streamlines represent the direction of heat flux through the system. (a) shows the temperature distribution for a high conductivity surrounding medium and a low conductivity sphere. (b) shows the temperature distribution for the opposite conditions, a high conductivity sphere surrounded by a low conductivity infinite medium.

It is also assumed that we are far enough away from the spheres $r \gg r_i$ that we are in the limit $|\mathbf{r} - \mathbf{r}_i|^3 \rightarrow |\mathbf{r}|^3$. In this case, the expression reduces to

$$T_{\text{out}} = T_0 + z \left(1 + N \frac{R_S^3 (1 - \delta)}{r^3 (2 + \delta)} \right) \left(\frac{dT}{dz} \right)_{\infty}, \quad (2.2.27)$$

where the sum over N spheres is replaced with a multiplication. Consider now a large sphere centered at the origin which is large enough to contain all of the current smaller spheres such that it has some volume fraction ϕ of spheres within it, i.e.

$$\phi = \frac{V_S}{V_L} = \frac{N 4\pi R_S^3 / 3}{4\pi R_L^3 / 3} = \frac{N R_S^3}{R_L^3}, \quad (2.2.28)$$

where V_S is the total volume of the N small spheres, V_L is the volume of the single large sphere centered at the origin of the system, R_S is the radius of the small spheres, and R_L

is the radius of the large sphere. Eq. (2.2.28) can be rearranged to obtain an expression for the large sphere radius, $R_L^3 = NR_S^3/\phi$, which will become useful later. The effective thermal conductivity k_E of the large sphere containing all smaller spheres is equal to the original N -sphere suspension only if the following equality is correct,

$$T_{\text{out}} = T_0 + z \left(1 + N \frac{R_S^3}{r^3} \frac{\left(1 - \frac{k_{\text{in}}}{k_{\text{out}}}\right)}{\left(2 + \frac{k_{\text{in}}}{k_{\text{out}}}\right)} \right) \left(\frac{dT}{dz} \right)_{\infty} \quad (2.2.29)$$

$$= T_0 + z \left(1 + \frac{R_L^3}{r^3} \frac{\left(1 - \frac{k_E}{k_{\text{out}}}\right)}{\left(2 + \frac{k_E}{k_{\text{out}}}\right)} \right) \left(\frac{dT}{dz} \right)_{\infty}. \quad (2.2.30)$$

Substituting the expression for R_L^3 into this equality and rearranging leads to

$$\phi \frac{\left(1 - \frac{k_{\text{in}}}{k_{\text{out}}}\right)}{\left(2 + \frac{k_{\text{in}}}{k_{\text{out}}}\right)} = \frac{\left(1 - \frac{k_E}{k_{\text{out}}}\right)}{\left(2 + \frac{k_E}{k_{\text{out}}}\right)} \quad (2.2.31)$$

$$\frac{k_E}{k_{\text{out}}} = \frac{2 + \delta + 2\phi(\delta - 1)}{2 + \delta - \phi(\delta - 1)}, \quad (2.2.32)$$

where the final equation is *Maxwell's equation* for the overall thermal conductivity of a mixture as a function of the pure component thermal conductivities of both materials in the mixture as well as the volume fraction of the dispersed material.

Alternating forms of Maxwell's model are known as the Maxwell bounds and are identical to thermal conductivity bounds derived by Hashin and Shtrikman [3, 4]. These bounds are calculated by alternating the configuration of the materials in the system as shown in Fig. 2.1. To calculate the first bound, one material is assumed to be the dispersed phase and, the other, the continuous medium. Subsequently, for the second bound, the continuous medium is now assumed to be the dispersed phase and the previous dispersed phase is now assumed to be the continuous medium. Assuming that $k_{\text{in}} > k_{\text{out}}$, the bounds can be written as

$$k_{\text{out}} \left(\frac{2 + \delta + 2\phi(\delta - 1)}{2 + \delta - \phi(\delta - 1)} \right) \leq k_E \leq k_{\text{in}} \left(\frac{2\delta + 1 + 2(1 - \phi)(1 - \delta)}{2\delta + 1 - (1 - \phi)(1 - \delta)} \right). \quad (2.2.33)$$

These bounds always lie within the series-parallel bounds [1] and represent the narrowest possible bounds which use only the pure thermal conductivities as well as the volume fraction. Improvement on these bounds require additional knowledge about the structure of the dispersed medium in the system.

As has been previously mentioned, these models are not strictly suited to solid-liquid mixtures such as nanofluids, as well as other fluid mixtures, as they assume that the mixture is stationary. Nevertheless, these models have been used throughout the literature when initially evaluating experimental nanofluid thermal conductivity measurements. In Ch. 3, these commonly used continuum models are compared with experimental measure-

ments of thermal conductivity in mixtures in order to gives a sense of their applicability and usefulness.

References

- [1] J. Eapen et al. “The Classical Nature of Thermal Conduction in Nanofluids”. In: *J. Heat Transfer* 132 (2010), p. 102402.
- [2] J. Maxwell. *Treatise on Electricity and Magnetism*. Vol. 1. Oxford at the Clarendon Press, 1873.
- [3] J. Eapen et al. “Mean-Field Versus Microconvection Effects in Nanofluid Thermal Conduction”. In: *Phys. Rev. Lett.* 99.9, 095901 (2007), p. 095901.
- [4] Z. Hashin and S. Shtrikman. “A variational approach to the theory of the effective magnetic permeability of multiphase materials”. In: *J. Appl. Phys.* 33.10 (1962), p. 3125.

EXPERIMENTAL EVIDENCE FOR UNUSUAL THERMAL CONDUCTIVITY

Thermal conductivity results which lie outwith the classical continuum bounds were shown in gas mixtures in the 1960s [1, 2]. These studies show that helium-hydrogen gas mixtures have a thermal conductivity which is below the series limit and which, at some concentrations, is below either of the pure component thermal conductivity values. These results are echoed by recent experimental studies of nanofluids which report markedly enhanced thermal conductivities with the addition of small amounts of solid nanoparticles, with some results lying outwith the classical bounds predicted by Maxwell and the series-parallel model. This chapter examines various experimental methods of measuring thermal conductivity in fluid/fluid-solid mixtures before reviewing experimental studies which report unusual values of thermal conductivities in gas mixtures and nanofluids. Finally, a number of theories which have been suggested in order to account for these unexplained values are discussed.

3.1 Experimental thermal conductivity measurement techniques

There are many thermal conductivity measurement techniques available when studying fluid / fluid-solid mixtures, of which, the transient hot wire method is the most popular [3]. Generally speaking, these techniques fall into two categories: transient methods and steady-state methods which differ significantly in the timescale over which thermal conductivity measurements are taken. For example, when using the transient hot wire method, previous studies have measured the thermal conductivity over the course of approximately 10 - 500 milliseconds [4]. This is a short time period relative to steady state methods, such as the steady-state parallel plates method [5], which are not subject to any time constraints and instead wait for a steady state heat flux or temperature gradient to become established in the system. This section gives a detailed explanation of the most popular measurement technique (transient hot wire method) as well as an overview of a

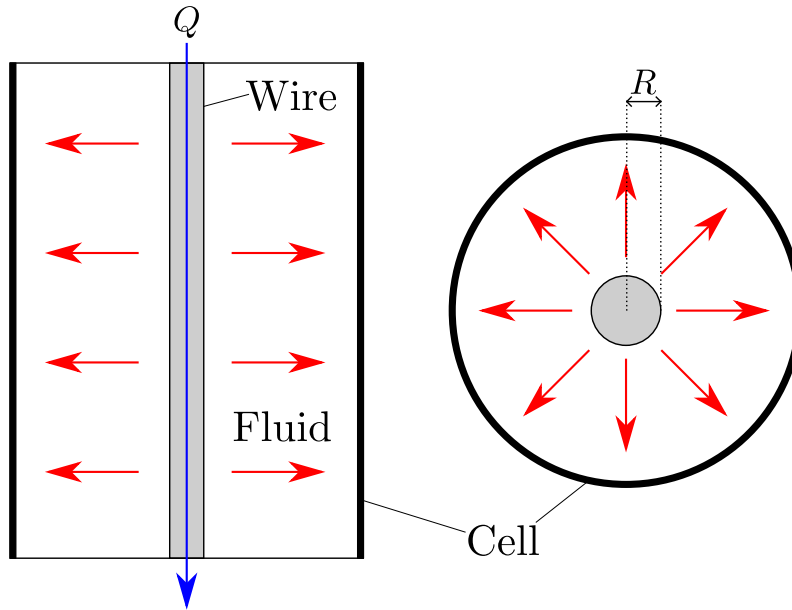


Figure 3.1: A schematic diagram of the transient heated wire thermal conductivity measurement technique. A side view and a top view of a vertical cylindrical cell are shown. A platinum wire with radius R runs down the center of the cell which is charged with the fluid of interest. An electrical pulse with a total power of Q is sent down the wire. This causes the wire to heat up and this heat is then conducted away from the wire through the fluid. The speed at which heat is conducted away from the wire is measured and used in order to determine the thermal conductivity of the fluid.

relatively theoretically simple steady-state measurement technique.

3.1.1 Transient heated wire

The transient heated wire method [6] operates by sending an electrical pulse through a thin platinum wire which is submerged in the fluid of interest and measuring the temperature response of the wire. A platinum wire is commonly used because of platinum's accurately known temperature/resistance relationship. This measured temperature response is then fitted to an analytical solution of the Fourier equation. Fig. 3.1 shows a schematic diagram of a transient hot wire experiment where the fluid of interest is contained within a cylindrical chamber and a thin platinum wire is held in suspension and runs through the middle of the chamber. After a voltage step is applied to the wire, the heat generated due to the wire's resistance will be conducted away from the wire and into the fluid as shown by the red arrows. In theory, the rate at which heat is removed from the wire is proportional to the thermal conductivity of the fluid. In practice, however, other effects also influence the temperature profile of the wire such as convection and radiation which must be accounted for.

When considering only the effects of conduction, the temperature of the fluid in the

experiment will evolve according to the Fourier equation which is written as follow,

$$\frac{\partial T}{\partial t} = \alpha \nabla^2 T, \quad (3.1.1)$$

where t is the time, and $\alpha = k/\rho c_p$ is the thermal diffusivity where k is the thermal conductivity, ρ is the mass density, and c_p is the specific heat capacity. The simplest mathematical solution of the problem can be generated by assuming that the physical properties (ρ , c_p , and k) of the fluid are constant. It is also assumed that the entire system is initially at a temperature T_0 ,

$$T(r, t) = T_0 \quad \text{for } t \leq 0. \quad (3.1.2)$$

In order to represent the heated wire, it is assumed that there is an infinitely thin line source of heat at the center of the system which produces a constant heat flux Q over the entire length of the wire,

$$\lim_{r \rightarrow 0} \left(r \frac{\partial T}{\partial r} \right) = -\frac{Q}{2\pi k} \quad \text{for } t > 0. \quad (3.1.3)$$

Far away from the wire (at $r \rightarrow \infty$) it is assumed that the temperature tends to the initial temperature of the fluid T_0 as follows,

$$\lim_{r \rightarrow \infty} T(r, t) = T_0 \quad \text{for } t > 0. \quad (3.1.4)$$

The solution to the Fourier equation in this case is

$$\Delta T(r, t) = \frac{Q}{4\pi k} \int_{\varepsilon}^{\infty} \frac{e^{-\varepsilon'}}{\varepsilon'} d\varepsilon', \quad (3.1.5)$$

where $\Delta T = T(r, t) - T_0$ represents the deviation of the temperature profile from the initial temperature, and the variable $\varepsilon = r^2/(4\alpha t)$. For the purposes of a transient heated wire experiment we are not interested in the temperature at an arbitrary point in the system r , we are only concerned with the temperature of the wire. Assuming that the wire has a radius of R , as well as assuming that the entire wire is at a uniform temperature of $T(R, t)$ equal to the temperature at the edge of the wire, means that the previous expression can be modified to give an expression for the temperature of the wire over time as follows,

$$\Delta T_w(t) = \frac{Q}{4\pi k} \int_{\varepsilon}^{\infty} \frac{e^{-\varepsilon'}}{\varepsilon'} d\varepsilon', \quad (3.1.6)$$

where $\Delta T_w(t)$ is the deviation of the wire temperature from the initial temperature and, now, $\varepsilon = R^2/4\alpha t$. Taking a series expansion of the integral at $\varepsilon = 0$ allows this equation

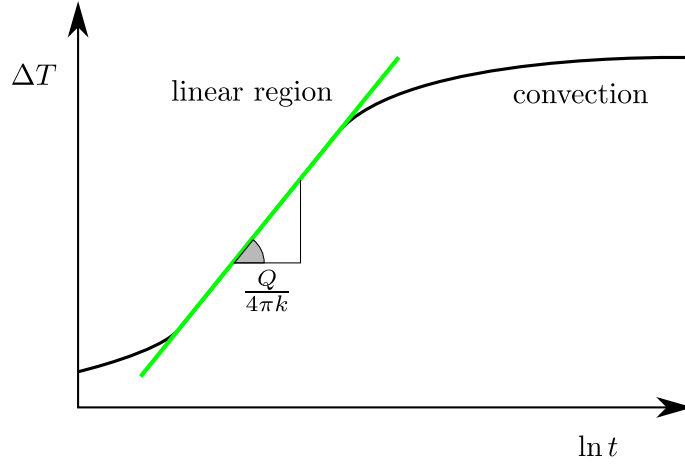


Figure 3.2: Temperature rise ΔT as a function of log time $\ln t$ during an example transient heated wire experiment. The graph shows region of linear temperature rise (Eq. (3.1.8)) which corresponds to the value $Q/4\pi k$. Calculating this gradient for a given material and applied heat flux Q allows the calculation of the material thermal conductivity. The graph shows the non-linear region which manifests at short times and also highlights the effect of convection on the temperature rise at long times.

to be rewritten as follows,

$$\Delta T_w(t) = \frac{Q}{4\pi k} \left(-\ln \varepsilon - \gamma + \varepsilon - \frac{\varepsilon^2}{4} + \frac{\varepsilon^3}{18} + \mathcal{O}(\varepsilon^4) \right), \quad (3.1.7)$$

where γ is Euler's constant. It is then assumed that the experiment is performed over a long time relative to the timescale of conduction $t \gg R^2/4\alpha$. Experimental studies attempt to match this assumption in practice by using platinum wires which are as thin as possible (often micrometers in diameter). With this assumption, the solution to the Fourier equation finally reduces to

$$\Delta T_w(t) = \frac{Q}{4\pi k} \ln t + C, \quad (3.1.8)$$

where all of the terms in Eq. (3.1.7) have vanished apart from the term which is a logarithmic function of ε , and the constant C is defined as follows,

$$C = \frac{Q}{4\pi k} \ln \left(\frac{4\alpha}{R^2} \right) - \gamma. \quad (3.1.9)$$

Eq. (3.1.8) implies that the rise in the wire temperature is a linear function of $\ln(t)$ and proportional to the thermal conductivity via the term $Q/(4\pi k)$ where Q is known. The thermal conductivity can therefore be extracted by determining the gradient of the temperature rise with $\ln(t)$. This process is shown in Fig. 3.2 which shows an example of a typical wire temperature profile as a function of $\ln(t)$ during a transient hot wire experiment. The straight green line highlights the region of linear temperature increase which is proportional to the thermal conductivity. Systematic deviations from the linear

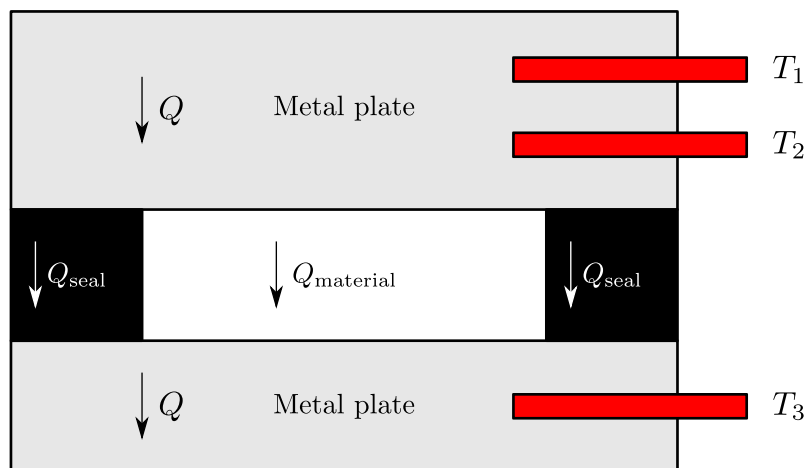


Figure 3.3: A schematic diagram of a steady-state thermal conductivity measurement technique with the fluid of interest sealed in place between two metal plates. Q represents the heat flux through the equipment. T_1 , T_2 , and T_3 represent three separate thermocouples used for measuring the temperature of the metal plates at different locations. In an actual experimental setup, there may be much more than three total thermocouples in order to measure temperature values at different locations and obtain a final spatially averaged value.

response occur for short and long times [4]. This is shown in Fig. 3.2 which highlights the effects of additional heat transfer caused by natural convection currents setting up in the system at large times.

Multiple corrections to this basic model have been derived [7] which account for additional effects which influence the wire temperature such as the variable properties of both the wire and the fluid as well as the Knudsen effect which becomes significant as the density of the fluid becomes small.

3.1.2 Heated/guarded plates

Fig. 3.3 shows a schematic diagram of a steady-state thermal conductivity measurement technique. This diagram most closely resembles a experimental setup which is known as a “cut-bar apparatus” [5]; however, there are numerous steady-state techniques which apply the same principals using different experimental configurations. In contrast to transient thermal conductivity measurement techniques, such as the transient heated wire method, this method does not seek to fit a mathematical solution to a the temperature response of a given material. These methods seek to apply a known heat flux to a given material and measure the resulting temperature gradient across the material. As shown in Fig. 3.3, the cut-bar experiment consists of two parallel metal plates enclosing the fluid of interest which is sealed between the plates. The sealant material is only necessary in the event that the material of interest is a fluid. The sealant could be a rubber o-ring for example or a silicon block. The thermal conductivity of the fluid is measured using temperature measurements taken at various locations in the metal plates as shown by the

thermocouples T_1 , T_2 , and T_3 in Fig. 3.3. In order to begin the experiment, the cell must be charged with the fluid of interest and a thermal load is applied across the equipment. The total heat flux Q is measured using the known thermal conductivity of the metal plates as follows,

$$Q = \frac{k_{\text{plate}} A_{\text{plate}} \Delta T_{1-2}}{\Delta H_{1-2}}, \quad (3.1.10)$$

where k_{plate} is the thermal conductivity of the metal plate, A_{plate} is the cross-sectional area of the metal plate, $\Delta T_{1-2} = T_1 - T_2$ is the measured temperature different between thermocouples 1 and 2, and ΔH_{1-2} is the distance between thermocouples 1 and 2. The thermal conductivity of the fluid is then determined using the temperature difference across the fluid cell while compensating for the heat which is transferred through the seal,

$$k_E = \frac{Q \frac{\Delta H_{\text{fluid}}}{\Delta T_{\text{fluid}}} - k_{\text{seal}} A_{\text{seal}}}{A_{\text{fluid}}}, \quad (3.1.11)$$

where ΔH_{fluid} is the distance across the fluid cell, $\Delta T_{\text{fluid}} = T_2 - T_3$ is the measured temperature difference across the fluid cell, k_{seal} is the thermal conductivity of the sealant material, A_{seal} is the cross-sectional area of the sealant, and A_{fluid} is the cross-sectional area of the fluid cell. In order to achieve accurate temperature difference measurements across the fluid, in a real experiment the thermocouples should be placed on the surface of the two metal plates unlike Fig. 3.3 where they are shown slightly inside the plates.

3.2 Experimental studies

If a mixture exhibits “anomalous” thermal conductivity which is outside of the classical bounds, this suggests that that mixture is not behaving as a continuum. If this is the case then a molecular model is required in order to describe the behaviour of the mixture. This section reviews studies which have investigated thermal conductivity in the helium-hydrogen binary gas mixture as well as in nanofluid systems, many of which have reported such behaviour.

3.2.1 The helium-hydrogen gas mixture

In the 1960s and 1970s, a number of studies were performed investigating thermal conductivity in helium-hydrogen gas mixtures. Experimental data generated by these studies are shown in Fig. 3.4 which presents the measured thermal conductivities which were first displayed in Ch. 1; however, in this case, the series-parallel limits are also presented. This research was spurred on by the presence of an apparent sharp minimum in the thermal conductivity profile which was reported by Mukhopadhyay and Barua [9] as well as Neal et al [1] as can be seen in Fig. 3.4. This sharp minimum was not reproduced in other measurements performed by Shashkov et al [8] among others, as shown in the

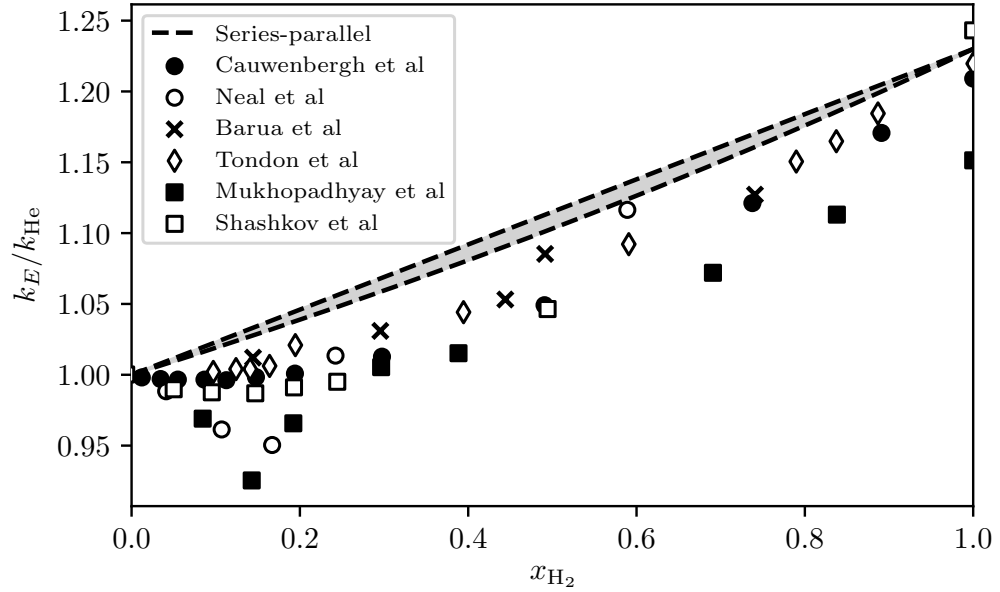


Figure 3.4: Reduced thermal conductivity of hydrogen-helium gas mixtures at temperatures ranging from 23.8–50 °C. The shaded grey area bounded by two dashed black lines represents the area bounded by the series-parallel thermal conductivity limits calculated using the pure component thermal conductivity values. The measured thermal conductivity deviates significantly from the series-parallel thermal conductivity limits over the entire mixture concentration range. The figure is adapted from Ref. [8] where further details on the references are given.

figure, and was determined to be the result of experimental error [10]. However, it is clear that a noticeable minimum is present in thermal conductivity profile. The measured He-H₂ thermal conductivity deviates significantly from the series-parallel limits over the entire range of mixture concentrations, suggesting that discussing models such as the series-parallel limits in the context of fluids may not be particularly useful as it is possible to break these limits even for a simple gas mixture. Fig. 3.4 also highlights the difficulty in accurately measuring thermal conductivity in gas mixtures and repeating results.

A later study [10] investigated the potential for Enskog-kinetic theory to explain the minimum in thermal conductivity profile. This study determined that shallow minima in the thermal conductivity profile are possible for mixtures where the pure component thermal conductivities are similar which is the case for helium-hydrogen. This feature of Enskog-kinetic theory is promising and suggests that a hard-sphere model may be successful in describing this mixture.

3.2.2 Solid-liquid mixtures / nanofluids

The obvious lack of applicability to gas mixtures also calls into question the use of these continuum models in the context of nanofluid systems. The continuum bounds are compared with experimental nanofluid thermal conductivity data in Fig. 3.5 which shows

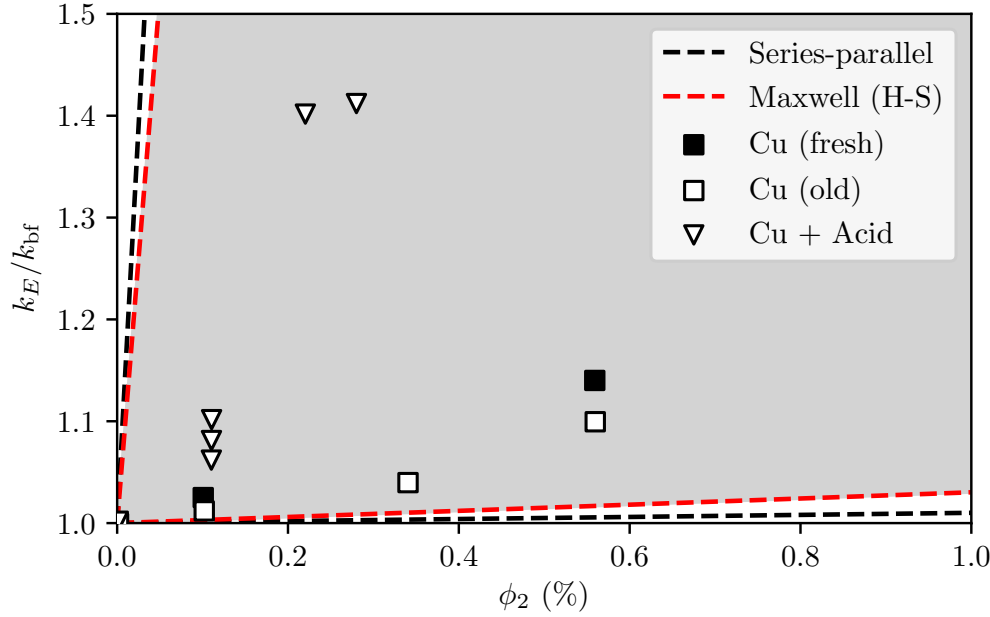


Figure 3.5: Thermal conductivity enhancement of a Copper - ethylene glycol suspension as a function of the volume fraction of copper ϕ_2 [11]. This graph shows the upper and lower thermal conductivity bounds as predicted by the series and parallel limits (Eqs. (2.1.1)) and the Maxwell (H-S) bounds (Eqs. (2.2.33)) assuming a copper thermal conductivity of $401 \text{ W m}^{-1} \text{ K}^{-1}$ and a ethylene glycol thermal conductivity of $0.258 \text{ W m}^{-1} \text{ K}^{-1}$. The area contained within the Maxwell bounds is shaded grey. The measured thermal conductivity is well within the series-parallel and the Maxwell bounds.

the series-parallel bounds, as well as the Maxwell bounds, along with the copper-ethylene glycol nanofluid thermal conductivity measurements from Fig. 1.2. Note that the volume fraction range studied here is much smaller than in Fig. 3.4. The continuum bounds are calculated assuming a copper thermal conductivity of $401 \text{ W m}^{-1} \text{ K}^{-1}$ and a ethylene glycol thermal conductivity of $0.258 \text{ W m}^{-1} \text{ K}^{-1}$. The series-parallel limits, as well as the narrower Maxwell model, effectively bound the measured thermal conductivity values for this nanofluid mixture; however, the results still represent a large enhancement of approximately 40 % above the base fluid conductivity for a nanoparticle volume fraction of only 0.3 %. This is the case for many nanofluid mixtures [12]; however, there are exceptions, such as the systems shown in Fig. 3.6. This figure shows thermal conductivity results for a water-iron oxide mixture as well as a water-fullerene mixture which exhibit thermal conductivity values which are well above and well below the series-parallel bounds respectively.

Other early studies of nanofluid mixtures also measured significant thermal conductivity enhancements [13–15] as well as a strong thermal conductivity dependence on nanoparticle size which spawned a large amount of activity and interest in this field of research. Studies initially focused on ceramic nanoparticles [5] which continued to yield unusual thermal conductivity results and, later, studies were also performed on nanofluids containing magnetic nanoparticles [16] under the influence of a magnetic field as well as

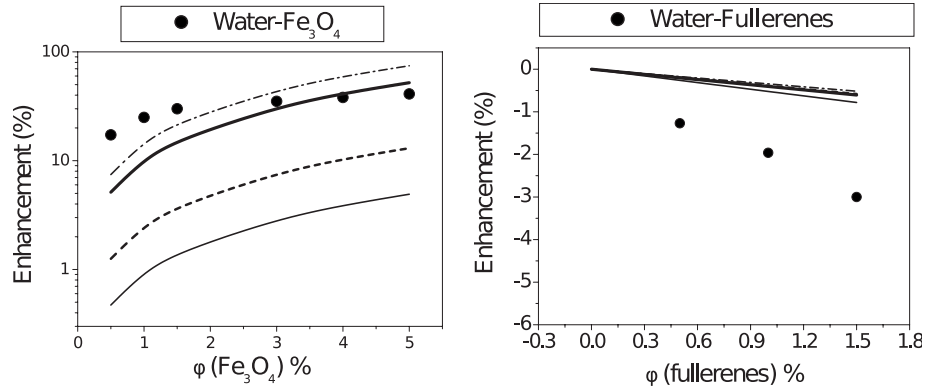


Figure 3.6: Thermal conductivity enhancement of a iron oxide - water nanofluid (left) as well as a fullerene - water nanofluid (right) as a function of the nanoparticle volume fraction taken from Ref. [12]. The upper and lower thermal conductivity bounds as predicted by the series and parallel limits (Eqs. (2.1.1)) and the Maxwell (H-S) bounds (Eqs. (2.2.33)) are shown. Both nanofluid mixtures exhibit thermal conductivity values which are outwith the continuum bounds.

nanofluids containing carbon nanotubes.

At this point, the reported thermal conductivity behaviour of nanofluids was inconsistent with regards to the magnitude of the enhancement relative to the base fluid thermal conductivity, as well as the thermal conductivity dependence on particle size. These inconsistent results could be caused by differences in the nanofluid synthesis process [17] which includes differences both in how the nanoparticles are produced and characterised and, also, how the nanoparticles are dispersed throughout the base fluid. Differences in the nanofluid “age” (time since nanoparticle dispersion) were also found to effect the thermal conductivity, as shown in Fig. 3.5. Also concerning, as shown in this figure, is the significant effect of adding a nanoparticle stabilising agent (acid) which is not standard and not included in the calculation of the series-parallel limits.

In order to clear up these inconsistencies and lay a firm foundation of experimental data on which to test various theories which could explain the nanofluid conductivity enhancement, a large international nanofluid property benchmark study [17] was commissioned in 2009. This study did not reach any conclusions on the effect of particle size; however, it did determine that all measured thermal conductivities were not anomalous and were within the Maxwell bounds for the studied set of nanofluids. The study also concluded that systematic differences between the thermal conductivity measurements were present for separate experimental techniques. This is shown in Fig. 3.7 where it is clear from the data that both the mean measured value and the measurement uncertainty differ significantly between measurement techniques. These systematic variations suggest that the understanding of how particular nanofluid mixtures interact with certain measurement techniques is incomplete.

It is important to note that classical models, such as the series-parallel bounds and Maxwell’s model, predict that the only variable that will affect the thermal conductivity

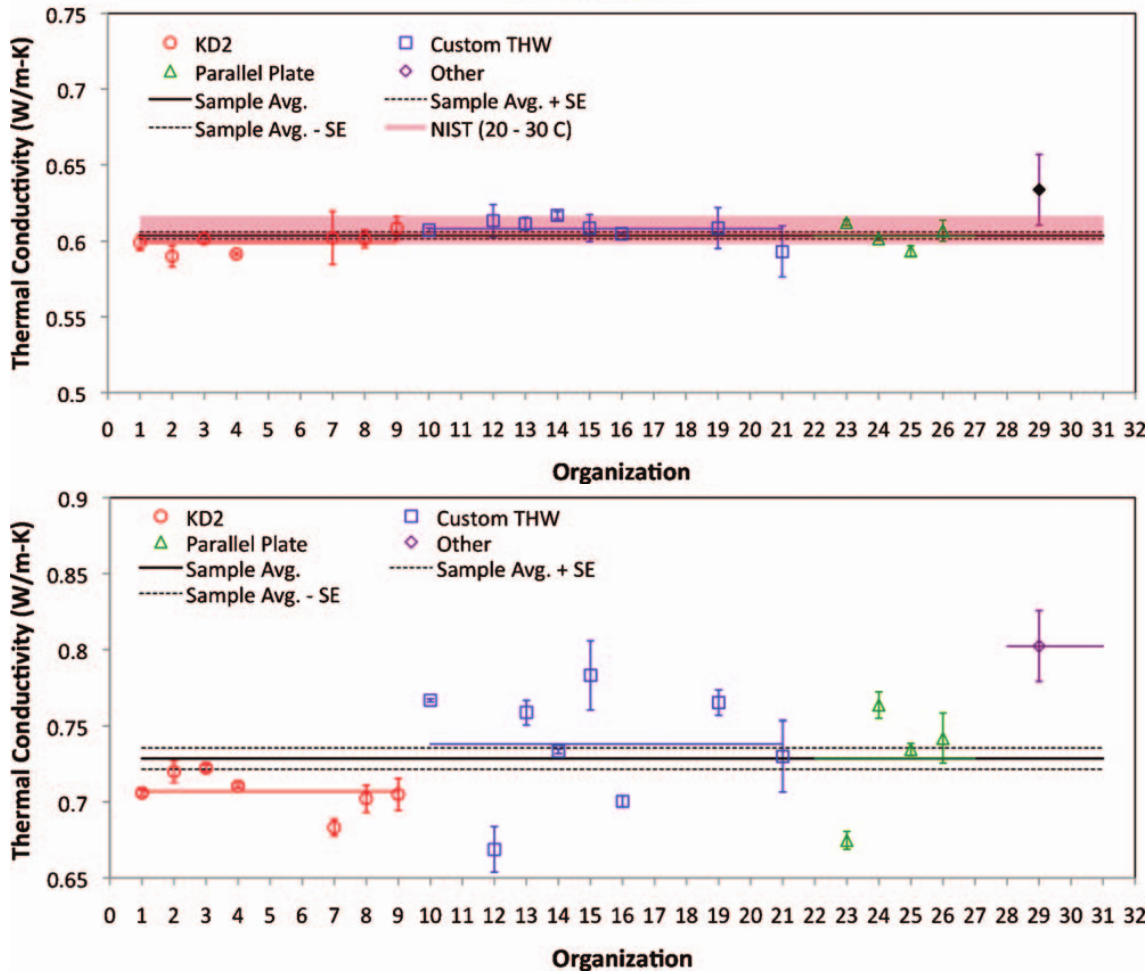


Figure 3.7: Thermal conductivity of two separate materials as measured by separate institutions. The top graph shows thermal conductivity measurements of de-ionised water while the bottom graph shows measurements for a nanofluid of 31 vol% 22 nm silica nanoparticles in water with a small amount of sodium sulphate added as a stabiliser. In the case of de-ionised water the shaded red band shows the known range of thermal conductivity from 20-30 °C. Several thermal conductivity measurement techniques were used by different institutions. Red markers represent measurements taken using a commercial KD2 thermal properties analyser from Decagon which utilises the transient hot wire method. Blue markers represent custom made transient hot wire measurement experiments, green markers represent steady-state parallel plate experiments, and purple markers represent all other measurement techniques. Solid black lines show the sample average measurement and dashed black lines show \pm one standard deviation. Solid coloured lines represent the average measurement for the corresponding measurement technique. Graphs are taken from Ref. [17].

of a mixture of two materials is the mixture volume fraction. Both of these models predict that variables such as the particle size of the suspended medium will have no effect on the degree of the thermal conductivity enhancement. This contradicts several studies [11, 14] performed on nanofluids which have reported that nanoparticle size strongly affects nanofluid thermal conductivity, suggesting that a continuum approach such as Maxwell's equation is not appropriate when discussing nanofluids. A recent study performed by

Pryazhnikov et al in 2017 [18] even reported that there is no correlation between the thermal conductivity of the nanoparticle material and the resulting thermal conductivity of the nanofluid containing this material. The unsuitability of the continuum approach means, therefore, that a molecular approach is required in order to characterise these materials and accurately predict the properties of real nanofluids.

3.3 Proposed nanofluid enhancement mechanisms / explanations

Various mechanisms have been proposed in the literature which attempt to explain thermal conductivity enhancements in nanofluids. This section will review the most popular theories which includes the theory of Brownian motion; this theory suggests that thermal conductivity enhancement could be caused by the random motion of nanoparticles through the base fluid causing local disturbances and turbulence and, hence, enhancing heat transfer. Studies also suggest the idea that interfacial nanoparticle layering could be responsible. In this case, it is suggested that base fluid particles could locally order around a solid nanoparticle creating a dense fluid layer with a relatively high thermal conductivity which would increase the overall conductivity of the fluid. The third theory that is reviewed here is the idea of nanoparticle clustering. Here, it is suggested that nanoparticles could spontaneously cluster and order themselves locally such that they form high-conductivity solid “pathways” which could conduct heat quickly through the base fluid.

3.3.1 Interparticle layering

Fig. 3.8 shows a possible representation of liquid layering near the surface of a nanoparticle. A solid nanoparticle is represented here by the large orange sphere and the liquid base fluid particles are represented by the smaller blue spheres. This figure shows a dense ordered layer of liquid particles surrounding the nanoparticle which is approximately two liquid particles in thickness. There is experimental evidence [19, 20] that liquid particles organise into ordered layers when in contact with a solid surface. This experimental evidence shows that a two-thick layer of water molecules in an ice-like structure appears at the liquid solid interface as well as the fact that as the distance from the crystal surface increases, the degree of fluid particle ordering decreases. Normal bulk fluid structure is restored at a distance of greater than 4 liquid particle layers from the solid.

This ordered particle layer would have a thermal conductivity which is greater than that of the bulk liquid as the increase in density would allow for faster, more efficient heat transfer. Models have been created which extend the Maxwell model (Eq. (2.2.32)) in order for the effect of the ordered interfacial layer [21]. This model predicts that for a nanofluid consisting of small nanoparticles with a diameter of < 10 nm with a inter-

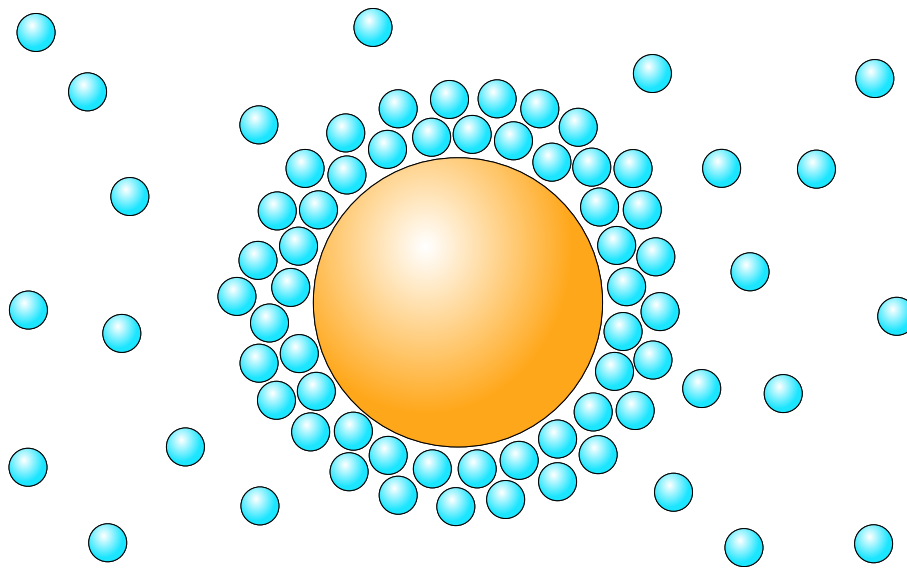


Figure 3.8: An illustration of an ordered interfacial layer of fluid particles around a single solid nanoparticle. The nanoparticle is represented by the large orange sphere and the base fluid particles are represented by the small blue spheres. The base fluid particles in contact with the nanoparticle are densely packed and packed in a crystal-like manner and the base fluid particles become less ordered as the distance from the nanoparticle increases.

facial liquid layer of ≥ 2 nm there is potential for a thermal conductivity enhancement which is more than eight times greater than the conventional Maxwell equation due to the large relative volume increase of high-conductivity solid-like material. However, as the radius of the nanoparticles increase and thickness of the interfacial layering decreases, the potential enhancement rapidly decreases and experiments have shown that the interfacial liquid layer is only typically < 1 nm in thickness [19, 20]. It has also been shown in Ref. [12] that, even for nanofluids containing small nanoparticles with a diameter of ≈ 4 nm, interfacial layering of this thickness would be inconsequential to the thermal conductivity enhancement in real systems. It is therefore unlikely that this mechanism is solely responsible for the large enhancements observed in nanofluids which commonly have nanoparticles which are ≈ 30 nm in diameter.

3.3.2 Nanoparticle clustering

It has been suggested that nanoparticles, when dispersed through a base fluid, could arrange themselves spontaneously into local nanoparticle clusters or a high conductivity chain-like pathway through the base fluid. Fig. 3.9 shows a possible representation of this effect. Assuming that the nanoparticle (large orange sphere) thermal conductivity is greater than that of the base fluid (small blue spheres), it is easy to see how the overall effective thermal conductivity of nanofluids could be significantly enhanced as heat can flow efficiently through the system from one high conductivity solid particle to the next unhampered by the lower thermal conductivity base fluid. Nanoparticles in Fig. 3.9 are not optimally distributed for increased nanofluid thermal conductivity as there is one

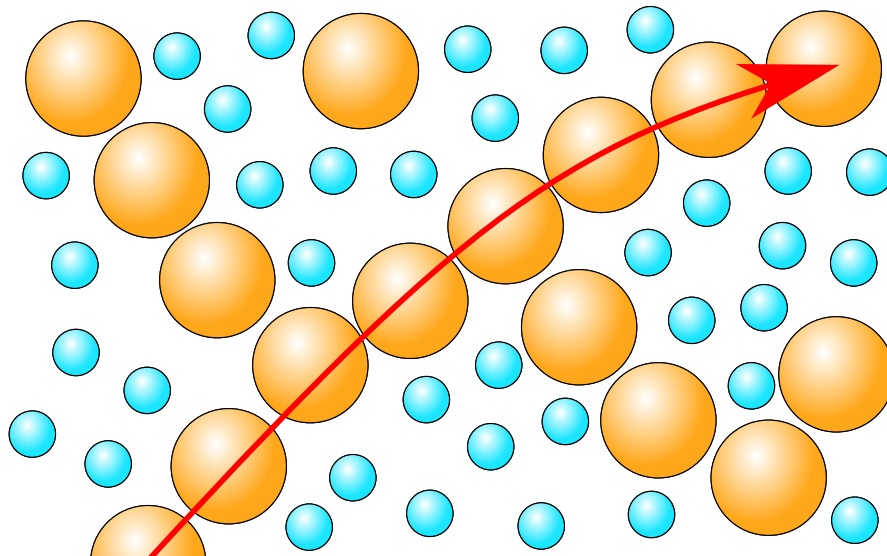


Figure 3.9: An illustration of one potential nanoparticle configuration within a base fluid producing a chain-like high thermal conductivity pathway through the base fluid. Nanoparticles are represented by the large orange spheres and base fluid particles are represented by the smaller blue spheres. The conduction of heat through one possible high conductivity pathway is shown by the red arrow.

visible nanoparticle which does not form part of a conductive nanoparticle chain; however, arranging all nanoparticles so that they form part of a conductive chain which spans the entire fluid would result in the nanofluid thermal conductivity tending to the parallel conductivity limit. The mechanism of nanoparticle clustering in isolation, therefore, will not cause a nanofluid to exhibit an anomalous thermal conductivity in the sense that it is beyond the upper parallel limit. However, it should be noted that large enhancements relative to the base fluid thermal conductivity are possible without producing anomalous thermal conductivities as shown in Fig. 3.5. For example, the parallel limit thermal conductivity for a copper-water nanofluid with a copper volume fraction of 1 % is ≈ 7 times greater than the pure water thermal conductivity. For a volume fraction of 0.5 %, it is ≈ 4 times greater.

Studies involving magnetic particles under the influence of an external magnetic field suggest that this mechanism has the potential to cause large increases in the thermal conductivity of nanofluids [16, 22]. It has, however, been shown that the probability of these nanoparticle configurations occurring consistently, and in a stable arrangement, is low [23] casting doubt over whether this mechanism is solely responsible for thermal conductivity enhancement. A study by Karthikeyan et al [24], which microscopically observed the formation of nanoparticle clusters, also showed that the measured thermal conductivity decreased as the nanofluid aged and the nanoparticles began to agglomerate. It is clear that percolating, chain-like nanoparticle structures in nanofluids have the potential to greatly increase heat transfer if it is possible for such structures to form consistently.

3.3.3 Brownian motion / thermal diffusion

It has also been suggested that the thermal conductivity enhancement could be due to Brownian motion of nanoparticles through the base fluid [12]. It has been proposed that the motion of large nanoparticles could induce convection in the surrounding base fluid particles when travelling through the fluid which could enhance heat transfer. Models of nanofluids that have included the effects of Brownian motion have had successes when compared with a small number of experimental measurements [25, 26]; however, studies have shown that the speed of the Brownian motion of nanoparticles through the fluid would be too slow relative to the direct flow of heat through the mixture to have any measurable effect on the thermal conductivity [23].

In addition to the diffusion of nanoparticles through random motion, the influence of a temperature gradient will also cause particles to diffuse due to thermal diffusion towards either the hot or cold section of the fluid. Diffusing particles will carry heat as they travel, hence increasing the total amount of heat transfer and increasing the effective thermal conductivity. Eapen et al [12] show that, for typical nanofluid systems, thermal diffusion coefficients are small and, therefore, the thermal conductivity enhancement corresponding to thermal diffusion is several orders of magnitude less than the thermal conductivity of the base fluid. This is in agreement with another study [27] which found that the effects of thermal diffusion had no significant effect on the observed thermal conductivity in nanofluids. Ref. [12] states, however, that thermal diffusion, as well as mutual diffusion, will have an indirect effect on thermal conductivity in nanofluids as these are the primary mechanisms which control the aggregation of solid nanoparticles. Accurately characterising diffusion in nanofluids is therefore key to developing a complete model of nanofluid thermal conductivity.

References

- [1] W. Neal, J. Greenway, and P. Coutts. “Thermal conduction in helium-hydrogen gas mixtures”. In: *Proceedings of the physical society of London* 87 (1966), pp. 556–577.
- [2] P. K. Tondon, J. M. Gandhi, and S. C. Saxena. “Thermal conductivity of H₂–He and D₂–He systems”. In: *Proc. Phys. Soc.* 92 (1967), pp. 253–255.
- [3] T. T. Loong and H. Salleh. “A review on measurement techniques of apparent thermal conductivity of nanofluids”. In: *IOP Conf. Ser.: Mater. Sci. Eng.* 226 (2017), p. 012146.
- [4] H. Roder. “A transient hot wire thermal conductivity apparatus for fluids”. In: *Journal of research of the national bureau of standards* 86.5 (1981).

-
- [5] H. Calvin and G. Peterson. “Experimental investigation of temperature and volume fraction variations on the effective thermal conductivity of nanoparticle suspensions (nanofluids)”. In: *Journal of Applied Physics* (2006).
- [6] J. J. de Groot, J. Kestin, and H. Sookiazian. “Instrument to measure the thermal conductivity of gases”. In: *Physica* 75 (1974), pp. 454–482.
- [7] J. J. Healy, J. J. de Groot, and J. Kestin. “The theory of the transient hot-wire method for measuring thermal conductivity”. In: *Physica* 82C (1975), pp. 392–408.
- [8] A. G. Shashkov, F. P. Kamchatov, and T. N. Abramenko. “Thermal conductivity of the hydrogen-helium mixture”. In: *J. Eng. Phys.* 24.4 (1973), pp. 461–464.
- [9] P. Mukhopadhyay and A. K. Barua. “Thermal conductivity of hydrogen-helium gas mixtures”. In: *J. Appl. Phys.* 18.5 (1967), p. 635.
- [10] L. Biolsi and E. A. Mason. “On the Existence of Minima and Maxima in the Composition Dependence of the Thermal Diffusion Factor and Thermal Conductivity”. In: *J. Chem. Phys.* 54.7 (1971), pp. 3020–3022.
- [11] J. A. Eastman et al. “Anomalously increased effective thermal conductivities of ethylene glycol-based nanofluids containing copper nanoparticles”. In: *Appl. Phys. Lett.* 78 (2001), pp. 718–720.
- [12] J. Eapen et al. “The Classical Nature of Thermal Conduction in Nanofluids”. In: *J. Heat Transfer* 132 (2010), p. 102402.
- [13] J. Eastman et al. “Enhanced thermal conductivity through the development of nanofluids”. In: *Mater. Res. Soc. Symp. Proc.* 457 (1997), pp. 3–11.
- [14] S. Lee et al. “Measuring Thermal Conductivity of Fluids Containing Oxide Nanoparticles”. In: *J. Heat Transfer* (1999).
- [15] X. Wang, X. Xu, and S. U. S. Choi. “Thermal Conductivity of Nanoparticle - Fluid Mixture”. In: *J. Thermophys. Heat Transfer* 13.4 (1999), pp. 474–480.
- [16] K. Parekh and H. S. Lee. “Magnetic field induced enhancement in thermal conductivity of magnetite nanofluid”. In: *J. Appl. Phys.* 107.9 (2010), 09A310.
- [17] J. Buongiorno et al. “A benchmark study on the thermal conductivity of nanofluids”. English. In: *J. Appl. Phys.* 106 (2009), p. 094312.
- [18] M. I. Pryazhnikov et al. “Thermal conductivity measurement of nanofluids”. In: *Int. J. Heat Mass Transfer* 104 (2017), pp. 1275–1282.
- [19] C. Yu et al. “Molecular Layering in a Liquid on a Solid Substrate”. In: *Physica B* (2000).
- [20] M. Reedijk et al. “Liquid order at the interface of KDP crystals with water: Evidence for icelike layers”. In: *Phys. Rev. Lett.* 90 (2003), p. 066103.

- [21] W. Yu and S. Choi. “The role of interfacial layers in the enhanced thermal conductivity of nanofluids: A renovated Maxwell model”. In: *J. Nanopart. Res.* 5 (2003), pp. 167–171.
- [22] J. Philip, P. D. Shima, and B. Raj. “Enhancement of thermal conductivity in magnetite based nanofluid due to chainlike structures”. In: *Appl. Phys. Lett.* 91.20 (2007), p. 203108.
- [23] P. Keblinski, R. Prasher, and J. Eapen. “Thermal conductance of nanofluids: is the controversy over?” In: *J. Nanopart. Res.* 10 (2008), pp. 1089–1097.
- [24] N. R. Karthikeyan, J. Philip, and B. Raj. “Effect of clustering on the thermal conductivity of nanofluids”. In: *Mater. Chem. Phys.* 109 (2008), pp. 50–55.
- [25] R. Prasher, P. Bhattacharya, and P. E. Phelan. “Thermal Conductivity of Nanoscale Colloidal Solutions (Nanofluids)”. In: *Phys. Rev. Lett.* 94.2 (2005), p. 025901.
- [26] S. P. Jang and S. U. S. Choi. “Role of Brownian motion in the enhanced thermal conductivity of nanofluids”. In: *Appl. Phys. Lett.* 84.21 (2004), pp. 4316–4318.
- [27] D. Wen, L. Zhang, and Y. He. “Flow and migration of nanoparticle in a single channel”. In: *Heat and Mass Transfer* 45.8 (2009), pp. 1061–1067.

THE HARD-SPHERE MODEL

It is clear from a review of gas mixture and nanofluid thermal conductivity in Ch. 3 that a molecular model is required in order to study the mechanics of how microscopic motion scales up to macroscopic thermal transport and accurately predict the properties of fluid/fluid-solid mixtures. The model must be simple such that it is computationally efficient, as there is a large time and length scale¹ separation between the micro and macroscopic scales, thus massive and long simulations must be run. Additionally, following a reductionist approach, if the chosen model is as simple as possible such that removing one element causes phenomena of interest to disappear, then the fundamental features which lead to those phenomena have been captured.

The simplest molecular model is the ideal gas which approximates molecules as point particles; however, this model has trivial dynamics and simple mixing rules for all of its physical properties. Thus there is no opportunity for anomalous conduction to arise. Hard spheres are completely impenetrable perfect spheres which are completely characterised by their diameter σ and their mass m as illustrated in Fig. 4.1. The hard-sphere interparticle potential is given by the following equation,

$$U_{ij} = \begin{cases} 0 & \text{for } |\mathbf{r}_{ij}| \geq \sigma_{ij} \\ \infty & \text{for } |\mathbf{r}_{ij}| < \sigma_{ij} \end{cases}, \quad (4.0.1)$$

where U_{ij} is the interparticle potential between particles i and j , $\sigma_{ij} = (\sigma_i + \sigma_j)/2$ is the collision diameter between particles i and j with diameters σ_i and σ_j respectively, and $|\mathbf{r}_{ij}| = |\mathbf{r}_i - \mathbf{r}_j|$ is the distance between particles i and j with positions \mathbf{r}_i and \mathbf{r}_j respectively. Eq. (4.0.1) is also shown graphically in Fig. 4.1. Hard-spheres do not interact until two spheres collide at which point they experience an impulsive force which causes them to move apart. Excluded volume effects which are introduced by this model immediately lead to a wealth of complex behaviour, when compared to the ideal gas model, including a fluid-solid transition which is demonstrated in Fig. 4.2, and non-trivial density and mixture effects [1]. The lack of any attractive forces this model means that other effects

¹For example, 1 m³ of water contains $N \approx 10^{25}$ water molecules

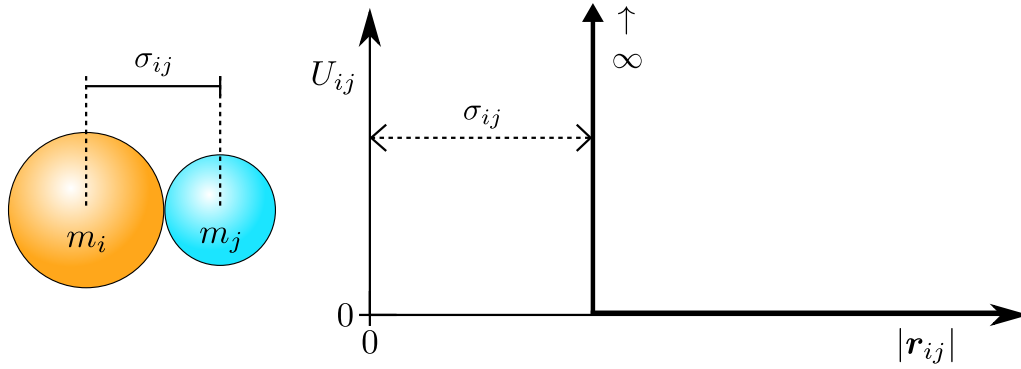


Figure 4.1: Interparticle potential U_{ij} as a function of the distance between two hard-spheres $|r_{ij}| = |\mathbf{r}_i - \mathbf{r}_j|$ for the hard-sphere model. $\sigma_{ij} = (\sigma_i + \sigma_j)/2$ is the collision diameter of two hard-sphere i and j . The figure also shows an illustration of two hard-spheres, highlighting the collision diameter along with the hard-sphere masses m_i and m_j .

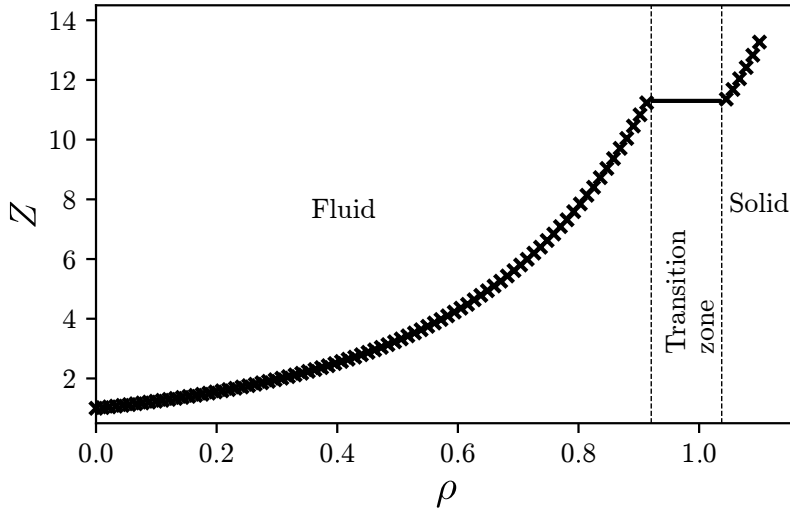


Figure 4.2: Hard-sphere phase diagram showing the compressibility Z as a function of density ρ as calculated in Ch. 11. Data shown are for monocomponent hard-sphere MD simulations containing 2916 spheres. Dashed black lines highlight the hard-sphere fluid-solid transition zone. The densities where hard-sphere systems exist as a fluid and as a solid are labelled.

such as a gas-liquid transition are not captured. Other commonly used particle potentials, such as the Lennard-Jones [2] and the square-well potentials [3] do attempt to model the attractive behaviour of real particles; however, one of the key benefits of the hard sphere model is its relatively complete hydrodynamic description obtained by kinetic theory. No other model has the same depth of predictive power, thus the hard sphere is ideal for investigating fundamental effects in thermal conduction with all the complexities of molecular mass and size differences as well as the effects of mixtures (including mutual diffusion and thermodiffusion).

Conventionally, in order to reduce the number of degrees of freedom when study-

ing hard-sphere systems, analysis is performed in reduced units. Properties of any hard-sphere systems will be a function of the system energy (which is purely a function of temperature in the case of hard-spheres), the system density, and the parameters (mass and diameter) of each hard-sphere species as shown in the following equation for a general system property f ,

$$f \left(\frac{k_B T \tau^2}{M L^2}, \rho L^3, \frac{\sigma_1}{L}, \frac{\sigma_2}{L}, \dots, \frac{m_1}{M}, \frac{m_2}{M}, \dots \right), \quad (4.0.2)$$

where the units of values are shown in terms of the unit time scale τ , the unit length scale L , and the unit mass scale M . k_B is the Boltzmann constant. Hard-spheres have no intrinsic energy scale, thus their temperature dependence remains trivial. It is therefore possible to define the time in the system in terms of the temperature as shown in the following set of equations,

$$L = \sigma_1 \quad M = m_1 \quad \tau = \sqrt{\frac{m_1 \sigma_1^2}{k_B T}}, \quad (4.0.3)$$

where the unit mass and length scales in the system have been set to the hard-sphere parameters of species 1. Defining the units of the system in this way means that Eq. (4.0.2) can be rewritten as,

$$f \left(\frac{k_B T}{k_B T}, \rho \sigma_1^3, \frac{\sigma_1}{\sigma_1}, \frac{\sigma_2}{\sigma_1}, \dots, \frac{m_1}{m_1}, \frac{m_2}{m_1}, \dots \right), \quad (4.0.4)$$

where several terms have cancelled to 1. Performing dimensional analysis in this way shows that in a monocomponent hard-sphere system, the only variable which matters is the reduced density $\rho \sigma_1^3$. Properties of the system at other values of m_1 or T can be calculated simply using the appropriate dimensional scaling. Furthermore, in a binary mixture, as well as the reduced density, the only important variables are the mass ratios m_2/m_1 and diameter ratios σ_2/σ_1 of the hard-sphere species. All results in this thesis are reported in this set of reduced units.

The following section describes how to solve for the dynamics of the hard-sphere model using *event-driven* molecular dynamics before proceeding to describe specific methods which can be used in order to extract the thermal conductivity of hard-sphere materials. These techniques fall into one of two categories: equilibrium or non-equilibrium.

4.1 Event-driven molecular dynamics

Molecular dynamics simulation, in contrast to modelling a fluid as a continuous medium, attempts to model a fluid as a collection of discrete particles. This involves solving for the dynamics of a set of particles according to the chosen particle potential and starting

from some initial state. Solving for the motion of particles in this way allows a detailed record of the position and velocity of every particle over time to be generated which allows for detailed analysis of the small scale molecular behaviour and mechanisms which contribute to macroscopic behaviour.

In order to simulate systems of *hard* particles such as hard spheres and square wells a simulation technique known as *event-driven* molecular dynamics is required. This simulation technique is similar to its counterpart, *time-driven* molecular dynamics, but fundamentally differs in the method used to resolve particle interactions. In the time driven approach, time is divided up into many discrete time steps which are small relative to the time over which a particle interaction takes place in order to properly resolve the dynamics of the interaction. The evolution of particle positions and velocities are calculated by integrating these values forward in time according to the current particle velocity and the force exerted on the particle by the rest of the system. It quickly becomes obvious why this method is incompatible with the hard-sphere model shown in Fig. 4.1 as the force exerted on a particle (derivative of the potential) will be a delta spike at $|\mathbf{r}_{ij}| = \sigma_{ij}$.

In order to overcome the challenge of handling impulsive forces and correctly resolve particle interactions, event-driven molecular dynamics utilises a collision rule which expresses the post-collision velocities of the two particles which are undergoing the collision as a function of the pre-collision velocities. In order to derive the hard-sphere collision rule, it is noted that in a fully elastic hard-sphere system, kinetic energy and momentum are conserved over the course of a collision. The momentum and kinetic energy balances of two fully elastic colliding hard-spheres is written as follows,

$$m_1 \mathbf{v}_1 + m_2 \mathbf{v}_2 = m_1 \mathbf{v}'_1 + m_2 \mathbf{v}'_2, \quad (4.1.1)$$

$$m_1 (\mathbf{v}_1)^2 + m_2 (\mathbf{v}_2)^2 = m_1 (\mathbf{v}'_1)^2 + m_2 (\mathbf{v}'_2)^2, \quad (4.1.2)$$

where \mathbf{v}_1 and \mathbf{v}_2 are the pre-collision velocities of particles 1 and 2 respectively, and \mathbf{v}'_1 and \mathbf{v}'_2 are the restituted (post-collision) velocities of spheres 1 and 2 respectively. Rearranging and combining these balance equations allows the restituted velocity to be expressed as a function of the pre and post collision relative velocities

$$\mathbf{v}'_1 = \mathbf{v}_1 + \frac{\mu_{12}}{m_1} (\mathbf{v}'_{12} - \mathbf{v}_{12}) \quad (4.1.3)$$

where $\mathbf{v}'_{12} = \mathbf{v}'_i - \mathbf{v}'_j$ is the restituted relative velocity, and $\mu_{12} = m_1 m_2 / (m_1 + m_2)$ is the relative mass. In hard-spheres this difference between the pre and post-collision relative velocities is a function of the contact vector and the previous relative velocity and is given by the rule of specular reflection where the velocity flips in the direction of collision as follows,

$$\mathbf{v}'_{12} - \mathbf{v}_{12} = -2 (\hat{\mathbf{r}}_{12} \cdot \mathbf{v}_{12}) \hat{\mathbf{r}}_{12}, \quad (4.1.4)$$

where $\hat{\mathbf{r}}_{12}$ is the unit vector representing the direction of the relative particle positions at the moment of collision. Substituting this expression into Eq. (4.1.3) gives the hard-sphere collision rules as follows,

$$\mathbf{v}'_1 = \mathbf{v}_1 - \frac{2\mu_{12}}{m_1} (\mathbf{v}_{12} \cdot \hat{\mathbf{r}}_{12}) \hat{\mathbf{r}}_{12}, \quad \mathbf{v}'_2 = \mathbf{v}_2 + \frac{2\mu_{12}}{m_2} (\mathbf{v}_{12} \cdot \hat{\mathbf{r}}_{12}) \hat{\mathbf{r}}_{12}. \quad (4.1.5)$$

After event handling, the next critical aspect of the event-driven molecular dynamics technique is event detection [4]. In order to update particle velocities on collision, one must first calculate when collisions will take place and advance the system to that point in time. In order to do this, an event-driven simulation examines the positions and velocities of each pair of spheres in order to determine, on their current trajectories and ignoring other spheres, the time until they will next collide. At the point of collision, the distance between two particles will be equal to the collision diameter of the particles which can be written as follows,

$$|\mathbf{r}_1(t + \Delta t_c) - \mathbf{r}_2(t + \Delta t_c)| = \sigma_{12}, \quad (4.1.6)$$

where Δt_c is the difference between the current time t and the time that a collision will occur. This equation is squared in order to remove the need to calculate the absolute value of the relative position,

$$(\mathbf{r}_1(t + \Delta t_c) - \mathbf{r}_2(t + \Delta t_c))^2 = \sigma_{12}^2. \quad (4.1.7)$$

The future position of a sphere in the simulation can be calculated by integrating forward in time using the current particle velocity as follows,

$$\mathbf{r}_1(t + \Delta t) = \mathbf{r}_1(t) + \mathbf{v}_1(t)\Delta t. \quad (4.1.8)$$

Substituting this equation into Eq. (4.1.7) gives

$$(\mathbf{r}_{12}(t) + \mathbf{v}_{12}(t)\Delta t_c)^2 = \sigma_{12}^2, \quad (4.1.9)$$

where the only remaining unknown is now the collision time Δt_c . Expanding out the term on the left hand side of Eq. (4.1.9) results in a quadratic in Δt_c ,

$$\mathbf{r}_{12}^2 + 2(\mathbf{v}_{12} \cdot \mathbf{r}_{12})\Delta t_c + \mathbf{v}_{12}^2\Delta t_c^2 = \sigma_{12}^2, \quad (4.1.10)$$

where the brackets denoting time dependence have been removed as everything is evaluated at the current time t . This equation can then be solved using the quadratic formula to exactly calculate the collision time as follows,

$$\Delta t_c = \frac{-2(\mathbf{v}_{12} \cdot \mathbf{r}_{12}) \pm \sqrt{4(\mathbf{v}_{12} \cdot \mathbf{r}_{12})^2 - 4\mathbf{v}_{12}^2(\mathbf{r}_{12}^2 - \sigma_{12}^2)}}{2\mathbf{v}_{12}^2}. \quad (4.1.11)$$

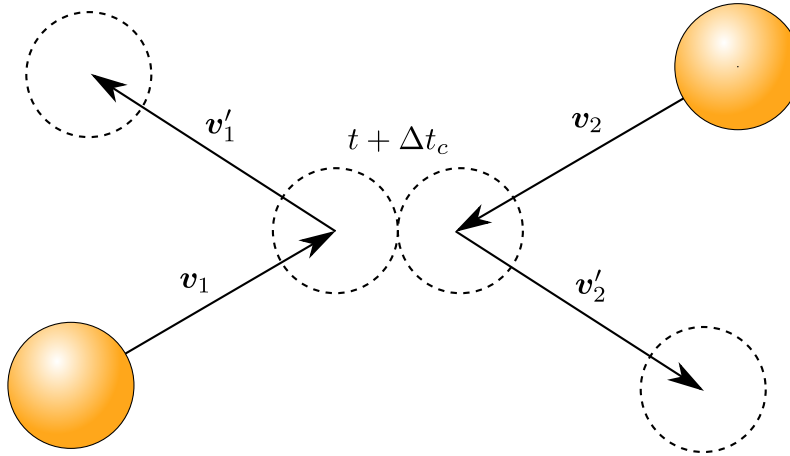


Figure 4.3: A schematic diagram of two hard-sphere particles (orange spheres) travelling through space with velocities v_1 and v_2 . The direction of the spheres through space is shown using arrows. Armed with the sphere velocities along with the current positions of both spheres, it is possible to calculate the collision time Δt_c . This is the time until these two spheres will collide if they remain on their current trajectories and it can be calculated exactly in event-driven molecular dynamics using the method outlined in Section 4.1. Dashed circles represent the position of the spheres during collision when they are in contact. Secondary arrows show the post-collision path of the spheres through space with restituted velocities v'_1 and v'_2 calculated using Eq. (4.1.5). Dashed circles also represent the position of the spheres after some time travelling on their post-collision trajectory.

If this equation has no real roots, this means that the two spheres will not collide. One real root means that the spheres will experience a glancing collision, and two real roots means that the spheres will collide. In this case, the earliest root corresponds to the moment that the spheres first come into contact and the second root corresponds to the moment at which the spheres finish passing through each other. When calculating the collision time in this way, care must be taken to ensure that the spheres are approaching each other ($v_{ij} \cdot r_{ij} < 0$) in order to ensure that the collision will take place on the future and not in past according to the current trajectories of the spheres. Fig. 4.3 illustrates the complete process of resolving a hard-sphere collision, showing two hard-sphere particles initially with velocities v_1 and v_2 . The simulation is advanced to the point in time at which the spheres will be in contact $t + \Delta t_c$ (calculated using Eq. (4.1.10)) and the sphere velocities are updated to the post collision values using the collision rules shown in Eqs. (4.1.5).

An outline of the event-driven molecular dynamics algorithm [4] is shown in Fig. 4.4. When performing a simulation, the positions and velocities of all particles are initialised according to the desired simulation parameters such as density and temperature. Hard-sphere mass and diameter values must then be assigned to each particle in line with the mono or multi-component mixture which is to be simulated. After initialisation is complete, the collision time is calculated for each pair of particles. It is then a matter of sorting all potential collisions in order to determine which collision will occur first. After identifying the next collision, the simulation is advanced Δt_c into the future to the point of contact and the collision is resolved as shown in Fig. 4.3. Once the collision is resolved,

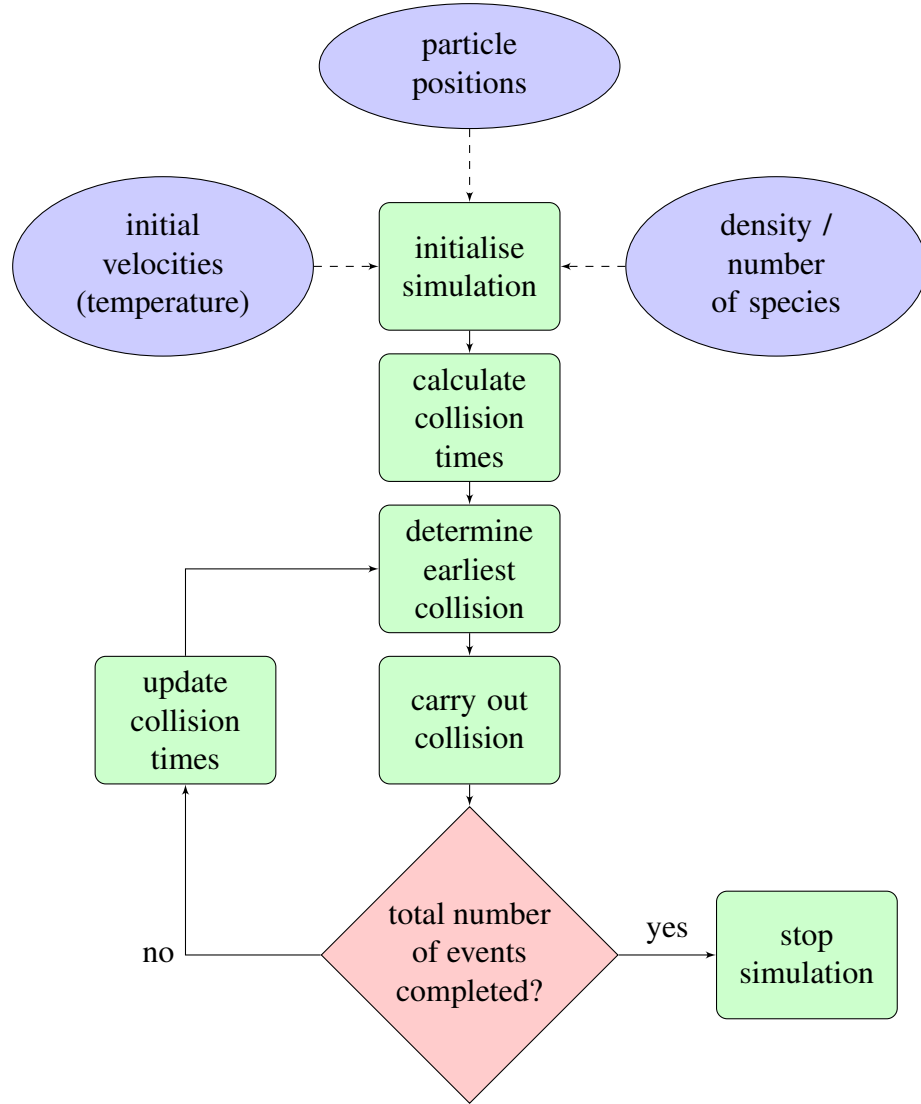


Figure 4.4: A flowchart showing the core operations of the event-driven molecular dynamics algorithm beginning with the initialisation of the system according to the desired system parameters such as temperature and density and subsequently resolving collisions in chronological order as they arise.

the collision times for the colliding spheres must be updated according to their new position and velocity values. At this point the shortest collision time is re-identified and the process is repeated for as many events as is desired.

Eq. (4.1.10) highlights one of the advantages of event-driven simulation which is that it is able to skip all free dynamics in the system while still resolving collisions. This is especially impactful at low density values where the mean free time between collisions is large. A further advantage of this method is that it is exact; both the time to the next collision Δt_c , and the velocity changes during the collision, are calculated to machine precision. Unlike time-driven simulation, results are not dependent on numerical parameters such as the time step size. All MD simulations reported in this thesis are performed using an event-driven molecular dynamics simulation package named DynamO [5].

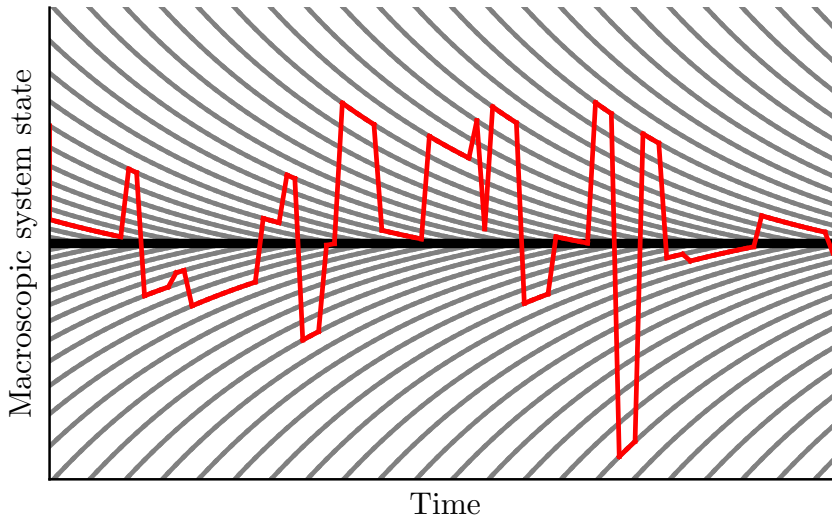


Figure 4.5: Hard-sphere system state as a function of time. The red line represents microscopic fluctuations around equilibrium which is represented by the central horizontal black line. The green lines show paths of relaxation of the macroscopic system towards equilibrium. Even though the system microscopically fluctuates around equilibrium, on average the system decays back to the equilibrium state. This figure is adapted from Ref. [6].

4.2 Equilibrium measurements

Equilibrium molecular dynamics simulation is characterised by the fact that there is no net flow of matter or energy into or out of the system. This means that when looking at the system of particles on a macroscopic level, the system will come to equilibrium and remain there. However, on a microscopic level, the properties of individual particles and local regions of the simulation will fluctuate around the mean value as particles travel through the system and interact. On average, local fluctuations in the system will decay back towards the equilibrium state as illustrated in Fig. 4.5. Local fluctuations in the system tend to dissipate proportionally to local system gradients [6] which means that recording the decay over time of these microscopic fluctuations provides a route to determining the transport properties of the system using methods such as the Green-Kubo [7, 8] relations. Equilibrium MD simulations in this thesis utilise the Einstein formulations [1, 9, 10] of the Green-Kubo relationships as the original formulations are not compatible with discontinuous particle potentials, such as the hard-sphere model, as the expressions require the interparticle force. The computation is therefore challenging as the hard-sphere force is impulsive.

The Einstein form of the Green-Kubo relations takes the general form of the following

time correlation function as given in Refs. [1, 9, 10]

$$L_{\alpha_1\alpha_2}(t) = \frac{\beta}{2tV} \langle W_{\alpha_1}(t)W_{\alpha_2}(t) \rangle, \quad (4.2.1)$$

where $\beta = 1/(k_B T)$, $L_{\alpha_1\alpha_2}(t)$ is a transport coefficient such as the thermal conductivity L_{uu} or the mutual diffusion coefficient L_{ab} , and W_{α_1} and W_{α_2} are the time integrals of microscopic system fluxes. The mutual diffusion L_{aa} , thermal diffusion L_{ua} , and thermal conductivity L_{uu} coefficients are calculated using varying combinations of the time integral of the microscopic kinetic energy flux W_u and the microscopic mass flux of species a W_a which are given by Ref. [1] as

$$W_a = \sum_{\Delta t_c}^t \sum_k^{N_a} m_k \mathbf{v}_k \Delta t_c - w_a \sum_k^N m_k \mathbf{v}_k \Delta t_c, \quad (4.2.2)$$

$$W_u = \sum_{\Delta t_c}^t \left(\sum_k^N \frac{1}{2} m_k \mathbf{v}_k^2 \Delta t_c + \frac{1}{2} m_i \Delta \mathbf{v}_i^2 \mathbf{v}_{ij} \right), \quad (4.2.3)$$

where Δt_c is the interval between collisions which take place during the total simulation time t , \mathbf{v}_i is the peculiar velocity of particle i , w_a is the mass fraction of species a , and N_a is the total number of spheres of species a

In order to mimic the behaviour of a bulk system as $N \rightarrow \infty$, periodic boundary conditions are commonly used in equilibrium MD simulation. This boundary condition results in spheres exiting the simulation through one boundary and reentering the simulation through the diametrically opposing boundary. However, this bulk approximation is temporary. Fluctuations in the properties of one particle will spread out from that particle at the speed of sound. As the simulation time extends beyond the sound wave traversal time, the effects of individual particle fluctuations will begin to be felt by that same particle as the effect loops back round through the periodic boundaries and causes a positive correlation. Hence, when using a time-correlation function such as the Green-Kubo relations, the correlation time must be limited in order to remove the effects of self-correlation. The sound wave traversal time is calculated using the simulation box length and speed of sound c which is given by Ref. [1] for a hard-sphere system as follows,

$$c^2 = \frac{k_B T}{\sum_a x_a m_a} \left(\frac{2Z^2}{3} + \frac{\partial \rho Z}{\partial \rho} \right), \quad (4.2.4)$$

where $Z = p/(T\rho)$ is the compressibility, and x_a is the mol fraction of species a . When estimating the sound wave traversal time for use with time correlation calculations in this thesis, the compressibility Z is calculated using the BMCSL [11, 12] equation of state (EOS).

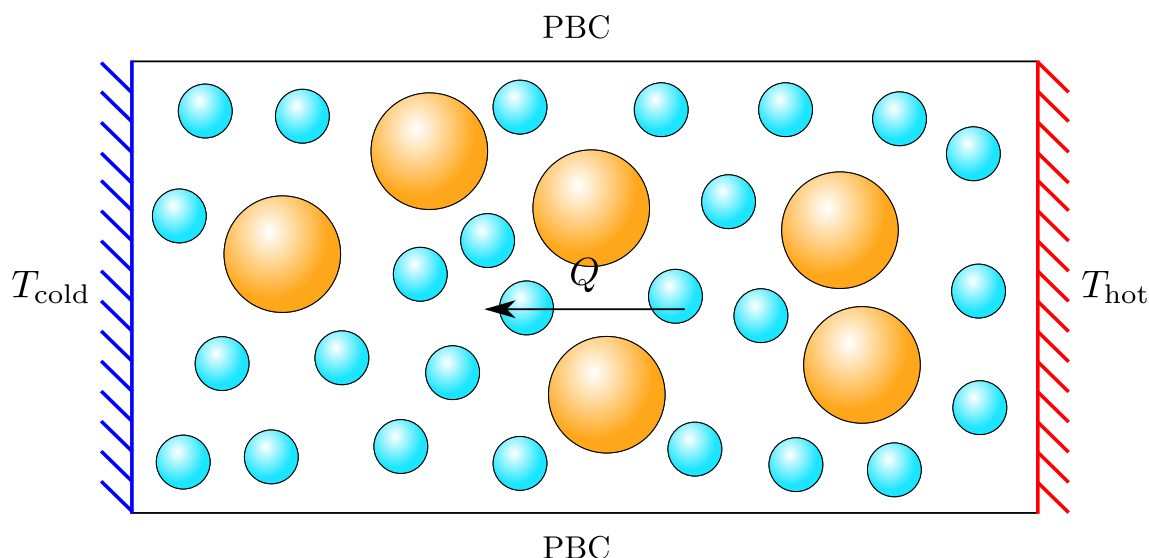


Figure 4.6: A schematic 2-D representation of a multicomponent hard-sphere NEMD simulation using the parallel heated walls algorithm in order to measure thermal conductivity. Two parallel smooth walls are placed at opposite ends of the simulation domain. These walls are set to temperatures of T_{cold} and T_{hot} , as labelled, in order to induce a temperature gradient across the simulation. The simulation is surrounded by periodic boundary conditions on the boundaries which are not covered by the parallel walls.

4.3 Non-equilibrium techniques

In contrast to equilibrium methods, non-equilibrium (NEMD) techniques measure the properties of molecular systems by imparting an external force on the system, forcing it out of equilibrium, and then measuring the resulting response. In this sense NEMD is more direct than equilibrium methods and more analogous to real life experimental measurements. In order to measure the thermal conductivity using NEMD simulation, a temperature gradient is imposed on the system which allows for the measurement of the resulting heat flux. It is also possible to carry out this process in reverse and impose a heat flux through the system and measure the resulting temperature gradient. This section discusses the various methods of measuring thermal conductivity using NEMD as well as the main differences of this method relative to equilibrium methods.

4.3.1 Heated walls

The NEMD parallel heated walls thermal conductivity measurement technique induces a temperature gradient across a simulation using two parallel heated walls at either end of a simulation as displayed in Fig. 4.6. As mentioned in Section 4.2, periodic boundary conditions are used on some simulation boundaries in order to mimic the effect of an infinite system. A new type of particle interaction is introduced into the simulation when using this method as hard walls now cover two ends of the simulation. Instead of the sphere reentering the simulation on the opposite side; spheres which collide with the walls are reflected back into the simulation. In the case of heated walls, each collision

also reassigns the kinetic energy of the particle according to Gaussian distribution with a temperature equal to the temperature of the wall (T_{hot} or T_{cold}).

The energy imparted by the heated wall at $T = T_{\text{hot}}$ is slowly conducted through the simulation, both through particles motion, as well as particle collisions. After being transported to the opposite end of the simulation, this energy is then removed by the corresponding wall at $T = T_{\text{cold}}$. Over the course of a simulation, the total amount of energy added to and removed from the simulation is recorded. This data can then be used in order to determine the total energy flux through the simulation.

The imposed temperature gradient as well as the resultant heat flux through the system are related to the thermal conductivity via Fourier's law which can be written as

$$Q = k\Delta T, \quad (4.3.1)$$

where $\Delta T = T_{\text{hot}} - T_{\text{cold}}$ is the temperature difference between the two parallel heated walls, and the heat flux is calculated as

$$Q = \frac{El_z}{l_x l_y t}, \quad (4.3.2)$$

where l_x , l_y , and l_z are the lengths of the simulation in the x , y , and z dimensions respectively, t is the total simulation time, and E is the total energy transferred through the system. This could be taken as the total heat added E_{added} , or removed E_{removed} . In this thesis, an average of the two values $(E_{\text{removed}} + E_{\text{added}})/2$ is used.

4.3.2 Energy exchange

As an alternative to the parallel heated walls method, a temperature gradient may be imposed using multiple thermalising zones. This is known as the method of energy exchange [13] and is illustrated in Fig. 4.7. This method utilises periodic boundary conditions on all boundaries similar to equilibrium methods. The red and blue shaded areas in Fig. 4.7 represent thermalising zones which modify the velocities of spheres which are situated within them in order to set the temperature inside the zone to T_{hot} or T_{cold} . Similar to the heated walls method (Fig. 4.6), a heat flux through the system will eventually become established as heat conducts from the hot zone to the cold zone. The total energy removed and added through the thermalising zones is recorded and the thermal conductivity can be calculated using Eq. (4.3.1). It is also possible to perform this measurement in reverse, inducing a heat flux by adding a fixed amount of energy through the thermalising zones over time and measuring the resulting temperature gradient. In this case, the thermal conductivity is, again, calculated via Fourier's law by relating the defined heat flux and the resultant temperature gradient.

System properties measured using NEMD simulation will not be pure values calculated at a single temperature and density value as is the case in equilibrium MD. By

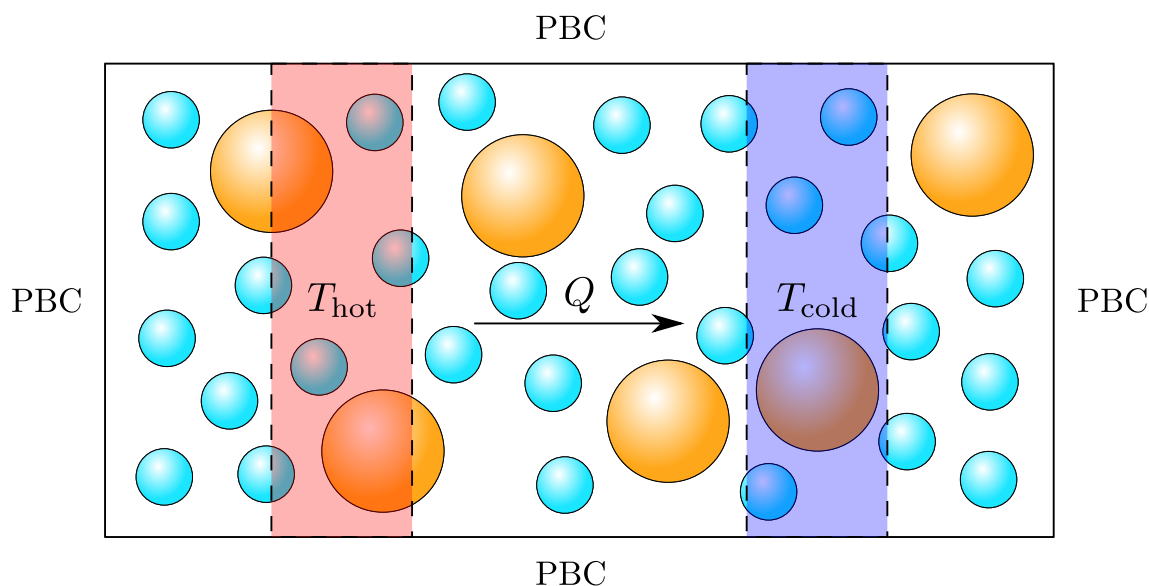


Figure 4.7: A schematic 2-D representation of a multicomponent hard-sphere NEMD simulation using the energy exchange algorithm in order to measure thermal conductivity. The simulation is surrounded on all sides by periodic boundary conditions represented by the label “PBC”. The simulation contains two thermalising zones represented by the red and blue shaded areas of the diagram. Particles inside these zones are thermalised to temperatures of T_{cold} and T_{hot} in order to induce a temperature gradient.

definition non-equilibrium methods require that the system is placed under an external force which shifts the system away from the natural equilibrium state. In the case of thermal conductivity measurement techniques, this involves inducing a temperature gradient across the system which will not only cause the obvious variation in temperature over the system, but it will also produce a density gradient over the system. This means that any property measured using non-equilibrium techniques is an average of that particular property taken at many different temperature and density values over the entire span of the simulation. This effect can be minimised by using a small temperature gradient; however, a small driving force will result in a low signal to noise ratio and potentially high uncertainty in the calculated thermal conductivity. Other effects such as interfacial resistance present at the walls in the parallel heated walls technique will significantly effect the measured thermal conductivity [14]. All NEMD simulations performed in this thesis utilise the parallel heated walls method in order to measure hard-sphere thermal conductivity.

References

- [1] M. N. Bannerman and L. Lue. “Transport properties of highly asymmetric hard-sphere mixtures”. In: *J. Chem. Phys.* 130.16, 164507 (2009), p. 164507.
- [2] J. E. Jones. “On the determination of molecular fields. - II. From the equation of state of a gas”. In: *Proc. R. Soc. Lond.* 106.738 (1924).

-
- [3] A. Rotenberg. “Monte Carlo equation of state for hard spheres in an attractive square well”. In: *J. Chem. Phys.* 43 (1965), pp. 1198–1201.
- [4] B. J. Alder and T. E. Wainwright. “Studies in molecular dynamics. 1. general method”. In: *J. Chem. Phys.* 31 (1959), p. 459.
- [5] M. N. Bannerman, R. Sargant, and L. Lue. “DynamO: a free $\mathcal{O}(N)$ general event-driven molecular dynamics simulator”. In: *J. Comput. Chem.* 32.15 (2011), pp. 3329–3338.
- [6] J. M. Haile. *Molecular dynamics simulation elementary methods*. Ed. by J. M. Haile. Wiley, 1992.
- [7] M. S. Green. “Markoff Random Processes and the Statistical Mechanics of Time-Dependent Phenomena. II. Irreversible Processes in Fluids”. In: *J. Chem. Phys.* 22.3 (1954), pp. 398–413.
- [8] R. Kubo. “Statistical-Mechanical Theory of Irreversible Processes. I. General Theory and Simple Applications to Magnetic and Conduction Problems”. In: *J. Phys. Soc. Jpn.* 12.6 (1957), pp. 570–586.
- [9] J. Hansen and R. McDonald. *Theory of simple liquids with applications to soft matter*. 4th ed. Elsevier, 2013.
- [10] J. J. Erpenbeck. “Transport-coefficients of hard-sphere mixtures theory and Monte-Carlo molecular-dynamics calculations for an isotopic mixture”. In: *Phys. Rev. A* 39.9 (1989), pp. 4718–4731.
- [11] T. Boublík. “Hard-Sphere Equation of State”. In: *J. Chem. Phys.* 53.1 (1970), pp. 471–472.
- [12] G. A. Mansoori et al. “Equilibrium thermodynamic properties of mixtures of hard spheres”. In: *J. Chem. Phys.* 54.4 (1971), pp. 1523–1525.
- [13] P. Wirnsberger, D. Frenkel, and C. Dellago. “An enhanced version of the heat exchange algorithm with excellent energy conservation properties”. In: *J. Chem. Phys.* 143 (2015), p. 124104.
- [14] C. Moir et al. “Anomalous heat transport in binary hard-sphere gases”. In: *Phys. Rev. Lett.* 99 (2019), p. 030102.

KINETIC THEORY AND FULL MULTI-COMPONENT HYDRODYNAMICS

The link between the *macroscopic* scale (where continuum hydrodynamics and heat transfer are considered) and the *microscopic* scale (where molecular motion is considered) must be made to build our fundamental understanding of thermal conductivity. This is also vital to ensure no effects are missed as heat transfer in mixtures is highly complex, involving simultaneous thermodiffusion, diffusion, and conduction. Therefore, this chapter derives the Enskog-Boltzmann equation and then uses it in order to derive the full multi-component hydrodynamic equations for the conservation of mass, momentum, and energy. Following this route provides a microscopic basis for all terms in the hydrodynamic equations and also reveals all assumptions made along the way. To be absolutely complete, the equations of kinetic theory are derived from the Liouville equation which describes the time-evolution of an ensemble of systems inside phase-space. In order to derive the Liouville equation, the conservation equation for a general conserved quantity is first derived.

5.1 Reynolds transport theorem

The Reynolds transport theorem is a key result for the study of the time evolution of any conserved quantity. With some hand-waving, it can be used to derive hydrodynamic equations, but a more rigorous route uses it to derive the kinetic equations first. Its derivation considers a multi-dimensional space with coordinates \mathbf{x} . Assume there is some quantity A which is present in varying amounts over this space such that the density $\rho_A(\mathbf{x}, t)$ is a well defined concept. Examples of the property A include mass, momentum, and energy in physical space or, more interestingly for kinetic theory, the count of physical systems in phase space. The total amount of the quantity $N_A(t)$ within a volume $V(t)$

whose shape and volume can change with time is defined as follows,

$$N_A(t) = \int_{\mathbf{x} \in V(t)} \rho_A(\mathbf{x}, t) d\mathbf{x}. \quad (5.1.1)$$

The limit of this integration states that the integral is performed over the range of \mathbf{x} contained within the time-dependent volume $V(t)$. If we wish to consider the full time dependence (total time derivative) of $N_A(t)$, care must be taken to include the time dependency of the integral limits/volume as well as the time-dependence of the density itself. In order to expose the time dependence of the limits explicitly, they are instead expressed using a Heaviside step function,

$$N_A(t) = \int_{\forall \mathbf{x}} \Theta_V(\mathbf{x}, t) \rho_A(\mathbf{x}, t) d\mathbf{x}, \quad (5.1.2)$$

where the integration is now over the whole space of \mathbf{x} and the step function Θ is defined as

$$\Theta_V(\mathbf{x}, t) = \begin{cases} 1 & \text{for } \mathbf{x} \in V(t) \\ 0 & \text{for } \mathbf{x} \notin V(t) \end{cases}. \quad (5.1.3)$$

Now that the integral limits are fixed, a total time derivative may move inside the volume integral,

$$\frac{d}{dt} N_A(t) = \frac{d}{dt} \int_{\forall \mathbf{x}} \rho_A(\mathbf{x}, t) \Theta_V(\mathbf{x}, t) d\mathbf{x} \quad (5.1.4)$$

$$= \int_{\forall \mathbf{x}} \left(\frac{d\rho_A(\mathbf{x}, t)}{dt} \Theta_V(\mathbf{x}, t) + \rho_A(\mathbf{x}, t) \frac{d\Theta_V(\mathbf{x}, t)}{dt} \right) d\mathbf{x}, \quad (5.1.5)$$

where, on the second line, the product rule is applied to the time derivative. The variable \mathbf{x} is independent of time as it is always integrated over the whole space of \mathbf{x} , thus the total time derivative can be replaced by the partial time derivative as ρ_A and Θ_V are explicit functions of time,

$$\frac{d}{dt} N_A(t) = \int_{\forall \mathbf{x}} \left(\frac{\partial \rho_A(\mathbf{x}, t)}{\partial t} \Theta_V(\mathbf{x}, t) + \rho_A(\mathbf{x}, t) \frac{\partial \Theta_V(\mathbf{x}, t)}{\partial t} \right) d\mathbf{x}. \quad (5.1.6)$$

The first term within the integral of Eq. (5.1.6) represents the change in $N_A(t)$ due to changes in the density within the volume $V(t)$. The final term represents changes in N_A due to a change in the region contained within $V(t)$. The value of the step function Θ_V remains constant when within or outwith $V(t)$, thus the value of Θ_V only changes at the volume surface $\delta V(t)$ which moves as the shape of $V(t)$ changes. Like the Heaviside step function, the derivative of Θ_V must be a delta function which “selects” for the surface of

$V(t)$. The rate of change at this surface is proportional to the velocity of the surface \mathbf{v}_V perpendicular to the surface of $V(t)$. Therefore, the final integral can be rewritten as follows,

$$\frac{d}{dt}N_A(t) = \int_{\forall \mathbf{x}} \frac{\partial \rho_A(\mathbf{x}, t)}{\partial t} \Theta_V(\mathbf{x}, t) d\mathbf{x} + \int_{\forall \mathbf{x}} \rho_A(\mathbf{x}, t) \delta_V(\mathbf{x}, t) \mathbf{v}_V(\mathbf{x}, t) \cdot \hat{\mathbf{n}}_V(\mathbf{x}, t) d\mathbf{x} \quad (5.1.7)$$

$$= \int_{\mathbf{x} \in V(t)} \frac{\partial \rho_A(\mathbf{x}, t)}{\partial t} d\mathbf{x} + \int_{\mathbf{x} \in \delta V(t)} \rho_A(\mathbf{x}, t) \mathbf{v}_V(\mathbf{x}, t) \cdot \hat{\mathbf{n}}_V(\mathbf{x}, t) d\mathbf{x}, \quad (5.1.8)$$

where $\delta_V(\mathbf{x}, t)$ is a delta function which selects for the surface of $V(t)$, $\delta V(t)$ is the surface of $V(t)$, and $\hat{\mathbf{n}}_V(\mathbf{x}, t)$ is the surface normal pointing outward from $V(t)$. In the second line, the step and delta functions are removed and the limits of the integral are changed to the volume and surface of $V(t)$ respectively. The final term can be converted to an integral over the volume using the divergence theorem,

$$\frac{d}{dt}N_A(t) = \int_{\mathbf{x} \in V(t)} \left(\frac{\partial \rho_A(\mathbf{x}, t)}{\partial t} + \nabla_{\mathbf{x}} \cdot \rho_A(\mathbf{x}, t) \mathbf{v}_V(\mathbf{x}, t) \right) d\mathbf{x}. \quad (5.1.9)$$

This result is known as the *general transport theorem* and is particularly useful if the volume $V(t)$ is defined to move at the velocity of the observed property, A , i.e., $\mathbf{v}_V = \dot{\mathbf{x}}_A$,

$$\frac{D}{Dt}N_A(t) = \int_{\mathbf{x} \in V(t)} \frac{\partial \rho_A(\mathbf{x}, t)}{\partial t} + \nabla_{\mathbf{x}} \cdot \rho_A(\mathbf{x}, t) \dot{\mathbf{x}}_A(\mathbf{x}, t) d\mathbf{x}. \quad (5.1.10)$$

In this case, the derivative has been changed to an uppercase D to distinguish that this is now a *material derivative*, which tracks the change of property A over time while also following the motion of the property A through space. If the property being observed is *conserved*, then this material derivative must be zero $DN_A/Dt = 0$ as the velocity $\dot{\mathbf{x}}_A$ tracks all movement of the property, i.e., A cannot pass through the boundary of $V(t)$ anymore. As this holds true for any arbitrary initial volume, the kernel of the integral itself must be zero,

$$\frac{\partial \rho_A(\mathbf{x}, t)}{\partial t} = -\nabla_{\mathbf{x}} \cdot \rho_A(\mathbf{x}, t) \dot{\mathbf{x}}_A(\mathbf{x}, t). \quad (5.1.11)$$

This is a general *conservation equation* for a conserved property A . It is possible to use Eq. (5.1.11) to derive the hydrodynamic continuity equation by considering the conservation of mass. The Navier-Stokes equation can be derived by examining the conservation of momentum; however, care must be taken when defining the momentum velocity, $\dot{\mathbf{x}}_{\text{momentum}}$, used in Eq. (5.1.11) as it is distinct from the mass velocity used in the continuity

equation¹. Eq. (5.1.11) forms the basis for the Liouville equation which is used in order to derive the equations of kinetic theory in the following section. These equations will then be used in order to derive the hydrodynamic conservation equations in Section 5.3.

5.2 Phase space and the Liouville equation

The Liouville equation is an application of the conservation equation to phase space and is the starting point for the derivation of kinetic theory. Phase space is constructed by creating a position vector, $\Gamma = \{\mathbf{r}, \mathbf{v}\}^N$, which is comprised of $3N$ position variables and $3N$ velocity variables for all N particles in a system. A particle, in this context, may describe a single atom, functional group, or entire molecule depending on the molecular model used. As the system moves through time it will trace out a trajectory in $6N$ dimensional phase space.

The trajectory of a hard-sphere system through phase space is not continuous as collisions between particles will result in instantaneous changes/jumps in velocity space due to the discontinuous repulsive force; however, as no physical process exists which can create or destroy one of these systems (i.e., time cannot end) the flow of any number of these systems in phase space is conserved (see Fig. 5.1). While individual systems are interesting, determining their individual motion through phase space is exactly equivalent to solving the motion of the system via molecular dynamics. Our interest lies in the long-time/average behaviour of the system (and simpler calculations), thus a statistically large ensemble of hard-sphere systems in phase space is considered. This collection of systems can be described by a distribution function $f(\Gamma, t)$ which represents the probability of finding a hard-sphere system in the state of Γ at time t . By construction, the distribution function is normalised to one,

$$\int_{\forall \Gamma} f(\Gamma, t) d\Gamma = 1, \quad (5.2.1)$$

where the integral represents a definite integral over the whole domain of Γ .

The primary benefit of using a statistically large ensemble is that f is now a continuous function over the accessible regions of phase space², thus the mathematics of it are simpler and open to further simplifying approximations. It should be noted that much (if not all) of the discussion below still applies to a distribution function describing a single system in phase space³.

As probability is conserved, the governing dynamic equation of the distribution function, f , is Reynolds Transport Theorem. Applying Eq. (5.1.11) yields the following ex-

¹Momentum may be transferred/move without the transfer of mass, thus their velocities are different. A classic example of this is the Newton's cradle, where momentum travels "instantaneously" from one side to another on impact without movement of the spheres.

²The inaccessible regions (where $f = 0$) are separated from the accessible regions by a discontinuity.

³i.e., $f(\Gamma) = \delta(\Gamma - \Gamma_{sys}(t))$ where $\Gamma_{sys}(t)$ is the state of the single system at time t .

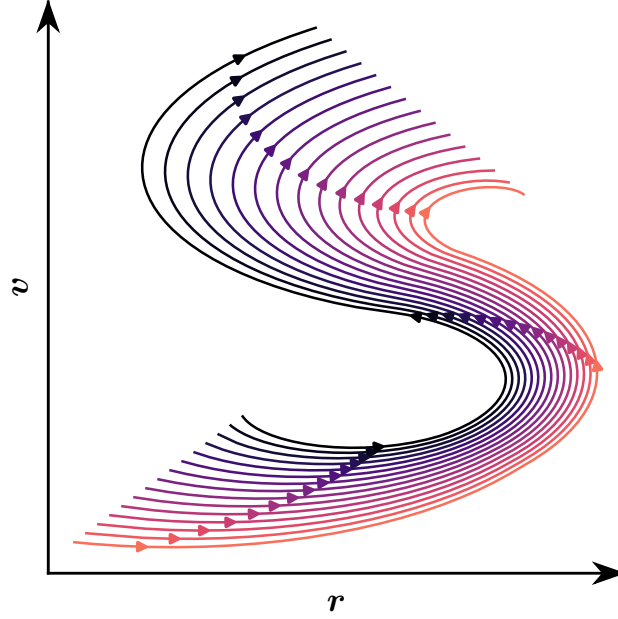


Figure 5.1: An illustration of the flow of an ensemble of systems in phase space. In deterministic systems, trajectories cannot cross as the same configuration must follow the same path; however, they may converge and even join if dissipative forces are present in the system (i.e., a bouncing ball in 1-D will eventually come to rest in the same location regardless of the starting position). This implies that, in general, the density of systems in phase space is not necessarily conserved but that the total number of systems is.

pression,

$$\frac{\partial}{\partial t} f = -\frac{\partial}{\partial \mathbf{\Gamma}} \cdot f \dot{\mathbf{\Gamma}} = -\sum_{i=1}^N \left(\mathbf{v}_i \cdot \frac{\partial}{\partial \mathbf{r}_i} f + \frac{\partial}{\partial \mathbf{v}_i} \cdot \left(\frac{\mathbf{F}_i}{m_i} f \right) \right). \quad (5.2.2)$$

where the equation has been broken down into the contribution of each particle i to the overall dynamics via its velocity, $\mathbf{v}_i = \dot{\mathbf{r}}_i$, and forces, $\mathbf{F}_i = m_i \dot{\mathbf{v}}_i$. As the velocity and position are independent variables, the velocity is removed from the position derivative without approximation.

At this stage, several simplifying approximations are made. First, all forces are assumed to be time-independent and only a function of the particle variables. A pairwise approximation then allows us to break the total force on a particle into a sum of pairwise contributions,

$$\mathbf{F}_i(\mathbf{\Gamma}) = \sum_{\substack{j=1 \\ j \neq i}}^N \mathbf{F}_{ij}(\mathbf{\Gamma}_i, \mathbf{\Gamma}_j),$$

where the sum excludes self-interactions and \mathbf{F}_{ij} is the force between particle i and j . In molecular systems, the inter-particle forces are only a function of position and, therefore, the force terms can be removed from the velocity derivatives of Eq. (5.2.2). Applying

these changes yields the following expression,

$$\begin{aligned}\frac{\partial f}{\partial t} &= - \sum_{i=1}^N \left(\mathbf{v}_i \cdot \frac{\partial f}{\partial \mathbf{r}_i} + \sum_{\substack{j=1 \\ j \neq i}}^N \frac{\mathbf{F}_{ij}}{m_i} \cdot \frac{\partial f}{\partial \mathbf{v}_i} \right) \\ &= - \sum_{i=1}^N \left(\mathbf{v}_i \cdot \frac{\partial f}{\partial \mathbf{r}_i} + \sum_{j=i+1}^N \mathbf{F}_{ij} \cdot \left[m_i^{-1} \frac{\partial}{\partial \mathbf{v}_i} - m_j^{-1} \frac{\partial}{\partial \mathbf{v}_j} \right] f \right),\end{aligned}\quad (5.2.3)$$

where the second line simplifies the sum on the particle interaction term by collecting terms using the identity $\mathbf{F}_{ij} = -\mathbf{F}_{ji}$ which arises from Newton's third law of motion¹. This result is known as the *Liouville equation*, but it is not particularly useful in this form as it still describes the motion of the full system, thus it is no simpler than direct molecular dynamics simulation.

In order to reduce the number of particles considered, a reduced distribution function of $n < N$ particles is now defined by integrating out $N - n$ particles,

$$f^{(n)}(\mathbf{\Gamma}_1, \dots, \mathbf{\Gamma}_n, t) = \frac{N!}{(N-n)!} \int_{\forall \mathbf{\Gamma}} f(\mathbf{\Gamma}_1, \dots, \mathbf{\Gamma}_N, t) d\mathbf{\Gamma}_{n+1} \dots d\mathbf{\Gamma}_N. \quad (5.2.4)$$

The purpose of the factorial terms is simply to give convenient normalisations of the reduced distribution functions. For example, the one-particle distribution $f^{(1)}$ normalises to the total particle count,

$$\int_{\forall \mathbf{\Gamma}} f^{(1)}(\mathbf{r}_1, \mathbf{v}_1, t) d\mathbf{\Gamma}_1 = N. \quad (5.2.5)$$

This normalisation implies the ensemble average mass density $\rho(\mathbf{r}, t)$ can be derived by applying the velocity integral and multiplying by the hard-sphere mass m ,

$$\int_{\forall \mathbf{\Gamma}} m f^{(1)}(\mathbf{\Gamma}_1, t) d\mathbf{v}_1 = \rho(\mathbf{r}, t). \quad (5.2.6)$$

This also allows other interesting hydrodynamic properties to be extracted, such as the ensemble average flow momentum

$$\int_{\forall \mathbf{\Gamma}} m \mathbf{v}_1 f^{(1)}(\mathbf{\Gamma}_1, t) d\mathbf{v}_1 = \rho(\mathbf{r}, t) \mathbf{u}(\mathbf{r}, t), \quad (5.2.7)$$

where $\mathbf{u}(\mathbf{r}, t)$ is the ensemble average velocity. Thus this normalisation allows us to access hydrodynamic properties from the reduced distribution function, yet a clear path to computing these distribution functions is still missing.

¹Every action has an equal and opposite reaction.

5.2.1 BBGKY Heirarchy

The single particle distribution function is obviously of great interest as it allows us to access useful hydrodynamic properties of the system. Therefore, an equation which can be solved for the reduced distribution functions, and in particular $f^{(1)}$, must be generated. In order to achieve this, an integration over the $n + 1$ th to the N th particle variables of the Liouville equation (Eq. (5.2.3)) followed by a multiplication by the normalisation factor of Eq. (5.2.4) is performed yielding the following expression,

$$\begin{aligned} & \frac{N!}{(N-n)!} \int_{\forall \Gamma} \frac{\partial f}{\partial t} d\Gamma_{n+1} \dots d\Gamma_N \\ &= -\frac{N!}{(N-n)!} \int_{\forall \Gamma} \sum_{i=1}^N \left(\mathbf{v}_i \cdot \frac{\partial f}{\partial \mathbf{r}_i} + \sum_{j=i+1}^N \mathbf{F}_{ij} \cdot \left[m_i^{-1} \frac{\partial}{\partial \mathbf{v}_i} - m_j^{-1} \frac{\partial}{\partial \mathbf{v}_j} \right] f \right) d\Gamma_{n+1} \dots d\Gamma_N. \end{aligned} \quad (5.2.8)$$

The integration is in independent variables, thus it can pass through the time derivative and reduce the distribution function on the left hand side of Eq. (5.2.4), as follows,

$$\frac{N!}{(N-n)!} \int_{\forall \Gamma} \frac{\partial f}{\partial t} d\Gamma_{n+1} \dots d\Gamma_N = \frac{\partial f^{(n)}}{\partial t}$$

This is also true for all terms on the right-hand side where $i \leq n$. Considering the position derivative term when $i \geq n$, if the integration of \mathbf{r}_i is performed first, it will undo the derivative and leave the distribution function f evaluated at the limits of \mathbf{r}_i . In infinite systems the distribution function f must tend to zero at the limits $\mathbf{r}_i = \pm\infty$ for there to be a finite probability, and in periodic systems the value of f must be symmetric at the periodic boundaries thus these terms are zero for all systems of interest. It is clear that for integrals such as Eq. (5.2.7) to converge, the distribution must go to zero at the extreme values of the velocity as well, thus the velocity derivative terms on the same line go to zero if the \mathbf{v}_i integral is carried out first (we can ignore the force term for the velocity integral as it assumed to only be a function of position). All that remains to be considered are the force terms for $j > n$ where the state of the derivation so far is summarised as follows,

$$\begin{aligned} \frac{\partial f^{(n)}}{\partial t} &= -\sum_{i=1}^n \left(\mathbf{v}_i \cdot \frac{\partial}{\partial \mathbf{r}_i} + \sum_{j=i+1}^n \mathbf{F}_{ij} \cdot \left[m_i^{-1} \frac{\partial}{\partial \mathbf{v}_i} - m_j^{-1} \frac{\partial}{\partial \mathbf{v}_j} \right] \right) f^{(n)} \\ &\quad - \frac{N!}{(N-n)!} \sum_{i=1}^n \sum_{j=n+1}^N \int_{\forall \Gamma} \frac{\mathbf{F}_{ij}}{m_i} \cdot \frac{\partial f}{\partial \mathbf{v}_i} d\Gamma_{n+1} \dots d\Gamma_N. \end{aligned} \quad (5.2.9)$$

As all particles of the same type are indistinguishable, the sum over terms $j = n + 1$ to $j = N$ in Eq. (5.2.9) can be replaced with a factor $(N - n)$ multiplied by any one of these

remaining terms. The $n + 1$ th term is chosen and the normalisations cancel completely as follows,

$$\begin{aligned} \frac{\partial f^{(n)}}{\partial t} = & - \sum_{i=1}^n \left(\mathbf{v}_i \cdot \frac{\partial}{\partial \mathbf{r}_i} + \sum_{j=i+1}^n \mathbf{F}_{ij} \cdot \left[m_i^{-1} \frac{\partial}{\partial \mathbf{v}_i} - m_j^{-1} \frac{\partial}{\partial \mathbf{v}_j} \right] \right) f^{(n)} \\ & - \sum_{i=1}^n \int_{\forall \Gamma} \frac{\mathbf{F}_{i,n+1}}{m_i} \cdot \frac{\partial}{\partial \mathbf{v}_i} f^{(n+1)} d\Gamma_{n+1}. \end{aligned} \quad (5.2.10)$$

This set of equations is known as the *BBGKY hierarchy* and expresses the time evolution of the n -particle distribution function via its dependency on the $n + 1$ -particle distribution function. As stated previously, the single particle distribution function $f^{(1)}$ is the most important equation to us in this set and is obtained by substituting a value of $n = 1$ into Eq. (5.2.10),

$$\frac{\partial f^{(1)}}{\partial t} = -\mathbf{v}_1 \cdot \frac{\partial f^{(1)}}{\partial \mathbf{r}_1} - \int \frac{\mathbf{F}_{12}}{m_1} \cdot \frac{\partial f^{(2)}}{\partial \mathbf{v}_1} d\Gamma_2, \quad (5.2.11)$$

In order to solve for $f^{(1)}$ one must know the value of $f^{(2)}$; however, as these equations stand this requires knowledge of $f^{(3)}$, $f^{(4)}$, ..., and so on. To solve this equation, the dependency of the $f^{(n)}$ equation on the $f^{(n+1)}$ distribution must be broken, thus the $f^{(n+1)}$ term, known as the interaction term or collision integral in hard sphere systems is considered in the following section.

5.2.2 Collision integral

In hard spheres, forces are impulsive and, therefore, the velocity derivative in the interaction term of Eq. (5.2.11) is complex. Careful reasoning allows the derivation of the interaction operator by its action on properties. This is an exact but involved derivation [1, 2], thus only the result is presented here.

$$\begin{aligned} \int \frac{\mathbf{F}_{12}}{m_1} \cdot \frac{\partial}{\partial \mathbf{v}_1} f^{(2)} d\Gamma_2 = & \sigma^{d-1} \iint_{\mathbf{v}_{12} \cdot \hat{\mathbf{r}}_{12} < 0} |\mathbf{v}_{12} \cdot \hat{\mathbf{r}}_{12}| \left(f^{(2)}(\mathbf{r}_1, \mathbf{v}'_1, \mathbf{r}_1 + \sigma \hat{\mathbf{r}}_{12}, \mathbf{v}'_2, t) \right. \\ & \left. - f^{(2)}(\mathbf{r}_1, \mathbf{v}_1, \mathbf{r}_1 - \sigma \hat{\mathbf{r}}_{12}, \mathbf{v}_2, t) \right) d\hat{\mathbf{r}}_{12} d\mathbf{v}_{12}, \end{aligned} \quad (5.2.12)$$

where σ is the hard sphere diameter, d is the dimensionality, $\mathbf{r}_{12} = \mathbf{r}_1 - \mathbf{r}_2$ is the relative position, and $\mathbf{v}_{12} = \mathbf{v}_1 - \mathbf{v}_2$ is the relative velocity of hard-spheres 1 and 2. The restituted velocities \mathbf{v}'_1 and \mathbf{v}'_2 are given by the hard-sphere collision rules shown in Eq. (4.1.5). The term outside the parenthesis in Eq. (5.2.12) represents an integration over the surface of a sphere. The first term inside the parenthesis shows the particles (with velocity values already equal to \mathbf{v}'_1 and \mathbf{v}'_2) which will collide in order to enter the current distribution. The second (negative) term shows the particles which are already members of the current

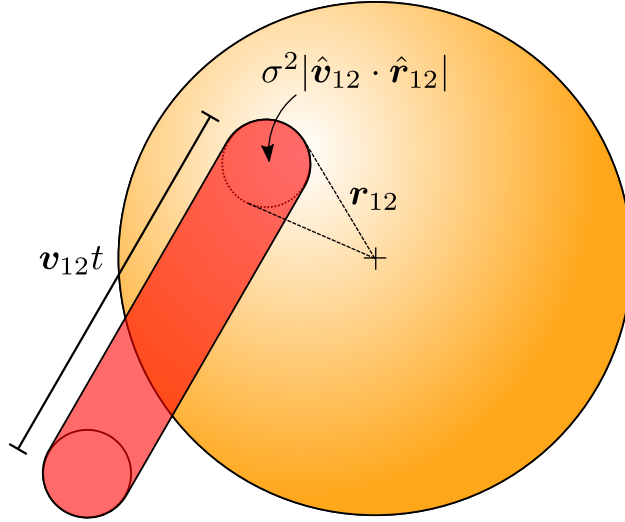


Figure 5.2: A physical representation of the collision integral showing a single snapshot of the integration over all values of \mathbf{r}_{12} and \mathbf{v}_{12} . The sphere shown has a relative velocity and position of \mathbf{v}_{12} and \mathbf{r}_{12} respectively. The collision “path” of the two spheres is extruded (red column) from the particle. The column originates from the cross sectional area on the surface of the particle which, upon collision, will give the particle a new post collision velocity of \mathbf{v}'_1 . This corresponds to the second term inside the parenthesis in Eq. (5.2.12) which makes sense as this collision reduces the probability of a single particle having the original velocity \mathbf{v}_1 based on the probability of two particles having these pre-collision characteristics.

distribution but will collide and exit as shown in Fig. 5.2.

One approach to “closing” the BBGKY hierarchy at some convenient level is to express the $f^{(n+1)}$ term in terms of $f^{(n)}$. Formally, this can be expressed as follows,

$$f^{(2)}(\mathbf{\Gamma}_1, \mathbf{\Gamma}_2, t) = \chi(\mathbf{\Gamma}_1, \mathbf{\Gamma}_2) f^{(1)}(\mathbf{\Gamma}_1, t) f^{(1)}(\mathbf{\Gamma}_2, t), \quad (5.2.13)$$

where $\chi(\mathbf{\Gamma}_1, \mathbf{\Gamma}_2)$ is the two particle correlation function. The actual approximation comes in how the χ term is implemented. The simplest choice is to assume molecular chaos as Boltzmann did such that the two particles are uncorrelated, i.e. $\chi \approx 1$. Often χ is made a simple function of density to ensure the correct pressure is obtained at moderate densities.

Boltzmann assumes that all particles in the system are point-particles with no volume which interact at a distance of $|\mathbf{r}_{ij}| = 0$. Substituting these assumptions into Eq. (5.2.12) gives the *Boltzmann equation* collision integral as

$$\int \frac{\mathbf{F}_{12}}{m_1} \cdot \frac{\partial}{\partial \mathbf{v}_1} f^{(2)} d\mathbf{\Gamma}_2 = \sigma^{d-1} \iint_{\mathbf{v}_{12} \cdot \hat{\mathbf{r}}_{12} < 0} |\mathbf{v}_{12} \cdot \hat{\mathbf{r}}_{12}| \left(f^{(1)}(\mathbf{r}, \mathbf{v}'_1, t) f^{(1)}(\mathbf{r}, \mathbf{v}'_2, t) - f^{(1)}(\mathbf{r}, \mathbf{v}_1, t) f^{(1)}(\mathbf{r}, \mathbf{v}_2, t) \right) d\hat{\mathbf{r}}_{12} d\mathbf{v}_{12} \quad (5.2.14)$$

This Boltzmann assumptions are only valid for dilute gases. Enskog [3] semi-empirically

modified the Boltzmann equation in order to account for the finite particle size of colliding hard-spheres and the invalid assumption of molecular chaos for dense gases. Finite particle size is accounted for by reintroducing the collision distance (as shown in Eq. (5.2.12)) where particles collide at a distance $|\mathbf{r}_{12}| = \sigma$. This is important because, upon collision, momentum and energy are transferred instantaneously from one hard-sphere to another over the distance σ and at high densities, this becomes the dominant method of momentum and energy transfer. The assumption of molecular chaos also breaks down at high densities as collisions between hard-sphere pairs become increasingly correlated as pairs of hard-spheres which are close to each other will collide with each other more frequently than with hard-spheres which are far away. Enskog theory [3] accounts for the increase in collision frequency by setting the factor $\chi(\mathbf{\Gamma}_1, \mathbf{\Gamma}_2)$ in Eq. (5.2.13) to the equilibrium value of the radial distribution function of two hard-spheres at the point of contact between the spheres, i.e. when $|\mathbf{r}_{ij}| = \sigma$. Substituting Eq. (5.2.13) into Eq. (5.2.12) using the updated χ value gives the expression for the Enskog version of the single-particle mono-component hard-sphere collision integral

$$\begin{aligned} \int \frac{\mathbf{F}_{12}}{m_1} \cdot \frac{\partial}{\partial \mathbf{v}_1} f^{(2)} d\mathbf{\Gamma}_2 = \sigma^{d-1} \iint_{\mathbf{v}_{12} \cdot \hat{\mathbf{r}}_{12} < 0} |\mathbf{v}_{12} \cdot \hat{\mathbf{r}}_{12}| \left(\chi f^{(1)}(\mathbf{r}_1, \mathbf{v}'_1, t) f^{(1)}(\mathbf{r}_1 + \sigma \hat{\mathbf{r}}_{12}, \mathbf{v}'_2, t) \right. \\ \left. - \chi f^{(1)}(\mathbf{r}_1, \mathbf{v}_1, t) f^{(1)}(\mathbf{r}_1 - \sigma \hat{\mathbf{r}}_{12}, \mathbf{v}_2, t) \right) d\hat{\mathbf{r}}_{12} d\mathbf{v}_{12} \quad (5.2.15) \end{aligned}$$

5.2.3 Multi-component systems

The expressions that have been derived so far are valid for monocomponent hard-sphere systems; however, we are interested in thermal transport in mixtures. In order to proceed and eventually derive the hydrodynamic conservation equations for multicomponent systems, we must extend Eq. (5.2.15) to consider collisions between hard-spheres of different sizes. If we consider a S -species hard sphere fluid, there are now S coupled single particle distribution functions corresponding to each species $a = 1, 2, \dots, S$, each characterised by a mass m_a and diameter σ_a ,

$$\frac{\partial f_a^{(1)}}{\partial t} = -\mathbf{v}_a \cdot \frac{\partial f_a^{(1)}}{\partial \mathbf{r}} - \sum_{b=1}^S \mathcal{T}_{ab} \left(f_a^{(1)}, f_b^{(1)} \right), \quad (5.2.16)$$

where, instead of the probability of finding any hard-sphere, $f_a^{(1)}$ represents the probability of finding a hard-sphere of species a at position \mathbf{r} with velocity \mathbf{v}_a at time t . \mathcal{T}_{ab} represents

the collision integral between two species a and b and is defined as follows,

$$\begin{aligned} \mathcal{T}_{ab}(f_a^{(1)}, f_b^{(1)}) = & \sigma^{d-1} \iint_{\mathbf{v}_{ab} \cdot \hat{\mathbf{r}}_{ab} < 0} |\mathbf{v}_{ab} \cdot \hat{\mathbf{r}}_{ab}| \left(\chi_{ab}(\mathbf{r}, \mathbf{r} + \sigma \hat{\mathbf{r}}_{ab}) f_a(\mathbf{r}, \mathbf{v}'_a, t) f_b(\mathbf{r} + \sigma \hat{\mathbf{r}}_{ab}, \mathbf{v}'_b, t) \right. \\ & \left. - \chi_{ab}(\mathbf{r}, \mathbf{r} - \sigma \hat{\mathbf{r}}_{ab}) f_a(\mathbf{r}, \mathbf{v}_a, t) f_b(\mathbf{r} - \sigma \hat{\mathbf{r}}_{ab}, \mathbf{v}_b, t) \right) d\hat{\mathbf{r}}_{ab} d\mathbf{v}_{ab} \quad (5.2.17) \end{aligned}$$

where χ , present in the monocomponent collision integral (Eq. (5.2.15)) is replaced with $\chi_{ab}(\mathbf{r}_a, \mathbf{r}_b)$ as the radial distribution function is now a function of the individual hard-sphere species parameters.

5.3 Hydrodynamic equations

Now that the complete set of multicomponent single particle distribution functions have been derived along with the multicomponent Enskog version of the hard-sphere collision integral, these equations are now used to derive the full multicomponent hydrodynamic equations for the conservation of mass, momentum, and energy. In order to streamline the following sections, the symbol f will now be used to refer to the single particle distribution function (previously $f^{(1)}$). The conservation equations, i.e. the continuity equation, the momentum equation, and the energy equation are obtained by multiplying Eq. (5.2.16) by those respective quantities, m_a , $m_a \mathbf{v}_a$, and $\frac{1}{2} m_a \mathbf{v}_a^2$ for species a , integrating the resulting equation with respect to \mathbf{v}_a , and summing over all species $a = 1, 2, \dots, S$.

5.3.1 Continuity equation

Multiplying Eq. (5.2.16) by the species a mass m_a and integrating over the velocity \mathbf{v}_a gives

$$\int m_a \frac{\partial f_a}{\partial t} d\mathbf{v}_a = - \int m_a \mathbf{v}_a \cdot \frac{\partial f_a}{\partial \mathbf{r}} d\mathbf{v}_a - \int m_a \sum_{b=1}^S \mathcal{T}_{ab}(f_a, f_b) d\mathbf{v}_a. \quad (5.3.1)$$

The mass of species a is invariant over any collision as no mass is ever transferred from particle a to particle b . Therefore the collision term will be equal to 0

$$\int m_a \sum_{b=1}^S \mathcal{T}_{ab}(f_a, f_b) d\mathbf{v}_a = 0. \quad (5.3.2)$$

Both m_a and \mathbf{v}_a are independent of position and time which means that these variables can be taken inside of any position or time derivatives. This also means that position and

time derivatives can be moved in and out of integrals with respect to \mathbf{v}_a leading to

$$\frac{\partial}{\partial t} \int m_a f_a d\mathbf{v}_a = -\frac{\partial}{\partial \mathbf{r}} \cdot \int m_a \mathbf{v}_a f_a d\mathbf{v}_a + \int f_a \mathbf{v}_a \cdot \frac{\partial m_a}{\partial \mathbf{r}} d\mathbf{v}_a, \quad (5.3.3)$$

where the product rule has been used in order to expand the right hand side of the expression. The term containing the position derivative of the species a mass $\partial m_a / \partial \mathbf{r} = 0$ as the mass of an individual component is independent of position. The remaining term on the right hand side of Eq. (5.3.3) is rewritten in terms of the mass-averaged velocity by introducing the peculiar velocity \mathbf{V}_a of a species a which is the velocity of species a relative to the mass averaged velocity defined as follows,

$$\mathbf{V}_a(\mathbf{r}, t) = \mathbf{v}_a - \mathbf{u}(\mathbf{r}, t), \quad (5.3.4)$$

where the peculiar velocity $\mathbf{V}_a(\mathbf{r}, t)$ depends on position because of the fact that the mass averaged velocity $\mathbf{u}(\mathbf{r}, t)$ is also a function of position. This leads to

$$\frac{\partial}{\partial t} \int m_a f_a d\mathbf{v}_a = -\frac{\partial}{\partial \mathbf{r}} \cdot \int m_a \mathbf{u} f_a d\mathbf{v}_a - \frac{\partial}{\partial \mathbf{r}} \cdot \int m_a \mathbf{V}_a f_a d\mathbf{v}_a. \quad (5.3.5)$$

Similar to how we defined the monocomponent ensemble average mass density in Eq. (5.2.6), the ensemble average species mass density ρ_a is defined here as

$$\int m_a f_a d\mathbf{v}_a = \rho_a(\mathbf{r}, t). \quad (5.3.6)$$

Applying this definition to Eq. (5.3.5) gives the *species continuity equation*

$$\frac{\partial \rho_a}{\partial t} = -\nabla \cdot (\rho_a \mathbf{u} + \mathbf{J}_a), \quad (5.3.7)$$

where \mathbf{J}_a represents the motion of species a relative to the bulk flow $\rho_a \mathbf{u}$, known as the diffusive flux of species a and defined as follows,

$$\mathbf{J}_a(\mathbf{r}, t) = \int m_a \mathbf{V}_a f_a d\mathbf{v}_a. \quad (5.3.8)$$

Eq. (5.3.7) allows us to calculate the time evolution of each individual species density in a hard-sphere system. It is also possible to derive the overall mass *continuity equation* by summing Eq. (5.3.7) over all species $a = 1, 2, \dots, N$,

$$\frac{\partial \rho}{\partial t} = -\nabla \cdot \rho \mathbf{u}, \quad (5.3.9)$$

where the total mass density ρ is defined as the sum of all species mass densities,

$$\rho = \sum_{a=1}^S \rho_a. \quad (5.3.10)$$

In the overall continuity equation, the diffusive fluxes of individual species are no longer present as the fluxes sum to zero $\sum \mathbf{J}_a = 0$ as can be seen by combining the definition of the diffusive mass flux

$$\mathbf{u}_a = \mathbf{u} + \frac{\mathbf{J}_a}{\rho_a}, \quad (5.3.11)$$

with the definition of the mass averaged velocity

$$\mathbf{u} = \frac{1}{\rho} \sum_{a=1}^S \rho_a \mathbf{u}_a. \quad (5.3.12)$$

5.3.2 Momentum equation

Deriving the momentum continuity equation begins in a similar manner to the derivation of the mass continuity equation. Multiplying Eq. (5.2.16) by the species a momentum $m_a \mathbf{v}_a$ and integrating over the velocity \mathbf{v}_a gives

$$\int m_a \mathbf{v}_a \frac{\partial}{\partial t} f_a d\mathbf{v}_a = - \int m_a \mathbf{v}_a \mathbf{v}_a \cdot \frac{\partial}{\partial \mathbf{r}} f_a d\mathbf{v}_a - \int m_a \mathbf{v}_a \sum_{b=1}^S \mathcal{T}_{ab}(f_a, f_b) d\mathbf{v}_a. \quad (5.3.13)$$

Again, making use of the fact that m_a and \mathbf{v}_a are independent of both time and position, and following an identical procedure to the first stages of Section 5.3.1 allows Eq. (5.3.13) to be manipulated into the following form,

$$\frac{\partial}{\partial t} \int m_a \mathbf{v}_a f_a d\mathbf{v}_a = - \frac{\partial}{\partial \mathbf{r}} \cdot \int m_a \mathbf{v}_a \mathbf{v}_a f_a d\mathbf{v}_a - \int m_a \mathbf{v}_a \sum_{b=1}^S \mathcal{T}_{ab}(f_a, f_b) d\mathbf{v}_a. \quad (5.3.14)$$

In this case, the collision integral is non-zero when integrated with respect to \mathbf{v}_a as, at the moment of collision, momentum is transferred instantaneously from one hard-sphere to the corresponding colliding hard-sphere over the collision distance σ_{ab} . Therefore, unlike the continuity equation (Eq. (5.3.7)), the collisional term will form part of the final momentum conservation equation. Substituting the definition of the peculiar velocity \mathbf{v}_a into Eq. (5.3.14) gives

$$\begin{aligned} \frac{\partial}{\partial t} \int m_a \mathbf{u} f_a d\mathbf{v}_a + \frac{\partial}{\partial t} \int m_a \mathbf{v}_a f_a d\mathbf{v}_a = \\ - \frac{\partial}{\partial \mathbf{r}} \cdot \int m_a \mathbf{u} \mathbf{u} f_a d\mathbf{v}_a - 2 \frac{\partial}{\partial \mathbf{r}} \cdot \int m_a \mathbf{u} \mathbf{v}_a f_a d\mathbf{v}_a - \frac{\partial}{\partial \mathbf{r}} \cdot \int m_a \mathbf{v}_a \mathbf{v}_a f_a d\mathbf{v}_a \\ - \int m_a \mathbf{u} \sum_{b=1}^S \mathcal{T}_{ab}(f_a, f_b) d\mathbf{v}_a - \int m_a \mathbf{v}_a \sum_{b=1}^S \mathcal{T}_{ab}(f_a, f_b) d\mathbf{v}_a. \end{aligned} \quad (5.3.15)$$

Because of the fact that the total momentum in the system is conserved, we can determine that the mass-averaged velocity \mathbf{u} is invariant over collisions as this value is simply the sum of individual species momentums divided by the overall density which is also a

conserved value. Therefore we see that the term,

$$\int m_a \mathbf{u} \sum_{b=1}^S \mathcal{T}_{ab}(f_a, f_b) d\mathbf{v}_a = 0, \quad (5.3.16)$$

as both the mass of species a (as discussed in Section 5.3.1) and \mathbf{u} are collisionally invariant. The terms containing the ensemble average value of the peculiar velocity \mathbf{v}_a also vanish,

$$\int \mathbf{v}_a f_a d\mathbf{v}_a = 0, \quad (5.3.17)$$

as the average of the deviation from the average is 0. This is not true for terms containing the ensemble average value of the peculiar velocity multiplied by itself (e.g. $\mathbf{v}_a \cdot \mathbf{v}_a$ or $\mathbf{v}_a \mathbf{v}_a$) which remain part of the final equation and can not be dismissed in this way.

Cancelling these terms, substituting the definitions of the ensemble average mass density (Eq. (5.3.6)) and summing Eq. (5.3.15) over all species $i = 1, 2, \dots, N$ gives the *momentum continuity equation* as follows,

$$\frac{\partial(\rho \mathbf{u})}{\partial t} = -\nabla \cdot \rho \mathbf{u} \mathbf{u} - \nabla \cdot \mathbf{P}, \quad (5.3.18)$$

where we have introduced the pressure tensor \mathbf{P} which is defined as follows,

$$\mathbf{P} = \mathbf{P}^k + \mathbf{P}^\Psi, \quad (5.3.19)$$

$$\mathbf{P}^k = \sum_{a=1}^S \int m_a \mathbf{v}_a \mathbf{v}_a f_a d\mathbf{v}_a, \quad (5.3.20)$$

$$\nabla \cdot \mathbf{P}^\Psi = \sum_{a=1}^S \int m_a \mathbf{v}_a \sum_{b=1}^S \mathcal{T}_{ab}(f_a, f_b) d\mathbf{v}_a, \quad (5.3.21)$$

where \mathbf{P}^k and \mathbf{P}^Ψ are the kinetic and collisional components of the pressure tensor respectively. Setting out the equations for the pressure tensor in this way highlights the two mechanisms by which pressure contributes to momentum transport. Firstly, consider a hard-sphere moving with velocity \mathbf{v}_a from its current position to a new position without colliding with any other hard-spheres. This sphere has transported its momentum $m_a \mathbf{v}_a$ over that same distance. This method of momentum transport is referred to as *kinetic* and is captured by Eq. (5.3.20), the kinetic component of the pressure tensor. The second method of momentum transport is via hard-sphere collisions where, at the moment of collision, the velocities of each sphere are updated while their respective positions remain constant causing a transfer of momentum over the corresponding collision distance. This mechanism is captured in the collisional component of the pressure tensor, Eq. (5.3.21).

5.3.3 Energy equation

Multiplying the species a single particle distribution function, Eq. (5.2.16), by the species a kinetic energy $\frac{1}{2}m_a v_a^2$ and integrating over the velocity v_a gives

$$\int \frac{1}{2}m_a v_a^2 \frac{\partial}{\partial t} f_a d\mathbf{v}_a = - \int \frac{1}{2}m_a v_a^2 \mathbf{v}_a \cdot \frac{\partial}{\partial \mathbf{r}} f_a d\mathbf{v}_a - \int \frac{1}{2}m_a v_a^2 \sum_{b=1}^S \mathcal{T}_{ab}(f_a, f_b) d\mathbf{v}_a. \quad (5.3.22)$$

As was the case when deriving the momentum conservation equation, the collisional term is non-zero when integrated with respect to v_a as kinetic energy is transferred from one hard-sphere to another on collision. Therefore, like the momentum equation Eq. (5.3.18), the collisional term will form part of the final energy conservation equation. Utilising the fact that m_a and v_a are independent of time and position and using the product rule to expand the right hand side of Eq. (5.3.22) (as in Sections 5.3.1 and 5.3.2) as well as inserting the definition of the peculiar velocity¹ \mathbf{v}_a allows Eq. (5.3.22) to be rewritten as follows,

$$\begin{aligned} \frac{\partial}{\partial t} \int \frac{1}{2}m_a \mathbf{u}^2 f_a d\mathbf{v}_a + \frac{\partial}{\partial t} \int \frac{1}{2}m_a \mathbf{v}_a^2 f_a d\mathbf{v}_a = \\ - \frac{\partial}{\partial \mathbf{r}} \cdot \int \frac{1}{2}m_a \mathbf{u}^2 \mathbf{u} f_a d\mathbf{v}_a - \frac{\partial}{\partial \mathbf{r}} \cdot \int \frac{1}{2}m_a \mathbf{v}_a^2 \mathbf{u} f_a d\mathbf{v}_a \\ - \frac{\partial}{\partial \mathbf{r}} \cdot \int \frac{1}{2}m_a \mathbf{v}_a^2 \mathbf{v}_a f_a d\mathbf{v}_a - \int \frac{1}{2}m_a \mathbf{v}_a^2 \sum_{b=1}^S \mathcal{T}_{ab}(f_a, f_b) d\mathbf{v}_a \\ - \frac{\partial}{\partial \mathbf{r}} \cdot \int m_a \mathbf{v}_a \mathbf{v}_a f_a d\mathbf{v}_a \cdot \mathbf{u} - \int m_a \mathbf{v}_a \sum_{b=1}^S \mathcal{T}_{ab}(f_a, f_b) d\mathbf{v}_a \cdot \mathbf{u}, \end{aligned} \quad (5.3.23)$$

where all terms containing the ensemble average peculiar velocity have been removed according to Eq. (5.3.17) and, similar to Eq. (5.3.16), the collisional term,

$$\int \frac{1}{2}m_a \mathbf{u}^2 \sum_{b=1}^S \mathcal{T}_{ab}(f_a, f_b) d\mathbf{v}_a = 0, \quad (5.3.24)$$

is also zero as both the mass-averaged velocity \mathbf{u} and the species a mass m_a are invariant over collision as discussed in Sections 5.3.1 and 5.3.2.

We define the temperature T as the peculiar kinetic energy, the hard-sphere kinetic energy relative to any underlying bulk motion of the system given by the mass-averaged

¹

$$\begin{aligned} (\mathbf{v}_a + \mathbf{u}) \cdot (\mathbf{v}_a + \mathbf{u}) &= \mathbf{v}_a \cdot \mathbf{v}_a + 2\mathbf{v}_a \cdot \mathbf{u} + \mathbf{u} \cdot \mathbf{u} \\ (\mathbf{v}_a + \mathbf{u})^2 (\mathbf{v}_a + \mathbf{u}) &= \mathbf{v}_a \cdot \mathbf{v}_a \mathbf{v}_a + 2\mathbf{v}_a \cdot \mathbf{u} \mathbf{v}_a + \mathbf{u} \cdot \mathbf{u} \mathbf{v}_a + \mathbf{v}_a \cdot \mathbf{v}_a \mathbf{u} + 2\mathbf{v}_a \cdot \mathbf{u} \mathbf{u} + \mathbf{u} \cdot \mathbf{u} \mathbf{u} \\ &= \mathbf{v}_a^2 \mathbf{v}_a + 2\mathbf{u} \cdot \mathbf{v}_a \mathbf{v}_a + \mathbf{u}^2 \mathbf{v}_a + \mathbf{v}_a^2 \mathbf{u} + 2\mathbf{v}_a \cdot \mathbf{u} \mathbf{u} + \mathbf{u}^2 \mathbf{u} \end{aligned}$$

velocity \mathbf{u} ,

$$\frac{3}{2}nk_{\text{B}}T = \int \frac{1}{2}m_a \mathbf{v}_a^2 f_a d\mathbf{v}_a, \quad (5.3.25)$$

where n is the ensemble average number density, and k_{B} is the Boltzmann constant. Applying the definition of the temperature as well as the ensemble average mass density (Eq. (5.3.6)) and summing Eq. (5.3.23) over all species $a = 1, 2, \dots, S$ gives the *energy equation* as

$$\frac{\partial(\rho e)}{\partial t} = -\nabla \cdot \rho e \mathbf{u} - \nabla \cdot \mathbf{J}_q - \nabla \cdot (\mathbf{P} \cdot \mathbf{u}), \quad (5.3.26)$$

where we have identified and extracted the pressure tensor \mathbf{P} as well as defining the total specific energy e

$$e = \frac{1}{2}\mathbf{u}^2 + \frac{3}{2}\frac{nk_{\text{B}}T}{\rho}, \quad (5.3.27)$$

as the sum of the specific kinetic and specific internal energy. We also define a new term known as the diffusive heat flux \mathbf{J}_q through,

$$\mathbf{J}_q = \mathbf{J}_q^k + \mathbf{J}_q^\Psi, \quad (5.3.28)$$

$$\mathbf{J}_q^k = \sum_{a=1}^S \int \frac{1}{2}m_a \mathbf{v}_a^2 \mathbf{v}_a f_a d\mathbf{v}_a, \quad (5.3.29)$$

$$\nabla \cdot \mathbf{J}_q^\Psi = \sum_{a=1}^S \int \frac{1}{2}m_a \mathbf{v}_a^2 \sum_{b=1}^S \mathcal{T}_{ab}(f_a, f_b) d\mathbf{v}_a, \quad (5.3.30)$$

where \mathbf{J}_q^k and \mathbf{J}_q^Ψ are the kinetic and collisional components of the heat flux respectively. Similar to the kinetic and collisional contributions to the pressure tensor \mathbf{P} , we see that the heat flux \mathbf{J}_q describes two mechanisms by which heat is transported. One is the motion of a non-colliding particle through the system with kinetic energy $m_a \mathbf{v}_a^2$ and the second is the instantaneous transfer of kinetic energy from hard-sphere to hard-sphere upon collision.

5.4 Closing the hydrodynamic equations

So far we have derived the mass Eq. (5.3.7), momentum Eq. (5.3.18), and energy Eq. (5.3.26) conservation equations which describe the time-evolution of a hard-sphere fluid. However, at the moment, the diffusive fluxes (the diffusive mass flux \mathbf{J}_a , the pressure tensor \mathbf{P} , and the heat flux \mathbf{J}_q) are not in a convenient form as they are all in terms of the distribution function f_a which is unknown. The conservation equations are closed by writing these diffusive fluxes in terms of the state variables and their gradients, i.e. ∇T , $\nabla \mathbf{u}$. In this thesis we assume straightforward linear closures; however, there is choice available when closing these phenomenological equations, utilising higher order gradi-

ent terms is known as Burnett or super-Burnett hydrodynamics [4]. Any disagreement between these models and kinetic theory may be the result of this choice and will be discussed later.

In order to derive the linear phenomenological equations, the first step is deriving the total entropy production [5] in terms of a general entropy balance equation which can be written as follows,

$$\frac{\partial(\rho s)}{\partial t} = -\nabla \cdot \rho s \mathbf{u} - \nabla \cdot \mathbf{J}_s + \Omega, \quad (5.4.1)$$

where s is the specific entropy, \mathbf{J}_s is the entropy flux, and Ω is the entropy production. The total entropy time derivative is given by Gibb's equation [6] as follows,

$$T \frac{ds}{dt} = \frac{d\Psi}{dt} + \frac{p}{\rho} \nabla \cdot \mathbf{u} + \frac{1}{\rho} \sum_a \mu_a \nabla \cdot \mathbf{J}_a, \quad (5.4.2)$$

where $\Psi = 3nk_B T/2\rho$ is the specific internal energy, and p is the isotropic pressure. It follows from the total energy conservation equation shown in Eq. (5.3.26) that the internal energy conservation equation is as follows,

$$\rho \frac{d\Psi}{dt} = -\nabla \cdot \mathbf{J}_q - \mathbf{P} : \nabla \mathbf{u}, \quad (5.4.3)$$

where $:$ denotes the double dot product of two tensors. Substituting this equation allows Eq. (5.4.2) to be written as,

$$\frac{\partial(\rho s)}{\partial t} = -\nabla \cdot \rho s \mathbf{u} - \frac{1}{T} \nabla \cdot \mathbf{J}_q - \frac{1}{T} \boldsymbol{\tau} : \nabla \mathbf{u} + \frac{1}{T} \sum_a \mu_a \nabla \cdot \mathbf{J}_a, \quad (5.4.4)$$

where use has been made of the fact that the pressure tensor \mathbf{P} can be rewritten in terms of a scalar hydrostatic piece $p\mathbf{1}$ and a symmetric viscous tensor piece $\boldsymbol{\tau}$ as follows,

$$\mathbf{P} = p\mathbf{1} + \boldsymbol{\tau}, \quad (5.4.5)$$

as well as the fact that,

$$\nabla \mathbf{u} : \mathbf{1} = \nabla \cdot \mathbf{u}. \quad (5.4.6)$$

Comparing Eq. (5.4.4) with Eq. (5.4.1) shows that the entropy flux can be written in terms of the diffusive mass flux and the heat flux as follows,

$$\mathbf{J}_s = \frac{1}{T} \left(\mathbf{J}_q - \sum_a \mu_a \mathbf{J}_a \right), \quad (5.4.7)$$

and the total entropy production can be written as follows,

$$\Omega = -\frac{1}{T^2} \mathbf{J}_q \cdot \nabla T - \frac{1}{T} \sum_a \mathbf{J}_a \cdot T \nabla \left(\frac{\mu_a}{T} \right) - \frac{1}{T} \boldsymbol{\tau} : \nabla \mathbf{u}. \quad (5.4.8)$$

5.4.1 Defining the heat flux

There is choice involved in the definition of the heat flux \mathbf{J}_q . It is possible to rewrite the expression for the entropy production shown in Eq. (5.4.8) in several different forms by extracting terms which are proportional to the temperature gradient ∇T from the chemical potential μ_a . De Groot [6] outlines three separate forms of the entropy production equation, the first of which is shown in Eq. (5.4.8). The second makes use of the following thermodynamic relationship,

$$T \nabla \left(\frac{\mu_a}{T} \right) = \nabla \mu_a - \frac{\mu_a}{T} \nabla T, \quad (5.4.9)$$

which allows Eq. (5.4.8) to be rewritten as,

$$\Omega = -\frac{1}{T^2} \mathbf{J}'_q \cdot \nabla T - \frac{1}{T} \sum_a \mathbf{J}_a \cdot \nabla \mu_a - \frac{1}{T} \boldsymbol{\tau} : \nabla \mathbf{u}, \quad (5.4.10)$$

where the term which is separated from the concentration driving force is now included in a new definition of the heat flux \mathbf{J}'_q which is defined as follows,

$$\mathbf{J}'_q = \mathbf{J}_q - \sum_a \mu_a \mathbf{J}_a = T \mathbf{J}_s. \quad (5.4.11)$$

The third and final form of the entropy production detailed by Ref. [6] is obtained using the following relationship,

$$T \nabla \left(\frac{\mu_a}{T} \right) = \nabla_T \mu_a - \frac{h_a}{T} \nabla T, \quad (5.4.12)$$

where ∇_T represents a derivative taken at constant temperature, and h_a is the partial specific enthalpy of species a . Eq. (5.4.8) can now be rewritten as

$$\Omega = -\frac{1}{T^2} \mathbf{J}''_q \cdot \nabla T - \frac{1}{T} \sum_a \mathbf{J}_a \cdot \nabla_T \mu_a - \frac{1}{T} \boldsymbol{\tau} : \nabla \mathbf{u}, \quad (5.4.13)$$

where, again, a new definition of the heat flux \mathbf{J}''_q is obtained which is defined as follows,

$$\mathbf{J}''_q = \mathbf{J}_q - \sum_a h_a \mathbf{J}_a. \quad (5.4.14)$$

Erpenbeck [7] terms these various forms of the heat flux (\mathbf{J}_q , \mathbf{J}'_q , and \mathbf{J}''_q), as well as the corresponding force terms and any transport coefficients which are subsequently derived from these expressions, as the “mainstream”, “prime”, and “double-prime” versions. The

values of \mathbf{J}_q , \mathbf{J}'_q , and \mathbf{J}''_q differ in terms of the respective contribution of diffusion to the heat flux. These differing forms of the flux terms can be more useful than others in certain applications, for example, it is inconvenient to calculate the “prime” transport coefficients with methods such as the Green-Kubo relations as it necessitates defining Planck’s constant whereas the “mainstream” and “double-prime” coefficients do not [7]. In principal there are infinitely many degrees to which terms containing the temperature gradient ∇T can be separated from the concentration driving force term $T\nabla(\mu_a/T)$ thereby altering the definition of the heat flux as part of the total entropy production. This thesis will consider the “mainstream” version of the heat flux as well as the resulting transport coefficients as detailed in the following section.

5.4.2 Phenomenological equations

The definition of the pressure tensor for a hard-sphere fluid is given in Ref. [7] as follows,

$$\mathbf{P} = p\mathbf{1} - \eta \left(\nabla \mathbf{u} + (\nabla \mathbf{u})^T \right) + \left(\left(\frac{2}{d} \right) \eta - \eta_B \right) (\nabla \cdot \mathbf{u}) \mathbf{1}, \quad (5.4.15)$$

where p is the isotropic pressure, η is the shear viscosity, \mathbf{A}^T denotes the transpose of a tensor \mathbf{A} , η_B is the bulk viscosity, d is the dimensionality, and $\mathbf{1}$ is the identity matrix. The isotropic pressure p is calculated using an equation of state where, in this thesis, the BMCSL equation of state [8, 9] is used. In addition to the pressure term, two stress terms are present which contain the velocity gradients. Note that linear closures are used. Transport coefficients (shear η and bulk η_B viscosity) then relate the magnitude of the velocity gradients to the behaviour of the system. These transport coefficients themselves, as well those present in the equations of \mathbf{J}_a and \mathbf{J}_q , contain a large amount of depth as they include a full state dependence; they are functions of the mixture concentration, density, and temperature via Enskog theory.

The diffusive flux \mathbf{J}_a of species a is given by Ref. [6] as follows,

$$\mathbf{J}_a = - \sum_b L_{ab} T \nabla \left(\frac{\mu_b}{T} \right) - \frac{L_{au}}{T} \nabla T, \quad (5.4.16)$$

where L_{ab} is the mutual diffusion coefficient of species a through species b , μ_b is the chemical potential of species b , and L_{au} is the thermal diffusion coefficient of species a . The diffusive heat flux \mathbf{J}_q is also given by Ref. [6] as follows,

$$\mathbf{J}_q = - \sum_a L_{ua} T \nabla \left(\frac{\mu_a}{T} \right) - \frac{L_{uu}}{T} \nabla T, \quad (5.4.17)$$

where L_{uu} is the phenomenological thermal conductivity. We note that Eq. (5.4.16) and Eq. (5.4.17) predict that mass will diffuse through the system as the result of a gradient in temperature. Note that both equations, like Eq. (5.4.15), contain only linear closures. The

chemical potential, like the isotropic pressure, is calculated using the BMCSL equation of state. In the context of fluid mixtures, the phenomenological thermal conductivity L_{uu} present in Eq. (5.4.17) is not what should be discussed when comparing to experimentally observed thermal conductivity values. This is discussed in more depth in Ch. 6.

Expressing the diffusive fluxes in terms of a series of system gradients allows corresponding transport coefficients to be predicted using Enskog theory [3, 10, 11] which assumes that the time evolution of the distribution function f will depend purely on the macroscopic quantities of the system, i.e. the species densities $\rho_{1,2,\dots,S}$, the average velocity \mathbf{u} , and the temperature T . A perturbation expansion [4] (Chapman-Enskog expansion) is then applied to the distribution function f_a in order to express it in increasing powers of the system gradients,

$$f_a(\Gamma_a, \rho_{1,2,\dots,S}, \mathbf{u}, T) = f_a^{[0]}(\Gamma_a, \rho_{1,2,\dots,S}, \mathbf{u}, T) + \mu f_a^{[1]}(\Gamma_a, \rho_{1,2,\dots,S}, \mathbf{u}, T) + \mu^2 f_a^{[2]}(\Gamma_a, \rho_{1,2,\dots,S}, \mathbf{u}, T) + \dots, \quad (5.4.18)$$

where the dependence of the distribution function on time t is replaced with a dependence on density, velocity, and temperature, $f_a(\Gamma_a, t) \rightarrow f_a(\Gamma_a, \rho_{1,2,\dots,S}, \mathbf{u}, T)$, and μ is an expansion parameter representing the order of magnitude of any gradients of the state variables and is used to collect and equate terms of equal orders of magnitude. For example, $f_a^{[1]}$ represents the first order solution to the distribution function with respect to one system gradient, and $f_a^{[0]}$ represents the undisturbed solution given that there are no gradients present in the system. In practice, only the first order term $f_a^{[1]}$ is solved for. This expansion is applied to Eq. (5.2.16) for the set of single particle distribution functions as well as the conservation equations Eq. (5.3.7), Eq. (5.3.18), and Eq. (5.3.26). Expanded terms that are of a common order of $\mathcal{O}(\mu)$ with common gradients are then compared in order to generate expressions for the transport coefficients. The method commonly used in order to calculate the actual transport coefficient values, and the method used in this thesis, is to expand these expressions using Sonine polynomials [12]. Third order polynomials are typically used in this work when predicting values using Enskog theory.

References

- [1] M. H. Ernst et al. “Hard-Sphere Dynamics and Binary-Collision Operators”. In: *Physica* 45 (1969), pp. 127–146.
- [2] J. R. Dorfman and M. H. Ernst. “Hard-Sphere Binary-Collision Operators”. In: *J. Stat. Phys.* 57 (1989), pp. 581–593.
- [3] M. López de Haro, E. G. D. Cohen, and J. M. Kincaid. “The Enskog Theory for Multicomponent Mixtures. 1. Linear Transport-Theory”. In: *J. Chem. Phys.* 78.5 (1983), pp. 2746–2759.

-
- [4] S. Chapman and T. G. Cowling. *The mathematical theory of non-uniform gases*. 3rd ed. Cambridge university press, 1970.
- [5] J. Armstrong and F. Bresme. “Thermal conductivity of highly asymmetric binary mixtures: how important are heat/mass coupling effects?” In: *Phys. Chem. Chem. Phys.* 16.24 (2014), p. 12307.
- [6] S. R. de Groot and P. Mazur. *Non-Equilibrium Thermodynamics*. Dover, 1984.
- [7] J. J. Erpenbeck. “Transport-coefficients of hard-sphere mixtures theory and Monte-Carlo molecular-dynamics calculations for an isotopic mixture”. In: *Phys. Rev. A* 39.9 (1989), pp. 4718–4731.
- [8] T. Boublík. “Hard-Sphere Equation of State”. In: *J. Chem. Phys.* 53.1 (1970), pp. 471–472.
- [9] G. A. Mansoori et al. “Equilibrium thermodynamic properties of mixtures of hard spheres”. In: *J. Chem. Phys.* 54.4 (1971), pp. 1523–1525.
- [10] J. M. Kincaid, E. G. D. Cohen, and M. López de Haro. “The Enskog Theory for Multicomponent Mixtures. 4. Thermal-Diffusion”. In: *J. Chem. Phys.* 86.2 (1987), pp. 963–975.
- [11] M. L. López de Haro and E. G. D. Cohen. “The Enskog Theory for Multicomponent Mixtures. 3. Transport-properties of dense binary-mixtures with one tracer component”. In: *J. Chem. Phys.* 80.1 (1984), pp. 408–415.
- [12] M. N. Bannerman and L. Lue. “Transport properties of highly asymmetric hard-sphere mixtures”. In: *J. Chem. Phys.* 130.16, 164507 (2009), p. 164507.

MICRO TO MACROSCOPIC THERMAL CONDUCTIVITY

Deriving the full multicomponent hydrodynamic equations for the conservation of mass, momentum, and energy in Ch. 5 has laid the foundations for a detailed discussion of heat transfer in fluid mixtures. As seen in Eq. (5.4.17), heat transport in these mixtures will be a complex story of simultaneous diffusion and conduction. The effects of both of these mechanisms must therefore be characterised and understood in order to accurately predict the properties of real systems.

It is already clear from the experimental results shown in Ch. 3 that continuum models such as the series-parallel thermal conductivity limits as well as the Maxwell and Hamilton-Crosser models are unable to describe the full range of behaviour reported in nanofluids and gas mixtures (especially gas mixtures such as H_2 -He). Phenomena such as minimums in the thermal conductivity profile, as shown in Fig. 3.4, as well as conductivity dependence on nanoparticle size are not captured by these models. We therefore turn to the phenomenological expressions for the heat and mass flux defined in Ch. 5 in order to generate a complete description of multicomponent heat transfer in fluids which includes molecular effects such as thermal diffusion.

6.1 Phenomenological thermal conductivity L_{uu}

Eq. (5.4.16) shows that, in a multicomponent hard-sphere fluid, a temperature gradient ∇T will cause species to diffuse through the system according to the corresponding thermal diffusion coefficient L_{ua} . This effect is known as thermophoresis or the Soret effect [1]. The related effect of a transfer of heat due to a gradient in concentration, shown in Eq. (5.4.17), is known as the Dufour effect. Previously in Section 5.4.1, this thesis discussed the ambiguity in the definition of the heat flux. Another level of ambiguity in the definition of the conductivity is added for fluid mixtures as a result of thermodiffusion which means that there is no one unique definition of the “thermal conductivity” in mixtures for all moments in time. Instead, there is a time dependent effective thermal conductivity which will have an initial value, corresponding to a time when the system

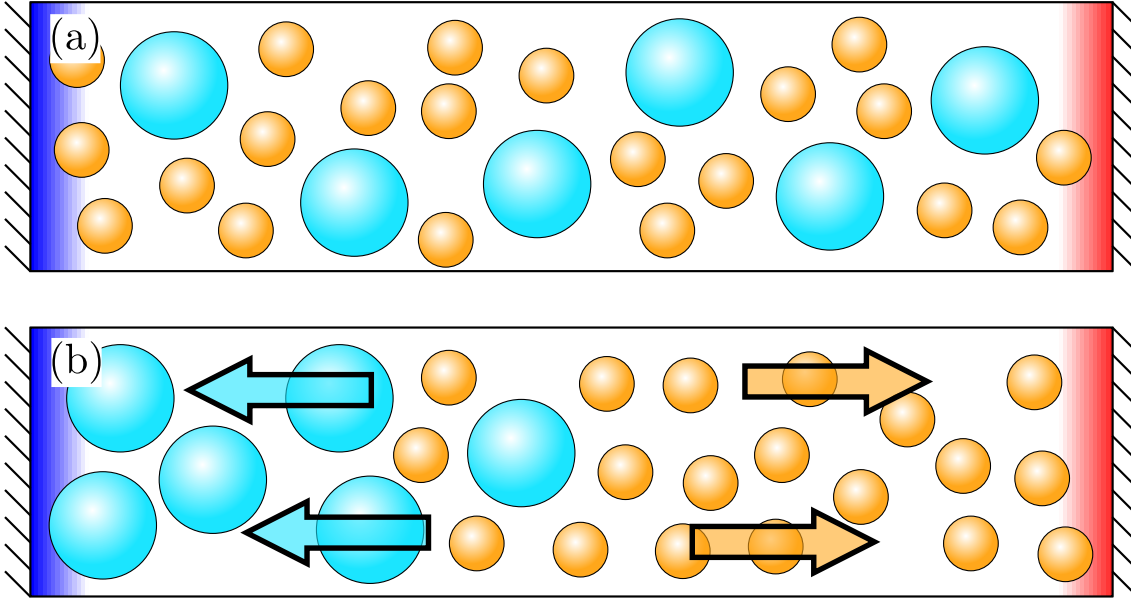


Figure 6.1: A multicomponent hard-sphere fluid at (a) the onset of heat transfer and (b) at steady-state conditions. As (a) shows a system at the onset of heat transfer, the system is still homogeneous and shows no concentration gradients. However, in (b), thermal diffusion has taken place, as shown by the coloured arrows, which has caused a concentration gradient to be established. These system shown in (b) corresponds to the steady-state thermal conductivity λ .

is homogeneous, which is “enhanced” by the presence of thermal diffusion. This homogeneous state corresponds to the system shown in Fig. 6.1(a) which is a snapshot of a multicomponent hard-sphere system under the influence of a temperature gradient before any conduction or diffusion has occurred. At the moment that a temperature gradient is established thermal diffusion will take place causing a flow of heat due to the diffusion of mass through the system. As diffusion continues, concentration gradients will appear in the system as shown in Fig. 6.1(b) and after a long time the system will reach an equilibrium state where diffusion caused by concentration gradients $\sum_b L_{ab} T \nabla \left(\frac{\mu_b}{T} \right)$ exactly counteracts diffusion as a result of the temperature gradient $\frac{L_{au}}{T} \nabla T$ and net diffusion in the system goes to zero. At this point, without the heat transfer contribution of diffusion, the thermal conductivity has decayed to the final value λ [1, 2] corresponding to a system where there is zero diffusion of mass $\mathbf{J}_{a,b,\dots,S} = 0$. In this thesis, this value is referred to as the steady-state thermal conductivity. As the difference between the phenomenological value and the steady-state value originates purely from the diffusion of mass through the system, the phenomenological thermal conductivity L_{uu} is always greater than the steady-state thermal conductivity λ [1]; the diffusion of mass through the system never detracts from the overall heat transfer.

A relatively small number of nanofluid studies report values which lie outwith the series-parallel limits [1]. However, when looking at the phenomenological thermal conductivity L_{uu} , Enskog theory predicts that it is possible for even simple, low density hard

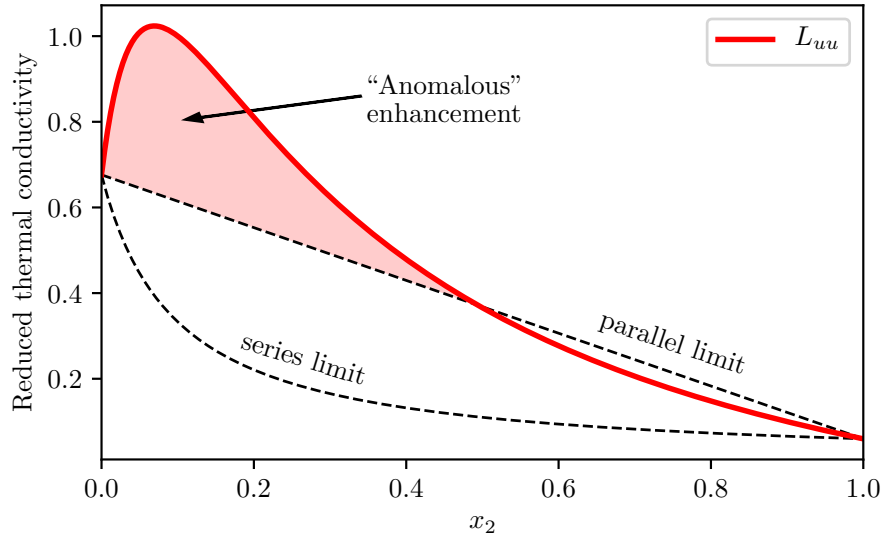


Figure 6.2: Thermal conductivity as a function of the mol fraction of species 2. The phenomenological thermal conductivity L_{uu} is predicted for a binary hard sphere mixture using Enskog theory. In this case, the hard-sphere species have masses of $m_1 = 1$ and $m_2 = 8$ and diameters of $\sigma_1 = 1$ and $\sigma_2 = 2$. The system is assumed to be at low density ($n = 10^{-8}$) where Enskog theory is most valid. The series and parallel limits are calculated using the pure component thermal conductivities of species 1 and 2. At low volume fractions L_{uu} greatly outperforms the parallel mode thermal conductivity and even produces a maximum which is greater than either pure component thermal conductivity.

sphere systems to exhibit L_{uu} values well outside these limits as shown in Fig. 6.2. This figure shows Enskog theory predictions of the phenomenological thermal conductivity as a function of concentration for a low density binary hard sphere fluid with species diameters of $\sigma_1 = 1$ and $\sigma_2 = 2$ and species masses of $m_1 = 1$ and $m_2 = 8$. The system exhibits L_{uu} values which are well above not only the upper parallel limit, but also the maximum pure component thermal conductivity value.

If the large thermal conductivity enhancements shown in Fig. 6.2 for hard-sphere mixtures were to translate to solid-liquid mixtures, it could potentially explain large thermal conductivity measurements such as those reported in nanofluid systems. However, in the context of real heat transfer applications, values of the pure phenomenological thermal conductivity, such as the results shown in Fig. 6.2, are likely to be irrelevant as a system only exhibits this thermal conductivity in the zero-time limit $t \rightarrow 0$ when there are zero gradients in the state variables and any transfer of heat necessitates a temperature gradient in the system. Although this temperature gradient may be small, any deviation from a completely undisturbed system will result in a departure from the phenomenological thermal conductivity and an eventual decay to the steady-state value. Even if it were possible to access the zero-time thermal conductivity experimentally, it is not obvious that the “mainstream” definition of L_{uu} is useful when comparing to real systems. As detailed in Section 5.4.1, the phenomenological thermal conductivity is commonly defined in two

other manners (“prime” and “double-prime”) which are given in Ref. [3] as follows,

$$L'_{uu} = L_{uu} - 2 \sum_a \mu_a L_{ua} + \sum_a \sum_b \mu_a \mu_b L_{ab}, \quad (6.1.1)$$

$$L''_{uu} = L_{uu} - 2 \sum_a h_a L_{ua} + \sum_a \sum_b h_a h_b L_{ab}, \quad (6.1.2)$$

where L'_{uu} , and L''_{uu} are the “prime”, and “double-prime” versions of the phenomenological thermal conductivity respectively. These values differ from the “mainstream” value of L_{uu} due to a different transfer of heat due to diffusion.

6.2 Steady-state thermal conductivity λ

It is desirable to define an experimentally accessible thermal conductivity value which is independent of the choice of flux. This section shows a derivation of a thermal conductivity value which accomplishes both of these aims and is referred to as the steady-state thermal conductivity with the symbol λ . In order to derive a general expression for the steady-state thermal conductivity λ of an S -component mixture, the equations for the mass fluxes \mathbf{J}_a and energy flux \mathbf{J}_q , which were shown originally in Eqs. 5.4.16 and 5.4.17 respectively, are restated here in a modified form as follows,

$$\mathbf{J} = \mathbf{D} \cdot \mathbf{X} + \mathbf{U} X_u, \quad (6.2.1)$$

$$\mathbf{J}_q = \mathbf{U} \cdot \mathbf{X} + L_{uu} X_u. \quad (6.2.2)$$

In this case, \mathbf{D} is a $S \times S$ matrix containing all mutual and self diffusion coefficients, and \mathbf{U} is a vector containing the S thermal diffusion coefficients defined as

$$\mathbf{D} = \begin{bmatrix} L_{11} & L_{12} & \dots & L_{1S} \\ L_{21} & L_{22} & & \\ \vdots & & \ddots & \\ L_{S1} & & & L_{SS} \end{bmatrix}, \quad \text{and} \quad \mathbf{U} = \begin{bmatrix} L_{u1} \\ L_{u2} \\ \vdots \\ L_{uS} \end{bmatrix} \quad (6.2.3)$$

respectively, $\mathbf{X}_u = -\frac{1}{T} \nabla T$ is the temperature driving force, \mathbf{X} is a vector containing the concentration driving forces for all species $a = 1, 2, \dots, S$,

$$\mathbf{X} = \begin{bmatrix} -T \nabla \left(\frac{\mu_1}{T} \right) \\ -T \nabla \left(\frac{\mu_2}{T} \right) \\ \vdots \\ -T \nabla \left(\frac{\mu_S}{T} \right) \end{bmatrix}, \quad \text{and} \quad \mathbf{J} = \begin{bmatrix} \mathbf{J}_1 \\ \mathbf{J}_2 \\ \vdots \\ \mathbf{J}_S \end{bmatrix} \quad (6.2.4)$$

is a vector containing the diffusive flux terms for each species $\mathbf{J}_{1,2,\dots,S}$. As stated previously, λ corresponds to the thermal conductivity in a system where heat transfer has been occurring for a long time and thermal diffusion has completed resulting in zero diffusive

flux $\mathbf{J}_{1,2,\dots,S} = 0$. Setting $\mathbf{J} = \mathbf{0}$ in Eq. (6.2.1) allows the concentration driving force \mathbf{X} to be expressed in terms of the temperature driving force \mathbf{X}_u as follows

$$\mathbf{X} = -(\mathbf{D}^{-1} \cdot \mathbf{U}) \mathbf{X}_u. \quad (6.2.5)$$

Substituting this expression into Eq. (6.2.2) gives an equation for the heat flux \mathbf{J}_q in terms of the temperature gradient only,

$$\mathbf{J}_q = -\frac{1}{T} (L_{uu} - \mathbf{U} \cdot (\mathbf{D}^{-1} \cdot \mathbf{U})) \nabla T. \quad (6.2.6)$$

The steady-state thermal conductivity λ and the energy flux \mathbf{J}_q are related by Fourier's law of conduction $\mathbf{J}_q = -\lambda \nabla T$ which implicitly defines λ as follows,

$$\lambda = \frac{1}{T} (L_{uu} - \mathbf{U} \cdot (\mathbf{D}^{-1} \cdot \mathbf{U})). \quad (6.2.7)$$

For a S -component mixture, the Onsager relationships [4] can be written in the following form,

$$\sum_{b=1}^S L_{ab} = 0, \quad (6.2.8)$$

$$\sum_{a=1}^S L_{ua} = 0, \quad (6.2.9)$$

which states that every row and column of \mathbf{D} are linearly dependent on the $S - 1$ other rows and columns of \mathbf{D} respectively. As there are only $S - 1$ linearly independent rows and columns, the $S \times S$ diffusion matrix \mathbf{D} has rank $S - 1$ and is therefore singular and uninvertible. Instead, the generalised inverse [5] of \mathbf{D} is utilised in order to solve for λ as shown in the following equation,

$$\lambda = \frac{1}{T} (L_{uu} - \mathbf{U} \cdot (\mathbf{D}^+ \cdot \mathbf{U})), \quad (6.2.10)$$

where $^+$ denotes a generalised inverse. It is clear from Eq. (6.2.10) that, in a mono-component fluid where the effects of thermal diffusion are not present, the steady-state and phenomenological thermal conductivities are related simply as $\lambda = L_{uu}/T$.

6.2.1 Binary derivation

This thesis focuses primarily on binary systems; hence, a derivation of λ for binary mixtures is shown here using a singular value decomposition (SVD) in order to determine the generalised inverse of the diffusion matrix \mathbf{D}^+ . For a binary mixture, \mathbf{D} is defined as

follows,

$$\mathbf{D} = \begin{bmatrix} L_{11} & L_{12} \\ L_{21} & L_{22} \end{bmatrix}, \quad (6.2.11)$$

and can be simplified using the Onsager relationship shown in Eq. (6.2.8) to

$$\mathbf{D} = \begin{bmatrix} L_{11} & -L_{11} \\ -L_{11} & L_{11} \end{bmatrix}. \quad (6.2.12)$$

Performing a SVD on \mathbf{D} allows this matrix to be factorised into three separate matrices as follows,

$$\mathbf{D} = \mathbf{G}\mathbf{\Sigma}\mathbf{F}^T, \quad (6.2.13)$$

where \mathbf{G} and \mathbf{F} are $S \times S$ unitary matrices and $\mathbf{\Sigma}$ is a $S \times S$ diagonal matrix where the diagonal terms are known as the singular values. Carrying out the SVD allows the generalised inverse \mathbf{D}^+ to subsequently be calculated as shown in Ref. [5] through,

$$\mathbf{D}^+ = \mathbf{F}\mathbf{\Sigma}^+\mathbf{G}^T, \quad (6.2.14)$$

where the matrix $\mathbf{\Sigma}^+$ is calculated by replacing all non zero diagonal entries of $\mathbf{\Sigma}$ with their inverse. Performing a SVD on the diffusion matrix \mathbf{D} determines the values of \mathbf{G} , $\mathbf{\Sigma}$, and \mathbf{F} to be,

$$\mathbf{D} = \begin{bmatrix} \frac{-1}{\sqrt{2}} & \frac{1}{\sqrt{2}} \\ \frac{1}{\sqrt{2}} & \frac{1}{\sqrt{2}} \end{bmatrix} \begin{bmatrix} 2L_{11} & 0 \\ 0 & 0 \end{bmatrix} \begin{bmatrix} \frac{-1}{\sqrt{2}} & \frac{1}{\sqrt{2}} \\ \frac{1}{\sqrt{2}} & \frac{1}{\sqrt{2}} \end{bmatrix}^T, \quad (6.2.15)$$

where the singular values of \mathbf{D} are $2L_{11}$ and 0^1 . The generalised inverse is now calculated Eq. (6.2.14) as follows,

$$\mathbf{D}^+ = \begin{bmatrix} \frac{-1}{\sqrt{2}} & \frac{1}{\sqrt{2}} \\ \frac{1}{\sqrt{2}} & \frac{1}{\sqrt{2}} \end{bmatrix} \begin{bmatrix} \frac{1}{2L_{11}} & 0 \\ 0 & 0 \end{bmatrix} \begin{bmatrix} \frac{-1}{\sqrt{2}} & \frac{1}{\sqrt{2}} \\ \frac{1}{\sqrt{2}} & \frac{1}{\sqrt{2}} \end{bmatrix}^T, \quad (6.2.16)$$

$$\mathbf{D}^+ = \begin{bmatrix} \frac{1}{4L_{11}} & \frac{-1}{4L_{11}} \\ \frac{-1}{4L_{11}} & \frac{1}{4L_{11}} \end{bmatrix}. \quad (6.2.17)$$

For binary mixtures the matrix of thermal diffusion coefficients \mathbf{U} is defined as

$$\mathbf{U} = \begin{bmatrix} L_{u1} \\ L_{u2} \end{bmatrix}, \quad (6.2.18)$$

¹Due to the nature of the Onsager relationships, the diffusion matrix \mathbf{D} for any S -component mixture will always have one singular value which is equal to 0.

which can be simplified by applying the Onsager relationship shown in Eq. (6.2.9) to

$$\mathbf{U} = \begin{bmatrix} L_{u1} \\ -L_{u1} \end{bmatrix}. \quad (6.2.19)$$

Substituting the final expressions for \mathbf{D}^+ and \mathbf{U} , shown in Eq. (6.2.17) and Eq. (6.2.19) respectively, into Eq. (6.2.10) gives the final expression for the steady state thermal conductivity in binary mixtures as

$$\lambda = \frac{1}{T} \left(L_{uu} - \frac{L_{u1}^2}{L_{11}} \right). \quad (6.2.20)$$

It is not necessary to go through the process of determining the generalised inverse in order to derive the steady-state thermal conductivity expression for binary mixtures as shown in Appendix B which showcases a method for deriving λ using only algebraic manipulation. Eq. (6.2.10) can be used in order to derive the expression for λ for any S component mixture. As an interesting aside, the $S = 3$ component steady-state thermal conductivity can be written as follows,

$$\lambda = \frac{1}{T} \left(L_{uu} - \frac{L_{11}L_{u2}^2 - 2L_{12}L_{u1}L_{u2} + L_{22}L_{u1}^2}{L_{11}L_{22} - L_{12}^2} \right). \quad (6.2.21)$$

Expressions for λ quickly become intractable beyond this number of components $S = 4+$.

In order to show that the steady-state thermal conductivity is independent of the choice of “mainstream”, “prime”, or “double-prime” fluxes, the expressions for the “prime” and “double-prime” diffusion coefficients are shown here as they are given in Ref. [3],

$$L'_{ab} = L_{ab} \quad L''_{ab} = L_{ab}, \quad (6.2.22)$$

$$L'_{ua} = L_{ua} - \sum_b \mu_b L_{ba} \quad L''_{ua} = L_{ua} - \sum_b h_b L_{ba}, \quad (6.2.23)$$

where the mutual diffusion coefficients are equal regardless of the choice of flux. It is easy to show, by substituting these expressions along with Eqs. (6.1.1) and (6.1.2) into Eq. (6.2.20), that

$$\lambda = \lambda' = \lambda''. \quad (6.2.24)$$

As λ is valid in the steady-state limit, it is likely that this thermal conductivity definition is more experimentally relevant than L_{uu} . This is especially true for measurement techniques such as the parallel heated plates method which is detailed in Section 3.1.2 as this method measures the thermal conductivity after the experiment has come to steady-state, hence allowing temperature and concentration gradients across the fluid to become established. This relevance is less obvious in the case of transient thermal conductivity measurement techniques such as the transient hot wire method which is outlined in

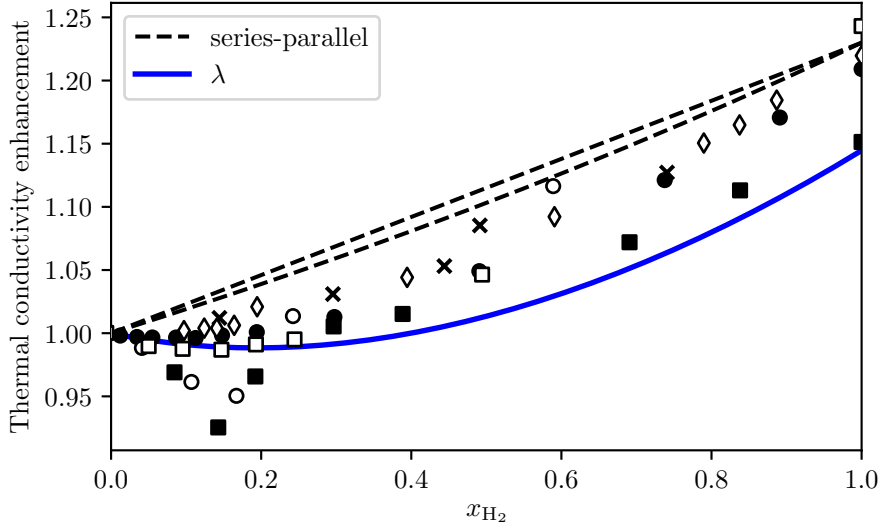


Figure 6.3: Thermal conductivity as a function of the volume fraction of species 2 ϕ_2 . The steady-state thermal conductivity λ is predicted using Enskog theory for a low density binary hard sphere mixture with a number density of $n = 10^{-8}$ with a diameter ratio of $\sigma_{H_2}/\sigma_{He} = 289/260$ and mass ratio of $m_{H_2}/m_{He} = 1/2$. The series-parallel limits are calculated using the pure component thermal conductivities of the two hard-sphere species. λ is less than the series mode thermal conductivity over the entire concentration range culminating in a minimum which is lower than either of the pure component thermal conductivity values.

Section 3.1.1. This method commonly measures the thermal conductivity over short timescales which are of the order of $10 \text{ ms} < 100 \text{ ms}$ [6]. It is not clear from the equations that have been derived so far over what timescale the thermal conductivity of a mixture decays from the phenomenological value to the steady state value and therefore what definition is the most useful. The decay time will depend on the relative strength and speed of conduction and the opposing mechanisms of mutual and thermal diffusion as well as other factors such as the specific measurement technique and the size of the fluid cell. If the effective thermal conductivity decays quickly to the steady-state value, over the course of nanoseconds for example, then even in the transient hot wire setup, the steady-state thermal conductivity will be the most experimentally relevant. However, if the rate of decay of the thermal conductivity is slow relative to the timescale of the experiment, then other thermal conductivity definitions which include the effects of diffusion may be more appropriate.

Fig. 6.3 shows a comparison of the predictions of Eq. (6.2.20) for the binary helium-hydrogen mixture with experimental data which was previously shown in Fig. 3.4. The transport coefficients are calculated using Enskog theory at low density ($n = 10^{-8}$) using a hard sphere diameter ratio of $\sigma_{H_2}/\sigma_{He} = 289/260$ and mass ratio of $m_{H_2}/m_{He} = 1/2$. The He- H_2 diameter ratio is calculated using values of the kinetic diameter given in Ref. [7] which are estimated using diffusion measurements. In this case, λ predictions capture the form of the thermal conductivity measurements which lie outwith the series-

parallel bounds as well as the reported minimum which falls below the pure component helium thermal conductivity. Here, λ underpredicts the pure component hydrogen thermal conductivity suggesting that the He-H₂ diameter ratio used here and estimated using diffusion measurements is not appropriate for use when calculating the mixture thermal conductivity. Fig. 6.3 suggests that λ is a much more useful predictor of the mixture thermal conductivity than the series-parallel bounds. The experimental measurements reported in Fig. 6.3 used various measurement techniques including steady-state methods and transient methods such as the transient hot wire method suggesting that λ is a relevant definition of the thermal conductivity at relatively short times. However, it is not possible to make a firm statement regarding the exact timescale over which λ is relevant as the exact measurement times are not mentioned in the experimental studies.

6.3 Initial thermal conductivity λ_I

This section details a further definition of the thermal conductivity, similar to a definition given by Eapen [1], which gives the thermal conductivity at short times where there are no gradients in the concentration due to thermal diffusion but after gradients in the temperature are present. Consider the heat flux \mathbf{J}_q which is written as follows,

$$\mathbf{J}_q = - \sum_a L_{ua} T \nabla \left(\frac{\mu_a}{T} \right) - \frac{L_{uu}}{T} \nabla T. \quad (6.3.1)$$

Use is made of the thermodynamic relationship shown in Eq. (5.4.12) which allows a term which is proportional to the temperature gradient to be separated from the the concentration driving force. Applying Eq. (5.4.12) to Eq. (6.3.1) allows the heat flux to be written as,

$$\mathbf{J}_q = - \sum_a L_{ua} \left(\nabla \mu_a^0 - \frac{h_a}{T} \nabla T \right) - \frac{L_{uu}}{T} \nabla T, \quad (6.3.2)$$

where it is assumed that the derivative of the chemical potential at constant temperature is zero. In order to examine what this means in practice, the expression for the ideal gas chemical potential is shown here. It is given in Ref. [3] as follows,

$$\frac{\mu_a}{T} = \frac{3k_B}{2m_a} \ln(2\pi h^2) - \frac{3k_B}{2m_a} \ln(m_a) - \frac{5k_B}{2m_a} \ln(k_B T) + \frac{k_B}{m_a} \ln(x_a p), \quad (6.3.3)$$

where $2\pi h$ is Planck's constant. Inserting the ideal gas pressure expression $p = nk_B T$ allows the temperature dependence of the chemical potential to be extracted as

$$\frac{\mu_a}{T} = - \frac{3k_B}{2m_a} \ln(T) + \dots \quad (6.3.4)$$

Taking the derivative of Eq. (6.3.4) gives

$$T \nabla \left(\frac{\mu_a}{T} \right) = -\frac{3k_B}{2m_a} \nabla T + \dots = -\frac{h_a}{T} \nabla T + \dots, \quad (6.3.5)$$

where use has been made of the chain rule identity $\nabla \ln(T) = T^{-1} \nabla T$, and $h_a = 3k_B T / (2m_a)$ is the ideal gas partial specific enthalpy which coincides with Eq. (5.4.12). The extra terms which are not explicitly detailed correspond to those contained within the the constant temperature derivative term $\nabla_T \mu_a$ in Eq. (6.3.2). These consist of several constant terms which vanish when differentiated as well as one term which is a complex function of concentration. Assuming that $\nabla_T \mu_a = 0$, as in Eq. (6.3.2), therefore assumes that there is no species concentration gradient in the system, i.e. $\nabla x_a = 0$. The expression for the partial specific enthalpy in hard sphere systems is slightly different to the ideal gas case and is given in Ref. [3] as follows,

$$h_a = \frac{3k_B T}{2m_a} + p v_a, \quad (6.3.6)$$

where v_a is the specific volume of species a which can be written as follows,

$$v_a = \frac{\left(\frac{\partial p}{\partial m_a} \right)_{T,V}}{\left(\frac{\partial p}{\partial V} \right)_T}, \quad (6.3.7)$$

where V is the volume. It is possible to include the effects of pressure volume work on the hard-sphere enthalpy by approximating p and v_a using a hard-sphere equation of state. Grouping together terms in Eq. (6.3.2) allows the heat flux to be written as follows,

$$\mathbf{J}_q = -\frac{1}{T} \left(L_{uu} - \sum_a h_a L_{ua} \right) \nabla T, \quad (6.3.8)$$

which can be compared with Fourier's law to yield new definition of the thermal conductivity which is as follows,

$$\lambda_I = \frac{1}{T} \left(L_{uu} - \sum_a h_a L_{ua} \right). \quad (6.3.9)$$

Finally, for a binary mixture, Eq. (6.3.9) can be rewritten as follows,

$$\lambda_I = \frac{1}{T} (L_{uu} - (h_1 - h_2) L_{u1}), \quad (6.3.10)$$

by using the Onsager relation given in Eq. (6.2.9). As mentioned previously, this thermal conductivity definition applies when there is a temperature gradient in the system but no gradient in concentration and is referred to as the initial thermal conductivity throughout this thesis. This definition may have relevance for systems undergoing rapid changes in temperature where the temperature equilibrates rapidly relative to the concentration. In

such a system, a temperature gradient would become established, thus promoting heat transfer, but would reverse fast enough such that concentration gradients would not form. As heat transfer in real systems necessitates a temperature gradient, this definition may represent a value which is close to the maximum experimentally attainable mixture thermal conductivity.

If this thermal conductivity definition is relevant over experimental timescales, it may play a part in helping to explaining nanofluids studies which have reported systematic differences in the thermal conductivity when using different measuring techniques [8] even though individual measurement techniques had low uncertainties and were consistent with other measurements using the same technique. Large potential enhancements in the initial thermal conductivity λ_I could help to explain these systematic deviations as different thermal conductivity measurement techniques take place over different timescales and may access the enhanced initial value to different extents.

Fig. 6.2 and Fig. 6.3 demonstrate that it is possible for the phenomenological as well as the steady-state thermal conductivity of hard-sphere mixtures to lie outwith the series-parallel bounds. The following chapters further investigate these phenomena in an effort to determine which other hard-sphere mixtures, as well as real mixtures, display this “anomalous” behaviour.

References

- [1] J. Eapen et al. “The Classical Nature of Thermal Conduction in Nanofluids”. In: *J. Heat Transfer* 132 (2010), p. 102402.
- [2] S. Bastea. “Transport in a highly asymmetric binary fluid mixture”. In: *Phys. Rev. E* 75 (2007), p. 031201.
- [3] J. J. Erpenbeck. “Transport-coefficients of hard-sphere mixtures theory and Monte-Carlo molecular-dynamics calculations for an isotopic mixture”. In: *Phys. Rev. A* 39.9 (1989), pp. 4718–4731.
- [4] S. R. de Groot and P. Mazur. *Non-Equilibrium Thermodynamics*. Dover, 1984.
- [5] A. Ben-Israel and T. N. E. Greville. *Generalized inverses: theory and applications*. 2nd ed. Springer, 2003.
- [6] J. Healy, J. Groot, and J. Kestin. “The Theory of the Transient Hot-Wire Method for Measuring Thermal Conductivity”. In: *Physica* (1975).
- [7] B. D. Freeman. “Basis of Permeability/Selectivity Tradeoff Relations in Polymeric Gas Separation Membranes”. In: *Macromolecules* 32 (1999), pp. 375–380.
- [8] J. Buongiorno et al. “A benchmark study on the thermal conductivity of nanofluids”. English. In: *J. Appl. Phys.* 106 (2009), p. 094312.

INVESTIGATING ANOMALOUS THERMAL CONDUCTIVITY DEHANCEMENT

This chapter has been published as a Rapid Communication in Physical Review E (see Appendix C). Authors: Craig Moir, Leo Lue, Julian D. Gale, Paolo Raiteri, and Marcus N. Bannerman

A small number of nanofluid experimental results remain outside the classical continuum bounds, such as the reported *dehancements* below the series limit for fullerene-water suspensions reported by Ref. [1] and shown in Fig. 3.6. Hence, the question still remains; are results outside these bounds correct and, if so, what are the underlying mechanisms? Ch. 3 presents several physical mechanisms which have been proposed in an effort to rationalise the behaviour of these systems; however, there is as-yet no unifying framework for predicting/explaining the thermal performance of nanofluid mixtures. Some of the confusion in interpreting thermal conductivity arises from the different manners in which it can be defined. The most natural macroscopic/experimental definition arises from applying a temperature gradient, ∇T , across a system and measuring the resultant heat flux, \mathbf{J}_q . The “observed” non-equilibrium thermal conductivity λ_N is then defined through the following expression,

$$\langle \mathbf{J}_q \rangle = -\lambda_N \nabla T, \quad (7.0.1)$$

where the brackets $\langle \dots \rangle$ indicate the implicit averaging over time and volume this approach entails. The first hurdle of this chapter is to establish that the macroscopic (λ_N) and microscopic (λ) definitions of the thermal conductivity are equivalent at steady state.

The definition of the steady-state thermal conductivity λ presented in Eq. (6.2.20) is distinct from λ_N as it is not averaged over the non-equilibrium conditions of a system undergoing conduction but is instead evaluated at a single temperature, concentration, and density. Fig. 6.3 demonstrates that the steady-state thermal conductivity of hard-sphere mixtures can not only lie outside the series and parallel bounds set by their pure component values, but can lie beyond even the pure component fluid values which is in agreement with experimental measurements of the helium-hydrogen gas mixture. This chapter presents results from Enskog theory as well as equilibrium and non-equilibrium

MD simulations which further investigate potential anomalous behaviour in the steady-state thermal conductivity for binary hard-sphere fluids. The MD simulations verify that Enskog theory can accurately predict non-equilibrium thermal conductivities at low densities and this theory is applied to explore the model parameter space. Only certain mass and size ratios are found to exhibit conductivity enhancements above the parallel bounds and dehancement below the series bounds. It is demonstrated that thermal conductivities outside the series/parallel bounds are a fundamental feature of even simple fluids.

In principle, atomistic NEMD simulations can be used to directly measure the heat flux \mathbf{J}_q through a system's boundaries to obtain the “observed” non-equilibrium thermal conductivity, λ_N . Equilibrium simulations can then be used to measure λ for comparison, as well as to elucidate any underlying mechanisms behind “anomalous” behavior. Unfortunately, large and long-duration non-equilibrium simulations are required to directly study heat conduction in nanofluids [2], and so only a limited range of molecular models and techniques are computationally accessible using this method. Due to these limitations, previous simulation work has primarily focused on equilibrium simulations of nanofluids at fixed size and mass asymmetries between the fluid molecule and nanoparticle [3–8] with only a few studies at larger asymmetries (e.g., [9, 10]). As equilibrium molecular simulations are conducted at a single temperature and concentration, Eq. 7.0.1 cannot be used, thus the equivalence between λ_N and λ cannot be conclusively established.

NEMD simulations of binary hard-sphere mixtures, consisting of spheres of diameter σ_1 and mass m_1 and spheres of diameter σ_2 and mass m_2 , confined between two smooth parallel walls (see Fig. 7.1) are performed using DynamO [11]. Although the hard-sphere model is simple, it qualitatively captures the fundamental effects of density, molecular size, and mass on the transport coefficients in gases [9]. This paper explores conditions close to the ideal gas limit for simplicity (and to avoid crystallisation as σ_2/σ_1 becomes large); however, the results obtained in this limit are fundamental to the behaviour of all fluids and comparison against experiments on gas mixtures can be made.

The first aim of this work is to establish an equivalence of the observed, λ_N , and steady-state, λ , thermal conductivities. This is conducted using a hard-sphere mass ratio of $m_2/m_1 = 2$ corresponding to a He-H₂ mixture with the approximate size ratio $\sigma_2/\sigma_1 = 260/289$, obtained from diffusion measurements [12]. A constant reduced pressure of $p\sigma_1^3/(k_B T) = 0.01$ (where k_B is the Boltzmann constant) is used and is set by adjusting the system density. This reduced pressure value corresponds to a packing fraction of approximately 0.005 over the studied mol fraction, x_2 . Once the equivalence of λ and λ_N is confirmed in this system, a systematic exploration for “anomalous” thermal conductivities is carried out over the mass and size ratio parameter space using kinetic theory.

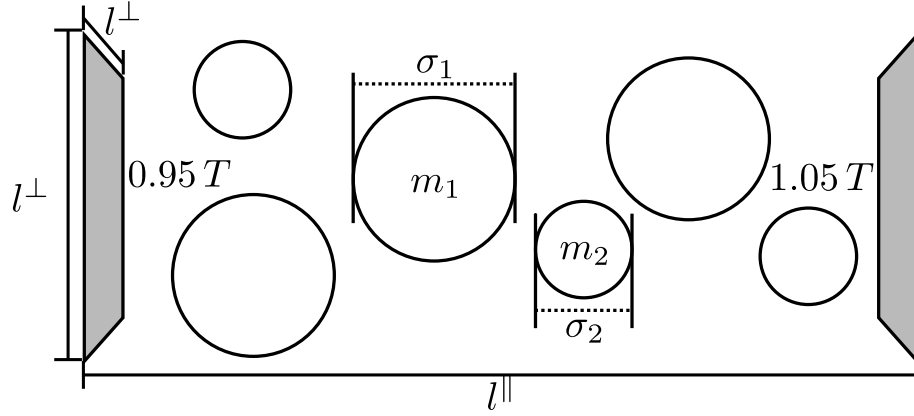


Figure 7.1: A schematic of the system configuration used for the simulations reported here which use a hard-sphere model consisting of two species with diameters σ_1 and σ_2 , and masses m_1 and m_2 respectively. For NEMD simulations, two walls are inserted into the simulation and a 10% temperature gradient is imposed via velocity reassignment on collision with the wall [13]. The total number of spheres N and aspect ratio l^{\parallel}/l^{\perp} of the simulation are varied to explore the effects of system size at a constant density/pressure.

7.1 Simulation method

Parallel smooth walls are located at both ends of the simulation domain as illustrated in Fig. 7.1 with periodic conditions on all other boundaries. On collision with the wall, the normal component of a sphere's velocity is reassigned to a Maxwell-Boltzmann distribution [13] at a defined temperature. The heat flux is then measured through the following expression, $\langle \mathbf{J}_q \rangle = \langle Q \rangle l^{\parallel} / (l^{\perp})^2$, where $\langle Q \rangle$ is the time-averaged rate of energy transferred to the simulation during sphere impacts with the walls averaged over both walls. This equation for the heat flux is identical to Eq. (4.3.2); here, instead of defining the simulation lengths in terms of the three spacial dimension (L_x , L_y , and L_z), the lengths are defined in terms of whether they are parallel (l^{\parallel}) or perpendicular (l^{\perp}) to the direction of heat flux. The two walls have different temperatures set to 95% and 105% of the system temperature T . This value is a trade-off between inducing a sufficiently large heat flux (compared to thermal fluctuations) and inducing unwanted inhomogeneity in the system.

An example of the inhomogeneity induced by the heat flux is given in Fig. 7.2. The temperature, number density, and concentration plots appear approximately linear. It is clear to see the effects of thermophoresis in the concentration profiles. These inhomogeneities make equating λ_N and λ suspicious as λ is only evaluated at a single representative concentration, temperature, and density, whereas NEMD simulations measure an average thermal conductivity across the system as temperature, density, and concentration varies. Boundary layers with high thermal resistance also exist very close to the heated walls and induce a significant system-size dependence in the NEMD results.

To explore this system-size dependence, the wall temperatures are held fixed while the aspect ratio l^{\parallel}/l^{\perp} and system size are varied with the number of spheres ranging from $N = 5000$ up to $N = 102400$. Each simulation is initialised in an FCC crystal lattice and

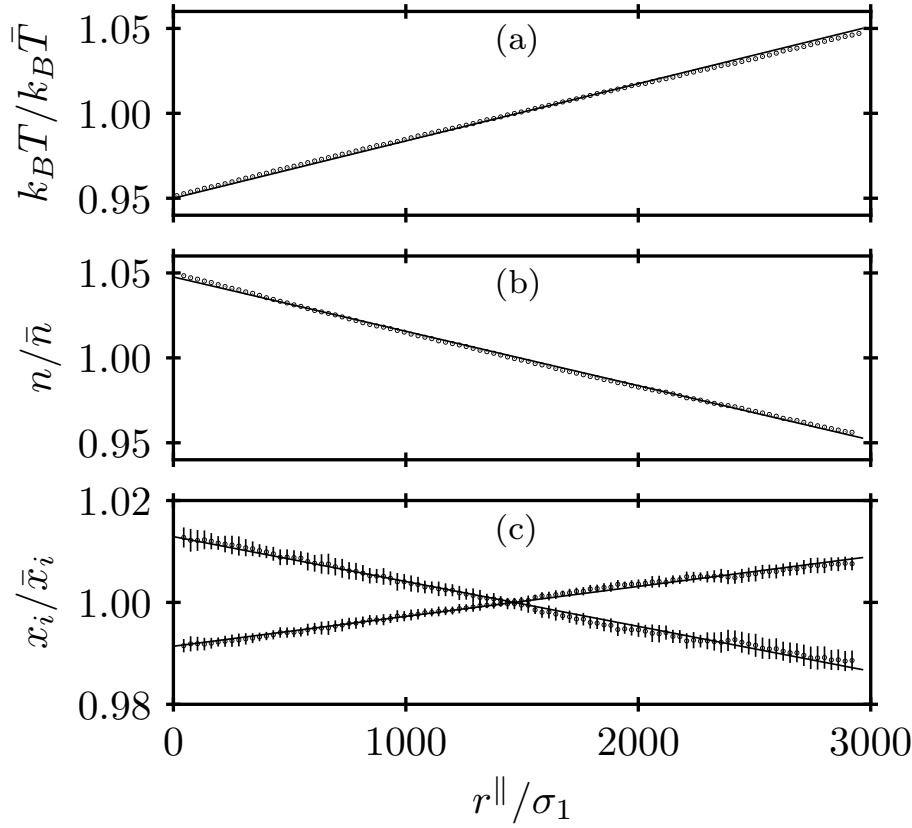


Figure 7.2: The profiles of (a) temperature, $k_B T$, (b) number density, n , and (c) species mol fraction, x_a , as a function of distance between the two heated walls, r^{\parallel} for a single representative simulation. This system has a mass ratio of $m_2/m_1 = 2$, a size ratio of $\sigma_2/\sigma_1 = 0.899654$, $N = 102400$ spheres, and an aspect ratio of $l^{\parallel}/l^{\perp} = 50$. All values are reduced by the average values for the system, which are $k_B \bar{T} = 1$, $\bar{n} \approx p \sigma_1^3 / (k_B T) = 0.01$, and $(1 - \bar{x}_1) = \bar{x}_2 = 0.6$. Error bars represent the standard deviation across 10 simulations and are smaller than the marker size for the temperature and number density fields. Solid lines are linear fits provided as a guide to the eye.

equilibrated for 1000 N collisions before a further production run of 10000 N collisions to collect data. This procedure is repeated ten times at each state point and average values between the production runs are collected while the errors of the average measurements are estimated using the standard deviation of values between each production run.

7.2 Enskog theory comparison with MD

A system-size dependence calculation for the mol fraction, $x_2 = 0.8$, in the He-H₂ system is reported in Fig. 7.3. The figure demonstrates that the aspect ratio of a system is relatively unimportant and that the system length in the direction of conduction, l^{\parallel} , dominates the system-size effects (due to the boundary layer resistance near the walls). To estimate the infinite system-size (near-zero thermal gradient) value of the thermal conductivity, linear extrapolation is applied to systems with the three largest aspect ratios ($l^{\parallel}/l^{\perp} = 10, 25$, and 50). This procedure yields a lower-bound for the thermal conduc-

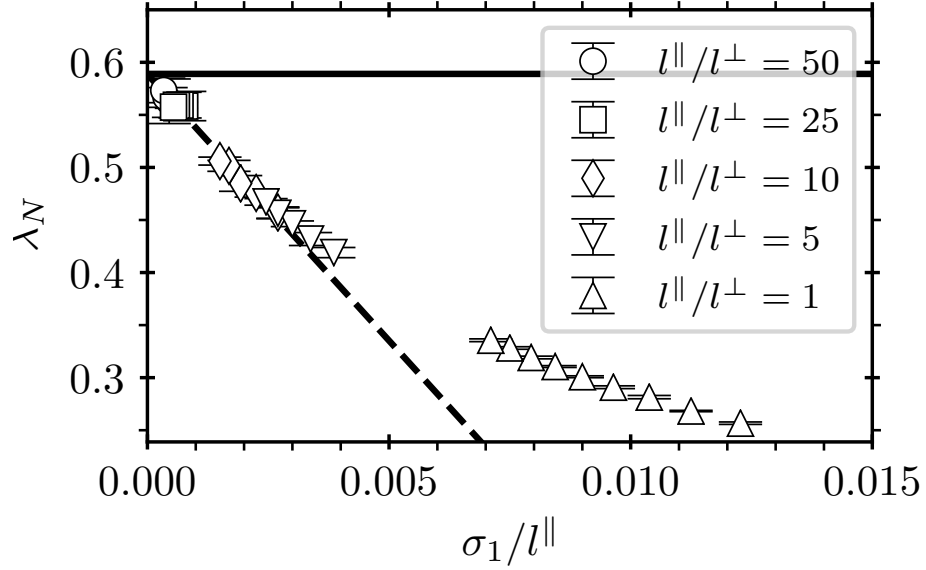


Figure 7.3: The observed thermal conductivity λ_N obtained from NEMD simulations as a function of the distance between the walls σ_1/l^{\parallel} from binary hard-sphere systems with varying numbers of spheres and aspect ratios at a mol fraction of $x_2 = 0.8$ for a $m_2/m_1 = 2$, $\sigma_2/\sigma_1 = 0.899654$, and $p\sigma_1^3/(k_B T) = 0.01$. A linear fit to the data points obtained using an aspect ratio of 10, 25, and 50 (dashed line) is used to extrapolate to infinite system size and approaches the value of λ predicted by Enskog theory (solid line).

tivity as the gradient of the system-size dependence monotonically increases with system size. The extrapolated λ_N value is in excellent agreement with the equilibrium thermal conductivity λ from Enskog theory evaluated at the average conditions of the system.

The above procedure is repeated over a range of mol fractions and the final infinite-system extrapolated results are reported in Fig. 7.4. This system exhibits thermal conductivities that are far outside the predictions of classical approaches such as Maxwell theory or the limits of series and parallel resistance. In accordance with the experimental results for He-H₂ [14–16], the system displays a minimum in the thermal conductivity below both the pure fluid thermal conductivities. This conclusively demonstrates that “anomalous” thermal conductivities are not only possible but a fundamental feature of simple molecular fluids such as the binary hard-sphere gas.

To further validate the Enskog and NEMD results, equilibrium simulations with $N = 32000$ spheres in a cubic system are equilibrated for 1000 N events before being run for a further 100000 N events to calculate L_{uu} , L_{u1} , and L_{11} for this system. The Einstein form of the Green-Kubo relations [17, 18] is used with the first 15 mean free times of the correlation discarded to avoid ballistic motion and a maximum correlation time of 50 mean free times used to avoid correlations from the periodic boundary conditions. This is beyond the sound wave traversal time of the system; however, as the density is so low, correlations from the boundary conditions take much longer to establish than in higher density systems. The excellent agreement in Fig. 7.4 between Enskog theory and equilibrium MD completes the verification of the anomalous deenhancement reported and

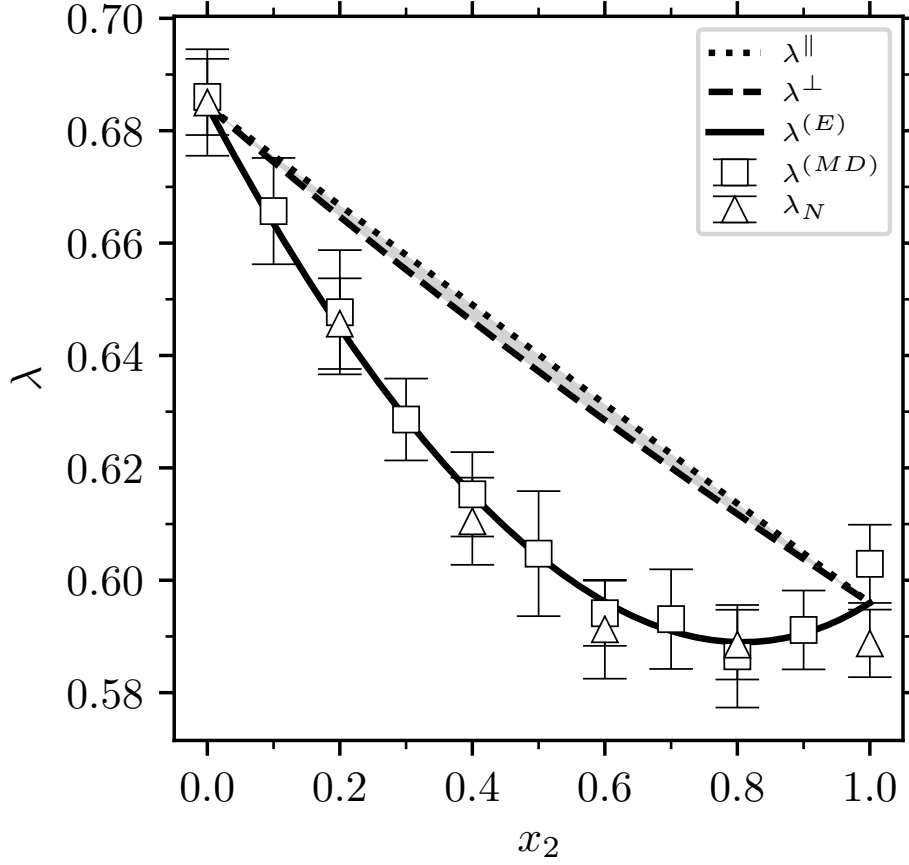


Figure 7.4: The extrapolated infinite system-size NEMD, λ_N , (triangles) and equilibrium steady-state, $\lambda^{(MD)}$, (square) thermal conductivities as a function of the non-unit species mol fraction x_2 . Parallel (dotted line) and series (dashed line) limits bound the region of classical/continuum values (shaded). The Enskog theory predictions for the steady-state conductivity, $\lambda^{(E)}$, (solid line) are in excellent agreement with the simulation results. A slight apparent overestimation arises from the remaining system-size dependence of our NEMD results.

the use of Enskog theory to further study hard-sphere systems at low densities.

7.3 Mapping the dehancement

The full parameter space of the binary hard-sphere model is explored using Enskog theory to determine the extent of the anomalous behavior. Fig. 7.5 maps the maximum possible departure from the series or parallel bounds achievable by varying the mol fraction of the system for a particular mass and size ratio. A reduced pressure of $p\sigma_1^3/(k_B T) = 10^{-7}$, corresponding to packing fractions below 0.044 for this parameter space, is used in these calculations to reveal the symmetry of the map in the ideal gas limit which is otherwise prevented by pure species 2 freezing (which occurs at a size ratio of $\sigma_2/\sigma_1 \gtrsim 4.87$ for $p\sigma_1^3/(k_B T) = 0.01$; however, this change makes little difference to the results below this boundary). Anomalous enhancement above the parallel bounds is found at extreme mass-ratios with size-ratios near unity. Reductions below the series bounds are

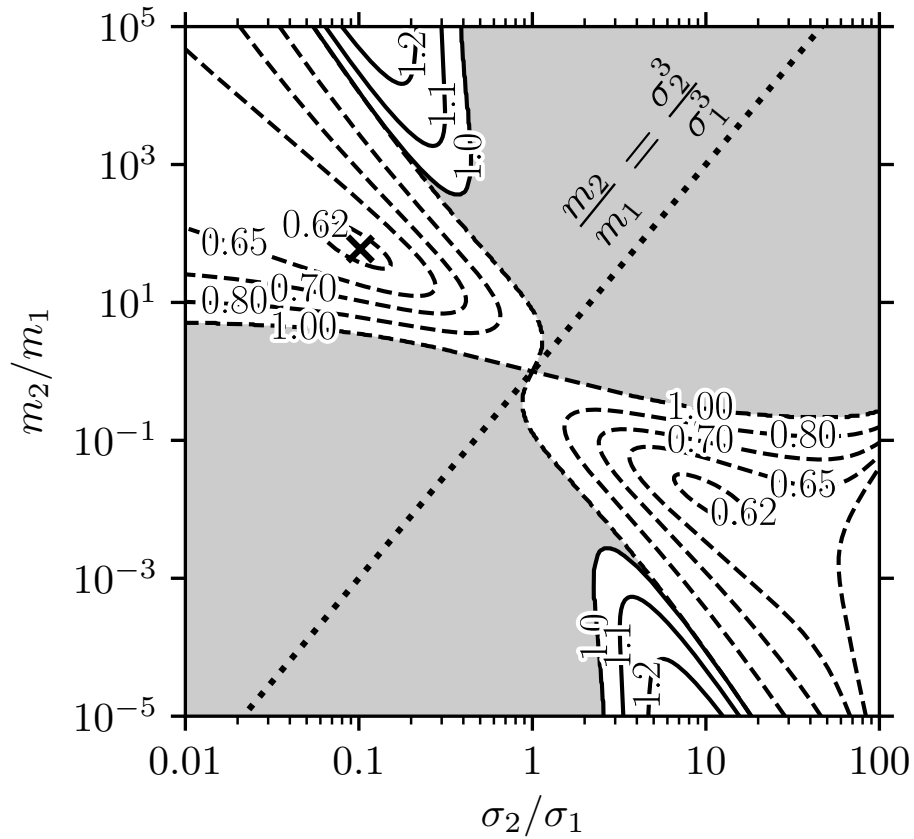


Figure 7.5: A contour map of steady-state thermal conductivities outside the series (dashed) and parallel (solid) bounds as a function of mass and size ratio. The contours denote the increase/decrease of the thermal conductivity relative to the parallel/series bound at the concentration of maximum deviation. A cross indicates the maximum decrease of the steady-state thermal conductivity which occurs at $m_2/m_1 \approx 59.6$ and $\sigma_2/\sigma_1 \approx 0.102$. A dotted line indicates where mass scales with molecular volume, assuming a constant density.

also found for smaller but heavier spheres. Surprisingly, a maximum achievable reduction in thermal conductivity is found which is $\approx 40\%$ below the series limit (see the cross in Fig. 7.5). The bulk of the anomalous parameter space lies in the larger-but-lighter region of the map; however, the region of anomalous reduction approaches the line where the species 2 mass scales with its volume which is the experimentally relevant region.

To explore the experimental relevance of the results, the kinetic diameter and molecular mass ratios for combinations of the noble gases, along with nitrogen and hydrogen gas, are plotted in Fig. 7.6. The map indicates that several real mixtures may exhibit anomalous dehancements; however, care should be taken to verify this as the Enskog theory expressions used here do not take into account the additional degrees of freedom of diatomic gases and in general are not capable of quantitatively predicting the behaviour of real gases, only general trends. It is expected that more complex molecules can exhibit more extreme effective size and mass ratios, although the anomalous enhancement region probably remains inaccessible and the applicability of the hard-sphere model is dubious in this limit.

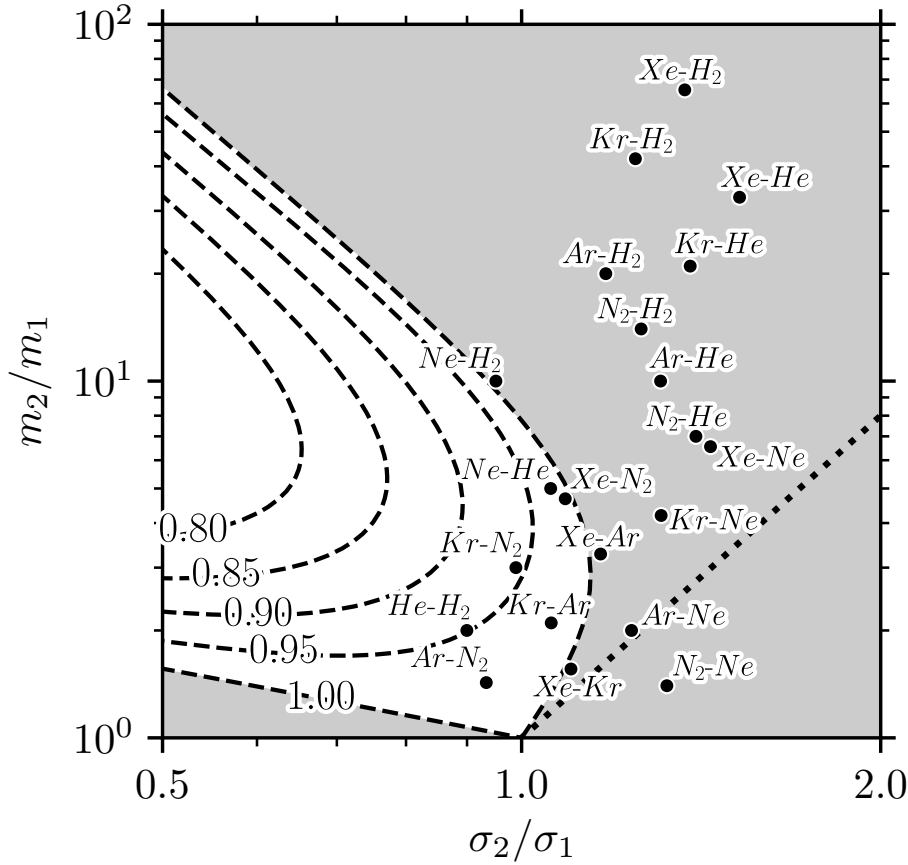


Figure 7.6: As described in Fig. 7.5 but focused on the parameter space relevant for the noble gases, hydrogen, and nitrogen. Kinetic diameters are taken from Ref. [19–21]

7.4 Conclusions and future work

This chapter examines the thermal conductivity of a binary hard-sphere mixture with hard-sphere parameters corresponding to the helium-hydrogen gas mixture. The thermal conductivity is measured using 3 techniques: NEMD simulation using the parallel heated walls method, equilibrium MD, and Enskog theory. The methods are found to be in strong agreement with each other. It is possible for the observed thermal conductivity of binary hard-spheres to exhibit values which lie outside the limits of series-parallel resistance, in agreement with experimental results on He-H₂ systems. These “anomalous” results are present even in the ideal gas limit, which implies that they cannot be explained by any structural/clustering effect such as those which are prevalent in the nanofluid literature. To better understand results in nanofluids, liquid densities can be explored using the techniques outlined here; however, the binary hard-sphere model has two serious shortcomings: an ideal-gas heat capacity and the absence of a gas-liquid transition. Future work should explore adding internal degrees of freedom to the spheres to account for varying heat capacity which will allow a better parameterisation of real fluids. Attractive systems, such as square-wells, may also be used to explore liquid systems which do not have strong density-pressure dependencies, and the comparison at pressures where the nanoparticle forms a crystalline phase should be explored.

References

- [1] Y. Hwang et al. “Stability and thermal conductivity characteristics of nanofluids”. In: *Thermochim. Acta* 455 (2007), pp. 70–74.
- [2] J. Armstrong and F. Bresme. “Thermal conductivity of highly asymmetric binary mixtures: how important are heat/mass coupling effects?” In: *Phys. Chem. Chem. Phys.* 16.24 (2014), p. 12307.
- [3] J. J. Erpenbeck. “Transport-coefficients of hard-sphere mixtures theory and Monte-Carlo molecular-dynamics calculations for an isotopic mixture”. In: *Phys. Rev. A* 39.9 (1989), pp. 4718–4731.
- [4] J. J. Erpenbeck. “Transport-coefficients of hard-sphere mixtures. 2. Diameter ratio 0.4 and mass ratio 0.03 at low-density”. In: *Phys. Rev. A* 45.4 (1992), pp. 2298–2307.
- [5] J. J. Erpenbeck. “Transport-coefficients of hard-sphere mixtures. 3. Diameter ratio 0.4 and mass-ratio 0.03 at high fluid density”. In: *Phys. Rev. E* 48.1 (1993), pp. 223–232.
- [6] D. M. Heyes. “Molecular dynamics simulations of liquid binary mixtures: Partial properties of mixing and transport coefficients”. In: *J. Chem. Phys.* 96.3 (1992), pp. 2217–2227.
- [7] J. Eapen, J. Li, and S. Yip. “Mechanism of Thermal Transport in Dilute Nanocolloids”. In: *Phys. Rev. Lett.* 98.2, 028302 (2007), p. 028302.
- [8] N. A. T. Miller et al. “Computation of thermodynamic and transport properties to predict thermophoretic effects in an argon-krypton mixture”. In: *J. Chem. Phys.* 139.14 (2013), p. 144504.
- [9] M. N. Bannerman and L. Lue. “Transport properties of highly asymmetric hard-sphere mixtures”. In: *J. Chem. Phys.* 130.16, 164507 (2009), p. 164507.
- [10] S. Bastea. “Transport in a highly asymmetric binary fluid mixture”. In: *Phys. Rev. E* 75 (2007), p. 031201.
- [11] M. N. Bannerman, R. Sargant, and L. Lue. “DynamO: a free $\mathcal{O}(N)$ general event-driven molecular dynamics simulator”. In: *J. Comput. Chem.* 32.15 (2011), pp. 3329–3338.
- [12] B. D. Freeman. “Basis of Permeability/Selectivity Tradeoff Relations in Polymeric Gas Separation Membranes”. In: *Macromolecules* 32 (1999), pp. 375–380.
- [13] T. Pöschel and T. Schwager. *Computational Granular Dynamics*. New York: Springer, 2005.
- [14] P. Mukhopadhyay and A. K. Barua. “Thermal conductivity of hydrogen-helium gas mixtures”. In: *J. Appl. Phys.* 18.5 (1967), p. 635.

- [15] L. Biolsi and E. A. Mason. “On the Existence of Minima and Maxima in the Composition Dependence of the Thermal Diffusion Factor and Thermal Conductivity”. In: *J. Chem. Phys.* 54.7 (1971), pp. 3020–3022.
- [16] A. G. Shashkov, F. P. Kamchatov, and T. N. Abramenko. “Thermal conductivity of the hydrogen-helium mixture”. In: *J. Eng. Phys.* 24.4 (1973), pp. 461–464.
- [17] M. S. Green. “Markoff Random Processes and the Statistical Mechanics of Time-Dependent Phenomena. II. Irreversible Processes in Fluids”. In: *J. Chem. Phys.* 22.3 (1954), pp. 398–413.
- [18] R. Kubo. “Statistical-Mechanical Theory of Irreversible Processes. I. General Theory and Simple Applications to Magnetic and Conduction Problems”. In: *J. Phys. Soc. Jpn.* 12.6 (1957), pp. 570–586.
- [19] D. W. Breck. *Zeolite Molecular Sieves: Structure, Chemistry, and Use*. New York: Wiley, 1973.
- [20] A. F. Ismail, K. Khulbe, and T. Matsuura. *Gas Separation Membranes*. New York: Springer, 2015.
- [21] S. Matteucci et al. “Materials Science of Membranes for Gas and Vapor Separation”. In: Wiley, 2006. Chap. Transport of Gases and Vapors in Glassy and Rubbery Polymers.

INVESTIGATING ANOMALOUS THERMAL CONDUCTIVITY ENHANCEMENT

In Ch. 7 it is demonstrated that it is possible for the steady-state thermal conductivity λ of binary hard-sphere fluids to exhibit values which lie outwith (both above and below) the series-parallel limits. The chapter concluded by mapping the maximum potential thermal conductivity enhancement over the hard-sphere mixture mass and diameter ratio parameter space. Proceeding on from the steady-state thermal conductivity, this chapter will focus on the transient thermal conductivity enhancement which is possible in binary hard-sphere mixtures. As discussed in Ch. 6, at the onset of heat transfer the combination of the effects of thermophoresis and conventional thermal conduction leads to a temporary increase in the effective thermal conductivity which will decay to the steady-state value as the temperature driving force behind thermal diffusion is eventually balanced by the resulting concentration driving force.

The chapter investigates the behaviour of the initial thermal conductivity λ_I in binary hard-sphere systems, which is given in Eq. (6.3.10), and maps out the area in hard-sphere mixture parameter space where the greatest potential enhancement above the parallel thermal conductivity limit is possible. This chapter will also map the potential increase in the initial thermal conductivity relative to the steady-state value. This will show the locations in hard-sphere mixture parameter space where the maximum potential percentage decrease in the thermal conductivity is predicted to occur over the course of the decay from the initial value at the onset of heat transfer $t \rightarrow 0$ to the steady-state value $t \rightarrow \infty$. This is the most relevant graph if the intent were to create a real world heat-transfer device which attempted to exploit this transient thermal conductivity increase by “switching” from a highly conductive heat transfer medium to a relatively insulating medium, by potentially reversing the direction of the temperature gradient. This map also shows which material mixtures would potentially be most useful when attempting to measure and detect this transient thermal conductivity increase owing to large relative enhancements in the conductivity. This chapter will also show the mixture concentrations at which the maximum thermal conductivity enhancements occur.

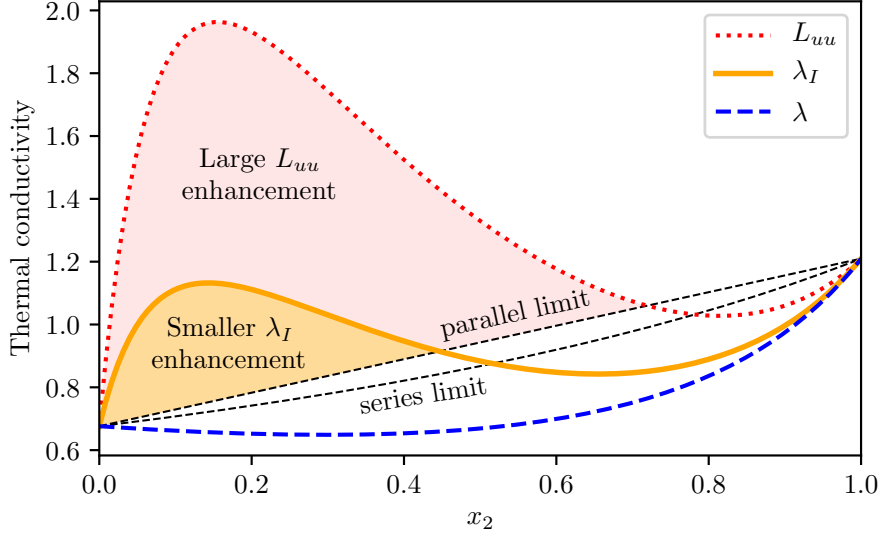


Figure 8.1: Thermal conductivity as a function of mixture mol fraction for a binary hard-sphere mixture with a mass ratio of $m_2/m_1 = 5$ and a diameter ratio of $\sigma_2/\sigma_1 = 0.5$. These results assume a reduced number density of $n\sigma_1^3 = 10^{-8}$. The Enskog theory predictions of the phenomenological thermal conductivity L_{uu} (red dotted line), the initial thermal conductivity λ_I (solid orange line), as well as the steady-state thermal conductivity λ (dashed blue line) are shown. The series-parallel thermal conductivity limits are represented by the dashed black lines.

8.1 Initial thermal conductivity enhancement

A graph of the thermal conductivity of a binary hard-sphere system (predicted by Enskog theory) as a function of mixture concentration is shown in Fig. 8.1 highlighting the potential enhancement above the upper parallel thermal conductivity limit which is possible in hard-sphere systems. The mixture showcased in this graph has a mass and size ratio of $m_2/m_1 = 5$ and $\sigma_2/\sigma_1 = 0.5$ respectively. For this particular system, the steady-state thermal conductivity is below the series conductivity limit over the entire mixture concentration space. The initial and phenomenological values also exhibit values which are below the series bound; however, for certain concentrations, these values are significantly above the parallel limit. The maximum enhancement of phenomenological value relative to the parallel limit (L_{uu}/k^{\parallel}) is larger than the maximum enhancement of the initial thermal conductivity λ_I/k^{\parallel} . This is expected, as discussed in Ch. 6, as the initial thermal conductivity assumes that there is no concentration gradients in the system. The peak enhancement for both definitions of the thermal conductivity occur at $x_2 \approx 0.15$.

Fig. 8.2 maps the maximum enhancement of the initial thermal conductivity above the parallel limit $(\lambda_I/k^{\parallel})_{\max}$ for binary mixtures over varying mass ratios m_2/m_1 and size ratios σ_2/σ_1 . The value of the initial thermal conductivities are calculated via Enskog theory using the corresponding mass and size ratios and assuming a reduced number density of $n\sigma_1^3 = 10^{-8}$. The graph is not rotationally symmetric as the inverse mass and size ratios are not equivalent. For example, a binary mixture of spheres with $\sigma_1 = 1$ and $\sigma_2 = 0.01$

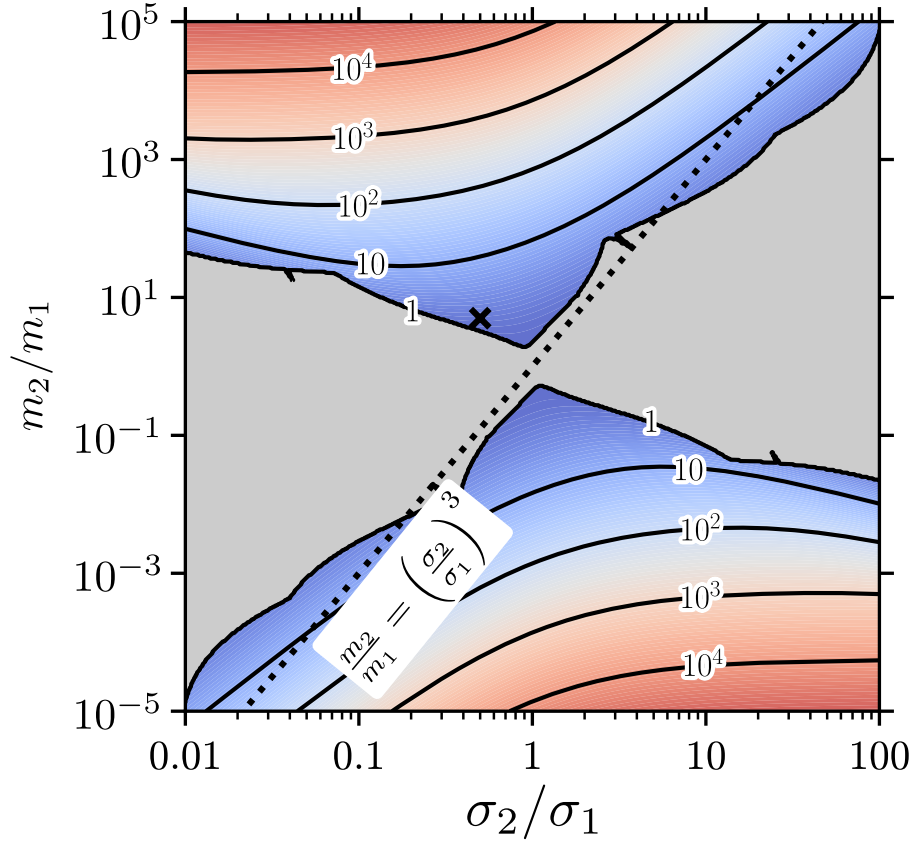


Figure 8.2: A contour map showing the maximum initial thermal conductivity enhancement above the parallel limit as a function of the hard-sphere mass m_2/m_1 and diameter σ_2/σ_1 ratio. The contours represent the maximum value of the initial thermal conductivity relative to the parallel mode thermal conductivity $(\lambda_I(x_2)/k^{\parallel}(x_2))_{\max}$ at the corresponding mixture concentration. The dotted line indicates where mass scales with hard-sphere volume assuming a constant particle density. The shaded grey area shows where no enhancement above the parallel thermal conductivity limit is possible. A black cross represents the state point corresponding to Fig. 8.1.

($\sigma_2/\sigma_1 = 0.01$) has a lower packing fraction than a mixture with $\sigma_1 = 1$ and $\sigma_2 = 100$ ($\sigma_2/\sigma_1 = 100$). However, the low number density means that maximum packing fraction for this parameter space is approximately 0.005 which is well below the liquid-solid transition point of approximately 0.5 meaning that Enskog theory remains applicable. Enskog theory is solved here using 3rd order Sonine polynomials. The dotted line represents the points on the map where the mass ratio scales as the cube of the diameter ratio as would be intuitively expected from a real-life composite particle which has a constant density. The values plotted on the graph represent the maximum value of λ_I/k^{\parallel} as a function of mixture concentration for a given mass and size ratio (corresponding to approximately $x_2 = 0.15$ in Fig. 8.1).

Enskog theory predicts that no enhancement of λ_I above the parallel thermal conductivity limit is possible when both hard-sphere masses are approximately equal ($m_2/m_1 \approx 1$). This is true for all hard-sphere diameter ratios examined here. As the diameter ratio approaches unity ($\sigma_2/\sigma_1 \rightarrow 1$), a smaller mass ratio is required in order to begin to see a

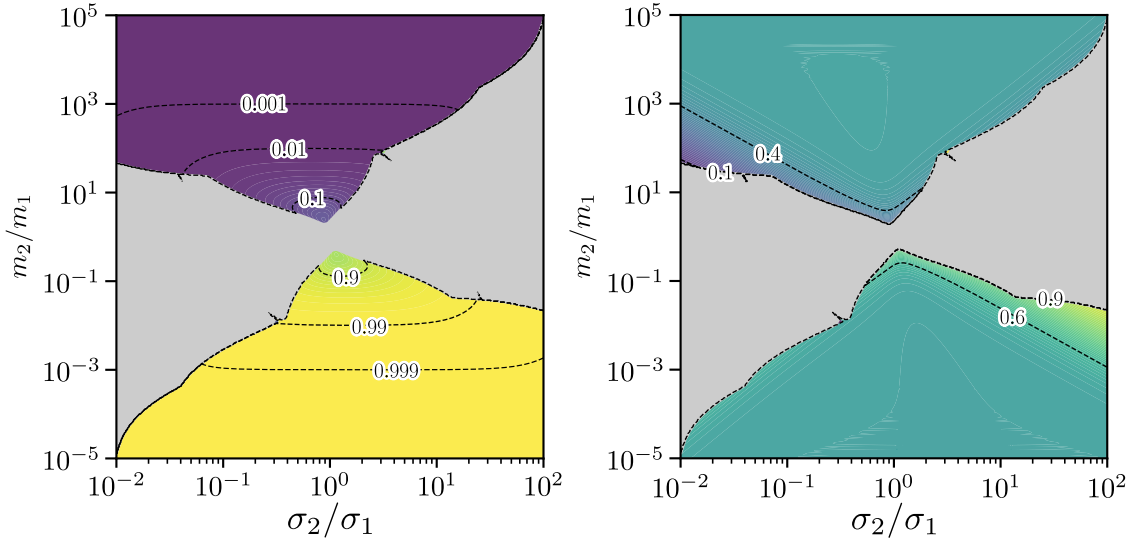


Figure 8.3: A contour map showing the mixture mol fraction x_2 which corresponds to the maximum initial thermal conductivity enhancement above the parallel limit $(\lambda_I(x_2)/k^\parallel(x_2))_{\max}$ as a function of the hard-sphere mass m_2/m_1 and diameter σ_2/σ_1 ratio. The shaded grey area shows where no enhancement above the parallel thermal conductivity limit is possible.

thermal conductivity enhancement. As the hard-sphere mass ratio deviates from unity the potential initial thermal conductivity enhancement increases. The dotted line representing constant density scaling of the hard-sphere mass shows that enhancement above the parallel limit is possible for particles following this rule at a mass and diameter ratio of $m_2/m_1 = (\sigma_2/\sigma_1)^3 \approx 100$. There does not appear to be a limit to the theoretical thermal conductivity enhancement which is possible in binary hard-sphere mixtures with increasingly large mass ratios. However, in reality there is obviously a limit to the possible mass ratio of different particles in fluid mixtures.

The maximum initial thermal conductivity enhancement values which are shown in Fig. 8.2 occur at varying mixture concentrations throughout the mass and diameter ratio parameter space. Fig. 8.3 shows the hard-sphere mixture mol fraction (left) at which the maximum thermal conductivity enhancement occurs in Fig. 8.2. Near a unity mass ratio $m_2/m_1 \approx 1$, the mixture mol fraction corresponding to the maximum initial thermal conductivity enhancement is approximately $x_2 = 0.5$. As the mass ratio increases, the mol fraction of the heavier ($m_2/m_1 > 1$) species drops to very small concentrations. The inverse behaviour is reflected in the graph and as at the hard-sphere mass ratio decreases $m_2/m_1 < 1$ where the mol fraction of the lighter species increases as the mass ratio decreases. Upon inspection, this behaviour corresponds to the fact that, where a maximum is present in L_{uu} above the pure species values, this maximum occurs at a mass fraction of $w_1 = w_2 = 0.5$. This is demonstrated in Fig. 8.3(right) which shows that, in general, the maximum initial thermal conductivity enhancement occurs at a mass of fraction of 0.5. The only exception to this appears to be in cases near to the boundary where enhancements of λ_I begin to appear ($\lambda_I/k^\parallel = 1$). Here, the value of the mass fraction corresponding to

the maximum enhancement deviates slightly from 0.5.

8.2 Enhancement relative to the steady-state value

Looking at the thermal conductivity enhancement relative to the series-parallel limits is helpful in identifying interesting effects which may not be intuitively expected from a mixture. However, it has been established in this chapter, as well as Ch. 7, that although the initial and steady-state hard-sphere thermal conductivities remain within the series-parallel bounds over large swathes of the binary mixture parameter space, the series and parallel limits can both be easily broken and have no bearing on thermal conductivity in mixtures. The thermal conductivity enhancement which is most relevant is not the enhancement relative to the series-parallel thermal conductivity limits, but the enhancement relative to the corresponding steady-state thermal conductivity for a given mixture.

The goal of this section is to characterise the initial thermal conductivity enhancement above the parallel conductivity limit for a range of hard-sphere gas mixtures. This will inform material choice when attempting to experimentally study transient thermal conductivity enhancement in the future, or create a heat transfer device which attempts to exploit this enhancement. A theoretical heat transfer device may seek to exploit the short-term transient thermal conductivity increase for a one-time, quick transfer of heat before leaving the fluid to reach steady-state, therefore lowering the thermal conductivity. Extending this concept, a device may seek to alter the geometry of the system, or otherwise reverse the direction of heat transfer, in order to maintain a small concentration gradient and facilitate the maximum amount of thermal diffusion. Such a process could dynamically change the thermal conductivity by halting the oscillation of the heat transfer direction and allowing thermal diffusion to complete, thus letting the mixture reach steady state.

Fig. 8.4 shows the maximum enhancement in the initial thermal conductivity relative to the steady-state thermal conductivity over the binary hard-sphere mass and diameter ratio parameter space. The initial and steady-state thermal conductivities are calculated via Enskog theory using a 3rd order Sonine polynomial. The graph shows that, like in Fig. 8.2, as the hard-sphere mass ratio deviates from unity the potential enhancement increases and as the diameter of the heavier species increases, the maximum possible enhancement decreases. This rate of decrease is small when the diameter of the heavier species is small relative to the lighter species, but accelerates when the diameter of the two species become similar. This is to be expected because, as we saw from Ch. 7, the largest enhancements in the steady-state thermal conductivity below the series limit are possible when using mixtures of one particle with particles which are both heavier and smaller (and vice versa). This is combined with the fact that, as shown in Fig. 8.2, binary mixtures generally exhibit larger enhancements of λ_I above the parallel limit when spheres are mixed with other heavier yet smaller spheres.

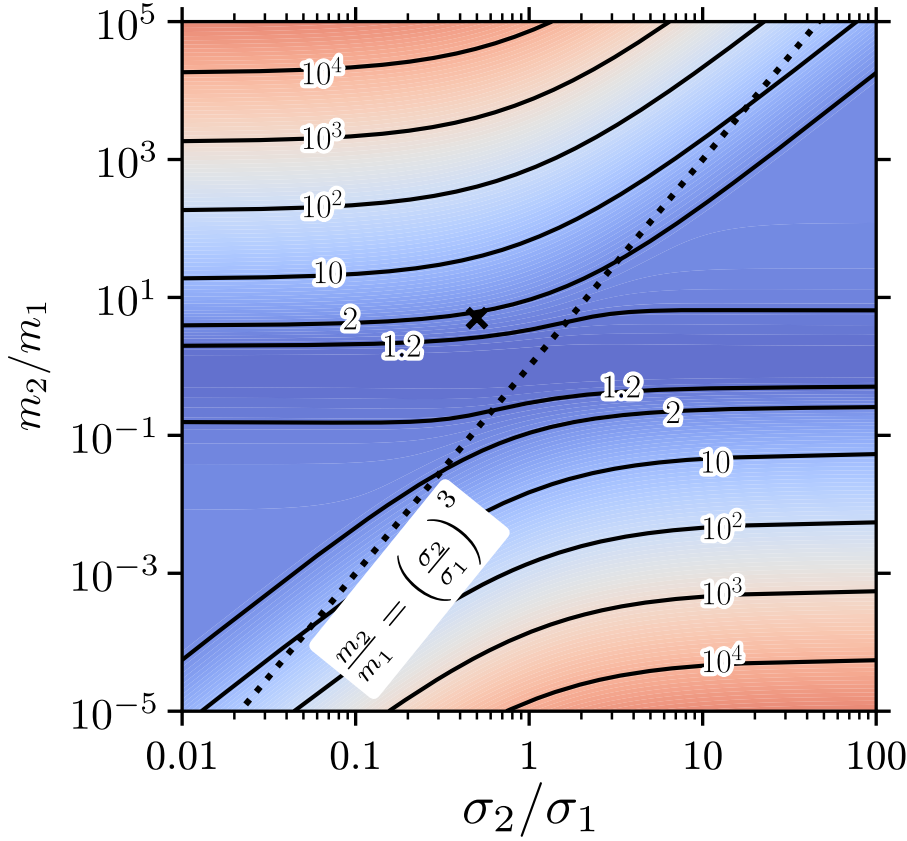


Figure 8.4: A contour map showing the maximum initial thermal conductivity enhancement above the steady-state thermal conductivity $(\lambda_I(x_2)/\lambda(x_2))_{\max}$ as a function of the hard-sphere mass m_2/m_1 and diameter σ_2/σ_1 ratio calculated via Enskog theory. The dotted line indicates where mass scales with hard-sphere volume assuming a constant particle density.

Fig. 8.5 shows the mol fraction (left) and mass fraction (right) of species 2 at which the maximum enhancement of the initial thermal conductivity above the steady state thermal conductivity occurs, mapped over the binary hard-sphere parameter space. Comparing the graphs to Fig. 8.4 shows that, as the maximum potential enhancement increases, the mol fraction of the heavier species decreases substantially, similar to the behaviour shown in Fig. 8.3. Fig. 8.5 also shows, again, that as the maximum potential enhancement increases, the mass fraction at which the maximum enhancement occurs tends towards 0.5. As the potential initial thermal conductivity decreases, the mol fraction of the heavier species at which the maximum potential enhancement occurs increases.

This chapter concludes in a similar manner to Ch. 7 by overlaying the the estimated position of actual gas mixtures on the thermal conductivity enhancement map shown in Fig. 8.4. The position of binary mixture combinations of the noble gases, hydrogen, and nitrogen are highlighted in Fig. 8.6. The size ratios are calculated in the same way as in Ch. 7 using data from Ref. [1–3]. Most of the gas mixtures shown here have relatively modest mass and size ratios and, therefore, the maximum thermal conductivity enhancement above the steady-state value is $(\lambda_I/\lambda)_{\max} < 2$. However, the value of the mass

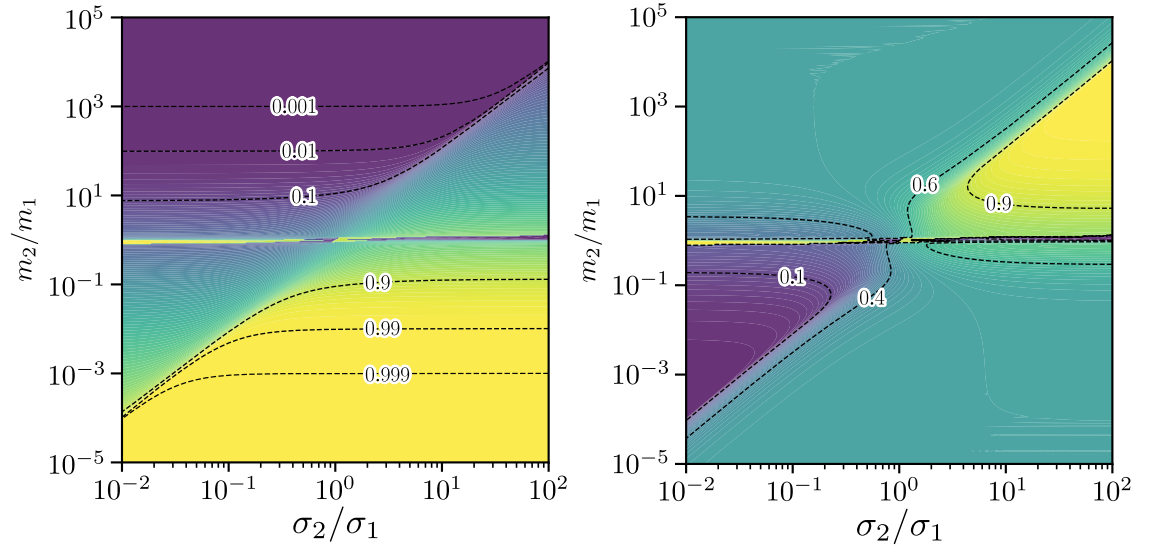


Figure 8.5: A contour map showing the mixture mol fraction x_2 which corresponds to the maximum initial thermal conductivity enhancement above the parallel limit $(\lambda_I(x_2)/\lambda(x_2))_{\max}$ as a function of the hard-sphere mass m_2/m_1 and diameter σ_2/σ_1 ratio.

ratio becomes more extreme for mixtures of heavy atoms such as xenon and krypton with atoms and molecules that are light such as helium and hydrogen. The binary mixture with the largest enhancement above the steady-state value, which is shown here, is Xe-H₂ which has a mass ratio of $m_{\text{Xe}}/m_{\text{H}_2} \approx 131/2$ and has a maximum enhancement value of $(\lambda_I/\lambda)_{\max} \approx 8$ which is almost an order of magnitude enhancement in the thermal conductivity at short times. These gases are widely available and therefore this mixture, along with others highlighted in Fig. 8.6, may represent an effective means of experimentally detecting short time thermal conductivity enhancements in future studies as a large thermal conductivity enhancement would be most easily detectable by experiment. However, the ease with which enhancements may be detected experimentally will also depend on the speed with which the thermal conductivity decays from the initial value λ_I to the steady-state value λ . The current theory does not give any insight into this timescale which will be influenced by many factors including the specific parameters of the mixture, the overall temperature difference, and how the temperature difference is applied to the system as well as the overall size of the system. In an attempt to fully describe all of the complex interactions present in a realistic system, a full coupled hydrodynamic-kinetic theory model is presented in Ch. 10.

This analysis in Fig. 8.6 assumes that the equivalent hard-sphere diameter values for the noble gases, hydrogen, and nitrogen, which are quoted from Refs. [1–3] and measured originally using diffusion measurements, are valid for use when predicting thermal conductivity values using Enskog theory. This assumption relies on the theory that the quoted gases behave in a hard-sphere-like manner in across these two different transport processes. This assumption is tested in Ch. 9 which seeks to fit new values of the equivalent hard-sphere diameter for these gases using existing experimental thermal conductivity

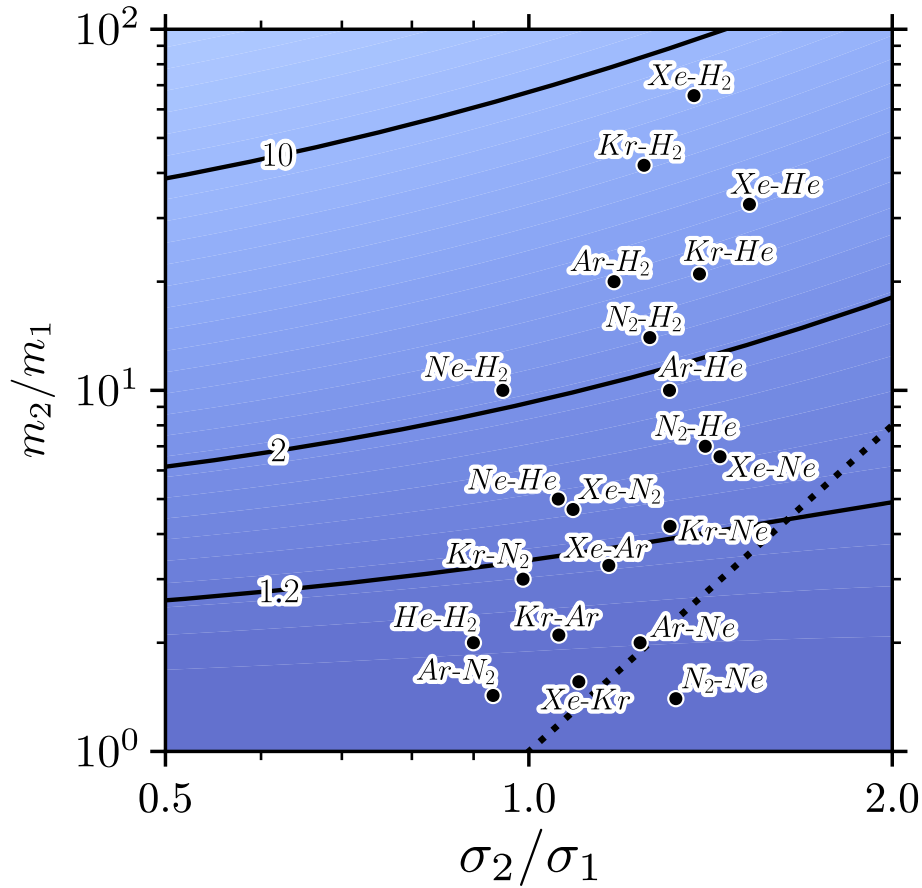


Figure 8.6: As described in Fig. 8.4 but plotted over a narrower section of the hard-sphere parameter space in order to highlight the estimated locations of the noble gases, hydrogen, and nitrogen on the plot. As in Fig. 7.5 the kinetic diameters values for the gases are taken from Refs. [1–3]

measurements.

8.3 Conclusions and future work

This chapter examines the initial enhanced thermal conductivity of binary hard-sphere mixtures with varying hard-sphere parameters. Values of the initial thermal conductivity are determined relative to both the parallel mode conductivity, and the steady-state value. Enskog theory predicts that it is possible for the initial enhanced thermal conductivity to exhibit values which are well above the steady-state and parallel conductivities. The primary predictor of the potential enhancement is the species mass ratio. Similar to Ch. 7, estimated kinetic diameters from literature are used in order to predict real gas mixtures which could exhibit large values of the initial thermal conductivity. This analysis predicts that mixtures with large mass ratios, such as hydrogen-xenon and krypton-helium mixtures, would exhibit values of the initial thermal conductivity which are approximately ten times larger than the corresponding steady-state value for certain mixture concentrations. Future research should take the form of experimental studies, or detailed computational

modelling, in order to determine if the initial thermal conductivity is accessible in real systems. Experimentally, this would take the form of a campaign of experimental measurements which take place over varying timescales in order to check for changes in the measured thermal conductivity as a function of measurement time. In theory, if the measurement time is short enough such that thermal diffusion enhances the effective thermal conductivity, the measured thermal conductivity should increase as the measurement time decreases. Alternatively, detailed molecular simulations could be performed in order to determine the full time-evolution of fluid mixtures during heat transfer at short times, giving insight into the timescale over which thermal diffusion completes in realistic systems and, therefore, the times at which significant enhancements in the effective thermal conductivity are possible. Ch. 10 showcases a coupled hydrodynamic-kinetic theory model which is designed for this purpose.

References

- [1] D. W. Breck. *Zeolite Molecular Sieves: Structure, Chemistry, and Use*. New York: Wiley, 1973.
- [2] A. F. Ismail, K. Khulbe, and T. Matsuura. *Gas Separation Membranes*. New York: Springer, 2015.
- [3] S. Matteucci et al. “Materials Science of Membranes for Gas and Vapor Separation”. In: Wiley, 2006. Chap. Transport of Gases and Vapors in Glassy and Rubbery Polymers.

FITTING ENSKOG THEORY TO REAL SYSTEMS

As shown in Ch. 7, Enskog theory predicts that it is possible for binary hard-sphere gas systems to exhibit values of the steady-state thermal conductivity λ which are out-with the series-parallel limits for certain hard-sphere mass ratios m_2/m_1 and diameter ratios σ_2/σ_1 . Comparison of these hard-sphere parameters with the estimated molecular mass and kinetic diameters of real materials, as shown in Fig. 7.6, predicts that a number of real binary gas mixtures such as Hydrogen-Helium, Krypton-Nitrogen, and Argon-Nitrogen will have steady-state thermal conductivity values, at certain mixture concentrations, which are below the series limit.

The goal of this chapter is to examine whether the anomalous thermal conductivity predictions for certain binary hard-sphere gas mixtures are reflected in experimental measurements of gases with similar parameters. More broadly, this will give insight into whether the hard-sphere model is appropriate when attempting to predict thermal conductivity behaviour in gas mixtures. Initial attempts to predict the thermal conductivity of the He-H₂ gas mixture, using equivalent hard-sphere diameters calculated using diffusion measurements, are shown in Fig. 6.3. These results were promising and appeared to capture the general form of the thermal conductivity profile; however, they ultimately failed to predict the correct thermal conductivity ratio of the two pure components. This suggests that kinetic diameters estimated via diffusion experiments may not be entirely appropriate when calculating thermal conductivities using Enskog theory. Therefore, this chapter will initially use experimental thermal conductivity data in order to fit new values of the kinetic diameter for various gases. These values are then compared with literature data. Fitted kinetic diameter values are then used, in conjunction with Enskog theory, to predict the mixture thermal conductivity of three separate binary gas systems and these Enskog predictions are compared against experimental data. Finally, the values of the kinetic diameter which are estimated in this chapter are used in order to briefly explore whether ternary hard-sphere gas mixtures display anomalous values of the steady-state thermal conductivity.

9.1 Predicting the kinetic diameter

In order to model a real particle (from a single atom to an entire molecule) as a hard sphere, an equivalent value for both the mass and the diameter of that particle is required for use with the equations of Enskog theory [1]. The molar masses of elements are well known and widely available and it is possible to calculate the mass of a single particle simply by dividing the molar mass by Avagadro's constant $m = M/A_C$ where m is the mass of an individual particle, M is the molar mass of the particle, and A_C is Avagadro's constant. The diameters of individual atoms and molecules are not as easily determined and are subject to different definitions. However, it is possible to calculate the equivalent hard sphere diameter of a particle by fitting the measured thermal conductivity to the reduced thermal conductivity calculated using Enskog theory as is detailed in this section.

The reduced hard-sphere thermal conductivity is given in Ref. [2] as follows,

$$k^* = \frac{k}{\left(\frac{k_B T}{m \sigma^2}\right)^{\frac{1}{2}} \frac{k_B}{\sigma}}, \quad (9.1.1)$$

where k is the thermal conductivity, the symbol $*$ signifies a reduced value, k_B is the Boltzmann constant, T is the temperature, m is the hard-sphere mass, and σ is the hard-sphere diameter. In this thesis, for the value of the λ^* , the reduced thermal conductivity in the limit of 0 density λ_0 is used. This value can be calculated using kinetic theory and is given in Refs. [3, 4] as follows,

$$\lambda_0 = 1.02513 \frac{75 k_B}{64 \sigma^2} \left(\frac{k_B T}{m \pi}\right)^{\frac{1}{2}}. \quad (9.1.2)$$

In order to estimate the kinetic diameter of a given material, we can rearrange Eq. (9.1.1) for the reduced thermal conductivity for the hard-sphere diameter σ

$$\sigma = \sqrt{\frac{\lambda^*}{\lambda} \left(\frac{k_B T}{m}\right)^{\frac{1}{2}} k_B}. \quad (9.1.3)$$

This equation allows the calculation of an equivalent hard-sphere diameter for any substance given the thermal conductivity, the temperature at which the thermal conductivity was measured, and the mass of one molecule (or atom) of that substance. In order to demonstrate this fitting process, an example calculation of the equivalent hard-sphere diameter of a neon atom is shown here. For neon, the molar mass is given as $M_{\text{Ne}} = 20.1797$ which means that the mass of an individual neon atom can be calculated as follows,

$$m_{\text{Ne}} = \frac{M_{\text{Ne}}}{A_C} = \frac{0.02018 \text{ kg mol}^{-1}}{6.02 \times 10^{23} \text{ mol}^{-1}} = 3.3509 \times 10^{-26} \text{ kg}. \quad (9.1.4)$$

The thermal conductivity of Neon is given in Ref. [5] as $0.0787 \text{ W m}^{-1} \text{ K}^{-1}$ at 600 K.

Table 9.1: Equivalent hard-sphere diameters for several materials calculated using experimentally measured thermal conductivity values. Experimental thermal conductivity values are quoted along with the temperature at which the experiment was performed. Reference values from literature, calculated using diffusion measurements, are shown for comparison.

Name	T K	Thermal conductivity $\times 10^{-3} \frac{\text{W}}{\text{m K}}$	Kinetic diameter pm	Reference pm
Hydrogen H_2	423.25	237.85 [6]	228	289 [7]
Nitrogen N_2	303.15	25.59 [8]	331	364 [7]
Helium He	423.25	202.02 [6]	208	260 [9]
Neon Ne	600	78.7 [5]	243	275 [10]
Argon Ar	363.15	20.976 [11]	350	340 [10]
Krypton Kr	303.15	9.621 [8]	411	360 [10]
Krypton Kr	363.15	11.137 [11]	399	360 [10]
Xenon Xe	600	10.4 [5]	418	396 [10]

Substituting these values, along with m_{Ne} , into Eq. (9.1.3) gives

$$\sigma_{\text{Ne}} = \sqrt{\frac{0.67619}{0.0787} \left(\frac{1.38 \times 10^{-23} \cdot 600}{3.3509 \times 10^{-26}} \right)^{\frac{1}{2}}} 1.38 \times 10^{-23}, \quad (9.1.5)$$

where the neon kinetic diameter is finally calculated to be

$$\sigma_{\text{Ne}} = 243 \text{ pm}. \quad (9.1.6)$$

The equivalent hard-sphere diameters for the noble gases, hydrogen, and nitrogen are calculated in the same manner using Eq. (9.1.3) and are shown in Table. 9.1. Experimental thermal conductivity data are taken from Refs. [5, 6, 8, 11]. The quoted experimental thermal conductivity values are all measured at a pressure of approximately 1 atm and at temperatures above 300 K. Calculated kinetic diameters are listed against values from literature calculated using diffusion measurements from Refs. [7, 9, 10]. In the case of the noble gases (excluding Helium), the calculated kinetic diameters agree with the literature values. The agreement is weaker for Helium as well as hydrogen. In these cases, the kinetic diameter values calculated in this section are approximately 20 % lower than literature values. This difference likely contributes to the disagreement between the experimental and predicted thermal conductivity profiles apparent in Fig. 6.3 for He- H_2 mixtures. Finally, in the case of nitrogen, the value calculated here is approximately 10 % below the literature value.

9.2 Enskog comparison

The calculated kinetic diameters shown in Table 9.1 are used in order to predict the thermal conductivity vs concentration profiles of three binary gas mixtures using Enskog theory. The estimated mixture thermal conductivities are compared with experimental measurements to determine whether the behaviour of these gas mixtures is well described by the hard-sphere model. In order to compare experimental thermal conductivity measurements with the predictions of Enskog theory, the experimental mixture thermal conductivity values are converted to reduced units using the size and mass values of one of the components according to Eq. (9.1.1) which is restated in a slightly modified form for clarity

$$k_m^* = \frac{k_m}{\left(\frac{k_B T}{m_1 \sigma_1^2} \right)^{\frac{1}{2}} \frac{k_B}{\sigma_1}}, \quad (9.2.1)$$

where k_m is the mixture thermal conductivity value, T is the temperature at which the thermal conductivity measurement was performed, and m_1 and σ_1 represent the mass and diameter values respectively of the chosen reducing species. The species which is chosen to be the reducing species is unimportant. Enskog theory predictions which are shown in this section are calculated using 5th order Sonine polynomials and assuming a reduced number density of $n\sigma_1^3 = 10^{-8}$. It is expected that the pure component thermal conductivity values, predicted by Enskog theory, should fit exactly (as is seen in Fig. 9.1, Fig. 9.2, and Fig. 9.3) as the equivalent hard-sphere diameters of these species were initially fit using these pure component measurements.

9.2.1 Mixture 1: Helium-Hydrogen

Thermal conductivity predictions of Enskog theory as a function of mixture concentration for the helium-hydrogen gas mixture are shown in Fig. 9.1 alongside the results of experimental measurements performed by Shashkov et al [6, 12]. The hard-sphere mass and size ratios used are $m_{\text{He}}/m_{\text{H}_2} = 4/2$, and $\sigma_{\text{He}}/\sigma_{\text{H}_2} = 208/228$ (taken from Table 9.1) respectively. This figure shows the Enskog theory predictions of three separate definitions of the thermal conductivity; the phenomenological thermal conductivity L_{uu} , the initial thermal conductivity λ_I , and the steady-state thermal conductivity λ . As noted in Ch. 3, the thermal conductivity of this gas mixture lies outwith the series-parallel conductivity bounds. The steady-state thermal conductivity profile for this system, predicted by Enskog theory, agrees strongly with the experimental measurements and predicts a minimum at approximately $x_{\text{He}} = 0.8$ which is of a similar magnitude to the experimental minimum. There is a deviation of the Enskog predictions from the experimental measurements at $x_{\text{He}} = 0.5$ which is large relative to the agreement in the rest of the data. Additional data in this concentration range would be useful in order to determine if this is an anomaly or whether it is indicative of a larger trend of deviation from Enskog theory.

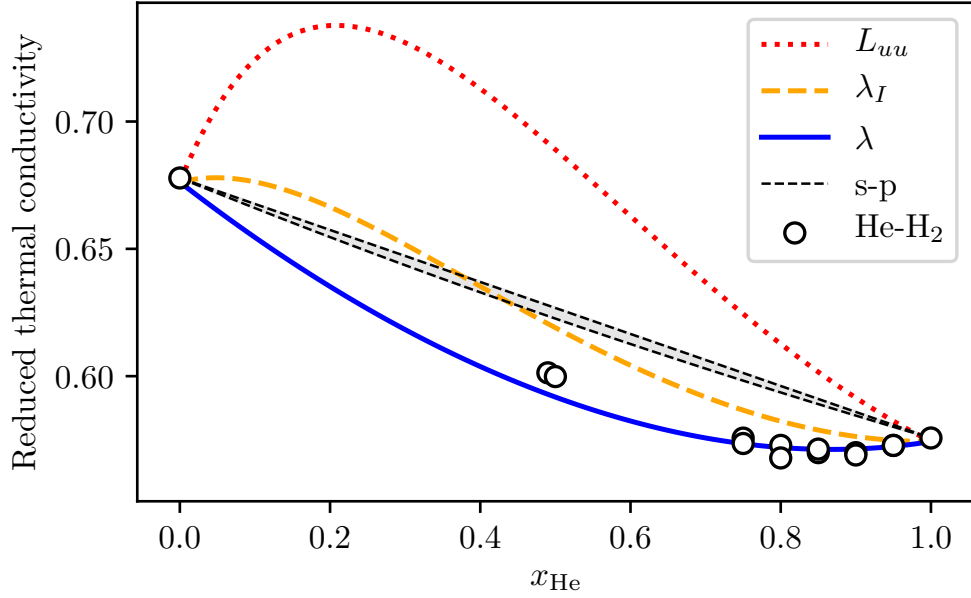


Figure 9.1: Reduced thermal conductivity as a function of helium mol fraction for a hydrogen-helium binary gas mixture. The hollow black circular symbols represent experimental thermal conductivity measurements performed by Shashkov et al [6]. The graph shows the Enskog theory predictions of the phenomenological thermal conductivity L_{uu} (red dotted line), initial thermal conductivity λ_I (orange dashed line), and steady-state thermal conductivity λ (blue solid line). The hard-sphere mass and diameter ratios used in order to calculate the Enskog values are $m_{\text{He}}/m_{\text{H}_2} = 4/2$, and $\sigma_{\text{He}}/\sigma_{\text{H}_2} = 208/228$ (taken from Table 9.1). The thin dashed black lines represent the series-parallel thermal conductivity limits. Experimental measurements were performed at atmospheric pressure and 423.15 K.

It is clear from Fig. 9.1 that the steady-state thermal conductivity is the correct definition to compare to experiments in this case, suggesting that the measurements were performed over a long enough time scale such that the transient increases in the total heat transport caused by thermal diffusion are irrelevant. Unfortunately, Refs. [6, 12] give no information about the timescale of the experiments which were performed. It is also clear that the hard-sphere model is a completely appropriate model to use when predicting the thermal conductivity behaviour of He-H₂ mixtures at atmospheric pressure and $T \approx 400$ K.

It is interesting to look at the profiles of both the phenomenological thermal conductivity L_{uu} and the initial thermal conductivity λ_I . Both of these thermal conductivity profiles exhibit a maximum as a function mixture concentration which is above either of the pure component values. The predicted maximum in L_{uu} is far greater than in λ_I and the maximum for each profile occurs at a different concentration where the maximum in L_{uu} occurs at approximately $x_{\text{He}} = 0.25$ while the maximum in λ_I occurs at approximately $x_{\text{He}} = 0.1$. This suggests that the timescale over which heat transfer takes place affects the concentration at which the maximum potential effective thermal conductivity

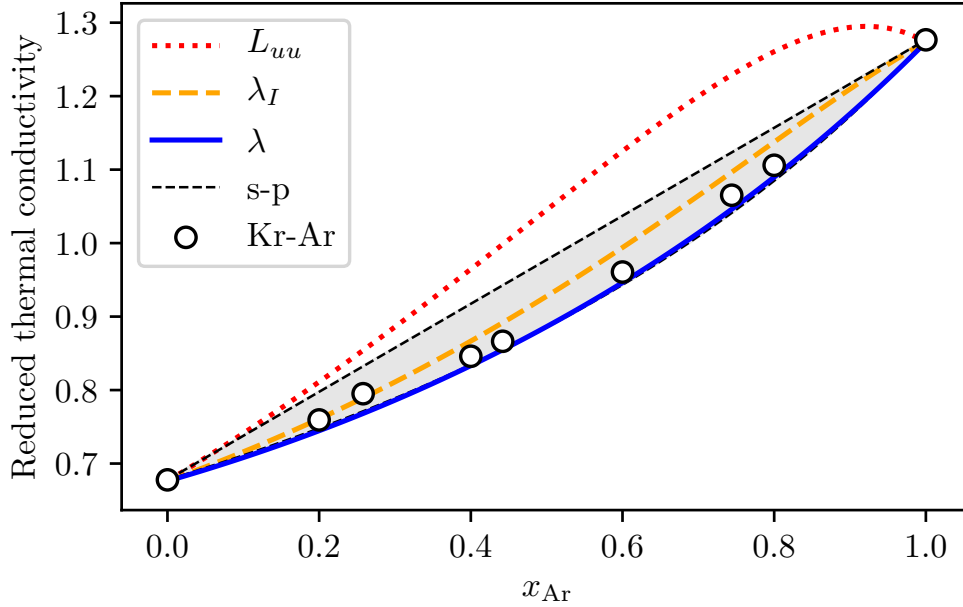


Figure 9.2: Reduced thermal conductivity as a function of argon mol fraction for a krypton-argon binary gas mixture. The hollow black circular symbols represent experimental thermal conductivity measurements reported by Refs. [11, 13]. The graph shows the Enskog theory predictions of the phenomenological thermal conductivity L_{uu} (red dotted line), initial thermal conductivity λ_I (orange dashed line), and steady-state thermal conductivity λ (blue solid line). The hard-sphere mass and diameter ratios used in order to calculate the Enskog values are $m_{Ar}/m_{Kr} = 39.9/83.8$, and $\sigma_{Ar}/\sigma_{Kr} = 350/399$ (taken from Table 9.1). The thin dashed black lines represent the series-parallel thermal conductivity limits calculated using the pure component thermal conductivities. Experimental measurements were performed at atmospheric pressure and 303.15 K.

increase can be realised.

9.2.2 Mixture 2: Argon-Krypton

Fig. 9.2 shows thermal conductivity predictions of Enskog theory as a function of argon mol fraction for an argon-krypton gas mixture. Predictions are shown alongside the results of experimental measurements performed by Saxena et al [13] and Gambhir et al [11]. The values of the equivalent hard-sphere mass and size ratios used to model the gas mixture are $m_{Ar}/m_{Kr} = 39.9/83.8$, and $\sigma_{Ar}/\sigma_{Kr} = 350/399$ (taken from Table 9.1). The predicted steady-state and initial thermal conductivity values are within the series-parallel bounds while the predicted phenomenological value is slightly above the parallel-limit. The experimental measurements are in reasonable agreement with the steady-state thermal conductivity predictions; however, this definition of the thermal conductivity consistently underpredicts the experimental values across the entire concentration space. Although the experimental values are consistently greater than λ , most do not deviate above the predicted initial thermal conductivity λ_I . This fact supports the theory that λ_I could form an upper limit to the thermal conductivity of a mixture which is ac-

cessible at short timescales. It is important to note, however, that this small disagreement could be due to a number of other factors such as inaccurate fitting of the equivalent hard-sphere diameter or the potential that this mixture, at these experimental conditions, is not well described by the hard-sphere model. No information is given on the timescale over which the experimental measurements, reported in Fig. 9.2, are performed.

Fig. 7.6 initially predicted that the maximum dehancement of the steady-state thermal conductivity from the series conductivity limit is $\lambda/k^\perp \approx 0.98$. Utilising the kinetic diameter values calculated using thermal conductivity data in this chapter, Enskog theory predicts that the λ is almost identical to the series limit over the entire concentration space $\lambda/k^\perp \approx 1$. This value is close to the previous prediction; however, the experimental values never drop below the series-limit in Fig. 9.2, suggesting that the kinetic diameter values calculated in this thesis, using thermal conductivity data, provide a more accurate model of gas mixture thermal conductivity.

9.2.3 Mixture 3: Krypton-Nitrogen

Enskog theory thermal conductivity predictions for a krypton-nitrogen gas mixture are shown in Fig. 9.3 alongside experimental results from the same gas mixture reported by Barua [8]. This gas mixture was modelled using equivalent hard-sphere mass and size ratios of $m_{\text{Kr}}/m_{\text{N}_2} = 83.8/28.0$, and $\sigma_{\text{Kr}}/\sigma_{\text{N}_2} = 411/331$ (taken from Table 9.1). As is the case in Fig. 9.2, the Enskog predictions of the steady-state and initial thermal conductivities lie largely within the series-parallel bounds, while the phenomenological value shows a significant increase above the parallel limit, and even the pure component nitrogen thermal conductivity. The experimental thermal conductivity values are largely bounded by the steady-state and initial Enskog predictions; however, the experimental values do not appear to be accurately predicted by either definition. Again, this may suggest that the experiment was carried out over a timescale short enough to measure the transient increase in thermal transport caused by thermal diffusion. No information is given in Ref. [8] about the timescale of the method used.

Fig. 7.6 initially predicted that the dehancement at the point of maximum deviation from the series conductivity limit in this mixture, based on kinetic diameter values taken from literature, would be approximately $\lambda/k^\perp \approx 0.95$. This is approximately the same dehancement as is observed in the case of a Helium-Hydrogen mixture as shown in Fig. 9.1. However, when fitting the kinetic diameter value using Eq. (9.1.3), utilising experimental thermal conductivity data, the new fitted kinetic diameters shown in Table 9.1 produce a mixture thermal conductivity profile which exhibits no dehancement below the series thermal conductivity limit. This is, however, in agreement with the experimental measurements which also show no dehancement below the series limit. The discrepancy between the kinetic diameter of Nitrogen N_2 taken from literature, and the value calculated in this chapter using thermal conductivity measurements, suggests that this molecule is not behaving in a consistently hard-sphere-like manner across different transport pro-

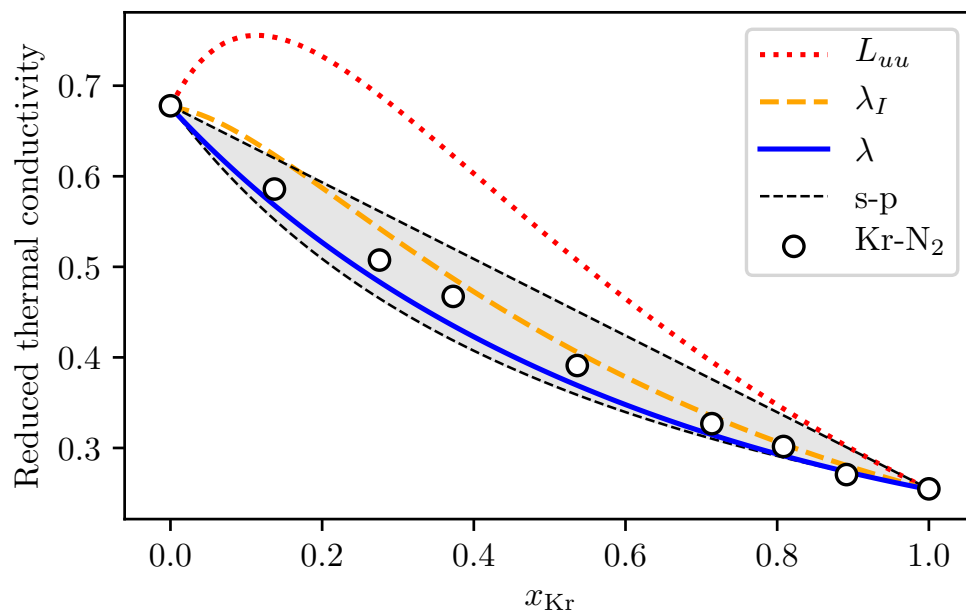


Figure 9.3: Reduced thermal conductivity as a function of krypton mol fraction for a krypton-nitrogen binary gas mixture. The hollow black circular symbols represent experimental thermal conductivity measurements reported by Barua [8]. The graph shows the Enskog theory predictions of the phenomenological thermal conductivity L_{uu} (red dotted line), initial thermal conductivity λ_I (orange dashed line), and steady-state thermal conductivity λ (blue solid line). The hard-sphere mass and diameter ratios used in order to calculate the Enskog values are $m_{\text{Kr}}/m_{\text{N}_2} = 83.8/28.0$, and $\sigma_{\text{Kr}}/\sigma_{\text{N}_2} = 411/331$ (taken from Table 9.1). The thin dashed black lines represent the series-parallel thermal conductivity limits calculated using the pure component thermal conductivities. Experimental measurements were performed at atmospheric pressure and 363.15 K.

cesses. This makes intuitive sense as N_2 is a diatomic molecule. Fig. 9.3 suggests that the diameter calculated using thermal conductivity data is more more appropriate for use when predicting the thermal conductivity of a mixture containing this molecule.

9.3 Dehancement in ternary mixtures

So far, this thesis has investigated thermal conductivity behaviour in binary mixtures. This section will briefly step into the world of ternary mixtures and explore whether it may be possible to elicit a larger thermal conductivity dehancement below the series limit by adding a third component. Mapping the potential dehancement of ternary mixtures in a similar manner to Chapters 7 and 8 would result in a large parameter space to search over and difficulties representing the data in a communicable manner. Therefore, this section will focus on one particular ternary mixture of neon, helium, and hydrogen, using parameters taken from Table 9.1, in order to study ternary dehancement.

A hydrogen-helium-neon ternary gas mixture is modelled as a ternary hard-sphere

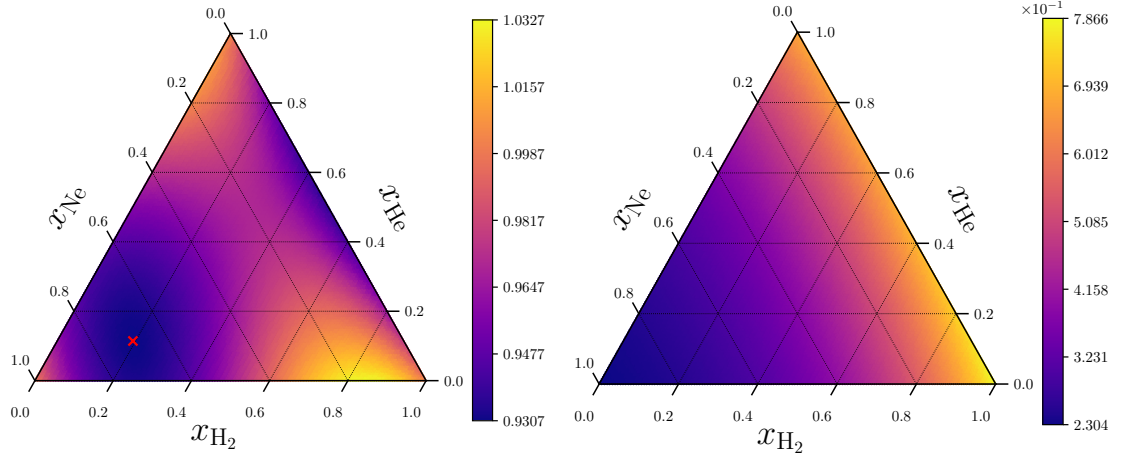


Figure 9.4: Steady-state thermal conductivity λ as a function of mixture concentration for a ternary gas mixture consisting of hydrogen H_2 , helium He , and neon Ne . The thermal conductivity value is calculated using Enskog theory. The value represented by the colour is the ratio of the steady-state thermal conductivity to the series value λ/k^\perp . The hard-sphere parameters for each component for use with kinetic theory are taken from Table 9.1. The red cross represents the location on the graph with the minimum thermal conductivity relative to the series bound. The bottom, left, and right axes represent the mol fractions of hydrogen, helium, and neon respectively.

mixtures using the following parameters,

$$m_{\text{H}_2} = 2.0 \text{ u} \quad m_{\text{He}} = 4.0 \text{ u} \quad m_{\text{Ne}} = 20.2 \text{ u} \quad (9.3.1)$$

$$\sigma_{\text{H}_2} = 228 \text{ pm} \quad \sigma_{\text{He}} = 208 \text{ pm} \quad \sigma_{\text{Ne}} = 243 \text{ pm}, \quad (9.3.2)$$

where the equivalent hard-sphere diameter values are taken from Table 9.1. This section investigates whether it is possible for this ternary gas mixture to exhibit a greater reduction of the steady-state thermal conductivity below the series limit value than is possible in any of the three potential binary gas mixtures of the same components. Fig. 9.4 contains two ternary plots showing (left) the steady-state thermal conductivity relative to the series thermal conductivity bound λ/k^\perp and (right) the absolute predicted steady-state thermal conductivity λ as a function of the mixture concentration. Thermal conductivity values are predicted by Enskog theory using a 3rd order Sonine polynomial.

Fig. 9.1 corresponds to the top right edge ($x_{\text{Ne}} = 0$) of both ternary plots. Fig. 9.4 shows that it is possible for a third material (Ne in this case) to be added to a binary mixture (H_2 - He) and produce a resulting mixture where the steady-state thermal conductivity λ is reduced further below the series-bound than was possible than with the previous two components alone. The maximum steady-state dehancement below the series limit in the He - H_2 binary mixture is $(\lambda/k^\perp)_{\min, \text{H}_2\text{-He}} \approx 0.944$, whereas in this ternary mixture, the maximum dehancement (denoted by the red cross in Fig. 9.4) is $(\lambda/k^\perp)_{\min, \text{H}_2\text{-He-Ne}} \approx 0.931$. However, although it is possible to produce a slightly greater dehancement in the case of the H_2 - He - Ne ternary mixture, this change is small relative to

the low absolute thermal conductivity of neon relative to both helium and hydrogen. This means that it is no longer possible to reduce the thermal conductivity below the pure component values as is possible in the binary H_2 -He mixture as shown in Fig. 9.1. Neon has a much smaller thermal conductivity than either hydrogen or helium and any combination of the three components will have a greater conductivity.

9.4 Conclusions and future work

This chapter presents a method of calculating the equivalent hard-sphere diameter of the atoms and molecules of any material using experimental thermal conductivity measurements of the bulk material in combination with kinetic theory. In principle it is not necessary to use thermal conductivity data, it is equally possible to carry out this calculation using any other transport property such as viscosity or diffusion measurements. Equivalent hard-sphere diameters are calculated for the noble gases as well as hydrogen H_2 and nitrogen N_2 and are shown in Table 9.1. These values are compared with literature values calculated using diffusion measurements. In general the values agree strongly with most of the noble gas results agreeing to within approximately 10 % and the measurements for the diatomic molecules as well as helium in agreement to within approximately 20 %.

The chapter goes on to utilise the newly calculated kinetic diameter values in order to predict the thermal conductivity profiles of certain binary gas mixtures. Comparisons between experimentally measured thermal conductivities, taken from literature, and the predicted values using Enskog theory are shown for binary mixtures of Hydrogen and Helium (H_2 -He), Argon and Krypton (Ar-Kr), and Argon and Nitrogen (Ar- N_2). Enskog theory is used in order to predict three separate definitions of the thermal conductivity; the phenomenological L_{uu} , the initial λ_I , and the steady-state λ values. The Enskog predictions for the H_2 -He thermal conductivity agree strongly with experimental measurements and accurately capture the thermal conductivity minimum which is shown through experiment. In the case of the Kr- N_2 and Ar-Kr mixtures, the Enskog steady-state thermal conductivity predictions do not agree as strongly with the experimental data; however, the experimental data appears to be bounded by the initial and steady-state thermal conductivity values as predicted by Enskog theory. This disagreement could be the result of a number of factors such as inaccurate estimates of the kinetic diameter; however, this could also be a result of the fact that the experimental measurements were carried out over a short timescale such that the measured thermal conductivity included the effects of the transient heat transfer increases due to thermal diffusion. If this is the case, carrying out the experiment over a longer timescale would lead to experimental measurements which were closer to the steady-state values. Unfortunately, the experimental literature does not record the length of time over which the experimental measurement was taken. Additional experimental studies, carried out over small, varying amounts of time, are required

in order to clarify the short timescales over which additional heat transfer due to thermal diffusion will be significant in these systems.

Efforts should be made to fit effective hard-sphere diameters to solid-liquid mixtures such as nanofluids in an attempt to correlate diffusion effects and potential enhancements in the initial thermal conductivity λ_I to experimentally observed increases in the thermal conductivity relative to the Maxwell bounds. This approach may not be as accurately predictive as for gas systems, as shown in this chapter; however, there is evidence, such as the study performed by Pryazhnikov et al in 2017 [14], that diffusion effects (as opposed to the increased conductive power of solid nanoparticles) in nanofluids could be responsible for an increase in thermal conductivity. This study reported that for mixtures of SiO_2 , Al_2O_3 , TiO_2 , ZrO_2 , CuO , and diamond nanoparticles with base fluids of water, ethylene glycol, and engine oil, there was no correlation between the thermal conductivity of the nanoparticles and the thermal conductivity of the resulting nanofluid mixture. There was, however, a dependence of nanofluid thermal conductivity on nanoparticle size and density as predicted by the hard-sphere model.

Finally, this chapter explored potential thermal conductivity deenhancement in ternary mixtures by modelling a ternary mixture of hydrogen, helium, and neon using the equivalent hard-sphere diameters listed in Table 9.1. Enskog theory predicts that it is possible for this ternary mixtures to exhibit steady-state thermal conductivity values, relative to the corresponding series thermal conductivity limit (λ/k^\perp), which are lower than for any of the potential binary combinations of the same gases. In the case of the H_2 -He-Ne mixture, this increased deenhancement is small relative to the low thermal conductivity of pure neon; however, this demonstrates that increasing number of mixture components can have compounding effects on effective mixture thermal conductivities. Investigating the effects of adding additional atoms or molecules with similar parameters (as opposed to the large size and mass differences introduced by neon) such as deuterium or tritium in the case of helium and hydrogen may yield relatively interesting thermal conductivity deenhancement and enhancement effects.

References

- [1] M. López de Haro, E. G. D. Cohen, and J. M. Kincaid. “The Enskog Theory for Multicomponent Mixtures. 1. Linear Transport-Theory”. In: *J. Chem. Phys.* 78.5 (1983), pp. 2746–2759.
- [2] S. W. Smith, C. K. Hall, and B. D. Freeman. “Molecular dynamics study of transport coefficients for hard-chain fluids”. In: *J. Chem. Phys.* 102 (1995), p. 1057.
- [3] S. Chapman and T. G. Cowling. *The mathematical theory of non-uniform gases*. 3rd ed. Cambridge university press, 1970.
- [4] D. M. Heyes. *The liquid state: applications of molecular simulations*. Chichester: Wiley, 1998.

- [5] D. R. Lide, ed. *CRC handbook of chemistry and physics*. 84th ed. CRC Press, 2003.
- [6] A. G. Shashkov, F. P. Kamchatov, and T. N. Abramenko. “Thermal conductivity of the hydrogen-helium mixture”. In: *J. Eng. Phys.* 24.4 (1973), pp. 461–464.
- [7] A. F. Ismail, K. Khulbe, and T. Matsuura. *Gas Separation Membranes*. New York: Springer, 2015.
- [8] A. K. Barua. “Thermal conductivity and Eucken type correction for binary mixtures of N₂ with some rare gases”. In: *Physica Amsterdam* 25 (1959), pp. 1275–1286.
- [9] S. Matteucci et al. “Materials Science of Membranes for Gas and Vapor Separation”. In: Wiley, 2006. Chap. Transport of Gases and Vapors in Glassy and Rubbery Polymers.
- [10] D. W. Breck. *Zeolite Molecular Sieves: Structure, Chemistry, and Use*. New York: Wiley, 1973.
- [11] R. S. Gambhiur and S. C. Saxena. “Thermal conductivity of binary and ternary mixtures of krypton, argon, and helium”. In: *Mol. Phys.* 11 (1966), pp. 233–241.
- [12] A. G. Shashkov and F. P. Kamchatov. “Experimental determination of the thermal conductivity of binary gas mixtures”. In: *J. Eng. Phys.* 22 (1972), pp. 586–590.
- [13] S. C. Saxena and P. K. Tondon. “Thermal conductivity of multicomponent mixtures of rare gases”. In: *Proc. Symp. Thermophys. Prop.* 4 (1968), pp. 389–404.
- [14] M. I. Pryazhnikov et al. “Thermal conductivity mmeasurement of nanofluids”. In: *Int. J. Heat Mass Transfer* 104 (2017), pp. 1275–1282.

HYDRODYNAMIC SIMULATIONS OF TRANSIENT EFFECTS

A major flaw with the definition of the initial thermal conductivity λ_I is that it gives no indication of the timescale over which thermal diffusion completes and, therefore, the time taken for the effective thermal conductivity to decay to the steady-state value. If thermal diffusion in a mixture takes place over a long period of time, the effective thermal conductivity will also remain enhanced for a long period as diffusing particles transport heat. If this time period is long enough, then this effect may be measurable by experiment and potentially exploitable in novel heat transfer devices. If, however, concentration gradients establish themselves rapidly, the enhanced thermal conductivity may be present for such a short period of time that it is extremely difficult to measure. Furthermore, the temperature gradient will not evolve independently, the path of a fluid mixture towards steady-state under the influence of a temperature gradient is complex and will involve simultaneous heat and mass diffusion. This means that, in reality, conditions within a mixture which is under the influence of a temperature gradient will not exactly mimic the conditions assumed in the derivation of λ_I (zero concentration gradient), as any gradient in the temperature will immediately result in a gradient in the concentration due to the thermophoresis effect. It is therefore desirable to determine the full evolution of both the temperature and mixture concentrations of a mixture undergoing heat transfer in order to determine the time taken for mixture concentration gradients to become established and, in addition, the *actual* time-averaged effective thermal conductivity which is observed over different timescales.

A molecular model, such as MD simulation, is required in order to capture all of the complex interactions present during heat transfer through fluid mixtures. However, simulating a realistic system with a view to comparing results with experimental measurements, or designing novel heat transfer devices involving multicomponent fluid flow in a complex geometry, would be prohibitively computationally expensive for conventional molecular simulation techniques as it would require many millions of particles to be representative of a real system. This chapter introduces a coupled hydrodynamic-kinetic theory model which overcomes this computational cost and allow the simulation of fluid

flow through realistically sized complex geometries in a timely manner.

This chapter first derives the finite volume method as a means of discretising the mass, momentum, and energy continuity equations which are derived in Ch. 5. It then moves on to describe the method of solving the hydrodynamic equations, showing the method of dividing the simulation space into discrete finite volume cells, the method of storing the information on individual hydrodynamic fields, and the method of time-integrating the equations. This chapter then shows the results of various hydrodynamic simulations which are performed in order to validate the model by comparing the results with direct MD simulations of an identical system. In the first instance, this validation is performed for a monocomponent hard-sphere fluid, showing that the hydrodynamic simulation and the MD simulation between two heated walls reach the same steady state conditions. The hydrodynamic code is then validated against MD in the transient regime by checking that the response of the system to a change in a wall temperature at the system boundary is consistent across both simulation techniques. Following on from monocomponent systems, results of the hydrodynamic code are then compared against MD for multicomponent systems.

Finally, this chapter lays out potential future research questions which could be addressed using this model. The potential future work outlined in this chapter includes one specific method for determining the time dependence of the effective thermal conductivity enhancement in hard-sphere mixtures which involves oscillating wall temperatures in order to facilitate perpetual thermophoretic motion.

10.1 Finite Volume Method

The finite volume method [1] is used to discretise differential equations in order to obtain a numerical solution. The desired simulation domain is split into multiple individual finite volumes, allowing a given differential equation to be approximated across the domain. It is possible to use other methods when discretising and solving differential equations such as the finite difference method or finite element method. The advantage of the finite volume method in the context of fluid dynamics simulations is that the flux terms are evaluated at the boundary between finite volume cells. This has the effect of implicitly enforcing conservation which is beneficial as we are modelling the evolution of conserved quantities. This is not guaranteed when using the conventional finite difference method as gradients in the material properties are evaluated at the center of finite volume cells. This derivation of the finite volume method begins by referring back to the *general conservation equation* derived in Ch. 5 in order to illustrate the method for a general property A . The conservation equation for a property A is given in Eq. (5.1.11) and is restated here in a slightly modified form as follows,

$$\frac{\partial}{\partial t}\rho_A(\mathbf{x}, t) = -\nabla_{\mathbf{x}} \cdot \rho_A(\mathbf{x}, t)\dot{\mathbf{x}}_A(\mathbf{x}, t) + \Phi_A(\mathbf{x}, t) \quad (10.1.1)$$

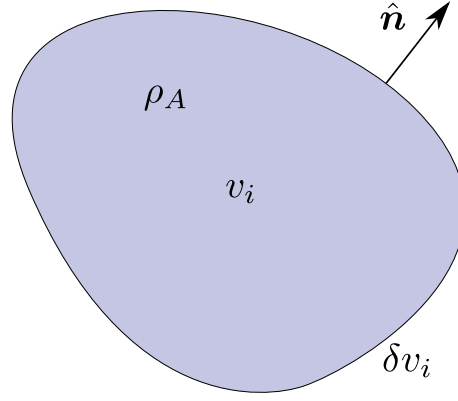


Figure 10.1: A schematic illustration of a individual finite volume cell which is indexed i and is represented by the shaded area. The cell has a total volume v_i which contains the quantity A such that the density ρ_A of A varies over the volume space. The volume is bounded by the volume surface δv_i and the vector \hat{n} represents the unit vector normal to the surface of the volume.

where a generation term $\Phi_A(\mathbf{x}, t)$ is now included. This term is not included in the original equation but is included here for generality. $\rho_A(\mathbf{x}, t)$ is the density of A at a position \mathbf{x} and time t , and $\dot{\mathbf{x}}_A(\mathbf{x}, t)$ is the velocity of the property A at position \mathbf{x} and time t .

The overall simulation domain contains multiple finite volumes, each with a volume v_i where i represents the finite volume cell index. An illustration of an example finite volume is shown in Fig. 10.1 which has a total volume v_i and contains the property A at different densities which vary over the volume. The volume is surrounded by a surface δv_i and every point on the surface is associated with a unit vector \hat{n} which is the vector normal to the surface at that point. Eq. (10.1.1) is now integrated over a finite volume v_i giving

$$\frac{\partial}{\partial t} \iiint_{\mathbf{x} \in v_i} \rho_A(\mathbf{x}, t) d\mathbf{x} = - \iiint_{\mathbf{x} \in v_i} \nabla_{\mathbf{x}} \cdot \rho_A(\mathbf{x}, t) \dot{\mathbf{x}}_A(\mathbf{x}, t) d\mathbf{x} + \iiint_{\mathbf{x} \in v_i} \Phi_A(\mathbf{x}, t) d\mathbf{x} \quad (10.1.2)$$

where v_i is the volume of the finite volume and the time derivative has been removed from the volume integral as the two variables are independent. The integration is carried out on the accumulation and generation terms in order to give volume averaged values of those terms and the divergence theorem is used in order to convert the convective term to a surface integral. The resulting equation is as follows,

$$v_i \frac{\partial}{\partial t} \bar{\rho}_{A,i}(t) = - \oint_{\mathbf{x} \in \delta v_i} \rho_A(\mathbf{x}, t) \dot{\mathbf{x}}_A(\mathbf{x}, t) \cdot \hat{n} d\mathbf{x} + v_i \bar{\Phi}_{A,i}(t) \quad (10.1.3)$$

where δv_i represents the surface of the finite volume, \hat{n} is the unit vector normal to the surface, and $\bar{\rho}_{A,i}(t)$ and $\bar{\Phi}_{A,i}(t)$ represent the averaged values of the density of A and the generation of A respectively over the i th finite volume v_i . The surface integral can be

written as a sum of the fluxes at each of the surfaces of the volume

$$\oiint_{\mathbf{x} \in \delta v_i} \rho_A(\mathbf{x}, t) \dot{\mathbf{x}}_A(\mathbf{x}, t) \cdot \hat{\mathbf{n}} d\mathbf{x} = \sum_{s \in \delta v_i} A_s \bar{\rho}_{A,s}(t) \bar{\dot{\mathbf{x}}}_{A,s}(t) \cdot \hat{\mathbf{n}} \quad (10.1.4)$$

where A_s is the area of the volume surface which the property A is flowing through, and $\bar{\rho}_{A,s}(t)$ and $\bar{\dot{\mathbf{x}}}_{A,s}(t)$ are the values of the density and velocity of A respectively, averaged over the same section of the volume surface s . Arranging a series of finite volumes in a ordered mesh within a solution geometry allows a solution to a partial differential equation to be calculated at those discrete locations. In the case of a mesh consisting of uniform rectangular cells, as shown in Fig. 10.3, this expression can be written as follows,

$$\oiint_{\mathbf{x} \in \delta v_i} \rho_A(\mathbf{x}, t) \dot{\mathbf{x}}_A(\mathbf{x}, t) \cdot \hat{\mathbf{n}} d\mathbf{x} = \sum_{j \in \mathbf{r}} A_j \left(\bar{\rho}_A(\mathbf{r} + \frac{1}{2} \Delta_j, t) \bar{\dot{\mathbf{x}}}_{A,j}(\mathbf{r} + \frac{1}{2} \Delta_j, t) - \bar{\rho}_A(\mathbf{r} - \frac{1}{2} \Delta_j, t) \bar{\dot{\mathbf{x}}}_{A,j}(\mathbf{r} - \frac{1}{2} \Delta_j, t) \right) \quad (10.1.5)$$

where $\mathbf{r} = \{x, y, z\}$ is the position vector of the finite volume cell in spacial coordinates (assuming the simulation is 3 dimensional), and Δ_j is the mesh spacing between finite volumes in the corresponding dimension.

This formulation of finite volume discretisation is used in this thesis to solve for the time evolution of the mass, momentum, and energy conservation equations which are derived in Ch. 5. As can be seen from Eq. (10.1.5), in this method, the flux which leaves through the surface of one finite volume will enter another volume thus conserving the total amount of A which in this case is mass, momentum, and energy.

10.2 Hydrodynamic model implementation

The central aim of the method is to model the evolution of three conserved quantities, the species mass densities $\rho_{1,2,\dots,S}$, the momentum $\rho \mathbf{u}$, and the total energy ρe . The hydrodynamic equations which are derived in Ch. 5 and which govern the evolution of these quantities are as follows,

$$\frac{\partial \rho_a}{\partial t} = -\nabla \cdot (\rho_a \mathbf{u} + \mathbf{J}_a), \quad (10.2.1)$$

$$\frac{\partial (\rho \mathbf{u})}{\partial t} = -\nabla \cdot (\rho \mathbf{u} \mathbf{u} + \mathbf{P}), \quad (10.2.2)$$

$$\frac{\partial (\rho e)}{\partial t} = -\nabla \cdot (\rho e \mathbf{u} + \mathbf{J}_q + \mathbf{P} \cdot \mathbf{u}). \quad (10.2.3)$$

The conservation equations have been restated in a form which matches Eq. (10.1.1) (where terms containing ∇ have been grouped together) and is therefore convenient for finite volume simulation. In this case, none of the conservation equations contain

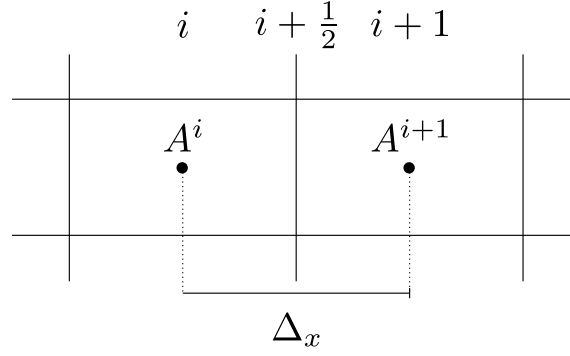


Figure 10.2: Diagram of a uniform rectangular finite volume grid highlighting two cells with index i and $i + 1$. These individual finite volume cells contain a value of a general property A which is assigned the corresponding index. The boundary between the two cells is said to be located at index $i + 1/2$. The distance between the center of the two cells i and $i + 1$ is labelled Δ_x .

a generation term as was shown in the general derivation of the finite volume method (Eq. (10.1.1)). The expressions for \mathbf{J}_a , \mathbf{J}_q and \mathbf{P} , which are given in Ch. 5, are also restated here as follows,

$$\mathbf{J}_a = - \sum_b L_{ab} T \nabla \left(\frac{\mu_b}{T} \right) - \frac{L_{au}}{T} \nabla T, \quad (10.2.4)$$

$$\mathbf{P} = p \mathbf{1} - \eta \left(\nabla \mathbf{u} + (\nabla \mathbf{u})^T \right) + \left(\left(\frac{2}{d} \right) \eta - \eta_B \right) (\nabla \cdot \mathbf{u}) \mathbf{1}, \quad (10.2.5)$$

$$\mathbf{J}_q = - \sum_a L_{ua} T \nabla \left(\frac{\mu_a}{T} \right) - \frac{L_{uu}}{T} \nabla T. \quad (10.2.6)$$

The values of the cell-averaged species density $\bar{\rho}_a$, velocity $\bar{\mathbf{u}}$, and energy \bar{e} are stored at the center of each finite volume cell. The transport coefficients such as the thermal diffusion coefficients and viscosity values are calculated for each cell using the corresponding species densities and temperature. As shown in Eq. (10.1.5), the terms on the right hand side of Eq (10.2.1), Eq (10.2.2), and Eq (10.2.3) must be evaluated at the boundaries of the finite volume cells where they can be used in order to integrate the simulation forward in time. In order to evaluate variables at the cell boundaries, values are linearly interpolated using the values at the center of neighbouring cells. This process is shown in the following equation,

$$A_{i+1/2} = \frac{A_i + A_{i+1}}{2}, \quad (10.2.7)$$

where a general property A is evaluated at the boundary between two cells (i and $i + 1$). The indexing scheme and locations corresponding to the the indexes i , $i + 1/2$, and $i + 1$ are illustrated in Fig. 10.2. For a uniform rectangular mesh, the linear interpolation reduces to the arithmetic average of the value of A at the center of the two neighbouring cells. The diffusive fluxes shown in Eq. (10.2.4), Eq. (10.2.5), and Eq. (10.2.6) require the gradients

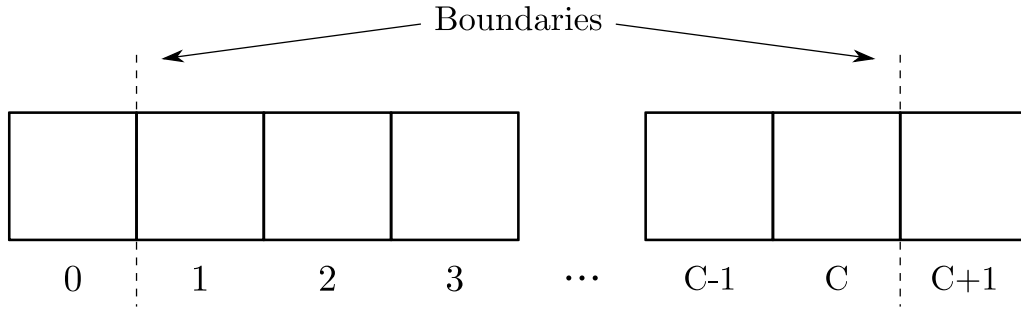


Figure 10.3: Diagram of a 1 dimensional finite volume simulation containing C regular rectangular cells labelled 1 to C . The location of the simulation boundaries are labelled and highlighted by dashed black lines. The cells labelled 0 and $C + 1$ are the “boundary cells” within which properties are modified in order to enforce the desired boundary conditions.

of the chemical potential $\nabla(\mu_b/T)$, mass-averaged velocity $\nabla \mathbf{u}$, and the temperature ∇T in order to be calculated. These values are calculated at the cell boundaries by taking a central difference numerical derivative as follows,

$$\frac{\partial}{\partial x} A_{i+1/2} = \frac{A_{i+1} - A_i}{\Delta_x}, \quad (10.2.8)$$

where Δ_x is the distance between the center of neighbouring cells in the x direction. The simulation is integrated forward in time using the forward Euler method which can be written as follows,

$$A_i(t + \Delta t) = A_i(t) + \Delta t \frac{\partial}{\partial t} A_i(t), \quad (10.2.9)$$

where the t is the current time, and Δt is the chosen timestep.

10.3 Boundary conditions

The conservation equations only apply within the simulation domain and cease to be valid at the simulation boundary. Therefore, in order to remain consistent, we extend the domain beyond the desired boundary and then apply constraints on the boundary cells in order to yield the desired boundary conditions. This is shown in Fig. 10.3 which shows a one-dimensional finite volume grid consisting of $C + 2$ total cells. The cells labelled 0 and $C + 1$ are fictitious boundary cells which lie outside of the domain of interest and are constrained in order to enforce the boundary conditions on the C other cells.

For a system containing S species, there are $S + 2$ independent variables consisting of the S different mass densities $\rho_{1,2,\dots,S}$ as well as the mass averaged velocity \mathbf{u} and the temperature T . We therefore require $S + 2$ constraining equations in order to solve for the $S + 2$ unknown independent variables in the boundary cell at every timestep.

The temperature boundary condition is implemented simply by fixing the value using

the following temperature Dirichlet boundary condition,

$$T_B = T_C, \quad (10.3.1)$$

where the value of the temperature at the boundary is fixed at a value of T_C , and $_B$ denotes a property at the simulation boundary. The simulation boundary refers to the boundary between the fictitious boundary cell and the simulation domain as shown in Fig. 10.3. Note that, in reality, the value of T_B is constrained by altering the value at the center of the fictitious boundary cell such that linear interpolation will yield the desired value of T_B . This is the case for all boundary conditions. Next, in order to ensure that there is zero flow of mass into or out of the simulation, and to ensure that the total mass of each species is conserved, each individual species velocity at the boundary is set using a no-slip and no-penetration boundary condition as follows,

$$\mathbf{u}_{a,B} = \mathbf{0} \quad \text{for all species } a = 1, 2, \dots, S. \quad (10.3.2)$$

Setting the individual species velocities to $\mathbf{0}$ at the boundary results in the overall mass averaged velocity also being equal to $\mathbf{0}$,

$$\mathbf{u}_B = \mathbf{0}. \quad (10.3.3)$$

If the simulation only considers one species then these statements are equivalent. So far, the temperature and mass averaged velocity at the boundary are constrained and, now, the S boundary density values must be constrained also. This is done using a simultaneous pressure-tensor-equality and zero-diffusion boundary condition. The first of these is extracted by examining the momentum equation at the boundary which is as follows,

$$\frac{\partial(\rho_B \mathbf{u}_B)}{\partial t} = -\nabla \cdot \rho_B \mathbf{u}_B \mathbf{u}_B - \nabla \cdot \mathbf{P}_B. \quad (10.3.4)$$

Substituting the value of the velocity at the boundary, using the no-slip/no-penetration boundary condition, means that the convective momentum term $\nabla \cdot \rho_B \mathbf{u}_B \mathbf{u}_B = 0$. As the boundary velocity is fixed, the term containing the time derivative will also vanish $\partial(\rho_B \mathbf{u}_B)/\partial t = 0$. This results in a condition of zero gradient in the pressure tensor at the boundary

$$\nabla \cdot \mathbf{P}_B = 0. \quad (10.3.5)$$

Although the boundary velocity is set to zero (and hence the time derivative is zero), the spacial derivative of the boundary velocity can be non-zero as the value of the velocity within the simulation varies as the simulation proceeds. In a completely stationary simulation, this boundary condition results in a condition of zero-gradient in the isotropic

pressure as follows,

$$\nabla \cdot p_B = 0. \quad (10.3.6)$$

In a mobile system, this condition shows that an isotropic pressure gradient must be established which counteracts any viscous forces caused by velocity gradients near to the boundary. Gradients are calculated by taking a central difference numerical derivative utilising the fictitious boundary cell. In a simulation containing $S = 1$ species, these 3 ($S + 2$) conditions are enough to fully specify the boundary cell.

The individual species velocities are a sum of the total mass averaged velocities and the individual diffusive flux of that species. When simulating $S = 1$ species, the diffusive flux is 0; however, this is not true for systems containing more than one species $S = 2+$. In this case we must also constrain the diffusion of species through the boundary as follows,

$$\mathbf{J}_{a,B} = 0 \quad \text{for all species } a = 1, 2, \dots, S, \quad (10.3.7)$$

in order to ensure that there is no loss or gain of mass through the system boundaries. The equation for the diffusive flux at the boundary is written as,

$$\mathbf{J}_{a,B} = - \sum_b L_{ab,B} T_B \nabla \left(\frac{\mu_{b,B}}{T_B} \right) - \frac{L_{au,B}}{T_B} \nabla T_B. \quad (10.3.8)$$

Substituting the condition of zero-diffusion results in additional constraining equations at the boundary where the density and temperature values at the simulation boundary must be set such that the rate of mutual diffusion and the rate of thermal diffusion are balanced resulting in zero net diffusion through the boundary. This is shown in the follow equation,

$$\sum_b L_{ab,B} T_B \nabla \left(\frac{\mu_{b,B}}{T_B} \right) = - \frac{L_{au,B}}{T_B} \nabla T_B. \quad (10.3.9)$$

For a simulation consisting of S species, this boundary condition results in S additional constraining equations for the boundary cell. In addition to the 3 constraining equations that we have previously found, this means that we have a total of $S + 3$ constraining equations for a system of $S + 2$ independent variables resulting in an overconstrained system. However, as was seen in Ch. 5, the S boundary fluxes sum to 0 as follows,

$$\sum_a \mathbf{J}_{a,B} = 0, \quad (10.3.10)$$

which means that we only need to ensure that $S - 1$ species boundary fluxes are equal to 0 in order to ensure that all boundary fluxes are, in fact, equal to 0, i.e., in a simulation with $S = 2$ species, it is only required to solve the diffusion boundary condition for the first species in order to fully specify the fluid properties at the boundary. The mutual

diffusion and thermal diffusion coefficients, as well as the species chemical potentials, are functions of temperature and density and the temperature is already constrained as per the previous temperature boundary condition. In this case, there is one unique set of S boundary density values which will satisfy the single pressure equality boundary condition as well as the $S - 1$ zero-diffusion boundary conditions. Practically, in order to solve for the boundary conditions in this model, the following objective function,

$$\sum_a^{S-1} |J_{a,B}| + |\nabla \cdot P_B|, \quad (10.3.11)$$

is minimised at every timestep.

10.4 Model validation

In order to validate the accuracy of the coupled hydrodynamic-kinetic theory model, results for hard-sphere fluids between two heated walls are compared with the results of MD simulations of identical systems. Comparisons of the two simulation techniques are shown in both the steady-state and the non-steady-state regimes. The simulation technique is evaluated by comparing the easily observable fluid properties of the mass density and the temperature over the length of the simulation.

System properties such as the temperature are easily available when using the hydrodynamic model as they are explicitly solved for using the energy conservation equation. However, when performing MD simulations, local values of the temperature, which make up the overall temperature profile, are not explicitly available and must be extracted manually using the known particle positions and velocities. A plug-in was written for the DynamO [2] simulation package which calculates the local density and temperature values within predefined bins in the simulation. In order to define the bins, the simulation is divided into some number of equal lengths along the axis parallel to heat transfer which in this case is the x -axis. The temperature is then calculated using the following equation,

$$T(x, t) = \frac{1}{3k_B N(x, t)} \sum_{j=1}^{N(x, t)} m_j \mathbf{v}_j^2, \quad (10.4.1)$$

where $T(x, t)$ is the temperature within the local bin at position x and time t , and $N(x, t)$ is the number of particles inside the same bin at time t . The density is calculated in a similar manner as follows,

$$\rho(x, t) = \frac{1}{V} \sum_{j=1}^{N(x, t)} m_j, \quad (10.4.2)$$

where $\rho(x, t)$ is the mass density within the local bin at position x and time t , and V is the volume of the local bin. Hence, the results of three-dimensional MD simulations are

averaged over the two dimensions which are perpendicular to heat transfer and can be compared with one-dimensional hydrodynamic simulations

10.4.1 Steady-state regime

MD simulations of both monocomponent and multicomponent hard-sphere fluids at total number densities of $n = 0.1$ are performed. Parallel heated walls are placed at either end of the simulation in the x -dimension. The walls are set to temperatures of $T_{\text{cold}} = 1.0$ and $T_{\text{hot}} = 1.2$. Simulations contain a total of $N = 10000$ hard-spheres which are initialised in an FCC lattice and are ran until the density and temperature profiles reach steady-state. The MD simulation box has an aspect ratio of $l_x/l_y = l_x/l_z = 20$ where l_x , l_y , and l_z are the lengths of the simulation in the x , y , and z dimensions respectively.

A one-dimensional simulation is then performed on a hard-sphere fluid with identical sphere parameters and the same density using the coupled hydrodynamic-kinetic theory model which is described in this chapter. The boundary temperatures in the hydrodynamic simulation are also set to $T_{\text{cold}} = 1.0$ and $T_{\text{hot}} = 1.2$. The hydrodynamic simulation is split into 100 separate finite volume cells. The hydrodynamic simulation is then also ran until it reaches steady-state and the results are compared.

Monocomponent system

The comparison between the monocomponent steady-state MD simulations and hydrodynamic simulation is shown in Fig. 10.4. Simulations are performed using hard spheres with a mass $m = 1$ and a diameter $\sigma = 1$. In the hydrodynamic model every cell is initialised with a density of $n = 0.1$, a velocity $u_x = 0$, and a temperature of $T = 1$ and the simulation was ran using a timestep of $\Delta t = 0.1$. The hydrodynamic model was ran for a total time of $t_{\text{HD}} = 10000$. The MD simulations are ran for a total of 6×10^7 events which corresponds to an approximate total time of $t_{\text{MD}} = 12000$. The MD results for the local temperature and density in each bin are averaged over 100 separate MD simulations and the error bars on the MD results represent the standard deviation over these simulations. Fig. 10.4 shows strong agreement between the temperature and density profiles of both simulation techniques. The temperature profile is approximately linear between the two boundary temperatures in both simulation methods. There is a small amount of spacial oscillation in the density profile for the hydrodynamic simulation; however, the hydrodynamic density profile closely matches the MD density profile which are both slightly non-linear.

Multicomponent system

Fig. 10.5 shows a comparison between the steady-state temperature and density profiles for a binary hard-sphere mixture with a diameter ratio of $\sigma_2/\sigma_1 = 0.5$ and a mass ratio of $m_2/m_1 = 0.125$. The system has a total number density of $n = 0.1$ and equal mol

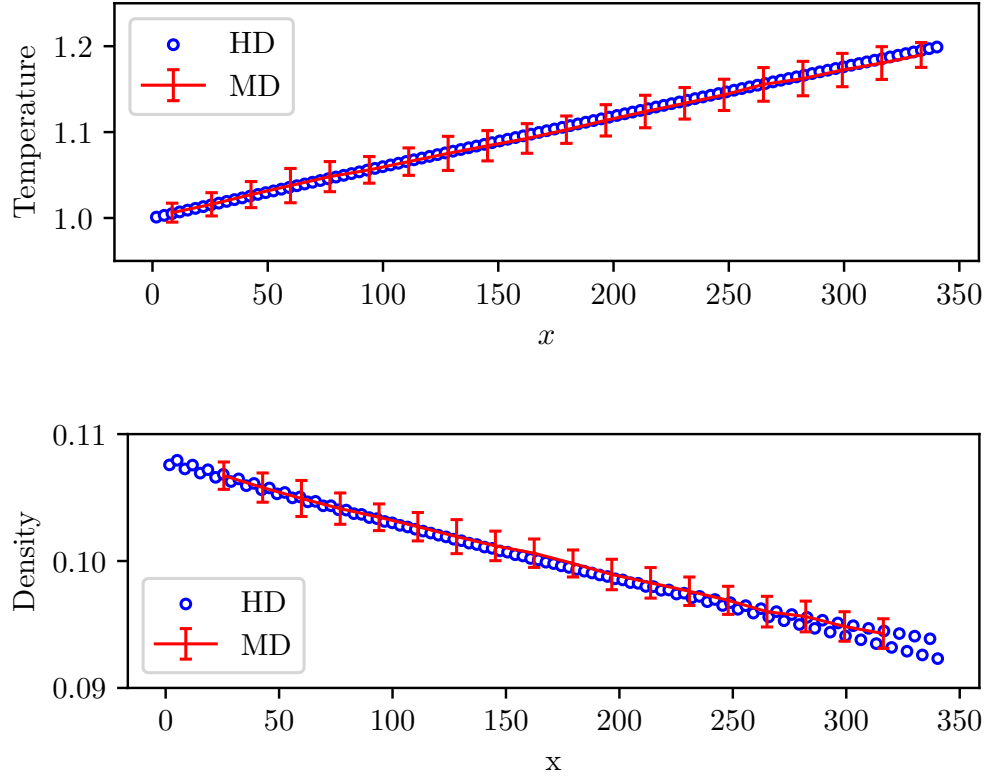


Figure 10.4: Temperature and density as a function of the distance between two heated walls for a monocomponent hard-sphere mixture. The heated walls are at temperatures of $T_{\text{hot}} = 1.2$ and $T_{\text{cold}} = 1.0$. The system is simulated using both MD (red line) and the coupled hydrodynamic-kinetic theory model (blue hollow circles). The density and temperature profiles are measured once the system has reached steady-state. The local temperature and density values for the MD simulation are averaged over 100 separate simulations and the error bars represent the standard deviation over those simulations.

fractions of both species ($x_1 = 0.5$ and $x_2 = 0.5$). All cells in the hydrodynamic model are initialised with species number densities of $n_1 = n_2 = 0.05$, velocities of $u_x = 0$, and temperatures of $T = 1$. The simulation is ran using a timestep of $\Delta t = 0.1$ and is ran for a total time of $t_{\text{HD}} = 10000$. Again, the MD simulations are ran for a total of 6×10^7 events corresponding to an approximate total time of $t_{\text{MD}} = 12000$ and results are averaged over 100 separate simulations. As in Fig. 10.4, the MD simulation predicts a linear temperature profile between the hot and cold wall temperatures. However, in this case the hydrodynamic model predicts a temperature profile which has a noticeably shallower gradient. Both models predict a differences in the concentration gradients of the two species as the result of thermal diffusion. However, the hydrodynamic model predicts a much more extreme separation of the concentration gradients, as well as significant spacial oscillation in the number density profile of species 1. The hydrodynamic and MD methods of simulation show significant disagreement in the case of multicomponent fluids and it is clear that more work must be done in order to ensure that the implementation of the hydrodynamic model is correct for multicomponent fluids.

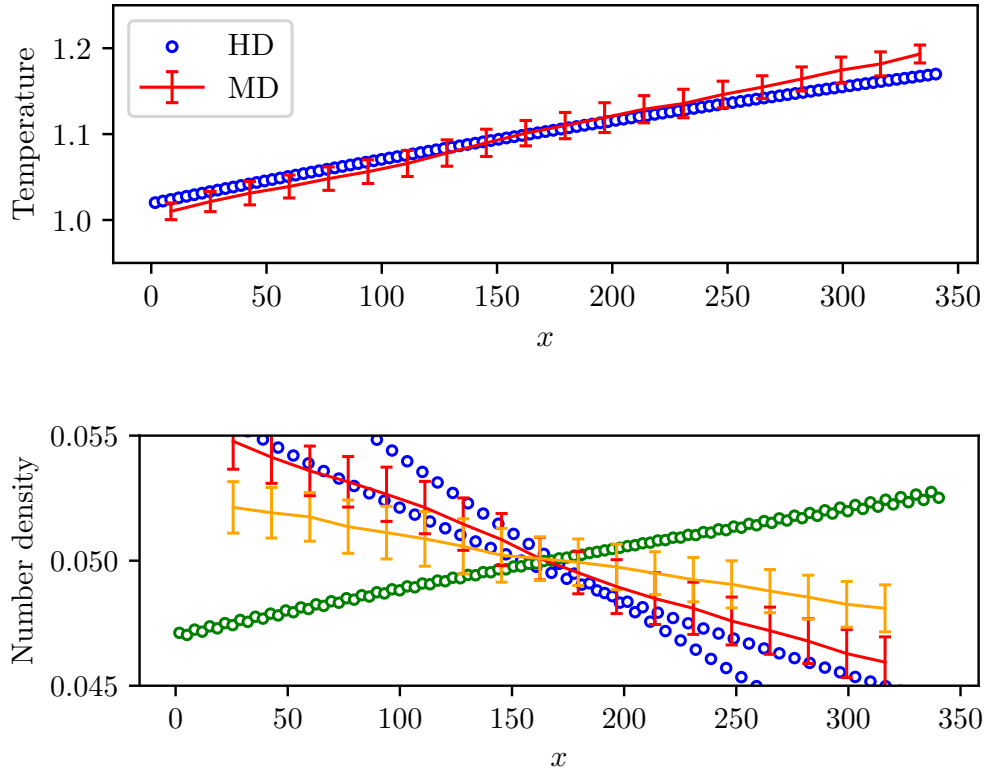


Figure 10.5: Temperature and species densities as a function of the distance between two heated walls for a multicomponent hard-sphere mixture. The heated walls are at temperatures of $T_{\text{hot}} = 1.2$ and $T_{\text{cold}} = 1.0$. The system is simulated using both MD and the coupled hydrodynamic-kinetic theory model. In the case of the temperature profile, the MD results are represented by red lines and the hydrodynamic results are represented by hollow blue circles. In the case of the species densities, the MD results for species 1 and 2 are given by red and orange lines respectively and the hydrodynamic results for species 1 and 2 are given by hollow blue and green circles respectively. The density and temperature profiles are measured once the system has reached steady-state. The local temperature and density values for the MD simulation are averaged over 100 separate simulations and the error bars represent the standard deviation over those simulations.

10.4.2 Transient regime

The ultimate goal of the hydrodynamic model is to simulate systems of hard-spheres in the transient regime as this is where it is possible for thermophoresis to cause large enhancements in the effective thermal conductivity of mixtures. In order to validate that the hydrodynamic model accurately captures the behaviour of hard-sphere fluids in the transient regime, MD and hydrodynamic simulations are performed which are similar to the validation simulations shown in Fig. 10.4, but, instead of focusing on the steady state solution, the focus is now on the agreement between the models at the onset of heat transfer. Parallel heated walls are located at either end of the simulation in the x -dimension; however, in this case, there is no temperature difference between the plates until time $t = 0$, when the temperature of one of the walls changes instantly. Temperature and density profiles of the MD and hydrodynamic simulations are then compared in the

moments after the change in wall temperature as the system is heading towards a new non-equilibrium steady state.

Monocomponent system

Monocomponent hard-spheres are simulated for a total reduced time of $t = 4000$ using MD and the hydrodynamic model. MD simulation are performed using $N = 10000$ hard-spheres at a number density of $n = 0.1$ and are performed in a simulation box with an aspect ratio of $l_x/l_z = l_x/l_y = 20$. Hard-spheres are initialised in a FCC lattice with 2 parallel heated walls at $\pm L_x/2$. Unlike the method used when trying to measure the steady-state conditions inside the simulation, the walls are both initially set to a reduced temperature of $T_{\text{wall}} = 1$. The MD simulation is then equilibrated using the unheated walls for $200N$ events. At this point ($t = 0$) the temperature of one of the walls is set to $T_{\text{hot}} = 1.2$ while the other remains at $T_{\text{cold}} = 1.0$. The simulation is divided in the x -direction into 25 bins where local temperatures and density values are calculated at different times over the course of a simulation using Eq. (10.4.1) and Eq. (10.4.2). The simulation is then restarted and is ran for 40 reduced time units. During this run, every 4 reduced time units, the calculated temperature and density values in each local bin are cumulatively summed. This cumulative sum is used in order to calculate time averaged temperature and density values for this particular 40 time unit window of the simulation. In addition to this time averaging, a total of 2000 separate MD simulations are performed and results are averaged over all simulations. The standard deviation in the local MD properties is calculated by taking the standard deviation over the 2000 separate MD simulations. When comparing to the hydrodynamic model, local time-averaged temperature and density values are compared to the equivalent hydrodynamic values at the average time over which the time-average is calculated. For example, local values which are averaged over the first 40 reduced time units (from $t = 0$ to $t = 40$) are compared to values from the hydrodynamic model at a reduced time of $t = 20$. This process is then repeated by restarting the simulation and running for the proceeding 40 reduced time units. This is repeated up to a total simulation time of $t_{\text{MD}} = 4000$.

All cells in the hydrodynamic simulation are initialised with number densities of $n = 0.1$, velocities of $u_x = 0$, and temperatures of $T = 1$. The temperatures at the simulation boundaries are set to $T_{\text{cold}} = 1$ and $T_{\text{hot}} = 1.2$ from the start as there is no need for equilibration when using a hydrodynamic approach. The simulation is ran using a timestep of $\Delta t = 0.01$ and is ran for a total time of $t_{\text{HD}} = 4000$. Data is stored periodically for comparison with MD.

Fig. 10.6 shows a comparison between the results of the hydrodynamic and the MD hard-sphere simulation at five separate points in time. The graphs show the evolution of the temperature and density profiles from a time shortly after the temperature gradient was applied at $t = 20$ to $t = 1220$. The graphs in the left column show the temperature profile in the simulation over time while the graphs in the right column show the evolution

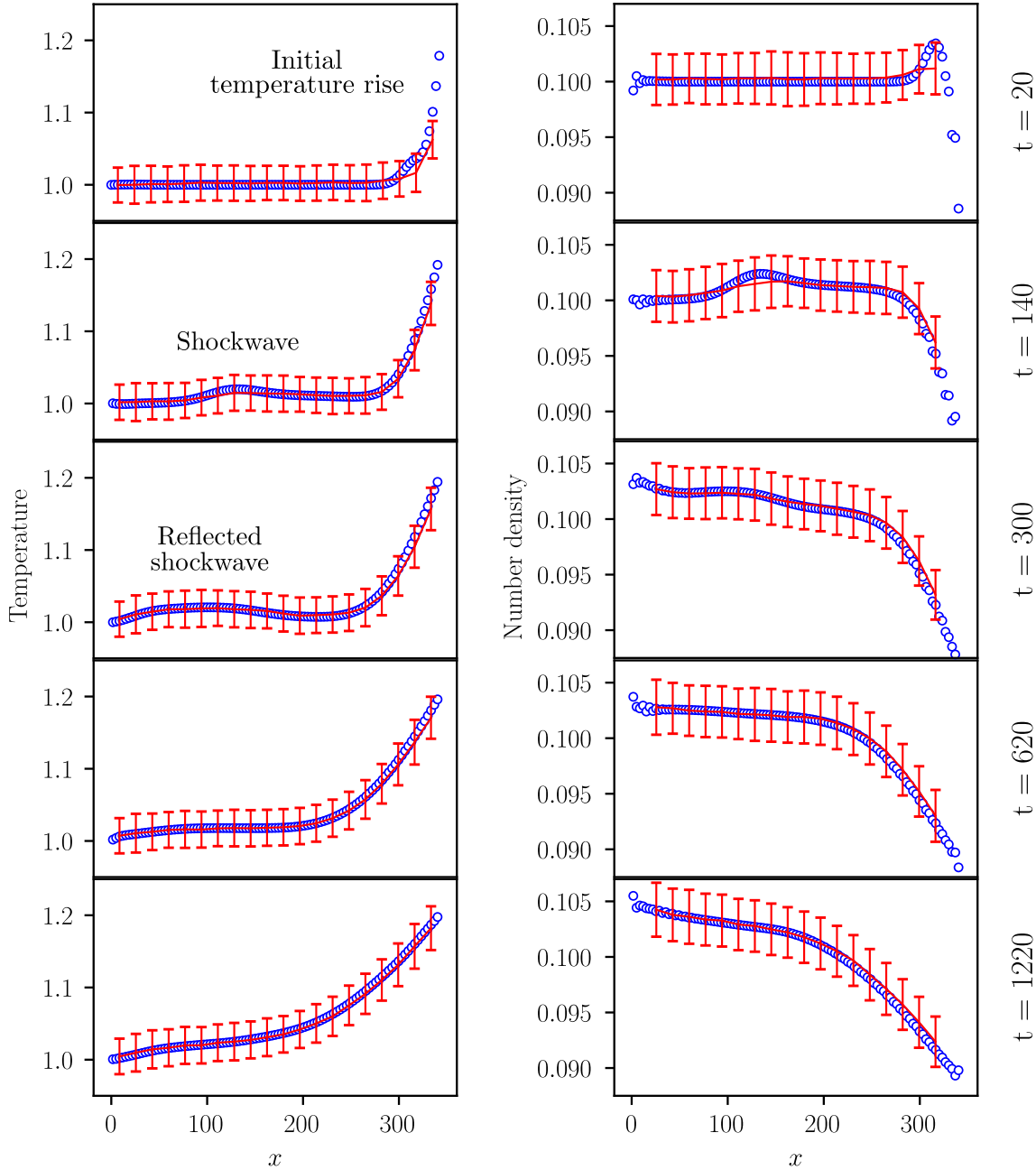


Figure 10.6: Temperature and density as a function of the distance between two heated walls for a monocomponent hard-sphere fluid at five points in time during a simulation ($t = 20$, $t = 140$, $t = 300$, $t = 620$, and $t = 1220$). The fluid is initially homogeneous with a density of $n = 0.1$ and a temperature of $T = 1$ where both heated walls are at temperatures of $T = 1$. At time $t = 0$ the temperature of one wall is changed to $T_{\text{hot}} = 1.2$ while the other wall remains at $T_{\text{cold}} = 1$. This system is simulated using both MD and the coupled hydrodynamic-kinetic theory model. The MD results are represented by red lines where the error bars represent the standard deviation of the local temperature or density calculated over 2000 separate MD simulations. The hydrodynamic model results are represented by hollow blue circles. Key features of the graphs such as the observed shockwave caused by the initial temperature change are labelled.

of the density profile over time. The first row of graphs show the simulation profiles at $t = 20$. At this point, the results of both the hydrodynamic and the MD simulations

show that the hot wall has begun to influence the simulation; the temperature of the fluid beside the hot wall has risen accordingly and as a result, the fluid density near the hot wall has dropped. Although the MD and hydrodynamic data broadly agree after this time, there are significant differences. The sharp density “spike” shown in the hydrodynamic simulation is not present to the same degree in the MD data. This density spike is a density shockwave travelling across the simulations induced by the sudden temperature change at the hot wall. The disagreement here is probably caused by the fact that the MD data is averaged over a long time relative to the speed of the shockwave while the hydrodynamic simulation represents an exact snapshot of the system at that point in time. If the shockwave travels fast relative to the time window over which the local MD density values are averaged, then the density spike will be spread over a larger length and appear artificially elongated compared to reality. The MD simulation also appears to lag behind the hydrodynamic simulation slightly in terms of the initial temperature increase near to the hot wall.

The second row of graphs in Fig. 10.6 show the temperature and density profiles at $t = 140$ in both simulation methods. The temperature and density profiles continue to evolve as heat is transported across the system from the hot wall. The shockwave travelling across the system is still clearly visible in both the density and temperature profiles as it travelling at the speed of sound towards the cold wall at the opposite end of the simulation. The agreement between the MD and hydrodynamic profiles is strong and the shockwave can be seen in both the MD and the hydrodynamic simulations. The hydrodynamic model accurately captures the rise of the fluid temperature near to the wall. The travelling temperature shockwave is also captured; although, MD data results show the shockwave as a shallower and wider temperature spike. As mentioned previously, this could be due to the fact that the local MD data is time-averaged over the period of time from $t = 120$ to $t = 160$ as opposed to the hydrodynamic data which is not. The MD and hydrodynamic density profiles show similar behaviour. The decrease in density near to the hot wall in the MD simulation is captured by the hydrodynamic model; however, the height of the density shockwave is significantly larger in the hydrodynamic results than in the case of MD. Noticeable spacial oscillations also present in the density profile after this time. This was also noted in Section 10.4.1 and likely represents a numerical issue with the model implementation.

The temperature and density profiles at $t = 300$ are shown in the third row of Fig. 10.6. At this point in time, the shockwave travelling through the hard-sphere system has reached the cold wall in the simulation and has reflected back, now travelling back through the simulation towards the hot wall. The agreement between the local density and temperature value for the MD and hydrodynamic simulations at this point in time is strong. The width and height of the shockwave in the MD results is captured accurately in the hydrodynamic simulation for both the temperature and density profiles. The continuing increase and decrease of the local temperature and density values respectively near to the heated wall

continues to be well captured by the hydrodynamic model; although, the MD results still appear to lag slightly behind the hydrodynamic results.

The final two rows of Fig. 10.6 show the MD - hydrodynamic comparison at $t = 620$ and $t = 1220$. At $t = 620$, the results of the hydrodynamic simulation are still in agreement with the MD results. At this point the shockwave has come into contact with both heated walls multiple times and has noticeably dissipated. This is reflected in both simulation methods. By $t = 1220$ the shockwave has all but disappeared from the simulation and the agreement between the simulation methods remains strong as the temperature and density profiles continue to evolve towards steady-state conditions.

This set of simulations demonstrates that the coupled hydrodynamic-kinetic theory model, which is presented in this chapter, accurately describes the time-evolution of hard-sphere fluids. For the system presented in this section, the short time results of the hydrodynamic model and MD, recorded moments after a large temperature gradient is imposed on a system, are in strong agreement. Even “extreme” phenomena such as shockwaves travelling through the system at the speed of sound are captured. This agreement is maintained at relatively long times as the system evolves towards steady-state.

Simulations of a multicomponent hard-sphere fluids in the transient regime are not performed in this thesis as a result of the fact that, at steady-state conditions, the MD and hydrodynamic results were not in agreement.

10.5 Conclusions and future Work

This chapter presents a coupled hydrodynamic - kinetic theory which solves the hard-sphere mass, momentum, and energy conservation equations, using Enskog theory in order to solve for the transport coefficients. The model is validated by comparing the simulation results with the results of direct NEMD simulation using DynamO [2]. Firstly, the results of the hydrodynamic model and MD are compared for a monocomponent hard-sphere fluid situated between two parallel heated walls at steady-state conditions. It is shown that there is agreement between the steady-state temperature and density profiles calculated using the two methods. Secondly, steady-state comparisons for a multicomponent hard-sphere fluid are performed. The results of the hydrodynamic model and MD simulation are shown to disagree significantly. In the future, work must be carried out to check that the model implementation is correct in order to determine if this is a theoretical error, or an error in calculation.

Relatively short simulations of monocomponent hard-spheres are then performed to validate the results of the hydrodynamic model in the transient regime. Temperature and density profiles, in the moments after a temperature gradient is imposed on the system, are calculated using MD and the hydrodynamic model. The results of the two methods are compared at different points in time during the simulations. At short times, after the temperature gradient is initially applied, and when the system is changing rapidly,

the two simulation methods agree strongly. The hydrodynamic model even describes the behaviour of shockwaves travelling across the system as a result of the initial large temperature change. At relatively long times, after initial shockwaves have dissipated and the system is evolving slowly towards steady-state conditions, the results of the two simulation methods continue to agree.

This chapter shows that a hydrodynamic description is valid for molecular systems which contain an extremely small number of particles. MD simulations which are performed in this chapter contain only $N = 10000$ hard-spheres and, yet, results shows that the behaviour of this model is well described by the coupled hydrodynamic - kinetic theory model. An interesting research question which could be investigated using this model is: At what number of particles does a molecular hard-sphere system cease to behave hydrodynamically?

The success of this model could call into question the use of other simulation techniques where the system of interest is well-described by the hard-sphere model. A wealth of simulation techniques are used in order to capture molecular effects, such as MD, direct simulation Monte Carlo [3] (DSMC), and lattice-Boltzmann [4]. This chapter shows that conventional hydrodynamics, in combination with a complete hard-sphere model, is a computationally efficient method of simulating hard-sphere behaviour.

In the future this model could also be used in order to simulate the transient heated wire experiment for gas mixtures (monocomponent or multicomponent gases). As discussed in Ch. 3, experimental measurements at short times are not fully understood and are often ignored in the final thermal conductivity calculation. Performing hard-sphere simulations of heat transfer in gases may give insight into the non-linear form of the wire temperature profile at short times and may, therefore, allow for more accurate measurements of gas thermal conductivity.

It was also mentioned, in Ch. 5, that higher order closures are available for the hydrodynamic equations. Formalising these equations in this way is known as Burnett or super-Burnett hydrodynamics. The results of this chapter strongly suggest that straightforward linear closures, which were used in this thesis, accurately capture the behaviour of hard-sphere systems (at least in the monocomponent case) and that there is, therefore, no need to utilise higher order gradients in the state variables.

10.5.1 Frequency-dependent thermal conductivity

The ultimate goal of the hydrodynamic - kinetic theory model, presented in this thesis, is to determine the timescale over which thermal diffusion effects in multicomponent fluids will significantly enhance the effective thermal conductivity. Determining this value will give an idea of how fast experimental measurements, using techniques such as the transient hot wire method, will need to be performed in order to access this enhanced thermal conductivity. This section showcases a method which could be used in order to gain insight into this value.

The enhanced initial thermal conductivity λ_I in multicomponent mixtures is valid for a system undergoing rapid changes in temperature. It is possible to create such a system through simulation by using heated walls at the boundaries which have oscillating temperatures. The analytical solution for the average temperature of a stationary material with constant density ρ , specific heat capacity c_p , and thermal conductivity k located between two heated walls located at $x \pm b$ with oscillating temperatures given by $T = T_0 + A \sin(\omega t)$ is developed in Appendix A and is given here as follows,

$$\bar{T}(t) = 2bT_0 + \frac{\sqrt{2}A}{\kappa} \frac{(e^{-2\kappa b} - e^{2\kappa b}) \sin\left(\frac{\pi}{4} - \omega t\right) + 2 \cos\left(\frac{\pi}{4} - \omega t\right) \sin(2\kappa b)}{e^{2\kappa b} + e^{-2\kappa b} + 2 \cos(2\kappa b)}, \quad (10.5.1)$$

where $\kappa = \sqrt{\omega/2\alpha}$, $\alpha = k/\rho c_p$, ω is the frequency of the heated wall temperature oscillation, and A is the amplitude of the heated wall temperature oscillation. Performing a simulation of a multicomponent hard-sphere fluid using the coupled hydrodynamic - kinetic theory model with identical oscillating temperature boundary conditions will allow an effective thermal conductivity to be fit to the resulting temperature profile using Eq. (10.5.1). Theoretically, as the frequency of the temperature oscillations is increased, and the system undergoes more rapid changes in temperature, the hard-sphere system should tend towards the state of zero concentration gradient, corresponding to the initial thermal conductivity λ_I . The rate of increase of the fitted effective thermal conductivity could give insight into the timescale which is required in order to access the enhanced thermal conductivity experimentally.

References

- [1] P. Wesseling. *Principles of computational fluid dynamics*. Springer, 2000.
- [2] M. N. Bannerman, R. Sargant, and L. Lue. “DynamO: a free $\mathcal{O}(N)$ general event-driven molecular dynamics simulator”. In: *J. Comput. Chem.* 32.15 (2011), pp. 3329–3338.
- [3] G. A. Bird. *Molecular gas dynamics*. Clarendon press, 1976.
- [4] S. Succi. *The lattice-Boltzmann equation for fluid dynamics and beyond*. Oxford University Press, 2001.

NOVEL METHOD FOR HARD-SPHERE FREE ENERGY DETERMINATION

This chapter is completed in collaboration with Dr. Leo Lue. In particular, Dr. Lue provided assistance with deriving the relationship between the tether cell collision rate and the system entropy, as well as with the equivalence of the tethered and untethered systems. Craig Moir is responsible for performing all MD simulations and data analysis as well as writing the chapter.

Free energy dictates the equilibrium properties of a material, including its phase transitions. For fluids, thermodynamic integration with respect to the system density can be used to accurately determine the system free energy with respect to the ideal gas state. This can be easily implemented with either MD or Monte Carlo (MC) methods; however, for solids which are separated by a transition from the fluid state, thermodynamic integration cannot be directly used to obtain the free energy with respect to the ideal gas state as there is no continuous path between these states. Consequently, other methods must be employed.

Hoover and Ree originally introduced the single occupancy (SO) cell model [1] to demonstrate the existence of a first-order melting transition for hard sphere systems and quantitatively determined the fluid and solid coexistence densities. In the SO model, space is partitioned into cells based on Voronoi polyhedra created from the sites of the crystal lattice under investigation (e.g., face-centered cubic) and the center of each sphere is required to remain in its respective cell. This model lowers the entropy of the low density state and forces it to remain ordered. This reduction in fluid entropy softens the freezing transition into a continuous pressure change which means that the crystalline SO state can then be connected to the ideal gas state. Thus the free energy of the unmodified hard-sphere crystal can be determined using this method. Woodcock [2, 3] used MD to simulate the SO model to determine the entropy of the face-centered cubic, body-centered cubic, and hexagonal close-packed structures of hard sphere systems.

A variation of this method was later proposed by Speedy [4] where spheres are instead restricted to remain within a set distance from their respective lattice sites, rather than within Voronoi polyhedra (i.e., they are tethered to a lattice). This tether particle model (TPM) uses spherical square-wells as the tether potential which allows the more efficient

simulation of cell collisions and simplifies the theoretical analysis. This basic approach has been generalised to arbitrarily shaped particles and implemented using an event-driven MD algorithm [5]. This bounding cell MD algorithm was successfully used to accurately calculate the free energy of different crystal phases, as well glassy states, of hard sphere systems.

Many other approaches use a tethering potential to tie particles to a tether lattice in order to determine the free energy of the untethered crystal systems. In the Einstein crystal approach [6, 7], particles are tethered to sites on a perfect lattice using a harmonic potential. The stiffness of the potential can be continuously adjusted, which is used in order to relate the system back to a perfect Einstein crystal which has an exactly known free energy. This continuous transformation between the system and the perfect Einstein crystal can be used to compute the free energy of system. Other, more elaborate methods that involve the use of tethers have been developed in order to efficiently calculate the free energy, such as the self-referential methods of Sweatman et al [8–10], the Schilling-Schmid algorithm [11], and the interface pinning method [12]. These are compared and reviewed by Sweatman [13]. More generally, tether models can be considered as confining the motion of the system to a particular region in phase space. Typically only the positional degrees of freedom are tethered; however, restricted velocity dynamics have also been employed [14, 15] and may be considered a form of tethering.

In this chapter, the tether model of Speedy [4] is revisited and a novel approach for calculating free energy in any state, including fluids, glasses, or crystals, is derived. As a demonstration of the efficiency of the approach, new high accuracy free energy calculations for the hard sphere crystal are performed and the fluid-solid transition conditions are determined. In Section 11.1, the collision statistics and thermodynamics of Speedy tethering model are described, including the ideal tether model, where the spheres do not interact with each other, and its relationship to the standard ideal gas model. It is demonstrated that the tether model provides a continuous path between the fluid and solid phases, avoiding a first order phase transition, for certain ranges of the tether length. In Section 11.2, the collision rates of tethered systems, both with other spheres and with the tethering potential that keeps the spheres within their cells, are related to the geometry of phase space. In particular, these collision rates are directly related to the surface areas of the region of phase space that is accessible by the system. These relations are used to develop a method to compute the free energy of hard sphere systems via an integration in tether length. These methods are used, in Section 11.3, to determine the free energy of hard sphere systems at various densities within the fluid and solid phases. The calculated free energies are then used to predict the fluid-solid coexistence point for hard-spheres. These calculations are all found to agree well with those previously given in the literature. Finally, the key conclusions of this chapter are given in Section 11.5, along with a discussion of directions for future work.

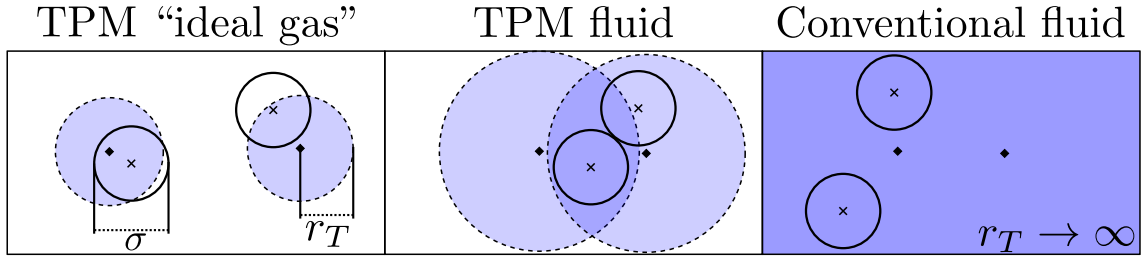


Figure 11.1: Schematic diagram of a two-dimensional tethered particle system in three different states: The “ideal” TPM (left) has particles tethered such that no particle-particle interactions can occur. The TPM fluid (middle) allows interactions and the conventional fluid (right) is simply the limit of infinite tether length. Black circles represent particles with diameter σ and black crosses represent the position of the particle centers. Dashed, shaded circles represent the confining tether cells with radius r_T whose centers are indicated with black diamonds.

11.1 Tethered systems

This work considers a system of hard sphere particles where a square-well tether potential is used which is equal to zero within a spherical region around the tether point and infinitely large outside this region. This forces the center of each particle to remain within a tether “cell” and is precisely the model introduced by Speedy [4]. A schematic representation of this system is presented in Fig. 11.1. For later derivations, it is convenient to consider that the tether length r_T allows each particle center in the system to explore a tether volume V_T . This allows the definition of a tether packing fraction $\phi_T = \rho V_T$ (where $\rho = N/V$ is the particle number density), which may take values greater than one if tether volumes overlap, as depicted in Fig. 11.1. Throughout this chapter, the number density is referred to by the symbol ρ in order to avoid conflict with other variables.

At sufficiently low densities, where the cells are separated by more than a particle diameter σ , particles cannot interact with each other. This implies there is a minimum density $\rho_{T,0}$ for particle interactions which is easily calculated if the tether lattice’s arrangement known. For example, for particles tethered to a face-centered cubic (FCC) lattice, it is given by the following expression,

$$\rho_{T,0}^{\text{FCC}} \sigma^3 = \max \left(0, \left[2^{1/6} - \left(\frac{6\phi_T}{\pi} \right)^{1/3} \right]^3 \right). \quad (11.1.1)$$

The max function prevents negative densities when tether cells become close-packed (i.e. $\phi_T \geq \sqrt{2}\pi/6$). An equivalent minimum tether radius at which interactions will occur can also be defined,

$$r_{T,0}^{\text{FCC}} \sigma^{-1} = \max \left(0, \left[2^{5/2} \rho \sigma^3 \right]^{-1/3} - 1/2 \right). \quad (11.1.2)$$

For $\rho < \rho_{T,0}$ (or equivalently $r_T < r_{T,0}$) there are no particle-particle collisions, only

tether collisions. The system thus corresponds to an “ideal” state, where the particles are independent of each other and the pressure p is given by the ideal gas law (i.e. $\beta p = \rho$). It should be noted that the system is not ergodic in this limit unless the system is thermalized (i.e., with a stochastic thermostat).

The “ideal” TPM differs from the standard ideal gas system for N particles in a volume V , as each particle can only explore a restricted volume V_T and the particles are distinguishable. The difference between the entropy of the “ideal” tethered particle model $S_T^{(\text{ideal})}$ and a conventional ideal gas $S^{(\text{ig})}$ is then given by the following expression,

$$S_T^{(\text{ideal})} - S^{(\text{ig})} = k_B \ln \frac{\Omega_T^{(\text{ideal})}}{\Omega^{(\text{ig})}} = k_B \ln \left(N! \frac{\phi_T^N}{N^N} \right) \quad (11.1.3)$$

where $\Omega_T^{(\text{ideal})}$ and $\Omega^{(\text{ig})}$ are the configurational partition functions for the “ideal” TPM and the conventional ideal gas, respectively, and identified separately as follows,

$$\Omega^{(\text{ig})}(N, V) = \frac{V^N}{N!} \quad \Omega_T^{(\text{ig})}(N, V) = V_T^N. \quad (11.1.4)$$

Comparing the expressions, a factor of $N!$ is missing in the TPM system as particles are assigned to a particular cell, thus there is no permutation of the particle ordering for each configuration. In periodic systems, care must be taken in how the tether volume, V_T , interacts with its periodic images but this complexity is avoided here by considering relatively short tether lengths relative to the system size.

In all cases, the entropy of the low-density “ideal” tether state is decreased by the presence of the tether when compared to the untethered system. This effect persists at moderate values of the tether length $r_T > r_{T,0}$, or density $\rho > \rho_{T,0}$, where particle-particle interactions take place and which is referred to here as the tether “fluid” state. At high densities, or as r_T becomes large, the system is dominated by particle-particle collisions and the tether cell collisions become exceedingly rare. In the crystalline limit, the effect of the tether potential disappears almost entirely well before $r_T \rightarrow \infty$ (assuming the crystal state of the untethered model prevents diffusion); therefore, the effect of the tether potential is to decrease the entropy (and thus the stability) of the fluid state over the crystalline state which is unaffected by the presence of the tether. This presents an interesting opportunity to construct a continuous thermodynamic path between the ideal tether state and the crystalline state.

11.1.1 Fluid-solid transition in the tethered particle model

To illustrate the influence of the tether potential, calculations are performed for systems of N hard spheres at constant absolute temperature T with diameter σ and mass m using DynamO [16]. As results are presented in reduced units, the only parameters in which the system has a non-trivial dependence are the reduced density $\rho \sigma^3$ and the

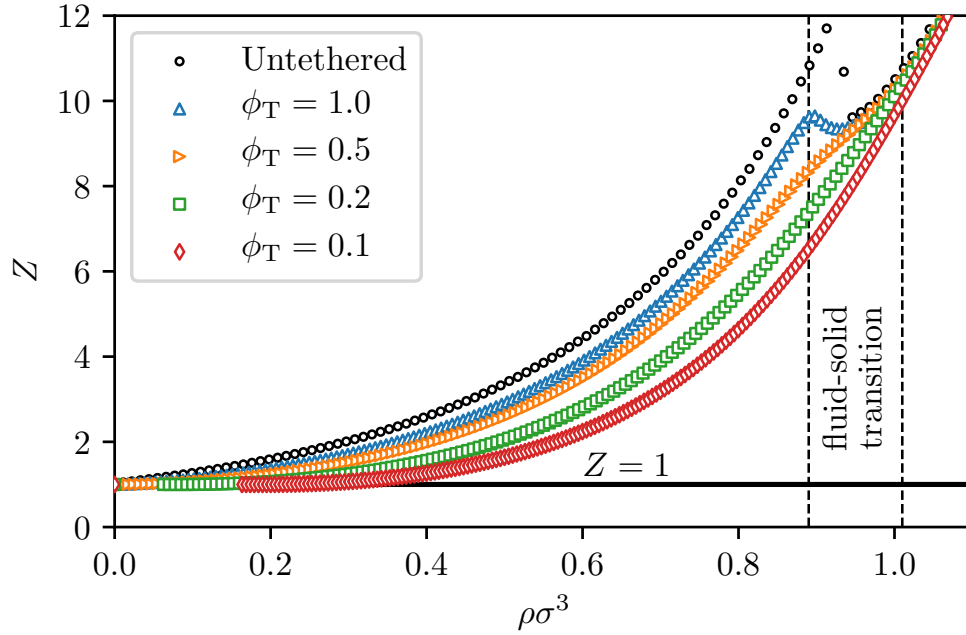


Figure 11.2: The compressibility factor Z as a function of reduced density $\rho\sigma^3$ for hard sphere TPM systems with $\phi_T = 0.1$ (blue), $\phi_T = 0.2$ (orange), $\phi_T = 0.5$ (green), and $\phi_T = 1$ (red). Data are shown for simulations containing $N = 2916$ spheres and are only run above $\rho > \rho_{T,0}$. Black circles represent conventional (untethered) hard sphere simulations. The solid black line indicates ideal compressibility. Dashed black lines highlight the untethered hard-sphere fluid-solid transition zone. The standard deviation in pressure measurements are smaller than the symbol size.

reduced tether length r_T/σ . Simulations use an Andersen thermostat to provide thermalisation; however, the only effect is to improve sampling as r_T approaches $r_{T,0}$, and the results are equivalent to systems without the thermostat once system size effects are taken into account. The thermostat mean free time is controlled to be approximately 1% of the total event count, which was chosen as it is a small additional computational cost of processing the thermostat events while increasing the equilibration rate.

The variation of the compressibility of the TPM as a function of density is shown in Fig. 11.2 for different values of ϕ_T in comparison to the conventional hard-sphere system (i.e. with no tethering) and that of an ideal gas where $Z = 1$. Simulations are not run below the minimum interaction density $\rho_{T,0}$ for each corresponding value of ϕ_T , and it is clear that the compressibility factor is equal to the ideal value at this point. At moderate densities where $\rho > \rho_{T,0}$, the smaller tether volumes restrict the motion of the particles and thus reduce the particle-particle collision rate which is directly proportional to the system pressure. It also is clear that at higher densities, above the crystal transition, that all systems converge to the conventional hard sphere crystal system, highlighting their equivalence in this limit.

For the untethered hard sphere system, there is a first order transition from a fluid phase to a solid phase as highlighted in Fig. 11.2. As expected, the simulations display

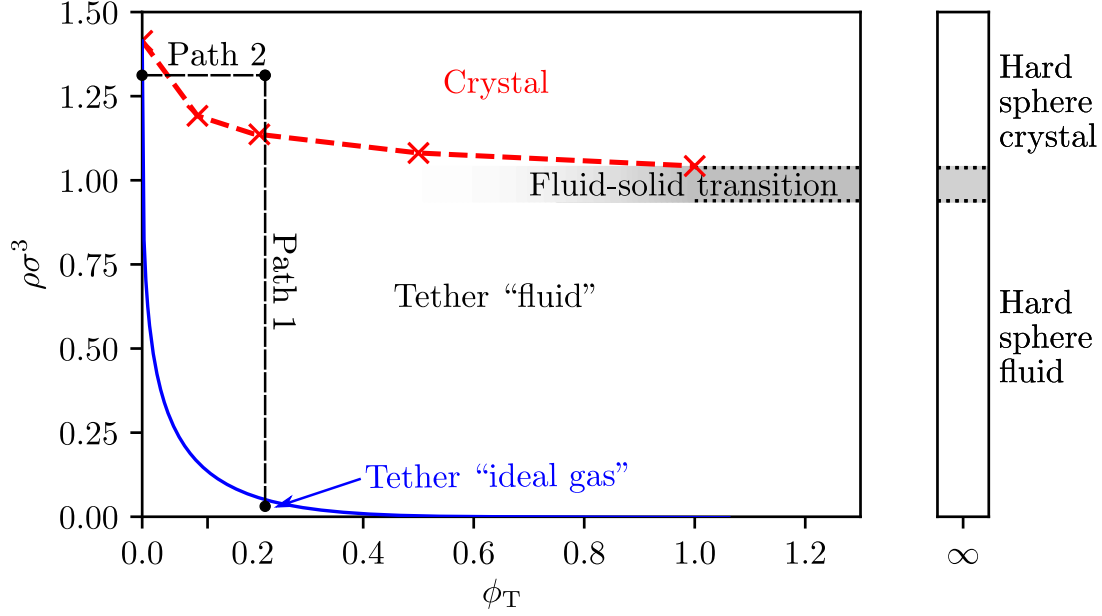


Figure 11.3: An illustration of the reduced density $\rho\sigma^3$ and tether packing fractions ϕ_T at which the tethered hard-sphere system enters various “phases”. The crosses (red) indicate the upper density where a $N = 2916$ system run for 2×10^9 events had more than 100 tether events. The dashed line (red) is added as a guide to the eye to indicate that the systems above this density have crystallized on the tether lattice and particles cannot interact with their tether anymore. The point at $\phi_T = 0$ is exact and equal to the FCC close packing density $\rho\sigma^3 = \sqrt{2}$. The lower solid curve (blue) indicates when the tether length prevents inter-particle interactions, thus it denotes the “ideal” tether state. The grey area is a guide to the eye and indicates where first-order transitions are observed numerically.

a metastable fluid branch due to the finite size and duration of the simulations; however, as ϕ_T decreases the system appears to approach an extension of the crystalline branch with no indication of a first-order transition appearing for $\phi_T \approx 0.5$ and lower. This is confirmed by examining the density derivative of the pressure which remains positive for $\phi_T = 0.5$ and lower values. Thus, for sufficiently small values of ϕ_T , there appears to be a continuous thermodynamic path between the high-density hard-sphere solid and the “ideal” tether model limit. This thermodynamic path can be easily understood in terms of a phase diagram for the tether model system, and an illustration of this type of path is given by path 1 in Fig. 11.3. Thermodynamic integration along this path can be used to establish the entropy (and thus free energy) of the crystalline state with respect to the ideal tether model, as given in Eq. (11.1.3).

The phase diagram of Fig. 11.3 indicates the approximate crystal region where tether events are so rare (in this case less than 10^{-7} tether events per event) that the system closely approximates the hard sphere crystal. The exact boundary of the ideal tether state is shown as a solid blue curve in Fig. 11.3, and it is immediately apparent that the ideal and crystalline states can be continuously connected using thermodynamic integration along a second path using tether length as the variable (see path 2 in Fig. 11.3).

11.1.2 Thermodynamic integration

In general, the entropy of an untethered model fluid at any density can be obtained via thermodynamic integration with reference to the ideal gas state,

$$\frac{S(\rho)}{Nk_B} = \frac{S^{(\text{ig})}(\rho)}{Nk_B} - \int_0^\rho \frac{d\rho'}{\rho'} [Z(\rho') - 1]. \quad (11.1.5)$$

Thus, determining the thermodynamics of hard-sphere *fluids* can be reduced to determining their pressure-density relationship. This relationship between the entropy and the pressure is only valid for bulk systems in equilibrium. Consequently, straightforward thermodynamic integration cannot be used reliably across first order phase transitions to access the crystal state; however, this type of integration is applicable to path 1 of Fig. 11.3 with the addition of the difference in entropy of the ideal states (Eq. (11.1.3)),

$$\frac{S_T(\rho)}{Nk_B} = \frac{S^{(\text{ig})}(\rho)}{Nk_B} - \int_{\rho_{T,0}}^\rho \frac{d\rho'}{\rho'} [Z_T(\rho') - 1] + \ln \left(N! \frac{\phi_T^N}{N^N} \right). \quad (11.1.6)$$

The thermodynamic integration is chosen to begin at $\rho_{T,0}$, where particles begin to interact (i.e. Eq. (11.1.1)), as the integral is zero below this density. The only approximation required to determine the crystal state free energies of the untethered system is to assume the equivalence to the tethered system at sufficiently high densities,

$$\lim_{\rho\sigma^3 \rightarrow \sqrt{2}} S_T(\rho) \rightarrow S(\rho). \quad (11.1.7)$$

The above limit is approximately satisfied when the collision rate with the cell boundary nearly vanishes; in this work, this is taken to be where tether events are less than 1 in 10^7 of the total events, which is denoted by the red dashed line in Fig. 11.3. Normal thermodynamic integration in the untethered crystal system is then applied in order to integrate up or down the solid curve from that reference point to determine all crystal state free-energies.

11.2 Phase space geometry

The configurational phase space $\Gamma = \{\mathbf{r}_1, \mathbf{r}_2, \dots, \mathbf{r}_N\}$ of a hard sphere system is schematically depicted in Fig. 11.4(a). Excluded volume interactions between the spheres will prohibit the system from being within regions in phase space where spheres overlap (depicted by the dark area in Fig. 11.4), thus confining the trajectory of the system to within an “accessible” region (white area in Fig. 11.4(a)). The hypervolume Ω of this accessible phase space is directly related to the entropy of the system by the Boltzmann-Planck equation $S = k_B \ln \Omega$. The boundary between the allowed and disallowed regions of phase space (depicted by the red line in Fig. 11.4) corresponds to two spheres being in contact with each other and this boundary has an associated hypersurface area Σ .

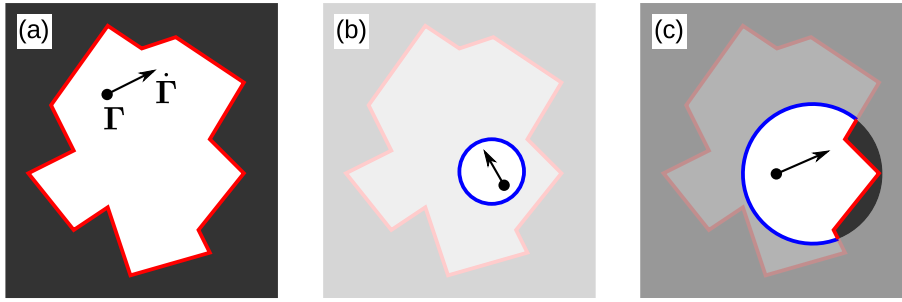


Figure 11.4: A schematic depiction of configurational phase space for (a) a hard sphere system, (b) a tightly tethered hard sphere system, and (c) a loosely tethered hard sphere system. The dark grey areas are regions of phase space that are disallowed due to sphere-sphere overlaps while the white areas correspond to the phase space volume accessible to the system. The interaction surfaces that bound the accessible region are highlighted in blue for the tether potential while inter-particle interaction surfaces are highlighted in red.

A hard sphere system evolving through time traces a straight line through phase space as there are no forces between collisions. Collisions between spheres correspond to the trajectory intersecting a point on the phase space boundary where the colliding pair of spheres are in contact; the trajectory will then reflect from the boundary and continue to travel in a straight line until it encounters another boundary in phase space. The process is then repeated.

When a square-well tether potential is applied, the accessible region of phase space becomes an intersection of the N tether volumes and the accessible volume of the untethered system. An illustration of two systems with different tether lengths is given in Figs. 11.4(b) and (c). The tether restricts the motion of the system and the system trajectory can now potentially reflect off the tether boundary (see the blue line in Figs. 11.4(b) and (c)). For short enough tether lengths, the system can only interact with the tether (see Fig. 11.4(b)); however, at longer tether lengths, portions of the sphere-sphere collision boundary will intrude into the accessible region (see Fig. 11.4(c)). If the exposed hypersurface area of the tether potential (see the blue line in Fig. 11.4(c)) can be measured, it can be numerically “extruded” by varying the tether length, and thus the accessible volume can be measured. The following details the specifics of this approach, and how collision rates might be linked to hypersurface areas in phase space.

11.2.1 Collision rates and hypersurface areas in phase space

If the system is ergodic, the hypersurface area of the various boundaries that confine the system to a particular region of phase space are directly related to the rate at which the system collides with the boundary. In this case, the expression for the collision rate $\dot{\mathcal{N}}$ that the system makes with a section of the phase space boundary of area Σ can be written

as follows,

$$\dot{\mathcal{N}} = \rho_{\Omega} \Sigma (\dot{\mathbf{r}} \cdot \hat{\mathbf{n}}_{\Sigma}), \quad (11.2.1)$$

where $\hat{\mathbf{n}}_{\Sigma}$ is a unit vector that is normal to the surface pointing outward from the accessible phase space volume, and ρ_{Ω} is the number density of systems in phase space. As only one system is considered here, $\rho_{\Omega} = 1/\Omega$. This leads to the first main result of this section:

$$\frac{\Sigma}{\Omega} = \frac{\dot{\mathcal{N}}}{\langle \dot{\mathbf{r}} \cdot \hat{\mathbf{n}}_{\Sigma} \rangle}. \quad (11.2.2)$$

The ratio of the hypersurface area to the accessible phase space volume is directly related to the collision rate of the system with this hypersurface, divided by the mean velocity of its approach to this hypersurface. Therefore, the various collision rates give an indication of the relative exposed hypersurface areas of each type of event (i.e. collision between spheres or collision between a sphere and its tether potential).

To determine the accessible volume Ω_T of phase space for the tethered model, the hypersurface area Σ_T associated with the tether interactions can be extruded by moving it slightly outwards in a direction normal to the hypersurface (i.e. parallel to $\hat{\mathbf{n}}_{\Sigma_T}$). Due to the spherical nature of the tether potential used in this study, this extrusion is easily achieved by increasing the tether length by an infinitesimal distance dr_T :

$$d\Omega_T = \Sigma_T dr_T. \quad (11.2.3)$$

This relation holds true as the tether potential hypersurface can only be accessed by the system if it appears in the accessible phase space volume of the untethered model (see Fig. 11.4) which then becomes the accessible region of the tethered model upon extrusion. A change of variables then directly relates this change in accessible volume to the change in the entropy of the system,

$$k_B^{-1} dS_T = d \ln \Omega_T = \frac{\Sigma_T}{\Omega_T} dr_T = \frac{\dot{\mathcal{N}}_T}{\langle \dot{\mathbf{r}} \cdot \hat{\mathbf{n}}_{\Sigma_T} \rangle} dr_T. \quad (11.2.4)$$

A straightforward integration yields the entropy change of a tethered system with a change in tether length,

$$S_T(r_{T,2}) - S_T(r_{T,1}) = k_B \langle \dot{\mathbf{r}} \cdot \hat{\mathbf{n}}_{\Sigma_T} \rangle^{-1} \int_{r_{T,1}}^{r_{T,2}} dr_T \dot{\mathcal{N}}_T. \quad (11.2.5)$$

The system is assumed to be at constant temperature so that the “velocity” $\dot{\mathbf{r}}$ of the system through phase space is given by the Maxwell-Boltzmann distribution. This implies that the velocities of the each of the spheres are independent of each other and also given by

the Maxwell-Boltzmann distribution,

$$f(\mathbf{v}) = (2\pi\beta m)^{-3/2} e^{-\beta m v^2/2}.$$

As each individual tether acts separately on a single particle, the surface of phase space associated with it is parallel to the degrees of freedom (dimensions) that correspond to the other particles. Therefore, during an intersection with a tether hypersurface other particles do not contribute to $\dot{\mathbf{\Gamma}} \cdot \hat{\mathbf{n}}_{\Sigma_T}$ and only the velocity of the confined particle is relevant. Additionally, only its component that is normal to the surface contributes, and consequently, the average phase trajectory velocity into the tether boundary is given as follows,

$$\langle \dot{\mathbf{\Gamma}} \cdot \hat{\mathbf{n}}_{\Sigma_T} \rangle = \langle \mathbf{v} \cdot \hat{\mathbf{n}} \rangle = (2\pi\beta m)^{-1/2}. \quad (11.2.6)$$

Combining this with Eq. (11.2.5) leads to the result that entropy changes as a function of tether length can be determined by simply monitoring the tether collision rate during a series of simulations at varying tether lengths.

To reconnect the tethered system to the untethered system for the purpose of computing its entropy there are two equivalences which can be utilised. The first arises in the crystalline state where the untethered system is confined to a phase space volume which is relatively localised around the tether lattice due to the immobilisation of the particles. In this case, a system with a sufficiently long tether has an entropy which is identical to the untethered system as it will explore the same accessible phase space volume.

Combining Eq. (11.2.6) and (11.2.5) gives the following expression,

$$S = \lim_{r_T \rightarrow \infty} S_T(r_T) = k_B N \ln \left(\frac{4\pi r_{T,0}^3}{3} \right) + k_B (2\pi\beta m)^{1/2} \int_{r_{T,0}}^{\infty} dr_T \dot{\mathcal{N}}_T, \quad (11.2.7)$$

where the integration has been shifted to start at the onset of particle interactions for computational efficiency. The practical usefulness of this expression depends on the tether event rate approaching zero (i.e., $\dot{\mathcal{N}}_T \rightarrow 0$) at some finite value of r_T so that the integral can be truncated which is not the case for fluid systems.

The method can be adapted for use in the fluid state through the second equivalence: both the tethered and untethered models will have identical interparticle exclusions in phase space, thus contribution to the entropy is identical in the limit of infinite tether length,

$$S - S^{(ig)} = \lim_{r_T \rightarrow \infty} \left(S_T(r_T) - S_T^{(ideal)}(r_T) \right). \quad (11.2.8)$$

Applying Eq. (11.2.5) twice, for the tethered and ideal tethered system, gives the follow-

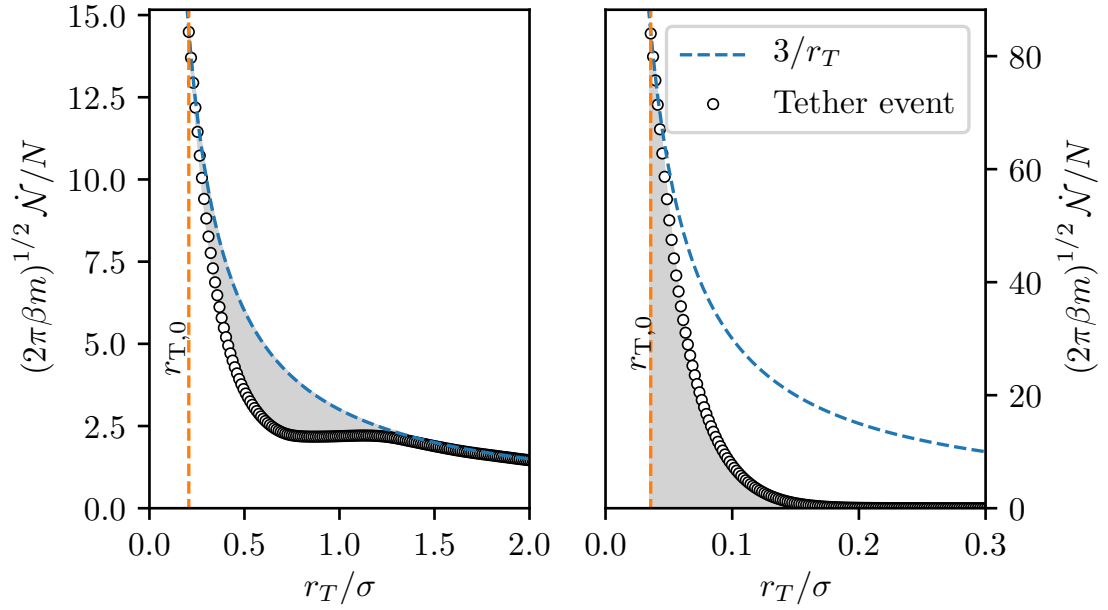


Figure 11.5: The variation of the tether event rate \dot{N}_T as a function of the tether length r_T/σ for an $N = 2916$ hard sphere system tethered to an FCC lattice at a reduced density of (a) $\rho\sigma^3 = 0.5$ and (b) $\rho\sigma^3 = 1.2$. The (blue) dashed line represents the reduced ideal tether event rate of Eq. (11.2.10). In (a), the grey shaded area between the ideal event rate and the measured tether event rate shows the integral of Eq. (11.2.9) used to calculate the entropy of fluid systems. The shaded area below the measured cell event rate in (b) shows the integral of Eq. (11.2.7) used when calculating the solid entropy. The vertical red dashed line shows the minimum cell radius r_T at which it is possible for particles to interact as given by Eq. (11.1.2).

ing identity,

$$S - S^{(ig)} = k_B (2\pi\beta m)^{1/2} \int_{r_{T,0}}^{\infty} dr_T \left(\dot{N}_T - \dot{N}_T^{(ideal)} \right), \quad (11.2.9)$$

where the lower bound of the integral is $r_{T,0}$ as below this value, the kernel of the integral is zero. The ideal rate of tether events $\dot{N}_T^{(ideal)}$ can also be obtained via straightforward kinetic arguments,

$$(2\pi\beta m)^{1/2} \dot{N}_T^{(ideal)} = \frac{dN}{r_T}. \quad (11.2.10)$$

Thus Eq. (11.2.7) provides a thermodynamic integration path for crystalline state points while Eq. (11.2.9) provides a path for fluid state points.

Whether Eqs. (11.2.7) or (11.2.9) are practically useful depends on how quickly the integrals converge. To explore this, simulation results for the tether collision rate are presented in Fig. 11.5 for a fluid system and a crystal system. It is found that both integrals converge remarkably quickly.

11.3 Calculation of the entropy

In this section, we present estimates for the entropy of hard sphere systems using the two methods which are described in the previous sections. In the first, MD simulations are run at constant ϕ_T and the sphere density is varied; this is referred to as method 1. In the second approach, simulations are run at constant density with varying tether lengths; this is referred to as method 2. All simulations were initialized in an FCC grid, and the tether cell for each particle was centered on the FCC lattice site for that particle. The tether cells are spherical with radius r_T ($\phi_T = 4\pi\rho r_T^3/3$). Simulations were run using $N = 500, 864, 1372, 2048$, and 2916 particles, and simulations were performed 10 times in order to estimate the standard deviation in the compressibility measurements. The size dependence of the calculated results are examined, and these results are compared with values from the literature. Finally, the free energy estimates are used to determine the fluid-solid coexistence point.

11.3.1 Method 1

For method 1, simulations were performed at 4 separate cell volume fractions $\phi_T = 0.1, 0.2, 0.5$, and 1.0 . Each cell volume fraction ϕ_T corresponds to a different final density value at which the system ceases interacting with the tether cells. Simulations were performed at 200 separate densities spaced evenly from $\rho_{T,0}(\phi_T)$ to a value at which particles collide with the tether cells with a negligible frequency and the system is equivalent to the conventional hard-sphere system. This final cell collision rate was verified after the simulations were completed. Measurements of the density at which the tether event fraction falls below 10^{-7} are given in Fig. 11.3. The maximum densities used in this chapter are $\rho\sigma^3 = 1.21, 1.18, 1.13$, and 1.06 , corresponding to values of $\phi_T = 0.1, 0.2, 0.5$, and 1.0 , respectively. Simulations were initially equilibrated for $10000N$ collisions before a production run of 3×10^8 events.

The entropy is calculated using Eq. (11.1.6) where the integration is performed using the trapezoidal rule and the individual entropy values obtained using this method are shown in Table 11.1. In each entropy calculation, there were no collisions with the tether cells at the maximum density value in any of the 10 individual simulations verifying that the tether cells no longer have any influence over the system. The calculated entropy of the TPM system at this density is therefore equal to the entropy of the non-tethered hard sphere system (see Eq. (11.1.7)).

Figure 11.6 shows the calculated entropy at a density of $\rho\sigma^3 = 1.13$ ($\phi_T = 0.2$) as a function of $1/N$, showing a significant size dependence. Final entropy values were obtained via linear interpolation to infinite system size against $1/N$ as shown. The extrapolated infinite size entropy values using this method are shown in Table 11.4 as well as reference values for comparison. No values for the hard sphere entropy were found in the literature at these densities. Here, comparison values are calculated by integrating

Table 11.1: Calculated entropy $(S - S^{(\text{ig})})/(Nk_B)$ for different values of N for constant tether cell volume fraction integration (method 1).

N	$\rho\sigma^3 = 1.06$	$\rho\sigma^3 = 1.13$	$\rho\sigma^3 = 1.18$	$\rho\sigma^3 = 1.21$
500	-5.15503(19)	-5.99523(16)	-6.69344(20)	-7.17123(18)
864	-5.15981(12)	-5.99971(13)	-6.69753(15)	-7.17538(11)
1372	-5.16218(10)	-6.00206(09)	-6.69983(10)	-7.179(5)
2048	-5.16369(09)	-6.00342(08)	-6.70099(08)	-7.17898(05)
2916	-5.16461(09)	-6.00424(07)	-6.70186(07)	-7.17983(04)
∞	-5.16652(08)	-6.00608(04)	-6.70356(07)	-7.18161(06)

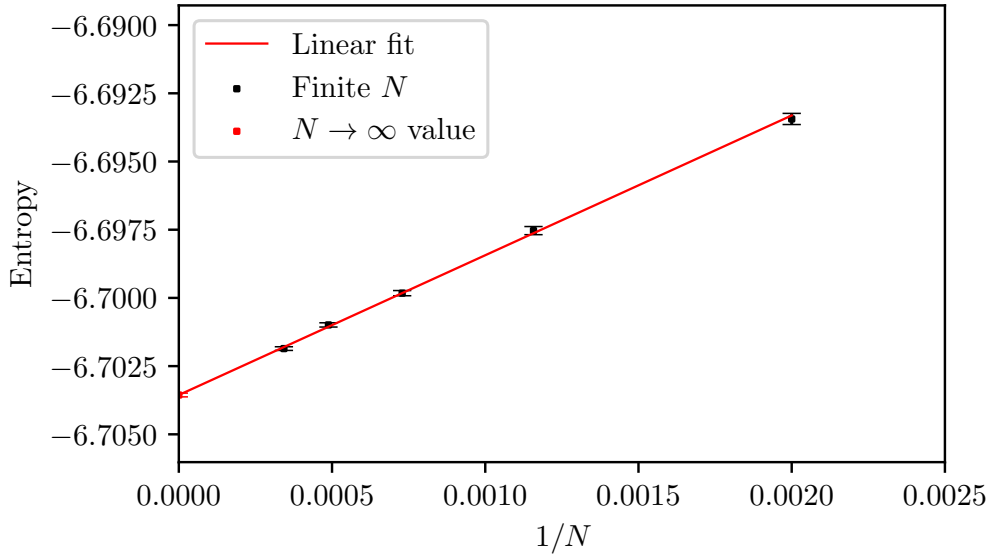


Figure 11.6: Entropy as a function of particle number N calculated using simulations with a tether cell volume fraction of $\phi_T = 0.2$. This entropy value corresponds to a hard sphere density of $\rho\sigma^3 = 1.13$. Black circles show the entropy calculated using simulations with $N = 500, 864, 1372, 2048$, and 2916 hard spheres. The red line shows a linear fit to the data using last squares minimization. The red circle shows the extrapolated $N \rightarrow \infty$ entropy value.

along the solid branch using

$$\frac{S(\rho)}{Nk_B} = \frac{S(\rho_{\text{ref}})}{Nk_B} - \int_{\rho_{\text{ref}}}^{\rho} \frac{d\rho'}{\rho'} Z(\rho'), \quad (11.3.1)$$

where ρ_{ref} is the density of the reference state and $S(\rho_{\text{ref}})$ is the entropy of the reference state. In this case, the averaged value of $S(\rho_{\text{ref}})/(Nk_B) = 4.9590 \pm 0.0002$ at $\rho_{\text{ref}}\sigma^3 = 1.04086$, as given by Pieprzyk et al [17], is used. The hard-sphere solid equation of state

is estimated using a modification of the equation of state proposed by Speedy [18]

$$Z_{\text{Solid}} = \frac{3}{1-w} + \frac{1}{c_1 w + c_2} + A e^{B(1-w)} + C e^{D(1-w)} + E \quad (11.3.2)$$

where $w = \rho/\rho_{\text{cp}}$ (with $\rho_{\text{cp}}\sigma^3 = \sqrt{2}$ the FCC close packing density) is a reduced number density, and the coefficients have been determined [17] to be $c_1 = 1$, $c_2 = 3/2$, $A = 0.061622$, $B = 6.151$, $C = 3.8437 \times 10^{-5}$, $D = 27.72$ and $E = -0.49541$. Entropy values agree with the corresponding reference values, although the values are outwith each others error bands. The entropy values calculated in this work are also consistently lower than their corresponding reference values.

11.3.2 Method 2

Proceeding now to method 2 (constant sphere density ρ with varying tether length r_{T}), simulations were performed at density values of $\rho\sigma^3 = 0.5, 1.04086, 1.15$, and 1.2 . Simulations were run at 200 separate tether lengths spaced evenly from $r_{\text{T},0}$ to a tether radius at which the tether collision rate is observed to decay exponentially towards 0 in the case of a hard sphere solid, or the collision rate of the ideal TPM in the case of a hard sphere fluid. The maximum values of r_{T} used here are $r_{\text{T,max}}/\sigma = 2.5, 0.55, 0.4$, and 0.3 , corresponding to $\rho\sigma^3 = 0.5, 1.04086, 1.15$, and 1.2 , respectively.

For low values of the cell radius $r_{\text{T}} \rightarrow r_{\text{T},0}$, where spheres primarily interact with the cells, the system must be thermalised in order to achieve a cell collision rate which is equal to the ideal collision rate. If the system is in the ideal TPM state, and is not thermalised, then spheres will perpetually reflect off two opposing edges of the spherical cell on a fixed path according to the initially assigned velocity and will never sample the entire available space as there is no influence of separate spheres which could change their trajectory. All simulations are thermalised using an Andersen thermostat [19] at a temperature of $T = 1$ with a fraction of 0.01 thermalising events. Simulations are initially run for $1000N$ equilibration events before a production run of 10^8 events.

The difference between the measured cell collision rate and the ideal TPM collision rate is shown in In Fig. 11.7. Note that there remains a small fraction of tether events in the system and, therefore, the entropy of the TMP system at this tether radius is not equal to the entropy of the conventional, non-tethered hard-sphere system. The two collision appear to approach each other approximately exponentially. Therefore, the entropy in the limit that $r_{\text{T}} \rightarrow \infty$ is estimated by fitting an exponential equation to the collision rate (blue line in Fig. 11.7). These entropy corrections ΔS_{corr} are shown in Table 11.3. Figure 11.9 shows the calculated entropy at a density of $\rho\sigma^3 = 1.15$ as a function of $1/N$. As in the first method, the entropy value at infinite system size $N \rightarrow \infty$ is obtained using linear interpolation with $1/N$. All entropy values calculated using this method are shown in Table 11.2. The entropy at a density of $\rho\sigma^3 = 0.5$ was calculated using Eq. (11.2.9), and entropy values at densities of $\rho\sigma^3 = 1.04086, 1.15$, and 1.2 were calculated using

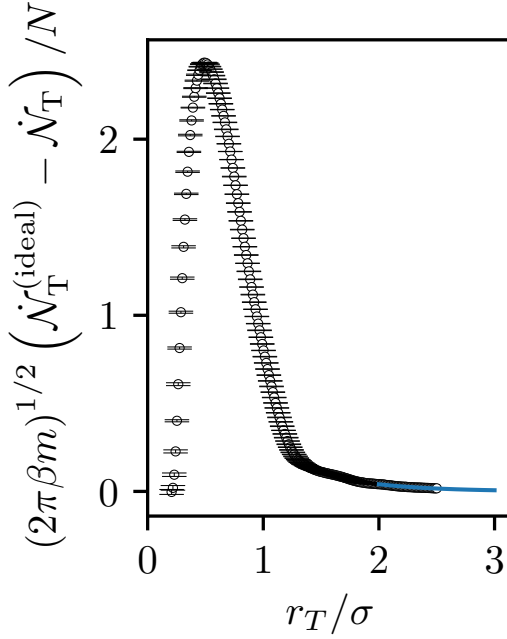


Figure 11.7: Deviation of tether event rate from the ideal tether event rate as a function of the cell radius for a hard sphere system at $\rho\sigma^3 = 0.5$ with $N = 2916$ spheres (hollow circles). The solid line is an exponential fit to the event rates at $r_T/\sigma > 1.4$. This fit is used to estimate the integral of Eq. (11.2.9) as $r_T \rightarrow \infty$.

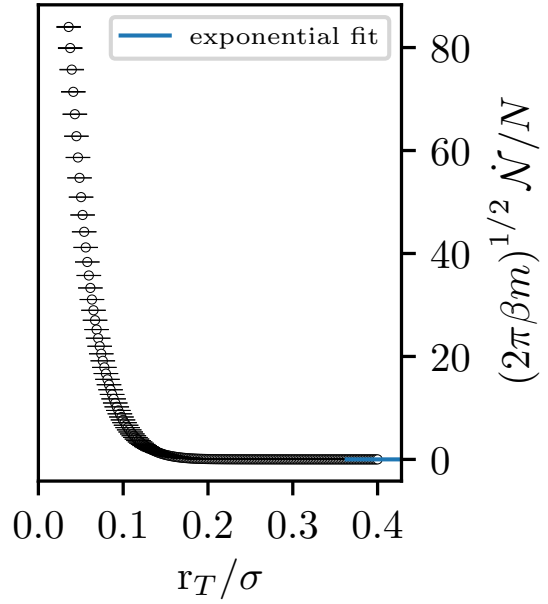


Figure 11.8: Tether event rate as a function of the cell radius for a hard sphere system at $\rho\sigma^3 = 1.15$ (hollow circles) with $N = 2916$ spheres. The solid line is an exponential fit to the final 10% $r_T/\sigma \gtrsim 0.25$ of the tether event rate data. This fit is used to estimate the integral of Eq. (11.2.7) as $r_T \rightarrow \infty$.

Eq. (11.2.7). Integration was performed using the trapezoidal rule.

Table 11.4 shows the entropy values at infinite system size alongside reference values taken from literature for comparison. At the fluid density value $\rho\sigma^3 = 0.5$, the calculated entropy value of $(S - S^{(ig)})/(Nk_B) = 0.15298 \pm 0.00006$ is in good agreement with the value reported by Schilling and Schmid [11] of $(S - S^{(ig)})/(Nk_B) = 0.152 \pm 0.002$. At the commonly used density value of $\rho\sigma^3 = 1.04086$, the entropy is in agreement with the value given by Ref. [17]; however, the values are outside their respective uncertainty bounds. At a density of $\rho\sigma^3 = 1.15$, the calculated entropy is in good agreement with the value reported by Vega and Noya [20] and is well within the reported uncertainty. No literature value for comparison at a density value of $\rho\sigma^3 = 1.2$ was found; therefore, a reference was calculated by integrating along the solid branch as described above. In this case the calculated entropy is in agreement with the reference; however, the values lie slightly outwith their respective uncertainty bounds.

Thermodynamic integration along the solid branch is used in order to collapse all of the calculated solid entropy values onto a single density value of $\rho\sigma^3 = 1.04086$ and take an overall average. The entropy is calculated at a single density with Eq. (11.3.1)

Table 11.2: Calculated entropy $S/(k_B T)$ for different values of N for constant density, varying tether radius integration (method 2).

N	$\rho\sigma^3 = 0.5$	$\rho\sigma^3 = 1.04086$	$\rho\sigma^3 = 1.15$	$\rho\sigma^3 = 1.2$
500	0.1439(6)	-4.9427(5)	-6.2551(5)	-6.9987(5)
864	0.1476(6)	-4.9489(6)	-6.2621(5)	-7.0059(6)
1372	0.1496(6)	-4.9526(4)	-6.2660(4)	-7.0091(6)
2048	0.1507(6)	-4.9542(4)	-6.2680(6)	-7.0117(4)
2916	0.1515(5)	-4.95563(32)	-6.2691(5)	-7.0128(4)
∞	0.15298(6)	-4.95816(16)	-6.27208(12)	-7.01576(18)

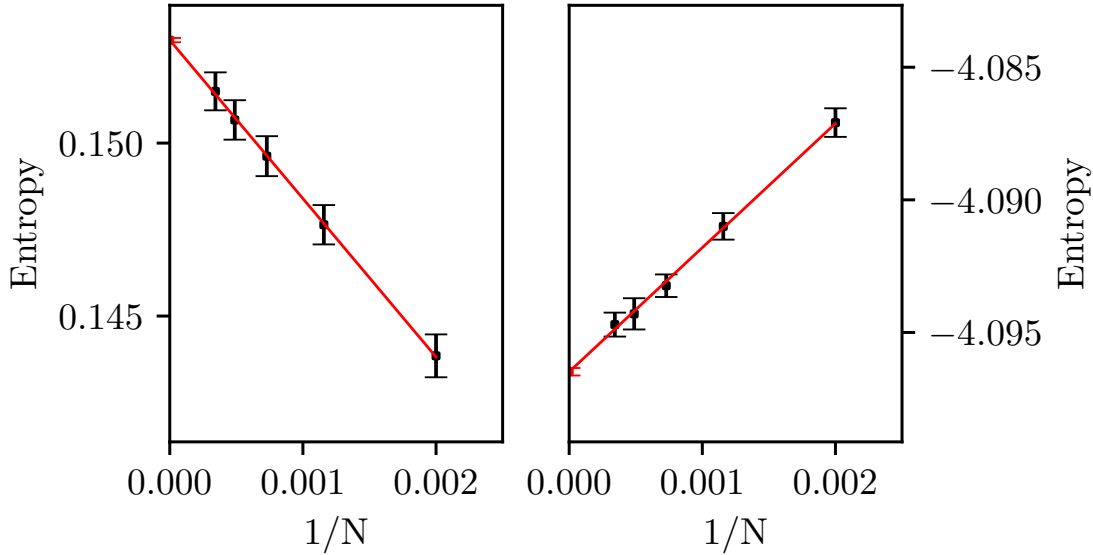


Figure 11.9: Entropy as a function of particle number N for systems at a density of $\rho\sigma^3 = 0.5$ (left) and $\rho\sigma^3 = 1.15$ (right). Black circles show the entropy calculated using simulations with $N = 500, 864, 1372, 2048$, and 2916 hard spheres. The red line shows a linear fit to the data using least squares minimization. The red circle shows the extrapolated $N \rightarrow \infty$ entropy value.

using the values quoted in Table 11.4 as the reference values (ρ_{ref} and $S(\rho_{\text{ref}})$). The solid phase compressibility is estimated using Eq. (11.3.2). The entropy calculated at $\rho\sigma^3 = 0.5$ is omitted from the average value, as it is not in the solid phase. The point at $\rho\sigma^3 = 1.06$ was also excluded, as it is still influenced by the first order fluid-solid phase transition, as shown in Fig. 11.2. The overall average entropy value is calculated to be $(S - S^{(\text{ig})})/(Nk_B) = -4.95803 \pm 0.00005$ at $\rho\sigma^3 = 1.04086$.

Figure 11.10 shows the deviation of the calculated solid entropy values calculated in

Table 11.3: Calculated entropy for different values of N for constant density, varying tether length integration (method 2) showing the entropy calculated with and without including the correction calculated by integrating the exponential fit to the data to $r_T \rightarrow \infty$.

N	$\rho\sigma^3$	$S_u/(Nk_B)$	$\Delta S_{\text{corr}}/(Nk_B)$	$S_{\text{tot}}/(Nk_B)$
500	0.5	0.1516(4)	-0.0078(5)	0.1439(6)
864	0.5	0.15531(35)	-0.0077(5)	0.1476(6)
1372	0.5	0.1572(4)	-0.0075(4)	0.1496(6)
2048	0.5	0.1584(4)	-0.0077(4)	0.1507(6)
2916	0.5	0.1591(4)	-0.0076(4)	0.1515(5)
500	1.04086	-4.94789(27)	0.0052(5)	-4.9427(5)
864	1.04086	-4.95196(28)	0.0031(6)	-4.9489(6)
1372	1.04086	-4.95432(30)	0.00174(23)	-4.9526(4)
2048	1.04086	-4.95545(28)	0.00128(23)	-4.9542(4)
2916	1.04086	-4.95638(29)	0.00076(13)	-4.95563(32)
500	1.15	-6.26027(34)	0.0052(4)	-6.2551(5)
864	1.15	-6.26518(31)	0.0031(4)	-6.2621(5)
1372	1.15	-6.26779(27)	0.00181(33)	-6.2660(4)
2048	1.15	-6.26947(34)	0.0014(5)	-6.2680(6)
2916	1.15	-6.26999(30)	0.00092(34)	-6.2691(5)
500	1.2	-7.00417(34)	0.0055(4)	-6.9987(5)
864	1.2	-7.00914(32)	0.0033(5)	-7.0059(6)
1372	1.2	-7.01141(32)	0.0023(5)	-7.0091(6)
2048	1.2	-7.01296(28)	0.00123(31)	-7.0117(4)
2916	1.2	-7.01384(29)	0.00101(31)	-7.0128(4)

this work, as well as values from literature, from the solid entropy calculated via thermodynamic integration (see Eq. (11.3.1)) along the solid branch using the average entropy value calculated in this work as the reference entropy value. The entropy calculated at a density of $\rho\sigma^3 = 1.06$ ($\phi_T = 1.0$) is an outlier when compared to other entropy values calculated in this work which cluster relatively close to the the reference solid branch values ($\Delta S = 0$). This could be due to the fact that ϕ_T is large enough for the first order fluid solid transition to still have a significant effect on this system. Entropy values at all other density values in this work appear to closely follow the solid entropy branch as predicted by Eq. (11.3.2) [17]. Entropy values at $\rho\sigma^3 = 1.099975$ and $\rho\sigma^3 = 1.15$ given by Vega and Noya [20] agree closely with the predictions using thermodynamic integration.

Table 11.4: Extrapolated entropy values for the hard sphere system for various number densities. Entropies are calculated using the two methods described in this work: density integration with constant tether cell volume fraction (method 1) and tether length integration at constant density (method 2). Values are compared to reference values from literature. The symbol † denotes a case where no literature comparison could be found. In this case the reference value is given by thermodynamic integration along the solid branch using Eq. (11.3.1) using the reference free energy given by Pierczyk et al. [17]. During the integration, solid compressibilities are estimated using Eq. (11.3.2).

$\rho\sigma^3$	$(S - S^{(\text{ig})})/(Nk_B)$	Reference
Method 1		
1.06	$-5.16652(8)$	$-5.16886(20)^\dagger$
1.13	$-6.00608(4)$	$-6.00686(20)^\dagger$
1.18	$-6.70356(7)$	$-6.70432(20)^\dagger$
1.21	$-7.18161(6)$	$-7.18249(20)^\dagger$
Method 2		
0.5	$0.15298(6)$	$0.152(2)$ [11]
1.04086	$-4.95816(16)$	$-4.9590(2)$ [17]
1.15	$-6.27208(12)$	$-6.273(2)$ [20]
1.2	$-7.01576(18)$	$-7.01699(20)^\dagger$

A number of studies report hard-sphere entropy values at a density of $\rho\sigma^3 = 1.04086$ as shown in Fig. 11.10. These values [20–23] agree to within their uncertainty values, however they lie well outwith the values (both directly calculated and averaged) in this work relative to their uncertainty.

11.4 Fluid-solid coexistence

The hard-sphere coexistence point is calculated using thermodynamic integration along with the condition of equal chemical potential μ and pressure p [7]. For monocomponent hard sphere systems, the chemical potential μ may be written in terms of the entropy, S , and compressibility factor Z , which are both functions of the number density ρ

$$\beta\mu = \beta\mu^{(\text{ig})} - \frac{S(\rho) - S^{(\text{ig})}(\rho)}{N k_B} + Z(\rho) - 1. \quad (11.4.1)$$

Equation (11.3.1) is used to integrate down the solid curve using Eq. (11.3.2) in order to predict the solid compressibility. The average entropy of $(S - S^{(\text{ig})})/(Nk_B) = -4.95803 \pm 0.00005$ at $\rho\sigma^3 = 1.04086$ calculated in this work is taken as the reference

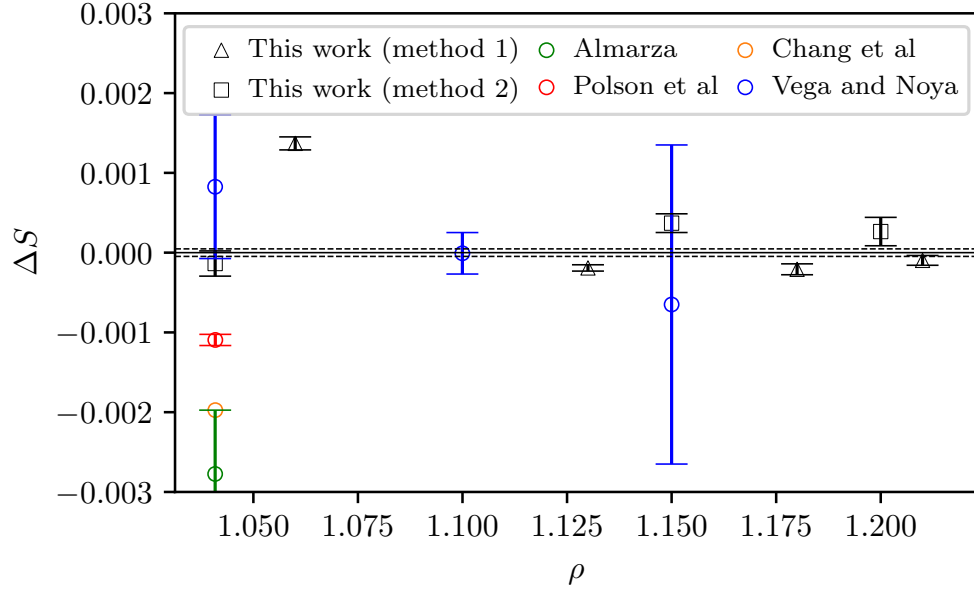


Figure 11.10: Deviation of entropy values calculated in this chapter, along with literature values [20–23], from the entropy calculated with Eq. (11.3.1) using the average entropy value of $(S - S^{(\text{ig})})/(Nk_B) = -4.95803 \pm 0.00005$ at $\rho\sigma^3 = 1.04086$ as the reference value and integrating up or down the solid curve using Eq. (11.3.2) in order to predict the solid entropy.

point for the integration. In order to obtain the fluid entropy and calculate the fluid chemical potential, a modified version of the hard-sphere fluid EOS originally produced by Kolafa, Labik, and Malijevsky [24] is used. It is given by Pieprzyk et al. [17] as

$$Z_{\text{Fluid}} = 1 + 4x + 6x^2 + 2.3647684x^3 - 0.8698551x^4 + 1.1062803x^5 - 1.1014221x^6 + 0.66605866x^7 - 0.0363343x^8 - 0.20965164x^{10} + 0.10555569x^{14} - 0.00872380x^{22} \quad (11.4.2)$$

where $x = \zeta/(1 - \zeta)$, and $\zeta = \pi\rho\sigma^3/6$ is the sphere packing fraction is used. Figure 11.11 shows chemical potential as a function of pressure for the hard-sphere system in the vicinity of the coexistence point. The standard deviation in the coexistence chemical potential $\delta(\mu/Nk_B)$ and coexistence pressure predictions δp are estimated by assuming that the fluid and solid chemical potential curves are linear around the coexistence point. This assumption allows the standard deviations to be written in terms of the derivatives of the fluid and solid chemical potential curves at the coexistence point as

$$\delta\mu = \left(\frac{\frac{d\mu_{\text{fluid}}}{dp}}{\frac{d\mu_{\text{fluid}}}{dp} - \frac{d\mu_{\text{solid}}}{dp}} \right) \delta S_{\text{ref}} \quad (11.4.3)$$

$$\delta p = \left(\frac{1}{\frac{d\mu_{\text{fluid}}}{dp} - \frac{d\mu_{\text{solid}}}{dp}} \right) \delta S_{\text{ref}} \quad (11.4.4)$$

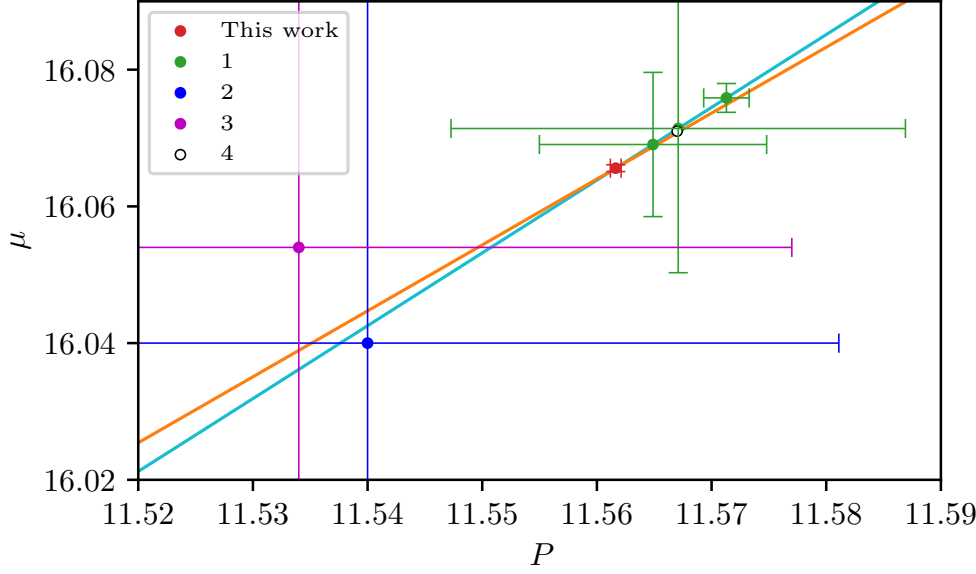


Figure 11.11: Chemical potential as a function of pressure showing the predicted hard-sphere fluid-solid coexistence point predicted in this work as well as the predictions from (1) Pieprzyk et al. [17] (2) Vega and Noya [20], (3) Usinov [25], (4) Frenkel and Smit [7].

where δS_{ref} is the standard deviation in the reference entropy value used in Eq. (11.3.1), $d\mu_{\text{fluid}}/dp$ is the derivative of the fluid chemical potential with respect to pressure evaluated at the coexistence point, and $d\mu_{\text{solid}}/dp$ is the derivative of the solid chemical potential with respect to pressure evaluated at the coexistence point. The coexistence pressure is calculated to be $\beta p_{\text{coex}} \sigma^3 = 11.56164 \pm 0.00047$ and the coexistence chemical potential is calculated to be $\beta(\mu_{\text{coex}} - \mu^{(\text{ig})}) = 16.06559 \pm 0.00050$. This leads to fluid and solid coexistence density estimates of 0.93912 and 1.03745, respectively.

By substituting the equation for the solid hard-sphere compressibility given in Eq. (11.3.2) into Eq. (11.3.1), carrying out the integration and using the final values for the entropy at the reference density ($(S - S^{(\text{ig})})/(Nk_B) = -4.95803 \pm 0.00005$ at $\rho\sigma^3 = 1.04086$) calculated in this chapter, the following expression for the hard-sphere solid entropy can be generated,

$$\frac{S(\rho)}{Nk_B} = c_1 + c_2 \log(\rho) + 3 \log(\sqrt{2} - \rho) + \frac{2}{3} \log\left(\rho + \frac{3}{\sqrt{2}}\right) + c_3 \text{Ei}(c_4 \rho) + c_5 \text{Ei}(c_6 \rho) \quad (11.4.5)$$

where $c_1 = -2.69381$, $c_2 = -2.80694$, $c_3 = -3.01404 \times 10^9$, $c_4 = -24.3082$, $c_5 = -153.668$, $c_6 = -6.14405$, and $\text{Ei}(x) = -\int_{-x}^{\infty} dt e^{-t}/t$ is the exponential integral.

11.5 Conclusions and future work

In this work, the behaviour of the tether particle model, first introduced by Speedy [4], is examined in detail. The variation of the compressibility factor with density is shown

for tethered particles systems with different tether lengths. For the standard hard sphere system, and for tethered system with sufficiently large tethers, a first order transition is present between the liquid and solid phases which weakens and vanishes with decreasing tether length. Therefore, for sufficiently short tether lengths, there is a continuous thermodynamic path between the fluid and solid states. At very low densities, where tether cells are spaced too far apart to interact, the tether system will reach an “ideal” state for which the free energy is known exactly with respect to the standard ideal gas state. At sufficiently high densities, which occur in the solid phase, sphere-sphere collisions prevent the tether interactions and the tether system becomes indistinguishable from the conventional hard sphere system. Therefore, thermodynamic integration can be directly used on MD simulations of the TPM for sufficiently short tether lengths in order to compute the free energy of solid hard sphere systems. This method is shown to give highly precise estimates of the free energy as well as for the fluid-solid coexistence point.

By considering the tethered hard sphere system from the perspective of its motion through phase space, a separate relation can be derived for the entropy of the system in terms of collision rate of spheres with the confining tether cells. By integrating the sphere collision rate, it is possible to directly determine the entropy of the system with respect to the ideal TPM. This is found to be an efficient method for calculating the entropy of hard sphere systems in any state.

Calculations of the hard-sphere entropy at several densities are presented using both integration methods which agree with existing estimates in the literature. The hard-sphere fluid-solid transition is determined to be at a reduced pressure of $\beta p \sigma^3 = 11.56164 \pm 0.00047$ which corresponds to a reduced chemical potential at transition of $\beta (\mu - \mu^{(ig)}) = 16.06559 \pm 0.00050$. The reduced fluid and solid transition densities are estimated to be $\rho \sigma^3 = 0.93912$, and $\rho \sigma^3 = 1.03745$ respectively.

While the scope of this chapter has been limited to monocomponent systems, the expressions presented here can easily be extended to any multicomponent, discontinuous potential system. Additionally, the tethering potential was considered to act only on single spheres, confining them to be located within a spherical cell; however, this is only one example of a tethering potential and many other alternatives could be implemented. For example, the tethering potential might act between pairs of spheres in order to keep them within a set distance from one another. This type of tethering simulation could be used in order to obtain the potential of mean force between particles or collections of particles, such as polymer chains. Another example is to confine a group of spheres to within a certain cell. This would allow the calculation of the entropy penalty of clustering spheres to form aggregates.

References

- [1] W. G. Hoover and F. H. Ree. “Melting transition and communal entropy for hard spheres”. In: *J. Chem. Phys.* 49 (1968), p. 3609.
- [2] L. V. Woodcock. “Computation of the free energy for alternative crystal structures of hard spheres”. In: *Faraday Discuss.* 106 (1997), pp. 325–338.
- [3] L. V. Woodcock. “Entropy difference between the face-centred cubic and hexagonal close-packed crystal structures”. In: *Nature* 385.6612 (1997), pp. 141–143.
- [4] R. J. Speedy. “The entropy of a glass”. In: *Mol. Phys.* 80.5 (1993), pp. 1105–1120.
- [5] A. Donev, F. H. Stillinger, and S. Torquato. “Calculating the free energy of nearly jammed hard-particle packings using molecular dynamics”. In: *J. Comput. Phys.* 225.1 (2007), pp. 509–527.
- [6] D. Frenkel and A. J. C. Ladd. “New Monte Carlo method to compute the free energy of arbitrary solids. Application to the fcc and hcp phases of hard spheres”. In: *J. Chem. Phys.* 81.7 (1984), pp. 3188–3193.
- [7] D. Frenkel and B. Smit. *Understanding Molecular Simulation: From Algorithms to Applications*. 2nd. San Diego, CA, USA: Academic Press, 2002.
- [8] M. B. Sweatman. “Self-referential Monte Carlo method for calculating the free energy of crystalline solids”. In: *Phys. Rev. E* 72.1 (2005).
- [9] M. B. Sweatman, A. A. Atamas, and J.-M. Leyssale. “The self-referential method combined with thermodynamic integration”. In: *J. Chem. Phys.* 128.6 (2008), p. 064102.
- [10] M. B. Sweatman, A. Atamas, and J.-M. Leyssale. “The self-referential method for linear rigid bodies: Application to hard and Lennard-Jones dumbbells”. In: *J. Chem. Phys.* 130.2 (2009), p. 024101.
- [11] T. Schilling and F. Schmid. “Computing absolute free energies of disordered structures by molecular simulation”. In: *J. Chem. Phys.* 131.23 (2009), p. 231102.
- [12] U. R. Pedersen. “Direct calculation of the solid-liquid Gibbs free energy difference in a single equilibrium simulation”. In: *J. Chem. Phys.* 139.10 (2013), p. 104102.
- [13] M. B. Sweatman. “Comparison of absolute free energy calculation methods for fluids and solids”. In: *Mol. Phys.* 113.9-10 (2015), pp. 1206–1216.
- [14] W. G. Hoover, C. G. Hoover, and M. N. Bannerman. “Single-Speed Molecular Dynamics of Hard Parallel Squares and Cubes”. In: *J. Stat. Phys.* 136 (2009), p. 164507.
- [15] E. P. Bernard, W. Krauth, and D. B. Wilson. “Event-chain algorithms for hard-sphere systems”. In: *Phys. Rev. E* 80 (2009), p. 056704.

-
- [16] M. N. Bannerman, R. Sargant, and L. Lue. “DynamO: a free $\mathcal{O}(N)$ general event-driven molecular dynamics simulator”. In: *J. Comput. Chem.* 32.15 (2011), pp. 3329–3338.
- [17] S. Peiprzyk et al. “Thermospheres and dynamical properties of the hard sphere system revisited by molecular dynamics simulation”. In: *Phys. Chem. Chem. Phys.* 21 (2019), pp. 6886–6899.
- [18] R. J. Speedy. “Pressure and entropy of hard-sphere crystals”. In: *J. Phys. Condens. Matter* 10 (1998), pp. 4387–4391.
- [19] H. C. Andersen. “Molecular dynamics simulations at constant pressure and/or temperature”. In: *J. Chem. Phys.* 72 (1980), p. 2384.
- [20] C. Vega and E. G. Noya. “Revisiting the Frenkel-Ladd method to compute the free energy of solids: The Einstein molecule approach”. In: *J. Chem. Phys.* 127 (2007), p. 154113.
- [21] N. G. Almarza. “Computation of the free energy of solids”. In: *J. Chem. Phys.* 126 (2007), p. 211103.
- [22] J. Chang and S. I. Sandler. “Determination of liquid-solid transition using histogram reweighting method and expanded ensemble simulations”. In: *J. Chem. Phys.* 118 (2003), p. 8390.
- [23] J. M. Polson et al. “Finite-size corrections to the free energies of crystalline solids”. In: *J. Chem. Phys.* 112 (2000), p. 5339.
- [24] J. Kolafa, S. Labik, and A. Milijevsky. “Accurate equation of state of the hard sphere fluid in stable and metastable regions”. In: *Phys. Chem. Chem. Phys.* 6 (2004), pp. 2335–2340.
- [25] E. A. Ustinov. “Thermodynamics and simulation of hard-sphere fluid and solid: Kinetic Monte Carlo method versus standard Metropolis scheme”. In: *J. Chem. Phys.* 146 (2017), p. 034110.

CONCLUSIONS

Anomalous thermal conductivity is typically defined as a measured thermal conductivity value which lies outside of either the series-parallel bound or the upper and lower Maxwell bounds which are shown in Ch. 2. The thermal conductivity of nanofluid mixtures largely remain within these bounds; however, certain gas mixtures exhibit thermal conductivity values which are well outside of these classical bounds. In order to study thermal conductivity in fluid mixtures, this thesis models fluid particles as hard-spheres. Enskog kinetic theory is derived in Ch. 5 which is then used in order to derive the full multicomponent hydrodynamic equations for the conservation of mass, momentum, and energy in hard-sphere mixtures.

Deriving multicomponent hydrodynamics in this way demonstrates that there is no one unique definition of the “thermal conductivity” for fluid mixtures due to the effects of thermal diffusion. This thesis primarily discusses two definitions of the thermal conductivity which are; the initial thermal conductivity λ_I which assumes that there are no concentration gradients in the system, and the steady-state thermal conductivity λ which is relevant in the steady-state limit when there is zero diffusive flux of mass through the system. The initial thermal conductivity is greater than the steady-state value which means that there is potential for enhanced “thermal conductivities” at short times during heat transfer.

The thermal conductivity of a binary hard-sphere fluid is measured using NEMD simulation and the parallel heated walls measurement technique. It is found that the steady-state thermal conductivity predictions of Enskog theory strongly agree with the measured thermal conductivity values using NEMD. Enskog theory predicts that it is possible for both the initial *and* the steady-state thermal conductivity to lie outwith the series and parallel thermal conductivity limits for certain hard-sphere mixtures. This suggests that using classical bounds (such as the Maxwell bounds or the series-parallel limits) as a criteria for what is considered an “anomalous” thermal conductivity is not useful as these bounds can be broken for even simple hard-sphere fluids. Estimated kinetic diameters which are taken from literature are used in order to predict real gas mixtures which could exhibit thermal conductivity values outwith the series-parallel limits. It is predicted that it

is possible for several binary gas mixtures including helium-hydrogen, and krypton-argon to exhibit steady-state thermal conductivity values which are below the series limit for certain mixture concentrations. Enskog theory is then used in order to map the potential enhancement of the initial thermal conductivity above both the parallel thermal conductivity limit as well as the steady-state value for binary hard-sphere mixtures. It is possible for the initial thermal conductivity to lie well above the parallel limit and the steady-state value. The main predictor of the potential initial thermal conductivity enhancement is the mass ratio of the two hard-sphere species. Estimated kinetic diameters are then used, again, to predict real gas mixtures which could exhibit large values of the initial enhanced thermal conductivity. It is predicted that it is possible for binary gas mixtures with large differences in the molar mass, such as hydrogen-xenon and krypton-helium, to exhibit large values of the initial thermal conductivity which are approximately ten times larger than the steady-state value.

Estimated values of the kinetic diameters which are taken from literature are calculated from diffusion measurements and it is demonstrated that Enskog theory predictions of the pure component thermal conductivity values which use these values as the equivalent hard-sphere diameters are not in agreement with experimental measurements. Equivalent hard-sphere diameters for hydrogen and nitrogen, as well as the noble gases are, therefore, estimated in Ch. 9 by fitting experimental thermal conductivity measurements from literature to kinetic theory. Enskog theory is used, in conjunction with the newly calculated kinetic diameters, in order to predict the mixture thermal conductivities of binary mixtures of helium-hydrogen, krypton-nitrogen, and krypton-argon at a range of mixture concentrations. These predictions are then compared with experimental measurements taken from literature. In the case of the helium-hydrogen mixture, the Enskog theory steady-state thermal conductivity predictions are in strong agreement with experimental measurements. This suggests that the behaviour of this particular gas mixture is well described by the hard-sphere model and, also, that this experimental measurement was taken over a sufficiently long time such that the effects of thermal diffusion on the effective thermal conductivity were small. In the case of the krypton-nitrogen and argon-krypton mixtures, the agreement between Enskog steady-state predictions and literature measurements is not as strong; however, the experimental measurements are bounded by the steady-state and enhanced initial values of the thermal conductivity. This suggests that the timescale which these measurements were taken over may have been short such that the measured effective thermal conductivity was enhanced by thermal diffusion. This disagreement, however, could be due to a number of reasons. The hard-sphere model may not be an appropriate model to describe these gas mixtures at these experimental conditions. In addition, inaccurate pure component thermal conductivity measurements could lead inaccurate estimates of the equivalent hard-sphere diameters of these components.

A coupled hydrodynamic - kinetic theory model is presented which can be used in order to simulate heat transfer in multicomponent hard-sphere systems. When simulating

realistic systems, this method is much less computationally expensive than other molecular simulations techniques such as molecular dynamics. This model could be used to determine the timescale over which thermal diffusion takes place and, therefore, the time over which the effective thermal conductivity decreases from the enhanced initial value to the steady-state value for hard-sphere fluids. This model is validated against direct NEMD simulations of heat transfer in hard-sphere systems between two parallel heated walls. The steady-state temperature and density profiles calculated separately, using the hydrodynamic model and MD, are compared for a monocomponent and a multicomponent hard-sphere fluid at steady-state conditions. Results of the two methods for the monocomponent fluid strongly agree; however, results for the multicomponent fluid disagree significantly. Additional work is required in order to verify that the model implementation is correct for multicomponent systems. Results of hydrodynamic and MD simulation are then compared for a monocomponent system in the transient regime, moments after a large temperature gradient is imposed across the simulation. It is shown that the hydrodynamic model accurately predicts the behaviour of monocomponent hard-spheres in the transient regime as the system settles towards steady-state conditions. The hydrodynamic model is able to capture complex behaviour such as shockwaves caused by initial temperature changes travelling through the system at the speed of sound and reflecting off the simulation boundaries. The initial success of this coupled hydrodynamic-kinetic theory model represents a promising new area of research whereby realistically sized fluid systems may be simulated with a view to measuring, and potentially exploiting, non-steady-state effects in mono and multicomponent systems.

Finally, this thesis presents two novel methods for computing the free energy of hard-sphere systems. Both methods are based on a tether model which confines particles to a particular volume in space. Calculations of the hard-sphere free energy at several density values are presented which agree with existing estimates in the literature. Utilising the free energy estimates, the hard-sphere fluid-solid transition is then determined to be at a reduced pressure of $\beta p \sigma^3 = 11.56164 \pm 0.00047$. This corresponds to a reduced chemical potential value at transition of $\beta (\mu - \mu^{(ig)}) = 16.06559 \pm 0.00050$, a reduced fluid transition density of $\rho \sigma^3 = 0.93912$, and a reduced solid transition density of $\rho \sigma^3 = 1.03745$.

OSCILLATING WALL TEMPERATURE ANALYTICAL SOLUTION

Consider a stationary material with a constant density, specific heat capacity, and thermal conductivity located between two walls which are at $x \pm b$. The temperature at both walls is given by $T = A \sin(\omega t)$ where A is the amplitude of the wall temperature oscillation, ω is the temperature oscillation frequency, and t is the time. The temperature distribution will be governed by the heat equation

$$\frac{\partial T}{\partial t} = \alpha \nabla^2 T \quad (\text{A.0.1})$$

where $\alpha = k/\rho C_p$ is the thermal diffusivity, k is the thermal conductivity, ρ is the density, and C_p is the specific heat capacity. The boundary conditions in this system are

$$\text{B.C. 1} \quad \text{at } x = b \quad T = A \sin(\omega t) = A \Im \{e^{i\omega t}\} \quad \text{for } t > 0 \quad (\text{A.0.2})$$

$$\text{B.C. 2} \quad \text{at } x = 0 \quad \frac{\partial T}{\partial x} = 0. \quad (\text{A.0.3})$$

We are interested in the behaviour of the system at steady-state, therefore an initial condition for the system is not needed.

An oscillatory solution for the system temperature is assumed of the form

$$T(x, t) = \Im \{T^\dagger(x) e^{i\omega t}\} \quad (\text{A.0.4})$$

where T^\dagger is a complex function of x so that $T(x, t)$ will differ from $T(b, t)$ in both amplitude and phase. This solution is substituted into Eq. (A.0.1) to obtain

$$\Im \{T^\dagger(x) i\omega e^{i\omega t}\} = \alpha \Im \left\{ \frac{\partial^2 T^\dagger(x)}{\partial x^2} e^{i\omega t} \right\} \quad (\text{A.0.5})$$

It is possible to simplify this equation by making use of the fact that, if $\Im \{z_1 a\} = \Im \{z_2 a\}$ where z_1 and z_2 are two complex quantities and a is an arbitrary complex quantity, the

$z_1 = z_2$. Eq. (A.0.5) therefore becomes a second order differential equation in temperature

$$\frac{\partial^2 T^\dagger(x)}{\partial x^2} - \left(\frac{i\omega}{\alpha}\right) T^\dagger(x) = 0.$$

This form of differential equation has a standard solution

$$T^\dagger(x) = C_1 e^{\sqrt{i\omega/\alpha}x} + C_2 e^{-\sqrt{i\omega/\alpha}x},$$

which, using the fact that $\sqrt{i} = \pm \frac{1}{\sqrt{2}}(1+i)$, can be rewritten as

$$T^\dagger(x) = C_1 e^{\kappa(1+i)x} + C_2 e^{-\kappa(1+i)x}, \quad (\text{A.0.6})$$

where $\kappa = \sqrt{\omega/2\alpha}$. We must now apply the boundary conditions of the system in order to determine the constants C_1 and C_2 . Applying B.C. 2, the zero condition of zero-gradient gives

$$\begin{aligned} 0 &= C_1 \kappa (1+i) e^{\kappa(1+i)0} - C_2 \kappa (1+i) e^{-\kappa(1+i)0} \\ C_1 \kappa (1+i) &= C_2 \kappa (1+i) \\ C_1 &= C_2. \end{aligned}$$

We find that the constants C_1 and C_2 are equal. Eq. (A.0.6) is therefore redefined in terms of a single constant $C_3 = C_1 = C_2$

$$T^\dagger(x) = C_3 (e^{\kappa(1+i)x} + e^{-\kappa(1+i)x}). \quad (\text{A.0.7})$$

Applying the wall temperature boundary condition, Eq. (A.0.2), allows us to determine the constant C_3

$$\begin{aligned} A &= C_3 (e^{\kappa(1+i)b} + e^{-\kappa(1+i)b}) \\ C_3 &= \frac{A}{e^{\kappa(1+i)b} + e^{-\kappa(1+i)b}}, \end{aligned}$$

which, when plugged in to Eq. (A.0.7), gives the final expression for T^\dagger

$$T^\dagger(x) = A \frac{e^{\kappa(1+i)x} + e^{-\kappa(1+i)x}}{e^{\kappa(1+i)b} + e^{-\kappa(1+i)b}}.$$

Plugging this expression into Eq. (A.0.4) gives the final expression for the system temperature distribution

$$T(x, t) = A \Im \left\{ \frac{e^{\kappa(1+i)x} + e^{-\kappa(1+i)x}}{e^{\kappa(1+i)b} + e^{-\kappa(1+i)b}} e^{i\omega t} \right\}.$$

As this equation stands here, it will result in negative temperatures in the system. This

is obviously not possible but can be easily rectified by shifting the solution by a constant temperature value T_0

$$T(x, t) = T_0 + A\Im \left\{ \frac{e^{\kappa(1+i)x} + e^{-\kappa(1+i)x}}{e^{\kappa(1+i)b} + e^{-\kappa(1+i)b}} e^{i\omega t} \right\}.$$

This does not affect the rest of the solution as this value is completely independant. It is possible to represent this equation in terms of a completely real numerator and denominator, and thus remove the imaginary sign \Im , by multiplying by the exponential complex conjugate and simplifying

$$\begin{aligned} T(x, t) &= T_0 + A\Im \left\{ \left(\frac{e^{\kappa(1+i)x} + e^{-\kappa(1+i)x}}{e^{\kappa(1+i)b} + e^{-\kappa(1+i)b}} \right) \left(\frac{e^{\kappa(1-i)b} + e^{-\kappa(1-i)b}}{e^{\kappa(1-i)b} + e^{-\kappa(1-i)b}} \right) e^{i\omega t} \right\} \\ &= T_0 + A\Im \left\{ \frac{e^{\kappa(x+b)} e^{i\kappa(x-b)} + e^{\kappa(x-b)} e^{i\kappa(x+b)} + e^{-\kappa(x-b)} e^{-i\kappa(x+b)} + e^{-\kappa(x+b)} e^{-i\kappa(x-b)}}{e^{2\kappa b} + e^{-2i\kappa b} + e^{2i\kappa b} + e^{-2\kappa b}} e^{i\omega t} \right\} \\ &= T_0 + A\Im \left\{ \frac{e^{\kappa(x+b)} e^{i(\kappa(x-b)+\omega t)} + e^{\kappa(x-b)} e^{i(\kappa(x+b)+\omega t)} + e^{-\kappa(x-b)} e^{i(-\kappa(x+b)+\omega t)} + e^{-\kappa(x+b)} e^{i(-\kappa(x-b)+\omega t)}}{e^{2\kappa b} + e^{-2\kappa b} + 2 \cos(2\kappa b)} \right\} \\ &= T_0 + A \left(\frac{e^{\kappa(x+b)} \sin(\kappa(x-b) + \omega t) + e^{\kappa(x-b)} \sin(\kappa(x+b) + \omega t) + e^{-\kappa(x-b)} \sin(-\kappa(x+b) + \omega t) + e^{-\kappa(x+b)} \sin(-\kappa(x-b) + \omega t)}{e^{2\kappa b} + e^{-2\kappa b} + 2 \cos(2\kappa b)} \right). \end{aligned} \tag{A.0.8}$$

This expression for T is integrated with respect to x in order to determine the average temperature in the system over time. This involves recursively integrating the terms present in the numerator of the previous equation. It is thankfully not necessary to involve the denominator in the integration as it is not a function of x . This integration is performed here term by term.

1st term

The first term in the numerator of Eq. A.0.8 is

$$\int e^{\kappa(x+b)} \sin(\kappa(x-b) + \omega t) dx$$

where the integral with respect to x is shown. Part of the exponential term can be separated from the integral as it is independant of position.

$$e^{\kappa b} \int e^{\kappa x} \sin(\kappa x - \kappa b + \omega t) dx$$

Using integration by parts recursively (where the constant term $e^{\kappa b}$ has been removed for simplicity) eventually allows the integral to be expressed in terms of itself

$$\begin{aligned} \int e^{\kappa x} \sin(\kappa x - \kappa b + \omega t) dx &= \frac{e^{\kappa x}}{\kappa} \sin(\kappa x - \kappa b + \omega t) - \int e^{\kappa x} \cos(\kappa x - \kappa b + \omega t) dx \\ &= \frac{e^{\kappa x}}{\kappa} \sin(\kappa x - \kappa b + \omega t) - \left(\frac{e^{\kappa x}}{\kappa} \cos(\kappa x - \kappa b + \omega t) + \int e^{\kappa x} \sin(\kappa x - \kappa b + \omega t) dx \right) \\ &= \frac{e^{\kappa x}}{\kappa} (\sin(\kappa x - \kappa b + \omega t) - \cos(\kappa x - \kappa b + \omega t)) - \int e^{\kappa x} \sin(\kappa x - \kappa b + \omega t) dx, \end{aligned}$$

where the final line implicitly defines the complete indefinite integral as

$$\begin{aligned} \int e^{\kappa(x+b)} \sin(\kappa(x-b) + \omega t) dx &= \\ \frac{e^{\kappa(x+b)}}{2\kappa} (\sin(\kappa x - \kappa b + \omega t) - \cos(\kappa x - \kappa b + \omega t)). \end{aligned}$$

Collapsing the sum of trigonometric terms using the fact that $\sin(x) - \cos(x) = -\sqrt{2} \sin\left(\frac{\pi}{4} - x\right)$ gives

$$\int e^{\kappa(x+b)} \sin(\kappa(x-b) + \omega t) dx = \frac{-e^{\kappa(x+b)}}{\sqrt{2}\kappa} \sin\left(\frac{\pi}{4} - \kappa x + \kappa b - \omega t\right),$$

and applying the integration limits gives the final integral as

$$\begin{aligned} \int_{-b}^b e^{\kappa(x+b)} \sin(\kappa(x-b) + \omega t) dx &= \\ &= \left[\frac{-e^{\kappa(x+b)}}{\sqrt{2}\kappa} \sin\left(\frac{\pi}{4} - \kappa x + \kappa b - \omega t\right) \right]_{-b}^b \\ &= \frac{-e^{2\kappa b}}{\sqrt{2}\kappa} \sin\left(\frac{\pi}{4} - \omega t\right) - \frac{-1}{\sqrt{2}\kappa} \sin\left(\frac{\pi}{4} + 2\kappa b - \omega t\right) \\ &= \frac{1}{\sqrt{2}\kappa} \left(-e^{2\kappa b} \sin\left(\frac{\pi}{4} - \omega t\right) + \sin\left(\frac{\pi}{4} + 2\kappa b - \omega t\right) \right) \end{aligned}$$

The process of integrating the 2nd, 3rd, and 4th terms of Eq. (A.0.8) is very similar to the 1st term which is described in detail above. Integrating these terms gives

2nd term

$$\begin{aligned} \int_{-b}^b e^{\kappa(x-b)} \sin(\kappa(x+b) + \omega t) dx &= \\ \frac{1}{\sqrt{2}\kappa} \left(-\sin\left(\frac{\pi}{4} - 2\kappa b - \omega t\right) + e^{-2\kappa b} \sin\left(\frac{\pi}{4} - \omega t\right) \right) \end{aligned}$$

3rd term

$$\int_{-b}^b e^{-\kappa(x-b)} \sin(-\kappa(x+b) + \omega t) dx = \frac{1}{\sqrt{2}\kappa} \left(\sin\left(\frac{\pi}{4} + 2\kappa b - \omega t\right) - e^{2\kappa b} \sin\left(\frac{\pi}{4} - \omega t\right) \right)$$

4th term

$$\int_{-b}^b e^{-\kappa(x+b)} \sin(-\kappa(x-b) + \omega t) dx = \frac{1}{\sqrt{2}\kappa} \left(e^{-2\kappa b} \sin\left(\frac{\pi}{4} - \omega t\right) - \sin\left(\frac{\pi}{4} - 2\kappa b - \omega t\right) \right)$$

Summing all the integrated terms together and inserting them back into Eq. (A.0.8) gives the expression for the average temperature in the oscillating wall temperature system as a function of time

$$\bar{T}(t) = 2bT_0 + \frac{\sqrt{2}A}{\kappa} \frac{(e^{-2\kappa b} - e^{2\kappa b}) \sin\left(\frac{\pi}{4} - \omega t\right) + \sin\left(\frac{\pi}{4} + 2\kappa b - \omega t\right) - \sin\left(\frac{\pi}{4} - 2\kappa b - \omega t\right)}{e^{2\kappa b} + e^{-2\kappa b} + 2 \cos(2\kappa b)}$$

where the trivial integration of the constant temperature “shift” T_0 has also been carried out. This equation can be further simplified using one final trigonometric identity to given the final expression as.

$$\bar{T}(t) = 2bT_0 + \frac{\sqrt{2}A}{\kappa} \frac{(e^{-2\kappa b} - e^{2\kappa b}) \sin\left(\frac{\pi}{4} - \omega t\right) + 2 \cos\left(\frac{\pi}{4} - \omega t\right) \sin(2\kappa b)}{e^{2\kappa b} + e^{-2\kappa b} + 2 \cos(2\kappa b)}. \quad (\text{A.0.9})$$

ALTERNATIVE λ DERIVATION FOR BINARY MIXTURES

The steady-state thermal conductivity λ is derived in Ch. 6 in the general case for an S -component mixture and also specifically for binary mixtures. This derivation method utilises the generalised inverse in order to handle the singular diffusion matrix \mathbf{D} . This appendix showcases the fact that it is not necessary to use the generalised inverse in order to derive an expression for λ . An expression for the steady-state thermal conductivity in binary mixtures is derived in a separate manner. The equations for the mass \mathbf{J}_a and energy \mathbf{J}_q flux in mixtures are given originally in Eqs. (5.4.16) and (5.4.17) respectively and are restated here,

$$\mathbf{J}_a = \sum_b -L_{ab}T\nabla\left(\frac{\mu_b}{T}\right) - \frac{L_{ua}}{T}\nabla T, \quad (\text{B.0.1})$$

$$\mathbf{J}_q = \sum_a -L_{ua}T\nabla\left(\frac{\mu_a}{T}\right) - \frac{L_{uu}}{T}\nabla T, \quad (\text{B.0.2})$$

where L_{ab} is the mutual diffusion coefficient of species a through species b , T is the temperature, μ_a is the chemical potential of species a , L_{ua} is the thermal diffusion coefficient of species a , and L_{uu} is the phenomenological thermal conductivity. As discussed in Ch. 6, for a binary mixture the Onsager relationships state that

$$L_{12} = -L_{11}, \quad (\text{B.0.3})$$

$$L_{1u} = -L_{u1}. \quad (\text{B.0.4})$$

These relationships are used in order to produce the simplest possible expression for λ in terms of the lowest number of variables. We expand the sum in Eq. (B.0.1) for a binary mixture and substitute in the corresponding Onsager relationships so that the expression is a function of three independent transport coefficients, L_{uu} , L_{u1} , and L_{11} . We also set the value of diffusive mass flux to $\mathbf{J}_a = \mathbf{0}$, as stated in Ch. 6, as we are looking for the

thermal conductivity at steady-state conditions,

$$0 = -L_{11} T \nabla \left(\frac{\mu_1}{T} \right) + L_{11} T \nabla \left(\frac{\mu_2}{T} \right) - \frac{L_{u1}}{T} \nabla T. \quad (\text{B.0.5})$$

The mutual diffusion coefficient L_{11} is now factored out of the chemical potential terms and the equation is rearranged in order to express the gradient in the chemical potentials in terms of the temperature gradient,

$$\nabla \left(\frac{\mu_2 - \mu_1}{T} \right) = \frac{L_{u1}}{L_{11} T^2} \nabla T. \quad (\text{B.0.6})$$

A similar set of operations are performed on Eq. (B.0.2), the sum over all species is expanded for a binary mixture and the Onsager relations are applied in order to express the heat flux in terms of only one thermal diffusion coefficient L_{u1} ,

$$J_q = -L_{u1} T \nabla \left(\frac{\mu_1}{T} \right) + L_{u1} T \nabla \left(\frac{\mu_2}{T} \right) - \frac{L_{uu}}{T} \nabla T. \quad (\text{B.0.7})$$

This, again, allows us to factor out the lone diffusion coefficient L_{u1} and combine the chemical potentials of species 1 and 2 inside the ∇ operator,

$$J_q = L_{u1} T \nabla \left(\frac{\mu_2 - \mu_1}{T} \right) - \frac{L_{uu}}{T} \nabla T. \quad (\text{B.0.8})$$

We notice that this equation contains the term $\nabla \left(\frac{\mu_2 - \mu_1}{T} \right)$ which we have previously derived a relationship for in Eq. (B.0.6). Substituting this relationship into the previous equation removes the dependence on chemical potential gradients and gives the heat flux J_q in term of the temperature gradient only,

$$J_q = L_{u1} T \frac{L_{u1}}{L_{11} T^2} \nabla T - \frac{L_{uu}}{T} \nabla T, \quad (\text{B.0.9})$$

$$= -\frac{1}{T} \left(L_{uu} - \frac{L_{u1}^2}{L_{11}} \right) \nabla T. \quad (\text{B.0.10})$$

At this point we have converged with the original derivation method as this expression for the heat flux is identical to the value derived in Ch. 6. The steady-state thermal conductivity λ is now extracted in the same manner as in Ch. 6 by relating to the energy flux J_q via Fourier's Law,

$$J_q = -\lambda \nabla T, \quad (\text{B.0.11})$$

which implicitly defines the steady-state thermal conductivity λ as

$$\lambda = \frac{1}{T} \left(L_{uu} - \frac{L_{u1}^2}{L_{11}} \right). \quad (\text{B.0.12})$$

REPRINT: ANOMALOUS HEAT TRANSPORT IN
BINARY HARD SPHERE GASES

Anomalous heat transport in binary hard-sphere gasesCraig Moir,^{1,2} Leo Lue,³ Julian D. Gale,² Paolo Raiteri,² and Marcus N. Bannerman^{1,*}¹*School of Engineering, University of Aberdeen, Aberdeen AB24 3UE, United Kingdom*²*Curtin Institute for Computation, Curtin University, P.O. Box U1987, Perth, WA 6845, Australia*³*Department of Chemical and Process Engineering, University of Strathclyde, James Weir Building, 75 Montrose Street, Glasgow G1 1XJ, United Kingdom*

(Received 8 December 2018; published 29 March 2019)

Equilibrium and nonequilibrium molecular dynamics (MD) are used to investigate the thermal conductivity of binary hard-sphere fluids. It is found that the thermal conductivity of a mixture can not only lie outside the series and parallel bounds set by their pure component values, but can lie beyond even the pure component fluid values. The MD simulations verify that revised Enskog theory can accurately predict nonequilibrium thermal conductivities at low densities and this theory is applied to explore the model parameter space. Only certain mass and size ratios are found to exhibit conductivity enhancements above the parallel bounds and dehancement below the series bounds. The anomalous dehancement is experimentally accessible in helium-hydrogen gas mixtures and a review of the literature confirms the existence of mixture thermal conductivity below the series bound and even below the pure fluid values, in accordance with the predictions of revised Enskog theory. The results reported here may reignite the debate in the nanofluid literature on the possible existence of anomalous thermal conductivities outside the series and parallel bounds as this Rapid Communication demonstrates they are a fundamental feature of even simple fluids.

DOI: [10.1103/PhysRevE.99.030102](https://doi.org/10.1103/PhysRevE.99.030102)

There has been a great deal of interest in increasing the transport rate of heat through fluids by the addition of nanometer-sized solid particles. Initial experiments on these nanosuspensions demonstrated significant enhancements of the thermal conductivity [1]; however, later measurements on other mixtures generated substantial controversy [2], with confusion over what results might be “unsurprising” and what might be deemed “anomalous.” Disagreements in reported values led to a comprehensive benchmark study with double blind tests conducted between several institutions [3]. The primary conclusion was that the vast majority of the reported “enhancement” effects lie within the continuum bounds given by the series λ^\perp and parallel λ^\parallel limits of the thermal conductivity [4], which for a binary mixture are

$$\frac{1}{\lambda^\perp} = \frac{1 - \phi_2}{\lambda_1} + \frac{\phi_2}{\lambda_2}, \quad (1)$$

$$\lambda^\parallel = (1 - \phi_2)\lambda_1 + \phi_2\lambda_2, \quad (2)$$

where ϕ_2 is the volume fraction of component 2 in the mixture, and λ_1 and λ_2 are the fluid thermal conductivities for pure 1 and pure 2, respectively.

A small number of experimental results still remain outside these conventional bounds, such as the reported *dehancements* below the series limit for fullerene-water suspensions [5]. Hence, the question still remains: Are results outside these bounds correct and, if so, what are the underlying mechanisms? Several physical mechanisms have been proposed in

an effort to rationalize the behavior of these systems [4]; however, there is as yet no unifying framework for predicting and explaining the thermal performance of nanofluid mixtures. To be able to understand these results, a deeper understanding of thermal conductivity and its underlying molecular mechanisms is required.

Some of the confusion in interpreting thermal conductivity arises from the different manners in which it can be defined. The most natural macroscopic and experimental definition arises from applying a temperature gradient ∇T across a system and measuring the resultant heat flux \mathbf{J}_q . The “observed” nonequilibrium thermal conductivity λ_N is then defined through the following expression,

$$\langle \mathbf{J}_q \rangle = -\lambda_N \nabla T, \quad (3)$$

where the brackets $\langle \dots \rangle$ indicate the implicit averaging over time and volume this approach entails.

In contrast, when considering hydrodynamic models it is natural to decompose the heat flux \mathbf{J}_q into contributions from thermal and mass diffusion of the individual species; however, this separation of these two effects is not unique and an arbitrary number of definitions of the thermal conductivity can be generated. The so-called mainstream, prime, and double prime definitions [6,7] are the most common choices. The mainstream definition is used here as it is convenient for molecular dynamics simulations and is given below for binary systems,

$$\mathbf{J}_q = -T^{-1} L_{uu} \nabla T - L_{u1} T \nabla \frac{(\mu_1 - \mu_2)}{T}, \quad (4)$$

where L_{uu} is the mainstream thermal conductivity, L_{u1} is the mainstream thermal diffusivity of species 1, and μ_1 is the

*m.campbellbannerman@abdn.ac.uk

chemical potential of species 1. One possible resolution to the ambiguity in the definition of L_{uu} is to assume local steady-state conditions (zero mass flux) [4,8] to yield the following expression,

$$\mathbf{J}_q = -T^{-1}(L_{uu} - L_{u1}^2 L_{11}^{-1})\nabla T = -\lambda \nabla T, \quad (5)$$

where L_{11} is the mutual diffusion coefficient of species 1 through itself and the final equality implicitly defines the “steady-state” thermal conductivity λ . The value of λ is independent of the choice of mainstream, prime, or double prime fluxes; however, it is still distinct from λ_N as it is not averaged over the nonequilibrium conditions of a system undergoing conduction but is instead evaluated at a single temperature, concentration, and density [9]. The first hurdle of this Rapid Communication is to establish that the macroscopic (λ_N) and microscopic (λ) definitions of the thermal conductivity are equivalent at steady state.

In principle, atomistic nonequilibrium molecular dynamics (NEMD) simulations can be used to directly measure the heat flux \mathbf{J}_q through a system’s boundaries to obtain the “observed” nonequilibrium thermal conductivity λ_N . Equilibrium simulations can then be used to measure λ for comparison, as well as to elucidate any underlying mechanisms behind “anomalous” behavior. Unfortunately, large and long-duration nonequilibrium simulations are required to directly study heat conduction in nanofluids [10], and so only a limited range of molecular models and techniques is computationally accessible using this method. Due to these limitations, previous simulation work has primarily focused on equilibrium simulations of nanofluids at fixed size and mass asymmetries between the fluid molecule and nanoparticle [7,11–15] with only a few studies at larger asymmetries (e.g., Refs. [8,16]). As equilibrium molecular simulations are conducted at a single temperature and concentration, Eq. (3) cannot be used, thus the equivalence between λ_N and λ cannot be conclusively established.

In this Rapid Communication, NEMD simulations of binary hard-sphere mixtures, consisting of spheres of diameter σ_1 and mass m_1 and spheres of diameter σ_2 and mass m_2 , confined between two smooth parallel walls (see Fig. 1), are performed using the DYNAMO [17] event-driven molecular simulation package. The hard-sphere model is both computationally accessible and well described by revised Enskog theory [7,18,19] which can be used to yield accurate predictions of λ at low densities [16]. Although the hard-sphere model is simple, it qualitatively captures the fundamental effects of density, molecular size, and mass on the transport coefficients in gases. This Rapid Communication explores conditions close to the ideal gas limit for simplicity (and to avoid crystallization as σ_2/σ_1 becomes large); however, the results obtained in this limit are fundamental to the behavior of all fluids and comparison against experiments on gas mixtures can be made. This limit is also particularly interesting as the current discussion in nanofluids echoes previous controversy over reported enhancements in the thermal conductivity of He-H₂ gas mixtures [20]. Although the source of the original controversy (a sharp minimum in conductivity with concentration) was later shown to be unrepeatable [21,22], a shallower minimum still remains and demonstrates that thermal conductivity can lie outside the series and parallel bounds

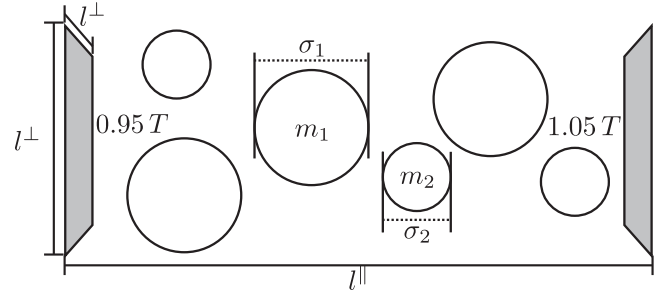


FIG. 1. A schematic of the system configuration used for the simulations reported here which use a hard-sphere model consisting of two species with diameters σ_1 and σ_2 , and masses m_1 and m_2 , respectively. For NEMD simulations, two walls are inserted into the simulation and a 10% temperature gradient is imposed via velocity reassignment on collision with the wall [24]. The total number of spheres N and aspect ratio l^{\parallel}/l^{\perp} of the simulation are varied to explore the effects of system size at a constant density and pressure.

and even beyond the pure fluid values. If this is correct, then it implies that such minima are also possible for nanofluid systems which are the subject of some controversy even today.

The first aim of this Rapid Communication is to establish an equivalence of the observed, λ_N , and steady-state, λ , thermal conductivities. This is conducted using a hard-sphere mass ratio of $m_2/m_1 = 2$ corresponding to a He-H₂ mixture with the approximate size ratio $\sigma_2/\sigma_1 = 260/289$, obtained from diffusion measurements [23]. A constant reduced pressure of $p\sigma_1^3/(k_B T) = 0.01$ (where k_B is the Boltzmann constant) is used and is set by adjusting the system density. This reduced pressure value corresponds to a packing fraction of approximately 0.005 over the studied mole fraction x_2 . Once the equivalence of λ and λ_N is confirmed in this system, a systematic exploration for “anomalous” thermal conductivities is carried out over the mass and size ratio parameter space using kinetic theory.

Parallel smooth walls are located at both ends of the simulation domain as illustrated in Fig. 1 with periodic conditions on all other boundaries. On collision with the wall, the normal component of a sphere’s velocity is reassigned to a Maxwell-Boltzmann distribution [24] at a defined temperature. The heat flux is then measured through the following expression, $\langle \mathbf{J}_q \rangle = \langle Q \rangle l^{\parallel} / (l^{\perp})^2$, where $\langle Q \rangle$ is the time-averaged rate of energy transferred to the simulation during sphere impacts with the walls averaged over both walls. The two walls have different temperatures set to 95% and 105% of the system temperature T . This value is a trade-off between inducing a sufficiently large heat flux (compared to thermal fluctuations) and inducing inhomogeneity in the system.

An example of the inhomogeneity induced by the heat flux is given in Fig. 2. The temperature, number density, and concentration plots appear approximately linear. It is clear to see the effects of thermophoresis in the concentration profiles. These inhomogeneities make equating λ_N and λ suspicious as λ is only evaluated at a single representative concentration, temperature, and density, whereas NEMD simulations measure an average thermal conductivity across the system as temperature, density, and concentration varies. Boundary layers with high thermal resistance also exist very close to the

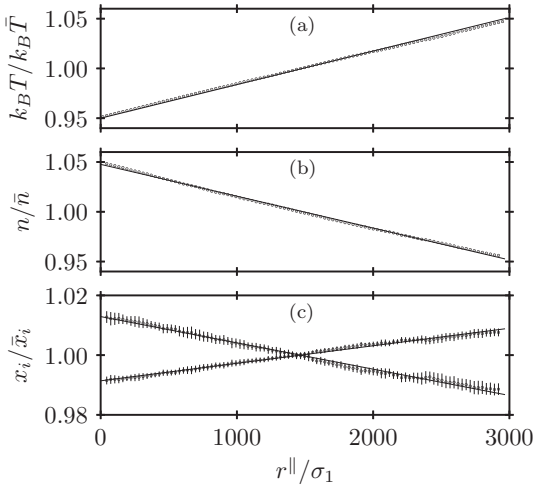


FIG. 2. The profiles of (a) temperature $k_B T$, (b) number density n , and (c) species mole fraction x_i as a function of distance between the two heated walls r^{\parallel} for a single representative simulation. This system has a mass ratio of $m_2/m_1 = 2$, a size ratio of $\sigma_2/\sigma_1 = 0.899\,654$, $N = 102\,400$ spheres, and an aspect ratio of $l^{\parallel}/l^{\perp} = 50$. All values are reduced by the average values for the system, which are $k_B \bar{T} = 1$, $\bar{n} \approx p\sigma_1^3/(k_B T) = 0.01$, and $(1 - \bar{x}_1) = \bar{x}_2 = 0.6$. Error bars represent the standard deviation across ten simulations and are smaller than the marker size for the temperature and number density fields. Solid lines are linear fits provided as a guide to the eye.

heated walls and induce a significant system-size dependence in the NEMD results.

To explore this system-size dependence, the wall temperatures are held fixed while the aspect ratio l^{\parallel}/l^{\perp} and system size are varied with the number of spheres ranging from $N = 5000$ up to $N = 102\,400$. Each simulation is initialized in an fcc crystal lattice and equilibrated for $1000N$ collisions before a further production run of $10\,000N$ collisions to collect data. This procedure is repeated ten times at each state point and average values between the production runs are collected while the errors of the average measurements are estimated using the standard deviation of values between each production run. Results are reported here in reduced units, with σ_1 the unit of length, m_1 the unit of mass, and $k_B T$ the unit of energy.

A system-size dependence calculation for the mole fraction $x_2 = 0.8$ in the He-H₂ system is reported in Fig. 3. The figure demonstrates that the aspect ratio of a system is relatively unimportant and that the system length in the direction of conduction l^{\parallel} dominates the system-size effects (due to the boundary layer resistance near the walls). To estimate the infinite system-size (near-zero thermal gradient) value of the thermal conductivity, linear extrapolation is applied to systems with the three largest aspect ratios ($l^{\parallel}/l^{\perp} = 10, 25$, and 50). This procedure yields a lower bound for the thermal conductivity as the gradient of the system-size dependence monotonically increases with system size. The extrapolated λ_N value is in excellent agreement with the equilibrium thermal conductivity λ from revised Enskog theory evaluated at the average conditions of the system.

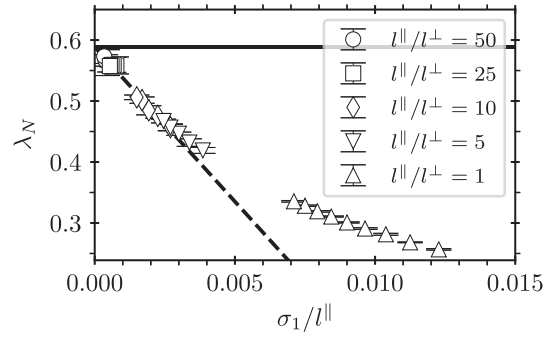


FIG. 3. The observed thermal conductivity λ_N obtained from NEMD simulations as a function of the distance between the walls σ_1/l^{\parallel} from binary hard-sphere systems with varying numbers of spheres and aspect ratios at a mole fraction of $x_2 = 0.8$ for a $m_2/m_1 = 2$, $\sigma_2/\sigma_1 = 0.899\,654$, and $p\sigma_1^3/(k_B T) = 0.01$. A linear fit to the data points obtained using an aspect ratio of 10, 25, and 50 (dashed line) is used to extrapolate to infinite system size and approaches the value of λ predicted by revised Enskog theory (solid line).

The above procedure is repeated over a range of mole fractions and the final infinite-system extrapolated results are reported in Fig. 4. This system exhibits thermal conductivities that are far outside the predictions of continuum approaches such as Maxwell theory or the limits of series and parallel resistance. In accordance with the experimental results for He-H₂ [20–22], the system displays a minimum in the thermal conductivity below both the pure fluid thermal conductivities. This conclusively demonstrates that anomalous thermal conductivities are not only possible but a fundamental feature of simple molecular fluids such as the binary hard-sphere gas.

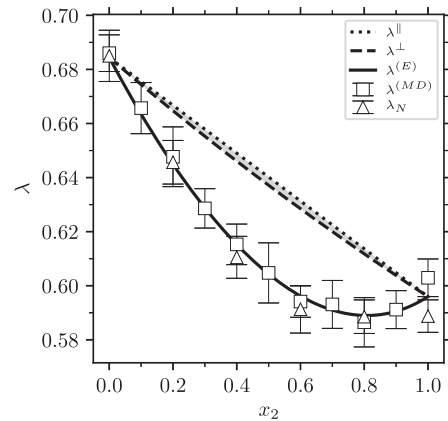


FIG. 4. The extrapolated infinite system-size NEMD λ_N (triangles) and equilibrium steady-state $\lambda^{(MD)}$ (square) thermal conductivities as a function of the nonunit species mole fraction x_2 . Parallel (dotted line) and series (dashed line) limits bound the region of continuum values (shaded). The revised Enskog theory predictions for the steady-state conductivity $\lambda^{(E)}$ (solid line) are in excellent agreement with the simulation results. A slight apparent overestimation arises from the remaining system-size dependence of our NEMD results.

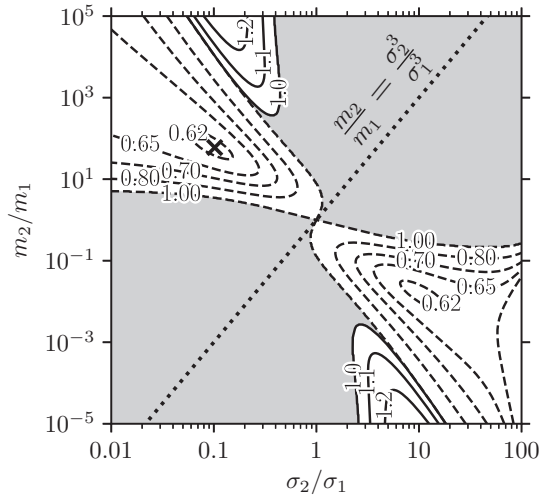


FIG. 5. A contour map of steady-state thermal conductivities outside the series (dashed) and parallel (solid) bounds as a function of mass and size ratio. The contours denote the increase and decrease of the thermal conductivity relative to the parallel and series bound at the concentration of maximum deviation. A cross indicates the maximum decrease of the steady-state thermal conductivity which occurs at $m_2/m_1 \approx 59.6$ and $\sigma_2/\sigma_1 \approx 0.102$. A dotted line indicates where mass scales with molecular volume, assuming a constant density.

To further validate the Enskog and NEMD results, equilibrium simulations with $N = 32\,000$ spheres in a cubic system are equilibrated for $1000N$ events before being run for a further $100\,000N$ events to calculate L_{uu} , L_{u1} , and L_{11} for this system. The Einstein form of the Green-Kubo relations [25,26] is used with the first 15 mean free times of the correlation discarded to avoid ballistic motion and a maximum correlation time of 50 mean free times used to avoid correlations from the periodic boundary conditions. This is beyond the sound wave traversal time of the system; however, as the density is so low, correlations from the boundary conditions take much longer to establish than in higher density systems. The excellent agreement in Fig. 4 between revised Enskog theory and the equilibrium molecular dynamics completes the verification of the anomalous dehancement reported and the use of revised Enskog theory to further study the system at low densities.

The full parameter space of the binary hard sphere model is explored using revised Enskog theory to determine the extent of the anomalous behavior. Figure 5 maps the maximum possible departure from series or parallel bounds achievable by varying the mole fraction of the system for a particular mass and size ratio. A reduced pressure of $p\sigma_1^3/(k_B T) = 10^{-7}$, corresponding to packing fractions below 0.044 for this parameter space, is used in these calculations to reveal the symmetry of the map in the ideal gas limit which is otherwise prevented by pure species 2 freezing [which occurs at a size ratio of $\sigma_2/\sigma_1 \gtrsim 4.87$ for $p\sigma_1^3/(k_B T) = 0.01$; however, this change makes little difference to the results below this boundary]. Anomalous enhancement above the parallel bounds is found at extreme mass ratios with size ratios near unity. Reductions below the series bounds are also found

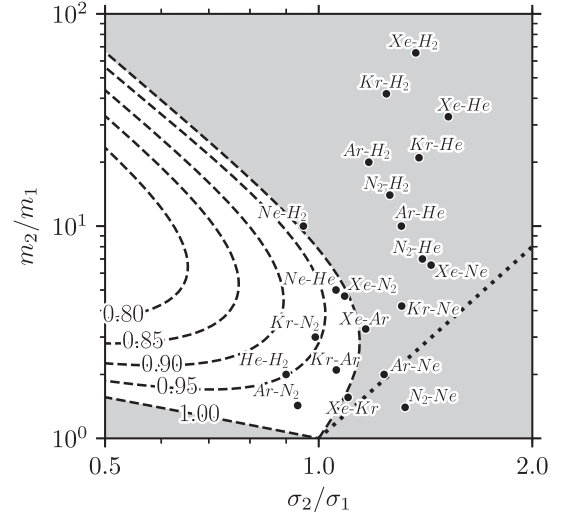


FIG. 6. As described in Fig. 5 but focused on the parameter space relevant for the noble gases, hydrogen, and nitrogen. Kinetic diameters are taken from Refs. [27–29].

for smaller but heavier spheres. Surprisingly, a maximum achievable reduction in thermal conductivity is found which is $\approx 40\%$ below the series limit (see the cross in Fig. 5). The bulk of the anomalous parameter space lies in the larger-but-lighter region of the map; however, the region of anomalous reduction approaches the line where the species 2 mass scales with its volume which is the experimentally relevant region.

To explore the experimental relevance of the results, the kinetic diameter and molecular mass ratios for combinations of the noble gases, along with nitrogen and hydrogen gas, are plotted in Fig. 6. The map indicates that several real mixtures may exhibit anomalous dehancements; however, care should be taken to verify this as the Enskog theory expressions used here do not take into account the additional degrees of freedom of diatomic gases and in general are not capable of quantitatively predicting the behavior of real gases, only general trends. It is expected that more complex molecules can exhibit more extreme effective size and mass ratios, although the anomalous enhancement region probably remains inaccessible and the applicability of the hard-sphere model is dubious in this limit.

In conclusion, the observed thermal conductivity of binary hard spheres can exhibit values which lie outside the limits of series-parallel resistance, in agreement with experimental results on He-H₂ systems. These anomalous results are present even in the ideal gas limit, which implies that they cannot be explained by any structural or clustering effect such as those which are prevalent in the nanofluid literature. To better understand results in nanofluids, liquid densities can be explored using the techniques outlined here; however, the binary hard-sphere model has two serious shortcomings: an ideal-gas heat capacity and the absence of a gas-liquid transition. Future work will explore adding internal degrees of freedom to the spheres to account for varying heat capacity which will allow a better parametrization of real fluids. Attractive systems, such as square wells, may also be used to explore liquid systems which do not have strong density-pressure dependences, and

the comparison at pressures where the nanoparticle forms a crystalline phase will be explored. Finally, work on a multiscale modeling approach using kinetic theory to provide phenomenological closures to a hydrodynamic description is underway to allow fluid dynamics simulations of nanofluidic devices where transient effects may dominate over steady-state conduction.

The authors acknowledge the support of the Maxwell computing service at the University of Aberdeen, and the Aberdeen-Curtin Alliance [30] between the University of Aberdeen (Scotland, U.K.) and Curtin University (Perth, Australia) which is funding the Ph.D. of C.M. Also, P.R. and J.D.G. thank the Australian Research Council for funding.

-
- [1] J. A. Eastman, S. U. S. Choi, S. Li, W. Yu, and L. J. Thompson, *Appl. Phys. Lett.* **78**, 718 (2001).
 - [2] P. Keblinski, R. Prasher, and J. Eapen, *J. Nanopart. Res.* **10**, 1089 (2008).
 - [3] J. Buongiorno, D. C. Venerus, N. Prabhat, T. McKrell, J. Townsend, R. Christianson, Y. V. Tolmachev, P. Keblinski, L.-w. Hu, J. L. Alvarado *et al.*, *J. Appl. Phys.* **106**, 094312 (2009).
 - [4] J. Eapen, R. Rusconi, R. Piazza, and S. Yip, *J. Heat Trans.* **132**, 102402 (2010).
 - [5] Y. Hwang, J. K. Lee, C. H. Lee, Y. M. Jung, S. I. Cheong, C. G. Lee, B. C. Ku, and S. P. Jang, *Thermochim. Acta* **455**, 70 (2007).
 - [6] S. de Groot and P. Mazur, *Non-Equilibrium Thermodynamics* (Dover, New York, 1984).
 - [7] J. J. Erpenbeck, *Phys. Rev. A* **39**, 4718 (1989).
 - [8] S. Bastea, *Phys. Rev. E* **75**, 031201 (2007).
 - [9] It should be noted that this is not the only definition of the thermal conductivity which is independent of the choice of fluxes. For example, another definition can be derived by assuming no concentration gradients are present (e.g., at the onset of thermal conduction) but allowing chemical potential gradients to arise due to gradients in the temperature. This is not explored here as it is demonstrated that $\lambda_N \approx \lambda$ at steady state, but this definition may have relevance for systems undergoing rapid changes in temperature.
 - [10] J. Armstrong and F. Bresme, *Phys. Chem. Chem. Phys.* **16**, 12307 (2014).
 - [11] J. J. Erpenbeck, *Phys. Rev. A* **45**, 2298 (1992).
 - [12] J. J. Erpenbeck, *Phys. Rev. E* **48**, 223 (1993).
 - [13] D. M. Heyes, *J. Chem. Phys.* **96**, 2217 (1992).
 - [14] J. Eapen, J. Li, and S. Yip, *Phys. Rev. Lett.* **98**, 028302 (2007).
 - [15] N. A. T. Miller, P. J. Daivis, I. K. Snook, and B. D. Todd, *J. Chem. Phys.* **139**, 144504 (2013).
 - [16] M. N. Bannerman and L. Lue, *J. Chem. Phys.* **130**, 164507 (2009).
 - [17] M. N. Bannerman, R. Sargant, and L. Lue, *J. Comput. Chem.* **32**, 3329 (2011).
 - [18] M. López de Haro, E. G. D. Cohen, and J. M. Kincaid, *J. Chem. Phys.* **78**, 2746 (1983).
 - [19] M. J. Lindenfield and B. Shizgal, *Chem. Phys.* **41**, 81 (1979).
 - [20] P. Mukhopadhyay and A. K. Barua, *Br. J. Appl. Phys.* **18**, 635 (1967).
 - [21] L. Biolsi and E. A. Mason, *J. Chem. Phys.* **54**, 3020 (1971).
 - [22] A. G. Shashkov, F. P. Kamchatov, and T. N. Abramenko, *J. Eng. Phys.* **24**, 461 (1973).
 - [23] B. D. Freeman, *Macromolecules* **32**, 375 (1999).
 - [24] T. Pöschel and T. Schwager, *Computational Granular Dynamics* (Springer, New York, 2005).
 - [25] M. S. Green, *J. Chem. Phys.* **22**, 398 (1954).
 - [26] R. Kubo, *J. Phys. Soc. Jpn.* **12**, 570 (1957).
 - [27] D. W. Breck, *Zeolite Molecular Sieves: Structure, Chemistry, and Use* (Wiley, New York, 1973).
 - [28] A. F. Ismail, K. Khulbe, and T. Matsuura, *Gas Separation Membranes* (Springer, New York, 2015).
 - [29] S. Matteucci, Y. Yampolskii, B. D. Freeman, and I. Pinnau, in *Materials Science of Membranes for Gas and Vapor Separation* (Wiley, Chichester, 2006), Chap. 1.
 - [30] <http://aberdeencurtinalliance.org>.